

THÈSE DE DOCTORAT

Soutenue à AMU — Aix-Marseille Université
le 13 décembre 2024 par

Ilaria CASTALDI

Mixing liquids of unequal viscosity

Discipline

Sciences pour l'Ingénieur

Spécialité

Mécanique et physique des fluides

École doctorale 353

Sciences pour l'Ingénieur :
Mécanique, Physique, Micro et Nanoélectro-
nique

Laboratoire/Partenaires de recherche

IUSTI

Composition du jury

Sylvie LORTHOIS DR, CNRS IMFT	Rapporteure
Detlef LOHSE PR, Université de Twente	Président du jury
Mauro SBRAGAGLIA PR, Università degli studi di Roma Tor Vergata	Examineur
Anne DE WIT PR, Université libre de Bruxelles	Examinatrice
Bloen METZGER DR, CNRS IUSTI	Directeur de thèse
Henri LHUISSIER CR, CNRS IUSTI	Co-directeur de thèse

Affidavit

Je soussigné·e, Ilaria Castaldi, déclare par la présente que le travail présenté dans ce manuscrit est mon propre travail, réalisé sous la direction scientifique de Bloen Metzger et Henri Lhuissier, dans le respect des principes d'honnêteté, d'intégrité et de responsabilité inhérents à la mission de recherche. Les travaux de recherche et la rédaction de ce manuscrit ont été réalisés dans le respect à la fois de la charte nationale de déontologie des métiers de la recherche et de la charte AMU relative à la lutte contre le plagiat.

Ce travail n'a pas été précédemment soumis en France ou à l'étranger dans une version identique ou similaire à un organisme examinateur.

Fait à Marseille le 13/10/2024



Cette œuvre est mise à disposition selon les termes de la [Licence Creative Commons Attribution - Pas d'Utilisation Commerciale - Pas de Modification 4.0 International](https://creativecommons.org/licenses/by-nc-nd/4.0/).

Liste de publications et participation aux conférences

Liste des publications et/ou brevets réalisées dans le cadre du projet de thèse :

1. Castaldi, I., B. Metzger, and H. Lhuissier. "Shearing Liquids of Unequal Viscosity : Can Mixing be Independent of Stirring Rate at a Large Viscosity Ratio?." *Physical Review Letters* 133.15 (2024) : 154001.

Participation aux conférences et écoles d'été au cours de la période de thèse :

1. "Frontiers of mixing" (15 août 2023 - 25 août 2023) *Institut d'Études Scientifiques de Cargèse*
2. 76th Annual Meeting of the APS Division of Fluid Dynamics (*Washington, USA*)

Résumé et mots clés

Cette thèse pose la question suivante : Comment deux liquides miscibles de viscosités différentes se mélangent, i.e. finissent par s'homogénéiser par diffusion moléculaire, lorsqu'ils sont brassés ? Le mélange de telles hétérogénéités de viscosité est au cœur de nombreuses applications industrielles (e.g. dans l'industrie alimentaire ou le génie civil) et de phénomènes naturels (e.g. dans le manteau terrestre), mais le problème n'a reçu que peu d'attention jusqu'à présent, en raison peut-être de sa complexité générale. En effet, le chemin vers l'homogénéisation dépend fortement de la déformation des hétérogénéités, qui peut, ou non, augmenter les surfaces d'échange et accentuer les gradients de concentration, tandis que la cinématique elle-même résulte de l'écoulement appliqué et du champ d'hétérogénéité. Ce problème d'advection-diffusion doublement couplé est généralement complexe, mais nous montrons dans cette thèse que des résultats fondamentaux importants peuvent être obtenus en étudiant le cas d'une hétérogénéité isolée et initialement localisée dans un écoulement visqueux.

Plus particulièrement, nous considérons expérimentalement et théoriquement le mélange d'un blob initialement sphérique et plus ou moins visqueux dans deux écoulements modèles : un écoulement de cisaillement simple et un écoulement chaotique laminaire, à nombre de Reynolds faible et nombre de Péclet élevé. Pour ces configurations bien contrôlées, les questions suivantes ont été abordées : Comment le rapport de viscosité avec le bain affecte-t-il la cinématique de déformation du blob et son taux d'étirement ? Comment s'opère l'interdiffusion entre deux liquides visqueux de compositions différentes ? Comment et à quelle vitesse le couplage entre cinématique et diffusion réalise finalement le mélange, pour différents rapports de viscosité et différentes intensités d'agitation ?

La configuration de cisaillement simple révèle une transition remarquable entre étirement et roulement lorsque le rapport de viscosité dépasse une valeur critique. Un blob suffisamment visqueux ne s'étire plus mais roule. Cette transition allonge considérablement le temps de mélange, car un blob roulant est entouré d'une région de recirculation à travers laquelle les transferts de masse sont essentiellement diffusifs et lents. En conséquence, le blob se mélange selon un lent processus de 'pseudo-dissolution', en un temps qui, de manière remarquable et contre-intuitive, ne dépend plus de la vitesse d'agitation ! Curieusement, l'écoulement chaotique laminaire conduit à une phénoménologie très différente aux conséquences presque opposées. Un blob très visqueux est étiré par l'écoulement, mais le taux d'étirement reste faible (en raison du rapport de viscosité élevé) jusqu'à ce que le blob se soit déformé significativement. Ensuite, le blob est étiré rapidement et mélangé presque

immédiatement par l'écoulement chaotique. Dans ce cas, le blob est mélangé en un temps fixé purement par la force d'agitation et la viscosité de la goutte, sans dépendance pratique à la diffusivité.

Cette description est basée sur des expériences systématiques qui ont été réalisées sur une large gamme de rapports de viscosité et de nombres de Péclet. Elle a été rationalisée par des prédictions théoriques, qui se comparent favorablement aux expériences, sans paramètre d'ajustement. Les résultats présentés dans cette thèse ouvrent de nouvelles directions de recherche, de l'exploration des instabilités induites par un champ de viscosité à l'étude du mélange d'hétérogénéités de viscosité dans des écoulements inertiels plus complexes, des milieux poreux ou des systèmes biologiques.

Mots clés : écoulement visqueux, mélange, instabilité du flux, écoulement chaotique

Abstract and keywords

This PhD thesis tackles the following question: How and how fast two miscible liquids having different viscosities mix, i.e., eventually homogenize by molecular diffusion, when they are stirred? Mixing such viscosity heterogeneities is the core of many industrial applications (e.g. in food industry or civil engineering) and natural phenomena (e.g. in the earth mantle), but the problem has received only little attention so far, maybe because of its general complexity. Indeed, the route to homogenization highly depends on the deformation kinematics of the heterogeneities, which may increase mixing surfaces and steepen concentration gradients, or not, while the kinematics itself is set by the applied flow and the heterogeneity field. This doubly coupled advection-diffusion problem is generally complex, but we show in this thesis that important fundamental results can be obtained by studying the case of an isolated and initially localized heterogeneity in a viscous flow.

More particularly, we consider experimentally and theoretically the mixing of an initially spherical and more or less viscous blob in two model stirring flows: a simple shear and a laminar chaotic flow under low Reynolds and high Péclet number conditions. On these well controlled configurations, the following questions have been addressed: How does the viscosity ratio with the stirred bath affect the deformation kinematics of the blob and its stretching rate? How does the inter-diffusion between two viscous liquids of different compositions proceed? How and how fast the combination between kinematics and diffusion eventually achieves mixing, for different viscosity ratio and different stirring intensities?

The simple shear flow configuration reveals a remarkable stretching-to-rolling transition when the viscosity ratio is increased above a critical value. Highly viscous blobs no longer stretch but roll. This kinematic transition dramatically lengthens the mixing time, because the rolling blob is surrounded by a recirculating region across which mass transfers are essentially diffusive and slow. As a consequence, the blob mixes through a slow 'dissolution-like' process, in a time, which remarkably and somehow counterintuitively, no longer depends on the stirring rate! Interestingly, the laminar chaotic flow configuration leads to a very different mixing phenomenology with almost opposite consequences. A highly viscous blob is eventually stretched by the flow, but the stretching rate remains very low (because of the high viscosity ratio) until the blob has deformed significantly. Beyond this point, the blob is stretched very rapidly and mixed close to immediately by the chaotic flow. In this case, the blob is mixed in a time which is purely set by the stirring strength and the blob viscosity, with virtually no dependence on the diffusivity.

This picture is based on systematic experiments, which have been performed over a wide range of viscosity ratios and Péclet numbers. It has been rationalized by theoretical predictions, which compare favorably with experiments without any fitting parameter. The results presented in this PhD thesis open new research directions, from the exploration of viscosity field induced instabilities, to the investigation of how viscous heterogeneities mix in more complex inertial flows, porous media or biological systems.

Keywords: viscous flows, mixing, flow instability, chaotic flow

Remerciements

Tre anni di vita non sono semplici da riassumere, tanto a livello scientifico, quanto a livello affettivo, ma da qualche parte bisogna pur cominciare.

I would like to start by thanking Henri Lhuissier, without whose passion and care I would be half of who I am today. *(And while I have learned something, I still feel extremely far from catching up.)* I have never doubted that I stand to learn “from one of the best theoretical and experimental physicists the world has to offer,” *(cit.)* and today, I am sure that in the future, others can gladly do so as well. *Along with that, I'd like to thank the turbulence that characterized our supervisor-student relationship through which, I am sure, we both have grown and that cannot make me more proud.*

And Bloen Metzger, for his creative and charismatic guidance and sharp and ever-ready insight. For every critique, feedback and advice received over the years and in the development of this thesis. *For all the things I've learned to do, but that he knows best anyway.* For his incredible competence and resourcefulness in the lab, which I aspire to achieve someday and will surely always remember with joy.

Special thanks to Mathieu Souzy - *whom I like to remind is the second reason I am here* - for laying the foundation for the project, being a caring and talented scientist as well as a wonderful and kind person. *I no longer count the times you have (often unknowingly) helped me over the years. Thank you.*

I would like to thank Sylvie Lorthois, Detlef Lohse, Anne De Wit and Mauro Sbragaglia, members of the jury, for agreeing to read and examine me and my thesis. *I feel extremely proud and honored to be able to present this work to you.*

I would like to thank Emmanuel Villermaux, for being the best teacher I have had. Being part of an ITN is a blessing. I have visited more places in these years than I did in my life before the Ph.D. and, more importantly, I have come into contact with realities, cultures and people so different, yet so close, that I can only be grateful. So thank you to my fellow adventurers spread all over Europe (and soon all over the world) : Alexandar, Guillermo, Johnson, Klebbert, Kostis, Kyrell, Luka, Manuel, Marco, Max, Nico, Rima, Simone, Vlady and, *last but not least, my friend Elisabeth.* I would like to thank Anne De Wit again for hosting me in Brussels and making me part of a wonderful side project on mixing. *The months in Brussels were a breath of fresh air (in every sense of the word) and a very pleasant break.*

Un ringraziamento speciale va al luogo dove sono nata e cresciuta come scienziata, precisamente il corridoio C1 della facoltà di Scienze Matematiche, Fisiche e Naturali dell'Università di Roma "Tor Vergata", popolato dagli incredibili ricercatori da cui ho avuto l'onore di imparare : Roberto Benzi, Luca Biferale e Mauro Sbragaglia. *Grazie.*

Ma anche sede di quel luogo magico dove ho trovato, ritrovato e costruito parte di me nelle persone più belle che la vita mi potesse donare : la '4501' con Fabio, Francesca e Martino.

Una menzione aggiuntiva a Mauro Sbragaglia - *per essere stato il primo ad aver conosciuto i miei ritardi nelle consegne* - per avermi accompagnata dalla tesi triennale, alla tesi magistrale, fino ad oggi. *Non davo per nulla per scontato che avresti accettato di far parte anche di quest'ultimo traguardo, grazie.*

On the list of most sincere thanks are undoubtedly Bruno, Hugo and Benoit, the students who actively contributed, enriched or initiated this project. *Your attentive, dedicated and motivated contribution has been more than essential to the outcome of this project and to my education, thank you from the bottom of my heart.*

Thank you to those who (more or less) with me and (surely) like me (*but with less drama*) have gone through this doctoral journey here : Chongwei, Nikhil, and Simon. *Having you close by as companions on this and a thousand other adventures has made it all the way more glad, rich and joyful. Thank you.*

I feel that the permanence in this lab would not have been very easy and pleasant if it were not for the young researchers who populate it (or have populated it in these three years of stay) : Alexis, Aubin, Chico, Denis, Hector, Lea, Mathieu, Terance, Victor and Vincent. *Each of you (each in their time-scale) has contributed in accompanying me on this journey, making me feel safe and in the right place, even when I was convinced I was not. Watching you work, grow and interact makes me believe that the future of the (scientific) world, after all, is in very good hands.*

Ringrazio mia sorella, Valeria, cui dedico questo traguardo. Per avermi insegnato la complicità, l'amore, la condivisione. *Ché in due la vita è più semplice, anche a distanza.*

I miei genitori, certamente fieri, e i nonni che lo sono ancora di più. *Per l'affetto e il supporto e per lasciarmi essere ancora figlia e nipote, prima di essere donna e scienziata.*

Gli amici di una vita : Dibbio, Gratta e Maco. *Per regalarmi una storia da raccontare ogni volta che siamo insieme. Grazie.*

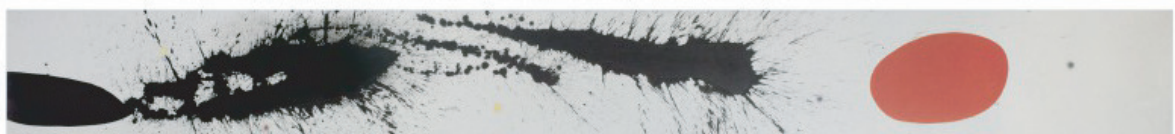
Un grazie alla mia numerosa ed affiatata famiglia. Per fare spazio a tutti e non lasciare indietro nessuno, per gioire e far fronte agli imprevisti insieme. Per accettare e incoraggiare, curare e supportare. *Sì, cugini, siamo proprio noi. Siete proprio voi, grazie.*

Alla famiglia che ho scelto per ridere, piangere, vivere, viaggiare e mangiare la domenica in questa vita da fuori sede : Davide, Giulia e Mariadebora. *Cuori pulsanti, pronti e sincronizzati. Non immaginate quanto mi sono sentita (e mi senta tuttora) fortunata ad aver incrociato le vostre strade, ogni mio traguardo è anche il vostro.*

Per ultima, ma mai meno importante, ringrazio quella che è la colonna portante della mia vita da che ho coscienza. Colei che scandisce i tempi macroscopici, l'unico sguardo ad un futuro prossimo, mai incerto. Quella dimensione di massima espressione che non teme una nuova lingua e non conosce inadeguatezza.

In altre parole : grazie, allo spazio fisico e affettivo dell'Accademia, a Ludovick, il mio maestro. E grazie a tutti quelli che, in un modo o nell'altro, hanno ballato con me.

-i.



Joan Miró, *Le jour*, 1974

Contents

I	Introduction	1
I.1	Context, motivation & challenges	1
I.2	Isoviscous mixing: state of the art	5
I.2.1	What is mixing?	5
I.2.2	Diffusion in a still liquid	5
I.2.3	Mixing in a strained liquid: the Ranz formalism	6
I.2.3.a	Simple shear flow	8
I.2.3.b	Purely extensional flow	9
I.2.3.c	Chaotic flow	9
I.3	Diffusivities in viscous liquids	11
I.3.1	In a uniform liquid	11
I.3.2	In a non-uniform liquid	12
I.4	Kinematics of deformation of an heterogeneity	14
I.4.1	Solid particle	14
I.4.2	Immiscible liquid drop	15
I.4.3	Miscible drop	17
I.5	Goal of the thesis & manuscript overview	18
II	Experimental methods & characterizations	19
II.1	Liquids	20
II.1.1	Choice of the liquids	20
II.1.2	Viscosity ratio λ	20
II.1.3	Density matching	21
II.1.4	Preparation of the liquids	22
II.2	Principle of the visualization techniques	23
II.2.1	Fluorescence	23
II.2.2	Index of refraction	24
II.3	Effective diffusivities	26
II.3.1	Experimental setup	26
II.3.2	The two measurements techniques	27
II.3.2.a	Fluorescence technique	27
II.3.2.b	Synthetic schlieren technique	28
II.3.3	Comparison between the fluorescence profile and the mass fraction profile & interpretation	31
II.3.4	Diffusion coefficients: summary of the results	34
II.4	Initial shape of the viscous blob	37
II.5	Conclusion	39

III	Mixing in a simple shear flow	41
III.1	Simple shear setup	43
III.1.1	Principle of the shear cell	43
III.1.2	Additional features of the shear cell	44
III.1.3	Quantification of the blob deformation & mixing	46
III.2	Kinematics of deformation of the blob (infinite Pe limit)	48
III.2.1	General observations	48
III.2.2	Model for the blob deformation kinematics	49
III.2.3	Comparison between model & experiments	51
III.2.4	Copy of the letter	52
III.2.5	Additional informations	68
III.2.5.a	Folding regime	68
III.2.5.b	Flow reversibility	69
III.3	Mixing of the blob	70
III.3.1	General observations	70
III.3.2	Mixing in the <i>stretching regime</i>	70
III.3.2.a	Phenomenology & quantification	71
III.3.2.b	Mixing model including the stretch shift factor β	71
III.3.2.c	Model versus experimental results	72
III.3.3	Mixing in the <i>rolling regime</i>	74
III.3.3.a	Phenomenology & quantification	74
III.3.3.b	Mixing model: a 'dissolving' rolling sphere	77
III.3.3.c	Model versus experimental results	78
III.4	Conclusion	82
IV	Mixing in a chaotic flow	85
IV.1	Chaotic flow setup	87
IV.2	Base flow characterization & reference isoviscous case	89
IV.2.1	Flow field	89
IV.2.2	Flow statistics	90
IV.2.3	Stretching statistics	91
IV.2.4	The reference isoviscous mixing case	92
IV.3	Kinematics & mixing of a more viscous blob	94
IV.3.1	General observations	94
IV.3.2	Influence of the viscosity ratio	95
IV.3.3	Model of the slow-stretching initial transient (large Pe limit)	96
IV.3.3.a	Large Pe kinematics in a steady extensional flow	96
IV.3.3.b	Heuristic model of the large Pe kinematics in a chaotic flow	98
IV.3.3.c	A more refined stochastic model of the large Pe kinematics in a chaotic flow	98
IV.4	Dependence on Pe & mixing time of the blob	101
IV.4.1	Dependence of the kinematics on Pe	101
IV.4.2	Mixing time of the blob	102
IV.5	Conclusion	104
V	Conclusion	107

A Stochastic model of the blob kinematics in a chaotic flow in the large Pe limit	113
A.1 Mean field approximation	114
A.1.1 Derivation	114
A.1.2 Isoviscous case & link with the Lyapounov exponent	115
A.1.3 Case of a highly viscous blob ($\lambda \gg 1$)	116
A.2 Brute force simulations	118

Chapter I

Introduction

I.1 Context, motivation & challenges

Mixing refers to the process by which two miscible substances evolve from an initial state of segregation to a final state of complete uniformity, *via* the combined contribution of stirring and molecular diffusion [1–6]. It is encountered everywhere in nature and everyday life, where it operates on vastly different scales, from the transport of oxygen through blood microcirculation [7], to transfers within and between the atmosphere, the oceans and the earth itself [8–16], to blending in culinary and pastry processes. Mixing determines the dispersion of odors and the research strategy of animals driven by chemotaxis [17, 18]. It is determinant in the access to nutrients and population growth for small organisms [19, 20], as well as for the exposure of all populations to pollutants [21]. Mixing is also central to many applications. In chemistry and transport, because it is necessary to trigger, enhance or maintain chemical reactions and combustion [22–24], in building and manufacturing industries to produce highly transparent glass [25, 26] or homogenize polymer blends, cements, plasters, and paints [27–29].

These phenomena are non-trivial to understand because their flow (natural convection, mechanical

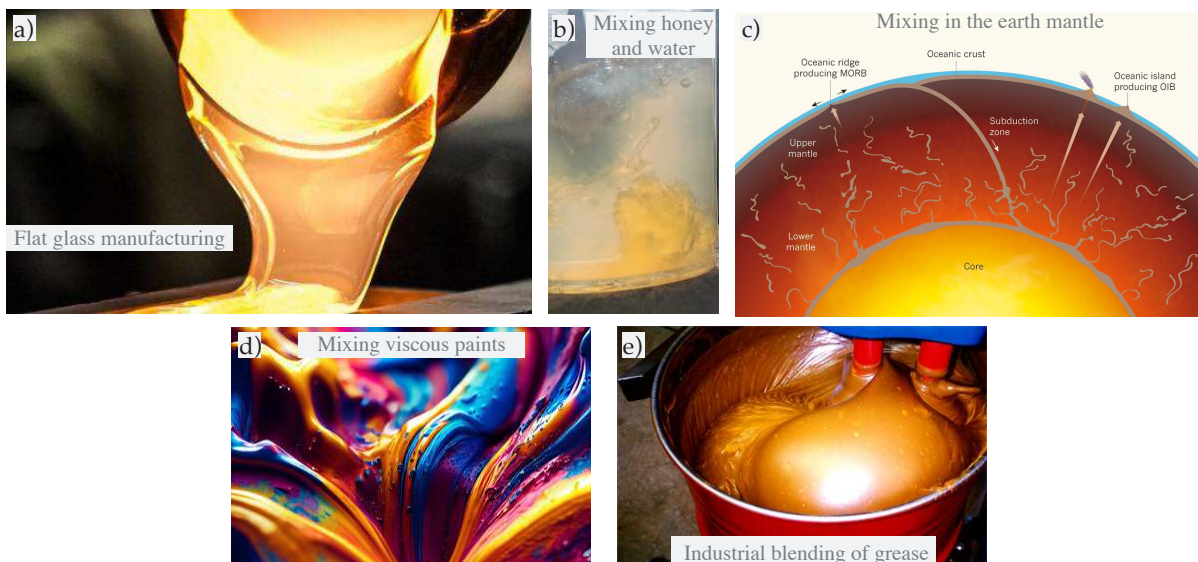


FIGURE I.1: *Mixing liquids of unequal viscosity.* (a) Flat glass manufacturing. (b) Some honey and water mix upon stirring with a spoon. (c) On geological time scales ($\sim 10^2$ million years) the earth mantle creeps and large scale heterogeneities between rocks are laminated and eventually homogenized (sketch reproduced from [14]). (d) Partly mixed viscous paints. (e) An industrial double helix stirrer homogenizes a grease.

stirring) is unsteady, chaotic or even turbulent, which gives non-trivial dispersion patterns, and eventually non-trivial mixing processes. These effects have been extensively documented, in particular for situations where all fluids flow in the same way, whether they are mixed or not [30–33]. However, many of the phenomena listed above (the earth mantle [8–12, 14], the molten glass paste [25, 26], the polymer blends [27–29], see Fig. I.1) involve mixing between very different fluids, which flow differently from each other, and even differently once they have mixed. Obviously, the case of fluids of different properties present additional complexities and involve different mechanisms, that we will stressed below. But, in spite of their major importance in many applications and natural phenomena, these mechanisms have received little attention so far. This is why, in this thesis, we have chosen to tackle the problem by asking the precise following question:

How two miscible liquids are mixed by a stirring flow when their viscosity is different ?

Anyone who has mixed a spoonful of honey in his teacup, or prepared a cake, knows that high viscosity contrasts make stirring poorly efficient and delay homogenization. This is also known by engineers, who are using specific stirrers or lamination devices (fast mixing is mostly dependent on the diameter of the impeller [34, 35]), or who study alternative geometries to break flow symmetries and promote homogenization [36], or who match the viscosity of the liquids with chemical additives to facilitate their mix, like for two-component epoxy glue [37]. However, it is a different question to document and understand how mixing proceeds in details, and how long will it take, for a given flow, given liquids, a given diffusivity and given initial conditions. The base equations for the flow and for diffusion are known, but not their general solution. Moreover, the parameter space is immense, which means that an insightful mechanistic approach is needed first.

A reasonable start point is of course the case of liquids with equal viscosity, with for instance one dyed and the other one not. This natural reference point will be called '*isoviscous case*' throughout the manuscript. In such case, both liquids are stretched and laminated by the flow, which forms thin and extended lamellae of dye and enhances mixing. Because of their thinness, these lamellae diffuse essentially transversally to their plane and they get significantly homogenized when the diffusive rate across them has become shorter than the thinning rate imposed by the flow. This lamellar description of mixing, introduced by Ranz [38], has proved successful in rationalizing mixing processes in various complex flows [1, 33, 39, 40]. However, this approach requires, first, that lamellae be indeed formed, which is not granted for liquids with unequal viscosity, second, that the thinning of the lamellae by the flow be known, which, again, is not trivial when they do not have the same viscosity.

This last remark, stresses one of the additional difficulties in understanding how heterogeneities in *viscosity* mix, which is related to the flow. Even when the viscosity field is known, determining the actual flow achieved in the different liquids by a given stirring or global forcing is a non-trivial, non-local and highly non-linear problem. Obviously, the heterogeneities are advected by the flow, which means the flow also depends on time. Another point to emphasize is that two liquids with significantly different viscosities contain at least two different substances (molecules), with a significant mass fraction of both. This situation is usually more complex than for diluted systems, where diffusion is linear and Fickian. In the concentrated case, the diffusivity can a priori vary between the two liquids, and when they mix. Moreover, the inter-diffusion may become non-linear for large concentration contrasts, if the mixture is non-ideal (i.e. has a significant enthalpy of mixing). These two points are already a challenge, but there is another specific feature of the non-isoviscous case, which is more fundamental and strongly limiting brute force approaches. A priori, the complexities of the flow and those of the diffusion problem *cannot* be separated. Indeed, when the viscosity field diffuses, the flow changes, which changes how the viscosity field is advected and, therefore, how it diffuses. This means that non-trivial feedbacks are expected. This also means that, even for vanishing inertia, the actual flow intrinsically depends on the stirring speed and

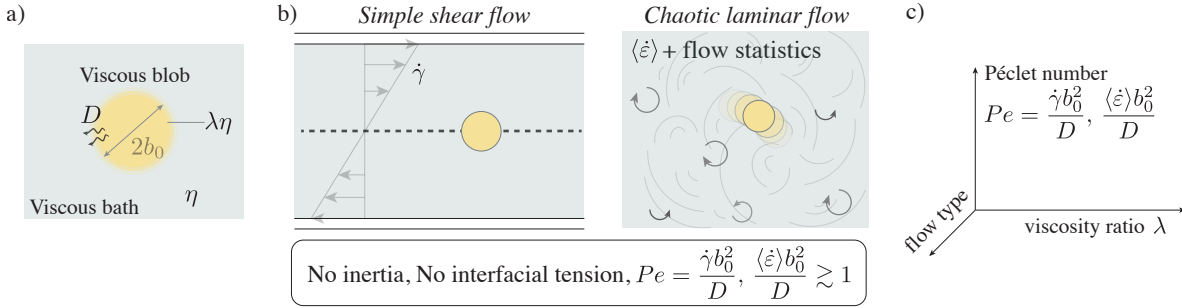


FIGURE I.2: *Problem studied.* (a) An initially spherical blob of viscosity $\lambda\eta$ stirred in a bath of viscosity η . (b) Archetypal flow configurations investigated: the simple shear flow and a laminar two-dimensional chaotic flow. (c) Parameter space.

the diffusivity of the viscosity field. For a fixed diffusivity, the flow obtained by, say, halving the stirring speed, is not simply twice as slow. It is qualitatively different, because the viscosity field has more time to diffuse, which changes the flow. In contrast to the isoviscous case, it is therefore a priori not enough to characterize or understand the flow for one stirring speed with one value of diffusivity, to know the flow for other speeds or diffusivities.

To tackle this intricate problem, we have chosen to focus on the case of a highly viscous flow (no effect of inertia) and an isolated and initially localized heterogeneity in viscosity. More particularly (see Fig. I.2), we consider the deformation of an initially spherical blob of viscosity η and radius b_0 immersed and stirred in a bath of a different viscosity $\lambda\eta$. We use fully miscible liquids, which interdiffuse with a mass diffusion coefficient D . Two archetypal flows will be addressed, a simple shear flow and a chaotic laminar flow. The first one is fully determined by the shear rate $\dot{\gamma}$. The second one is set by its average strain rate $\langle \dot{\epsilon} \rangle$, as well as by the statistics and typical correlation scales of the flow, that we will specify later in the thesis. We are interested in mixing by flow, and we will therefore consider situations where advection effects are important, which means that the Péclet number of the flow $Pe = \frac{\dot{\gamma} b_0^2}{D}$ or $\frac{\langle \dot{\epsilon} \rangle b_0^2}{D}$ will be kept much above 1 (given the 0 Reynolds number condition, the Schmidt number $Sc = Pe/Re$ is infinite). These model conditions are chosen because they a priori involve all the mechanisms discussed above, while keeping a minimal number of parameters, namely, the viscosity ratio λ , the Péclet number Pe and the flow type. These conditions are also relevant to many applications. As an example, given the typical depth of the earth mantle, $\sim 10^3$ km, its typical convection velocity, ~ 100 mm/year, and the typical viscosity, $\sim 10^{17}$ m²/s, and effective mass diffusion coefficient, $\sim 10^{-20}$ m²/s, inside it [8, 41], the creeping flow of the mantle, which participates to mix it, has a Reynolds number of order $\sim 10^{-20}$, and a Péclet number of order $\sim 10^{17}$. As a last comment, we need to stress that experimental constraints will force us to track the mixing of the viscosity field with a dye that does not necessarily diffuse as fast as the viscosity field itself. This effect, which will be studied in detail and considered, is actually a chance since it gives us two mixing problems for the price of one: “how fast does the viscous liquids mix?” and “how fast does another scalar initially segregated in one of the two liquids mix?”. We will be brought to discuss interesting aspects of the two questions in this thesis.

In the following of this chapter, we present some elements from the literature that will be useful for the remainder of the manuscript. In particular, we begin with a brief summary of the lamellar description of mixing, so far limited to isoviscous mixing situations. We will then recall basic concepts on molecular diffusion in the presence of several substances and of a viscosity gradient. After recalling some important results on the behavior of an heterogeneity in a simple shear flow, whether it is a solid inclusion, or a liquid drop with or without interfacial tension, we will further develop the problematics of this thesis and provide a short overview of the manuscript organization.

I.2	Isoviscous mixing: state of the art	5
I.2.1	What is mixing?	5
I.2.2	Diffusion in a still liquid	5
I.2.3	Mixing in a strained liquid: the Ranz formalism	6
I.2.3.a	Simple shear flow	8
I.2.3.b	Purely extensional flow	9
I.2.3.c	Chaotic flow	9
I.3	Diffusivities in viscous liquids	11
I.3.1	In a uniform liquid	11
I.3.2	In a non-uniform liquid	12
I.4	Kinematics of deformation of an heterogeneity	14
I.4.1	Solid particle	14
I.4.2	Immiscible liquid drop	15
I.4.3	Miscible drop	17
I.5	Goal of the thesis & manuscript overview	18

I.2 Isoviscous mixing: state of the art

I.2.1 What is mixing?

Understanding mixing is understanding how a scalar quantity, say, the concentration of a substance, evolves in time and space towards uniformity. This evolution involves the stirring flow and the molecular diffusion of the substance. Stirring alone does not mix. It can disperse the substance and steepen the concentration gradients, but it does not change the concentration levels by itself. Only the coupling with the microscopic action of molecular diffusion leads to the progressive homogenization of concentration. In many studies dedicated to mixing [38], *e.g.*, in a chaotic flow [42, 43], in a turbulent flow [1, 44], inside porous media [45, 46] or in particulate suspensions [47, 48], the stirring fluid is homogeneous [49–51]. The mixing efficiency of the system is then generally investigated by dyeing a sub-region of the fluid and by tracking the evolution of the dye concentration field. Importantly, the dye concentration is generally low enough to not modify the fluid properties (density, viscosity, ...). In this case, the dye behaves as a passively advected diffusive tracer, which does not affect the flow. We will principally discuss this case, for which advection is decoupled from diffusion. However, we must stress that, even for isoviscous liquids, there is a broad range of situations, where there is no decoupling. They concern natural convection problems, where the flow is driven by density differences due to humidity, temperature or concentration gradients [52–54]. These problems involve an additional dimensionless number (the Rayleigh number) and will not be reviewed here.

I.2.2 Diffusion in a still liquid

In a still liquid, molecules and small particles (typically smaller than a few micrometer) are significantly displaced by thermal agitation. Random collisions with surrounding molecules drive a random motion of the particles, called ‘Brownian motion’, with a characteristic jerky trajectory. As an example, figure I.3a shows the movement of a small pollen particle suspended in water [55]. Although the phenomenon bears Brown’s name, the first observations of the phenomenon date back to the advent of the microscope (16th-17th century). The use and improvement of the instrument led to Brongniart’s first scientific observations and documentation in 1827, before the botanist Brown published his own in 1828 [56]. In the early 20th century, what is now known as Brownian motion was studied by physicists such as Einstein [57], Sutherland [58], Smoluchowski [59], Langevin [60] and Perrin [61]. They have established, in particular, that after a very short ballistic transient, the mean square displacement $\langle x^2(t) \rangle$ of a Brownian particle evolves linearly with time through a diffusion coefficient $D \equiv [\text{m}^2/\text{s}]$, according to

$$\langle x^2(t) \rangle = 2Dt, \quad (\text{I.1})$$

where $\langle \rangle$ denotes an ensemble average. In a uniform system, the diffusion coefficient is proportional to both the particle mobility μ and temperature T according to

$$D = \mu k_B T, \quad (\text{I.2})$$

with k_B the Boltzmann constant.

In the presence of a gradient of concentration $\nabla \mathcal{C}(x, t)$, the Brownian motion of all the molecules results in a net macroscopic diffusive evolution of the concentration field $\mathcal{C}(x, t)$:

$$\frac{\partial \mathcal{C}(x, t)}{\partial t} = D \Delta \mathcal{C}(x, t), \quad (\text{I.3})$$

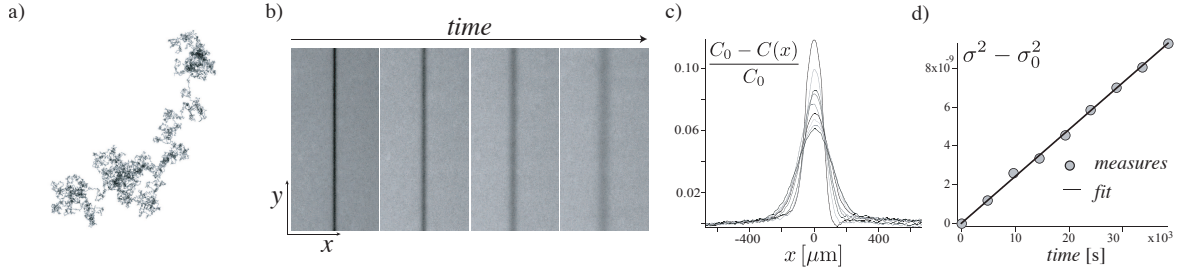


FIGURE I.3: *Diffusion on a still substrate.* (a) Trajectory of a pollen particle suspended in water [55]. (b-d) Measure of the diffusion coefficient D . (b) Successive snapshots of a purely diffusing process. (c-d) Corresponding concentration profiles and evolution of the variance, $\sigma^2 = \sigma_0^2 + 2Dt$, versus time (adapted from [64]).

which recovers the diffusion equation, or heat equation, introduced by Fourier [62] and Fick [63]. For an initially localized concentration $\mathcal{C}(x, 0) = C_0 \delta(x)$, with $\delta(x)$ the delta-Dirac distribution, the solution of Eq. I.3 is the Gaussian function

$$\mathcal{C}(x, t) = \frac{1}{\sqrt{2\pi}\sigma} C_0 e^{-\frac{x^2}{2\sigma^2}}, \quad \text{with variance} \quad \sigma^2 = 2Dt. \quad (\text{I.4})$$

As an illustration, figure I.3b-d shows an experimental measurement of the diffusion coefficient of a fluorescent dye in a viscous liquid [64]. The liquid, which is contained between two cover slides and dyed homogeneously, is photobleached with a high intensity laser to obtain a non-fluorescent lamella (in black). The bleached lamella gradually recovers its fluorescence by diffusion of the surrounding fluorescent molecules. The concentration profiles are Gaussian and broaden with a variance σ^2 growing linearly with time, from which the diffusion coefficient $D = (\sigma^2 - \sigma_0^2)/2t$ of the dye is obtained, with σ_0 the initial variance of the lamella. In this purely diffusive process, the mixing time of a the lamella is typically

$$t_M \sim \frac{b_0^2}{D}, \quad (\text{I.5})$$

with $b_0 \sim \sigma_0$ the initial half-width of the lamella.

I.2.3 Mixing in a strained liquid: the Ranz formalism

In a stirred liquid, both the straining flow and molecular diffusion influence mixing. The evolution of the mix is thus conditioned by the Péclet number,

$$Pe = \frac{\dot{\gamma} b_0^2}{D}, \quad (\text{I.6})$$

which compares the typical time scale of the flow $\dot{\gamma}^{-1}$, with $\dot{\gamma}$ the typical strain rate, to the typical diffusion time scale for a still liquid, b_0^2/D . For an incompressible flow, the concentration field \mathcal{C} follows the advection-diffusion equation

$$\partial_t \mathcal{C} + \mathbf{u} \cdot \nabla \mathcal{C} = D \Delta \mathcal{C}, \quad (\text{I.7})$$

which has no general solution when the stirring flow field \mathbf{u} is complex.

However, for conventional liquids, most flows organize the concentration field in the form of lamellae. In that case the diffusion problem becomes essentially unidimensional and can be simplified. Ranz introduced a change of variable [38], analog to that used by Plesset & Zwick [65] and Taylor [51] before, which transforms the advection-diffusion equation into a simple diffusion equation, for which solutions

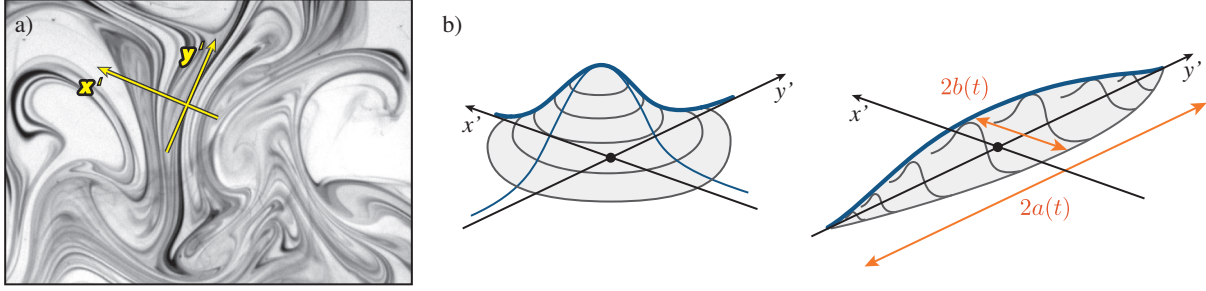


FIGURE I.4: Ranz formalism used to treat advection-diffusion of the thin lamellae formed by stretching (adapted from [1]). (a) Coordinate definition in the lamella reference system. (b) Diffusion of a blob which is stretched in the y' -direction and compressed in the x' -direction.

are known. Let us consider a two-dimensional flow and place ourselves in the Lagrangian frame of reference (x', y') moving, in position and in orientation, with a slender lamella of width $2b(t)$ (see Fig. I.4). The y' -axes is aligned with the stretching direction, the x' -axes is transverse and close to the direction of the concentration gradient, and locally the flow is approximately $\{u', v'\} = \{\dot{b}x'/b, -\dot{b}y'/b\}$. In this reference frame, assuming that the concentration gradient $\partial_{y'}C$ along the lamella is negligible compared to the gradient $\partial_{x'}C$ across the width, equation (I.7) becomes

$$\partial_t C + \frac{\dot{b}}{b} x' \partial_{x'} C = D \partial_{x'}^2 C. \quad (\text{I.8})$$

Introducing the following change of variables [38]

$$\xi = \frac{x'}{b(t)}, \quad \text{and} \quad \mathcal{T} = D \int_0^t \frac{dt'}{b(t')^2}, \quad (\text{I.9})$$

which express lengths relative to b and time as a dimensionless warped time \mathcal{T} , equation I.8 can be recasted into the simple diffusion equation

$$\partial_{\mathcal{T}} C = \partial_{\xi}^2 C. \quad (\text{I.10})$$

The solution of equation I.10 gives the evolution of the blob concentration, namely

$$C(\xi, \mathcal{T}) = \frac{C_0}{2} \left[\operatorname{erf} \left(\frac{\xi + 1/2}{\sqrt{2\mathcal{T}}} \right) - \operatorname{erf} \left(\frac{\xi - 1/2}{\sqrt{2\mathcal{T}}} \right) \right], \quad (\text{I.11})$$

for a top-hat initial condition, or

$$C(\xi, \mathcal{T}) = \frac{C_0}{\sqrt{1+2\mathcal{T}}} e^{-\frac{\xi^2}{1+2\mathcal{T}}}, \quad (\text{I.12})$$

when the initial profile of the lamella is Gaussian. In the long time, the width of the lamella, which is both stretched by the flow and broadened by diffusion, evolves as

$$b_{AD}(t) \rightarrow \sqrt{1+2\mathcal{T}} b(t). \quad (\text{I.13})$$

The mixing time t_M , at which the maximal concentration starts decaying significantly, is reached when $\mathcal{T} = 1$, and the width of the lamella at this time, which is also called the Batchelor scale, is given by $b_{AD}(t_M)$. The expressions of t_M and b_M depend on the thinning history $b(t)$ of the lamella, which itself depends on the stirring flow. To gain some insight and intuition about simple cases of mixing, we will apply below the Ranz formalism to simple flow configurations.

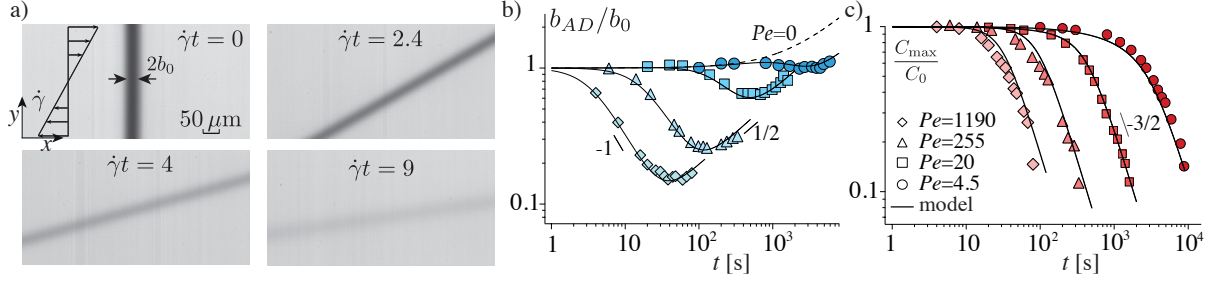


FIGURE I.5: *Mixing in a simple shear flow* (adapted from [47]). (a) Successive snapshots of a lamella mixing in a simple shear flow. (b) Normalized blob width b_{AD}/b_0 versus time for different Péclet numbers. (c) Normalized maximal concentration C_{\max}/C_0 versus time.

I.2.3.a Simple shear flow

We consider a lamella of dye, with an initial concentration C_0 , an half-width b_0 , which is initially perpendicular to the flow direction, in the simple shear flow $\{u, v\} = \{\dot{\gamma}y, 0\}$ shown in figure I.5a. As the lamella is sheared, it is thinned down by the flow as

$$b_A(t) = \frac{b_0}{\sqrt{1 + (\dot{\gamma}t)^2}}, \quad (\text{I.14})$$

which accounts only for the effect of the advection field (i.e. for $Pe = \infty$). From this 'advective' thinning, the Ranz dimensionless time $\mathcal{T} = D \int_0^t \frac{dt'}{b_A(t')^2}$ is computed as

$$\mathcal{T} = \frac{1}{Pe} \left[\dot{\gamma}t + \frac{(\dot{\gamma}t)^3}{3} \right] \simeq \frac{1}{Pe} \frac{(\dot{\gamma}t)^3}{3}, \quad \text{for } Pe \gg 1. \quad (\text{I.15})$$

From the solution of the diffusion equation in the Ranz coordinate system (attached and scaled with the lamella), the maximal concentration evolves as

$$C_{\max}(t) = \frac{C_0}{\sqrt{1 + 2\mathcal{T}}} \simeq \frac{C_0}{\sqrt{1 + \frac{2}{3} \frac{(\dot{\gamma}t)^3}{Pe}}}, \quad (\text{I.16})$$

while the width of the lamella follows

$$b_{AD}(t) = \sqrt{1 + 2\mathcal{T}} b_A(t) \simeq \frac{\sqrt{1 + \frac{2}{3} \frac{(\dot{\gamma}t)^3}{Pe}}}{\sqrt{1 + (\dot{\gamma}t)^2}} b_0, \quad (\text{I.17})$$

which accounts for both the kinematic thinning (bottom term) and the diffusive broadening (top term). This evolution of the lamella width is shown in figure I.5b (adapted from [47]), for different imposed Péclet numbers. The width first decreases like $b/b_0 \sim (\dot{\gamma}t)^{-1}$ due to the compression imposed by the shear. However, as the lamella thins down and aligns with the flow direction, the compression rate decreases while the diffusive broadening rate increases. Both rates balance at the mixing time, given by $\mathcal{T} = 1$,

$$t_M \simeq \frac{1}{\dot{\gamma}} (3Pe)^{1/3}. \quad (\text{I.18})$$

when the width has decreased down to the Batchelor scale

$$b_M \simeq b_0 \frac{3^{1/6}}{Pe^{1/3}}. \quad (\text{I.19})$$

Beyond t_M , the diffusive broadening dominates and the width increases as $b/b_0 \sim \sqrt{\dot{\gamma}t/Pe}$. Meanwhile, the maximal concentration, which has remained unchanged until approximately t_M , decreases like $C_{\max}/C_0 \sim \sqrt{Pe}(\dot{\gamma}t)^{-3/2}$.

I.2.3.b Purely extensional flow

In a purely extensional steady flow, $\{u, v\} = \{-\dot{\epsilon}x, \dot{\epsilon}y\}$, any blob of dye will be rapidly stretched in a lamella aligned with the extensional direction and compressed as

$$b_A(t) = b_0 e^{-\dot{\epsilon}t}. \quad (\text{I.20})$$

The Ranz dimensionless time is

$$\mathcal{T} = \frac{1}{2Pe} (e^{2\dot{\epsilon}t} - 1) \simeq \frac{e^{2\dot{\epsilon}t}}{2Pe}, \quad \text{for} \quad Pe \gg 1, \quad (\text{I.21})$$

which gives

$$\frac{C_{\max}}{C_0} \simeq \frac{1}{\sqrt{1 + \frac{2}{Pe} e^{2\dot{\epsilon}t}}} \xrightarrow{t \gg t_M} \sqrt{\frac{Pe}{2}} e^{-\dot{\epsilon}t}, \quad \frac{b_{AD}}{b_0} \simeq \frac{\sqrt{1 + \frac{2}{Pe} e^{2\dot{\epsilon}t}}}{e^{\dot{\epsilon}t}} \xrightarrow{t \gg t_M} \sqrt{\frac{2}{Pe}}, \quad (\text{I.22})$$

with a lamella width converging to the Batchelor scale

$$b_M \simeq b_0 \sqrt{\frac{2}{Pe}}, \quad (\text{I.23})$$

and a mixing time

$$t_M \simeq \frac{1}{\dot{\epsilon}} \frac{\ln 2Pe}{2}, \quad (\text{I.24})$$

which depends only logarithmically on diffusivity, as a consequence of the exponential stretching by the flow.

I.2.3.c Chaotic flow

Let us consider now flows that are not steady anymore and complex enough to be chaotic. A flow is chaotic when it is not deterministic, in practice, because of a diverging sensitivity to initial conditions. Stretching by the flow is not deterministic anymore, but it is determined in a statistical sense, by the average and variations over a large number of histories. Such chaotic flows are frequently encountered, for instance at very large Reynolds numbers, where flows are turbulent. However, chaoticity does not necessarily require inertia. Many viscous flows are chaotic (for instance in porous media [19, 66, 67], in suspensions of solid particles [48, 68], or with rather simple stirring protocols [42, 43]), and these are generally referred to as laminar chaotic flows. The diverging sensitivity to initial conditions, means that two infinitesimally close tracers of the flow will eventually separate, on average, at a certain exponential rate, $\kappa \langle \dot{\epsilon} \rangle$, where $\langle \dot{\epsilon} \rangle$ is the average strain rate of the flow and κ is a positive number known as the dimensionless *Lyapunov exponent*. This exponential rate of separation is important for mixing, because it implies that a blob of dye with a size smaller than the smallest scale of the flow experiences, on average, an exponential thinning [69] given by

$$\frac{b_A}{b_0} \sim e^{-\kappa \langle \dot{\epsilon} \rangle t}, \quad (\text{I.25})$$

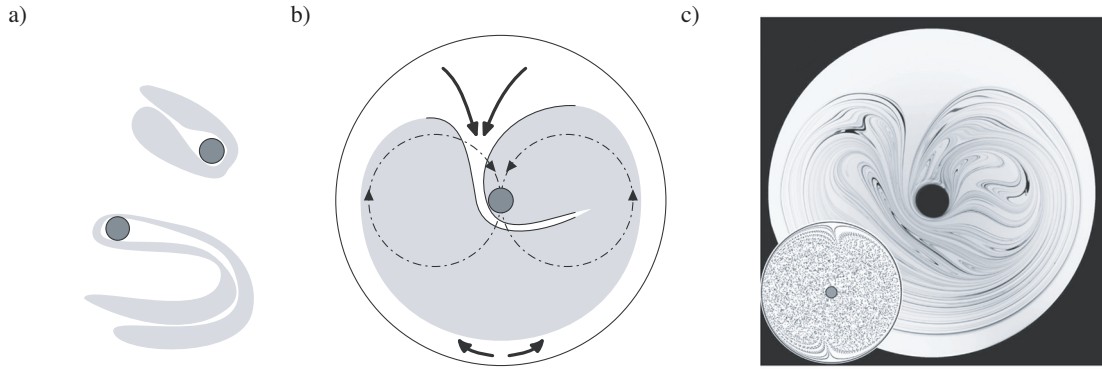


FIGURE I.6: Example of a chaotic laminar flow (adapted from [42]). (a-b) Schematics of the deformation of a blob by the stirring rod and schematics of the ‘eight-shaped’ stirring pattern. (c) Experimental observation of the chaotic advection pattern highlighted by the stretched blob of dye.

from which the characteristic mixing time is

$$t_M \simeq \frac{\ln(2\kappa Pe)}{2\kappa \langle \dot{\epsilon} \rangle}, \quad \text{with} \quad Pe = \frac{\langle \dot{\epsilon} \rangle b_0^2}{D}. \quad (\text{I.26})$$

The origin of the exponential stretching emerging in chaotic flows can be understood by considering that fluid material lines undergo successive cycles of stretching and folding. For instance, for the stirring protocol illustrated in figure I.6 (adapted from [42]), the stirring rod moves in a viscous fluid along an ‘eight-shaped’ trajectory, repeatedly crossing its previous path, which stretches and folds the liquid iteratively. In this flow, a blob of dye is stretched exponentially and mixed fast (after only a few typical flow timescales $(\kappa \langle \dot{\epsilon} \rangle)^{-1}$).

Of course, the description of mixing in complex and chaotic flows has been pushed much further than the above picture. First, the full statistics of stretching can generally be documented. On long times, the accumulated stretch becomes equivalent to that of a random sequence of uncorrelated stretching events and its statistics converge to a log-normal distribution set only by the average and standard deviation of the stretching of a Lagrangian fluid particle over the correlation time τ of the flow [44, 68, 70]. When the typical correlation strain scale $\langle \dot{\epsilon} \rangle \tau$ is small, the average and variance of the Lagrangian stretching can also be related to the Eulerian quantities [68]. The stretching distribution, which simply quantifies how some parts of the blob are much more stretched than others, can be used to obtain more accurate predictions for the evolution of the concentration distribution, either in the so-called limit of the *solitary strip*, when the different parts of the lamella do not interact, or in at later times, when portions of lamella partly overlap because the distance between them keeps decreasing as a consequence of the repeated foldings [1, 19, 45, 46, 48]. We do not detail here these statistical descriptions of mixing which, although very interesting, will not be of use for the remainder of the manuscript.

I.3 Diffusivities in viscous liquids

Dealing with liquids of different viscosities means dealing with at least two substances, which both have a significant mass fraction in practice. In our particular case, to access a wide range of viscosity ratio, we use solutions of polymers in water, for which the two substances have very different molecule sizes. This difference in size implies different modes of motion and eventually different mobilities of the two substances. We will briefly review, below, what are the different mobilities and their dependence on viscosity, and how solutions with different concentration diffuse into each other.

I.3.1 In a uniform liquid

When there are no gradients of concentration or temperature and no external force, the system is at equilibrium. Diffusion does not drive net macroscopic motions, since concentrations are not evolving, and it only concerns individual molecules. As mentioned above, in this case, the diffusion coefficient of any molecule, also referred to as ‘self-diffusion’ coefficient of this molecule in the mixture, is set by the thermal agitation as [57–59]

$$D = \mu k_B T, \quad (\text{I.27})$$

with μ the mobility of the molecule in the mixture introduced in §I.2.2. If the mixture contains both large and small molecules, like our aqueous solution of long polymers, equation I.27 implies that the self-diffusion of the large polymer molecules is much slower than that of the small water molecules, because the mobility μ of the polymer is much smaller. Additionally, if the polymer molecules are much larger than *most* of the other molecules of the mixture (e.g. for the diluted solution of long coiled polymers sketched in figure I.7), their mobility follows the Stokes-like form $\mu = 1/6\pi\eta a$, with η the viscosity of the mixture and a the hydraulic equivalent radius of the coiled molecule, from which the self-diffusion coefficient of the polymer molecule

$$D \approx \frac{k_B T}{6\pi\eta a} \propto 1/\eta, \quad (\text{I.28})$$

is inversely proportional to the mixture viscosity [57, 71, 72].

However, in most of the cases we will consider, the mass fraction of polymer in the solution is significant, and the polymer molecules diffuse with different modes of motion, which breaks the inverse dependence on the viscosity of the mixture. In this concentrated case, polymers are entangled and diffuse with a ‘reptative-like’ motion between the other polymer molecules [74, 75]. As illustrated in figure I.7c,

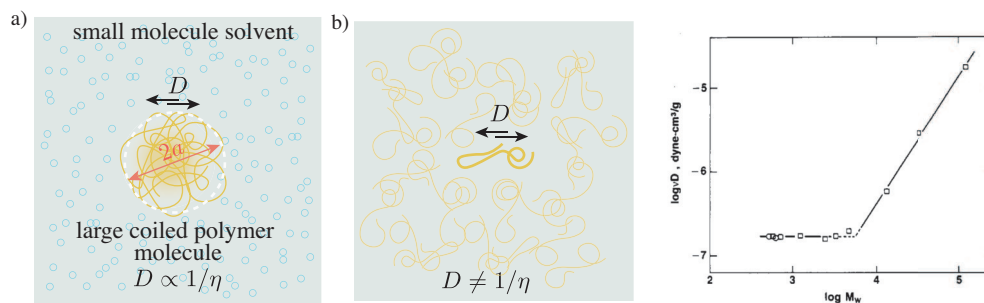


FIGURE I.7: *Diffusivity of a single long polymer molecule.* (a) In a solvent of smaller molecules, the diffusivity of a long coiled polymer molecule is close to the Stokes-Einstein law $D \propto 1/\eta$. (b) In a solution with a large mass fraction of polymers, the mobility of a long polymer molecule is limited by other modes of motion (reptation...), and its diffusivity is not inversely proportional to the viscosity of the solution anymore ($D \neq 1/\eta$). Right: product between the self-diffusivity and viscosity of a polymer melt (no solvent) versus the molar weight of the polymer (adapted from [73]).

with experimental data by [73] for long polymer chains in their own melt (no water), the self-diffusion coefficient does not decrease as fast as the viscosity of the mixture increases.

Experimentally, to access the self-diffusion coefficient one needs to tag one or an assembly of molecules in a uniform solution without changing the way these molecules diffuse. This can be done using similar molecules of different colors or fluorescent molecules, which may be photobleached over a certain region ([76] and see Fig. I.5), but the most exhaustive measurements use Nuclear Magnetic Resonance (NMR) techniques. These echo-based techniques (pulsed-gradient-spin-echo NMR) use pulse sequences [73, 77, 78]. A first ‘write’ pulse sequence spatially labels the mixture (changing the magnetization of the proton spatially). After a certain delay of typically 100 ms, during which molecules diffuse, a second ‘read’ pulse sequence, refocuses the signal. The larger the protons have moved the lower the refocused signal, which allows to infer the diffusion coefficient of the labeled molecules. This technique introduced by Carr and Purcell in 1954 [79] allows to distinguish between the different type of molecules of the mixture, and obtain the self-diffusion coefficient for each.

I.3.2 In a non-uniform liquid

In a non-uniform liquid, diffusion *does* drive a net macroscopic motion, which tends to equilibrate concentrations. If we consider for instance the diffusive front between two solutions of polymers in water with different concentrations sketched in figure I.8a, there is a net diffusive motion of polymers to the right and a net motion of water to the left. This combined motion is called interdiffusion or mutual diffusion. It depends on the ‘relative mobility’ or inverse ‘friction factor’ between the two substances (polymer and water) moving through each other, and on whether there is a significant enthalpy of mixing or not. The ‘relative mobility’ itself is *qualitatively* related with the mobilities of the two substances in the uniform mixture, but no simple *quantitative* relation exists in general [81]. Just like for self-diffusion, the interdiffusion coefficient for entangled solutions of polymers is not inversely proportional to viscosity. Altogether, the interdiffusion coefficient $D(C, \nabla C)$ may depend non-trivially on the local concentration and possibly on the concentration gradient.

However, when the enthalpy of mixing is low (meaning the energy of the mix is close to that of the segregated state), the mixture is called ‘ideal’, diffusion is driven by thermal agitation only, and the diffusion coefficient $D(C)$ does not depend on the concentration gradient. In this case, the linearity of the diffusion equation is lost ($\partial_t C = D(C)\Delta C$, is nonlinear), which implies that the diffusion time may depend

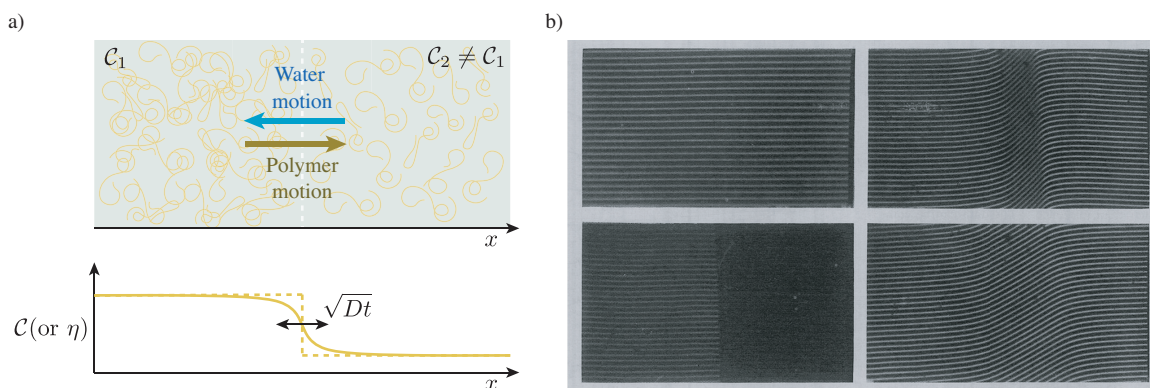


FIGURE I.8: *Diffusion between solutions of different concentration.* (a) Sketch of a binary diffusion problem (top) and time-evolution of the concentration profile (bottom). (b) Diffusion between a solvent (dimethylacetamide) with 25 w% of polymers (vinyl acetate-acrylonitrile copolymer, $M_w \sim 200k$) and the pure solvent (figure adapted from [80]). Top left: Interference pattern observed through a medium with constant refractive index. Lower left: Initial front between the two solutions. Right: Diffusive evolution of the front after 150 s (top) and 510 s (bottom).

on the initial concentration difference and that the shape of the concentration profile across a mixing front may deviate from the case $D = \text{cste}$ (the Gaussian or error functions given in Eq. I.3). Nevertheless, the long term solutions of $\partial_t \mathcal{C} = D(\mathcal{C}) \Delta \mathcal{C}$ remains self-similar in \sqrt{t}/x , which means that at long time the front keeps spreading diffusively with a variance $\sigma_C^2 \propto D^* t$, where D^* is related to the diffusivity $D(\mathcal{C})$ over the concentration range spanned by the front.

In the present thesis, we are interested in the diffusive evolution of the viscosity field $\eta(x, t)$. Since in our system the viscosity is determined uniquely by the concentration of polymer as $\eta(\mathcal{C})$, it will have the same long time diffusive evolution as the polymer concentration \mathcal{C} , *i.e.*, with a spatial variance $\sigma_\eta^2 \propto D^* t$. We will see below (§II.2.1) that we actually track the viscosity field with the help of a fluorescent dye bound to some of the polymers, and that it will turn necessary to clarify how much the fluorescent signal follows the viscosity field. This subtle point will be the topic of a full section of this thesis.

In practice the interdiffusion coefficient is measured, by observing the mixing front between solutions of unequal concentration, and the concentration of the two solutions is usually varied to infer the dependence $D(\mathcal{C})$. This demands to create a sharp front and monitor the evolution of concentration, using dyed substances [82, 83], or optical techniques based on refraction index contrast between the two solutions, for instance interferometry [80, 84], as illustrated in figure I.8, or schlieren techniques, as we will use in this thesis (see §II.3.2.b, [85]).

I.4 Kinematics of deformation of an heterogeneity

Having stressed how a non-uniform viscosity influences the diffusion process, we now present the literature regarding how heterogeneities in viscosity affect the flow kinematics, in the absence of diffusion ($Pe = \infty$). We focus most of the discussion on the case of an heterogeneity with a viscosity ratio λ in a simple shear flow. For our mixing problem, the liquids are miscible, and there is thus no surface tension between the heterogeneity (blob) and the bath. In this case (infinite Pe , no surface tension), the kinematics depend only on the viscosity ratio λ and the initial shape of the heterogeneity. This parameter space is sketched in figure I.9, for the particular case of ellipsoidal shapes. We have chosen such ellipsoidal shapes because some results are known for them, which illustrate precisely the different dependences of the flow, and also because they will turn to be particularly relevant for our mixing study, given the spherical initial condition we use.

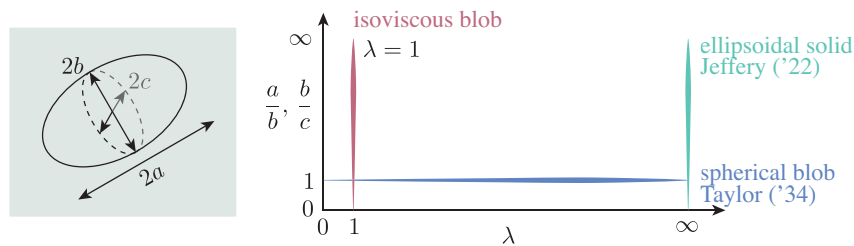


FIGURE I.9: Parameter space for the non-diffusive deformation kinematics of a viscous ellipsoidal heterogeneity in a simple shear flow.

We have seen so far what happens to an isoviscous blob ($\lambda = 1$). It is linearly stretched by the flow, whatever its initial shape is (arbitrary a/b , b/c), and eventually converges to a more and more slender lamella which aligns with the flow direction. This covers the red vertical line in the plot of figure I.9. In the case when the blob is much more viscous than the surrounding bath ($\lambda \gg 1$), a useful reference is the limit $\lambda = \infty$ studied by Jeffery [86], for the motion of ellipsoidal solid particles sheared in a viscous liquid (vertical green line in the parameter space). On the other hand, for the case of close to spherical heterogeneity ($a \approx b \approx c$) and arbitrary viscosity ratio (all λ , horizontal line in the parameter space), there is a vast literature initiated by Taylor [87]. This literature concerns droplets, having a surface tension, but it contains some limit results (for large capillary numbers), which are actually directly relevant to the no surface tension case. Beside these limiting cases, much less literature has considered the non-isoviscous miscible case (finite $\lambda \neq 1$ and arbitrary a/b , b/c), which covers all the parameter space but the three lines we have mentioned. This may be related with the experimental difficulties of controlling the initial condition, which is actually crucial for the deformation process. We will review successively all these different cases.

I.4.1 Solid particle

The simplest case is, of course, that of a solid sphere. In a flow with shear rate $\dot{\gamma}$, a sphere rotates steadily around the vorticity axis with the same rotation rate as the flow vorticity $\dot{\gamma}/2$ (see Fig. I.10a). The flow around has been solved by Einstein [89], and the streamlines, which feature a recirculating region, computed by Cox [90]. For the case of an arbitrary ellipsoidal solid (arbitrary a/b , b/c), Jeffery [86] has shown that the ellipsoid follows a complex orbital motion around its center, which depends on its initial orientation relative to the flow. The orientation and the motion involve three angles, in the general case. For the particular case of an axisymmetric ellipsoid ($b = c$), the azimuthal and polar angles φ and θ , represented

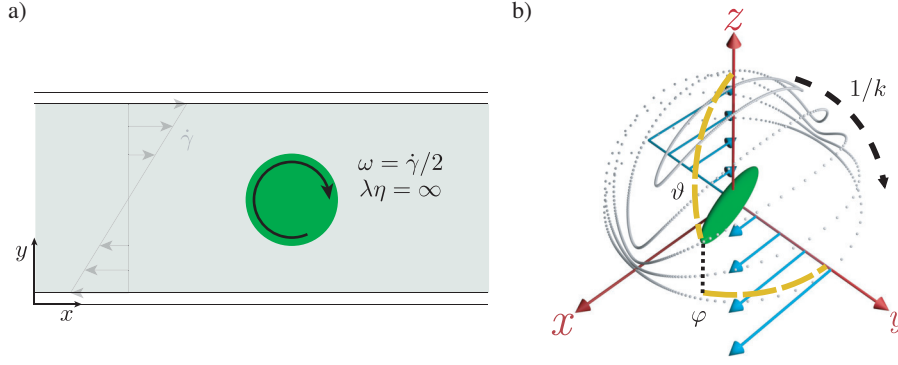


FIGURE I.10: *A solid ellipsoid in a simple shear flow.* (a) A solid sphere in a simple shear flow rolls with a rate $\omega = \dot{\gamma}/2$. (b) A solid ellipsoid follows an orbital motion, described by Jeffery [86]. Five different orbits corresponding to five different initial orientations for an axisymmetric ellipsoid with aspect ratio $a/b = 10$ (adapted from [88]).

in figure I.10b, follow

$$\tan \varphi = \frac{a}{b} \tan \frac{\dot{\gamma} t}{\frac{a}{b} + \frac{b}{a}}, \quad \tan^2 \vartheta = \frac{1/k^2}{\frac{a^2}{b^2} \cos^2 \varphi + \frac{b^2}{a^2} \sin^2 \varphi}, \quad (\text{I.29})$$

with k an integration constant defining the initial polar angle ϑ . For these orbits, some of which are represented in figure I.10b [88], the ellipsoid rotates about the vorticity axis (z) with a non uniform velocity and with a precession angle φ oscillating periodically. The period depends on the aspect ratio as

$$T = \frac{2\pi}{\dot{\gamma}} \left(\frac{a}{b} + \frac{b}{a} \right). \quad (\text{I.30})$$

I.4.2 Immiscible liquid drop

The case of drops has been intensively studied both experimentally [87, 91–96] and theoretically [87, 95–102], with concerns regarding the viscosity, the formation and the stability of liquid-liquid emulsions. Since drops have an interfacial energy σ , the kinematics depends on an additional dimensionless number, the capillary number $Ca = \frac{\eta a \dot{\gamma}}{\sigma}$, which gives the magnitude of viscous stresses relative to capillary stresses, with $\dot{\gamma}$ the shear rate of the flow and η the bath viscosity.

Following the influential works by Taylor [87, 97], much attention has been devoted to the deformation and the conditions for the burst of the drop in a simple shear flow, which lead to its fragmentation. In particular, for low shear rates ($Ca \ll 1$) capillarity dominates, and the drop, which is exactly spherical at rest, remains close to spherical in the shear. In this case, the drop rapidly reaches a steady shape with a deformation [87]

$$\frac{a-b}{a+b} \simeq \frac{1 + \frac{19}{16}\lambda}{1 + \lambda} \frac{\eta a \dot{\gamma}}{\sigma}, \quad \text{for} \quad Ca = \frac{\eta a \dot{\gamma}}{\sigma} \ll 1, \quad (\text{I.31})$$

which is proportional to the shear rate. Higher order expansions, valid at slightly larger capillary numbers, have also been proposed [98–101].

When viscous stresses becomes more important (larger Ca , i.e., larger shear rate), the situation is qualitatively different depending on the value of the viscosity ratio λ . As illustrated in figure I.11a, for low viscosity ratios ($\lambda \lesssim 4$), increasing the shear rate leads to more and more elongated drops, which destabilize and break above a certain critical capillary number. But for larger ratios ($\lambda \gtrsim 4$), increasing the shear does not increase deformation. The drop maintains a steady rolling-like motion, which becomes

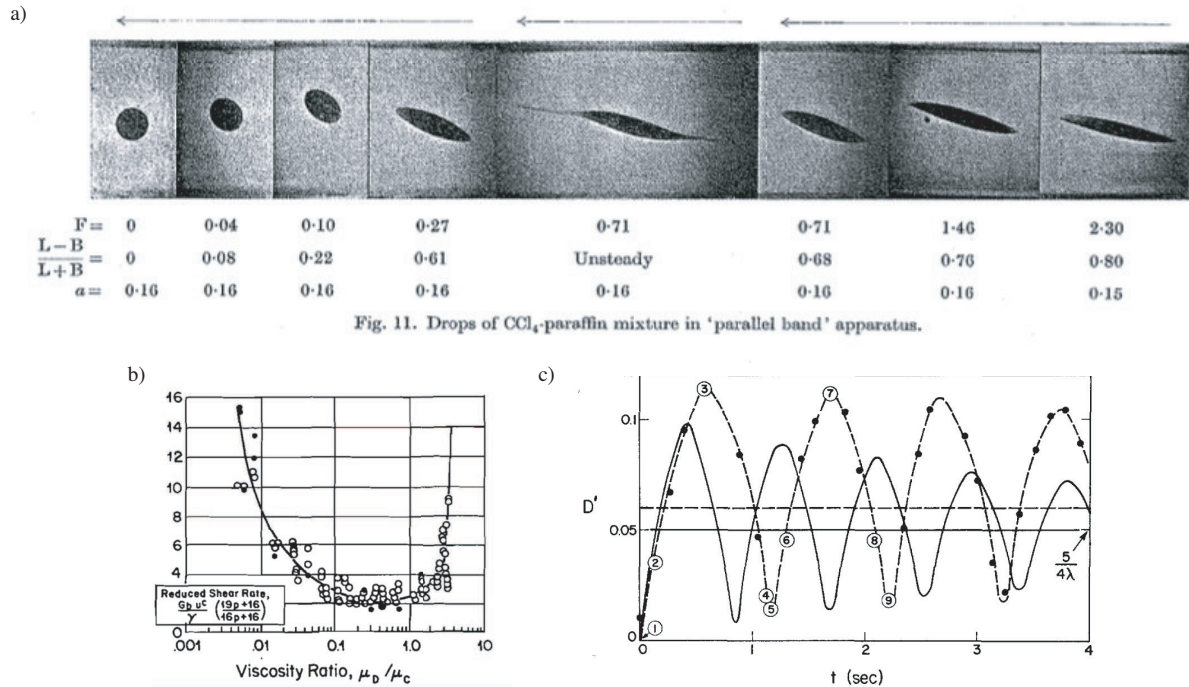


FIGURE I.11: A droplet in a simple shear flow. (a) Snapshots illustrating the deformation of a low viscosity droplet in a simple shear flow ($\lambda = 0.001$, the capillary number, indicated as F , is increasing from 0 to $\simeq 2.30$, from left to right). As the shear rate is increased, the deformation increases (adapted from [87]). (b) Critical capillary number at which a drop breaks up versus viscosity ratio (adapted from [91]). (c) The initial oscillating deformation of a much more viscous drop ($\lambda = 25$) is 'damped' by capillarity until the drop converges to a steady shape ($Ca \simeq 0.36$, adapted from [92]).

independent of the shear rate (at sufficiently large shear rate), and which is only set by the viscosity ratio. In this case, the larger the viscosity ratio, the closer the drop from the solid sphere case. Asymptotically, the deformation of the drop follows

$$\frac{a-b}{a+b} \simeq \frac{5}{4\lambda}, \quad \text{for} \quad Ca = \frac{\eta a \dot{\gamma}}{\sigma} \gg 1, \quad \text{and} \quad \lambda \gg 1, \quad (\text{I.32})$$

which has also been derived by Taylor [87]. This qualitatively different behavior between low ($\lambda \lesssim 4$) and large viscosity ratios ($\lambda \gtrsim 4$), is illustrated in figure I.11b, which reports the critical capillary number for the burst of the drop as a function of the viscosity ratio λ [91]. The critical capillary number is finite for low λ but diverges at a value of λ close to 4, because above this value the viscous flow can maintain an endless rolling-like motion of the drop even without surface tension.

Importantly, even if the steady shape hardly depends on capillarity, the fact that the drop eventually reaches a steady shape (if it does not burst) is in all case due to capillarity. Indeed, at rest the drop has an exactly spherical shape, and when the shear is started the drop does not pass by the steady equilibrium shape, but 'overshoots' and orbits around. For a large viscosity ($\lambda \gtrsim 4$), this initial motion combines a rotation and small amplitude periodic stretching, as illustrated in figure I.11c. The amplitude of the oscillation is 'damped' by capillarity after a few oscillations (in this overdamped flow, capillarity is indeed a 'damping' term).

Last, as already realized and experimentally verified by Taylor [97], the qualitatively different behavior observed for vanishing capillary effects, between drops with a low viscosity ratio ($\lambda \lesssim 4$) and those with a large ratio ($\lambda \gtrsim 4$), is related with the vorticity of the simple shear flow. In a purely extensional flow, i.e., with no vorticity ($\partial_x v - \partial_y u = 0$), all drops behave qualitatively the same. For large viscous

stresses ($Ca \gg 1$), they are eventually stretched by the flow, however large the viscosity ratio λ .

I.4.3 Miscible drop

The case without surface tension has also been considered explicitly, not for addressing miscibility effects, but rather because studies were concerned with geological applications, in particular convective motions in the Earth mantle, which can, on geological timescales be seen as a creep flow with large viscosity contrasts. Theoretical studies have considered both simple shear and purely extensional flows. For the simplified geometry of a two-dimensional elliptical blob Spence *et al.* [8] and Manga [10, 103], have recovered qualitatively the viscous phenomenologies identified by Taylor. In particular, in a shear flow for a viscosity ratio $\lambda \gtrsim 4$, an initially spherical blob does not stretch but follows a rolling-like motion with periodic stretching. They have also identified that when the blob is sufficiently elongated (because it was initially slender, or had a sufficiently low viscosity to be stretched by the flow) the deformation of the blob becomes essentially independent of the viscosity ratio. Bilby, Eshelby & Kuldu [104] and later Wetzel & Tucker extended the modelization to the case of a three dimensional ellipsoidal blob, by time integrating the exact solutions of the analog elastic problem solved earlier by Eshelby [105], with qualitatively similar conclusions. Chaotic flows have also been considered with simulation by Merveilleux DuVigneau and Fleitout [11] and later by Florek & Tucker [106], who have reported an initial slow-down of the stretching of the blob by the flow.

Experimentally, Comas-Cardona & Tucker [107] managed to confirm the phenomenology for an initially spherical blob in a simple shear flow, using a protocol where the viscous blob is immersed in the bath in a frozen state to obtain a close to spherical initial condition.

I.5 Goal of the thesis & manuscript overview

The brief introduction above highlights the need to study and better quantify the evolution of viscous heterogeneities. This problem is particularly relevant given the considerable range of applications, in geophysics, biology or industry. From a more fundamental point of view, motivation also stems from the lack of information on the deformation kinematics of such heterogeneities for the different regimes of deformations. So far, most studies on heterogeneities concern solid objects or drops for which surface tension eventually plays a role, in particular for highly stretched heterogeneities. Only a few studies have focused on miscible liquids, but a systematic and analytically tractable knowledge on the deformation kinematics is still needed. It is needed, obviously, as a base for studying the mixing problem, but also for its importance to address other potential consequences of the kinematics, such as rheology or pattern formation. Regarding the mixing question itself, most studies are restricted to isoviscous situations, and to date there is no theoretical framework developed to predict how, and in how much time, heterogeneities in viscosity mix.

As already motivated above, we have chosen to tackle this mixing question for the case of an isolated and initially localized heterogeneity, in a purely viscous flow, at large Péclet number, in both a simple shear and a chaotic laminar flow. This may seem two rather simplified situations, but we will see that they are, above all, very insightful situations, which will allow us to reach a deep fundamental understanding of many of the key mechanisms involved in the problem. We will in particular address the following questions: How does the viscosity contrast between the blob and the stirring bath affect the blob kinematics of deformation and its stretching rate? How to describe the inter-diffusion process between two liquids of unequal viscosity? How does diffusion couple to the stretching kinematics to set the mixing time of the blob? Are there significant feedback mechanisms due to the influence of the diffusion of the viscosity field on the flow? Would a dye initially segregated in one of the two liquids mix differently than the viscosity itself?

The manuscript is organized as follows. Chapter II provides a description of the material, protocols and experimental methods developed for this thesis, in order to control the Péclet number of the flow, the viscosity ratio of the liquids, the initial condition, and to characterize the whole mixing process. Chapter III is devoted to the simple shear flow configuration. The deformation kinematics and mixing process of viscous blobs are studied for a wide range of viscosity ratios and Péclet numbers. This work characterizes the remarkable kinematic transition from a stretching to a rolling-like deformation of the blob, as the viscosity ratio is increased, and shows how the mixing time may become independent of the stirring rate. Chapter IV extends the study to chaotic laminar flows, where the mixing time at large viscosity ratio is dominated by a long substretching regime and becomes, by contrast, virtually independent of the diffusivity. Last, a summary of the results and a discussion about their generality is provided in the conclusion.

Chapter II

Experimental methods & characterizations

To study experimentally the mixing of liquids of different viscosities, we need to choose and design a model experimental system which allows us to vary the viscosity ratio between the two liquids, to control the flow, and last, to visualize and quantify the evolution of the viscosity field for different Péclet numbers. The present chapter motivates the experimental choices and details the methods and necessary characterizations that will be used in the following chapters. In particular, we first introduce the liquids and characterize their viscosity as well as other relevant physical quantities. We present, then, the fluorescence technique used for visualizing and quantifying the deformation and mixing of the blob. A large part of this chapter is also devoted to characterize the different diffusivities involved in the mixing dynamics, using a purely diffusive (no flow) setup and complementary observation techniques. Last, we present the technique developed to prepare and control the initial shape of the blob.

II.1	Liquids	20
II.1.1	Choice of the liquids	20
II.1.2	Viscosity ratio λ	20
II.1.3	Density matching	21
II.1.4	Preparation of the liquids	22
II.2	Principle of the visualization techniques	23
II.2.1	Fluorescence	23
II.2.2	Index of refraction	24
II.3	Effective diffusivities	26
II.3.1	Experimental setup	26
II.3.2	The two measurements techniques	27
II.3.2.a	Fluorescence technique	27
II.3.2.b	Synthetic schlieren technique	28
II.3.3	Comparison between the fluorescence profile and the mass fraction profile & interpretation	31
II.3.4	Diffusion coefficients: summary of the results	34
II.4	Initial shape of the viscous blob	37
II.5	Conclusion	39

II.1 Liquids

II.1.1 Choice of the liquids

The choice of the liquids used for the blob and the bath is subjected to three main experimental constraints. First, the two liquids must be fully miscible and have a Fickian effective inter-diffusion coefficient, which is large enough to keep a reasonable experiment duration for the millimeter-size blob we use. Second, both liquids should be Newtonian and viscous enough to ensure a low Reynolds number condition. Their viscosity ratio λ must be varied continuously over a broad range, from the isoviscous case ($\lambda = 1$) to highly contrasted viscosities ($\lambda \ll 1$ and $\lambda \gg 1$). Last, the liquid of the bath should be transparent and the liquid of the blob should be made visible to follow its deformation and mixing.

To cope with these requirements, we work with aqueous polymer solutions. We use a commercial copolymer provided by Dow (Ucon 75-H-90000). It is a linear polyalkylene with 75wt% of ethylene oxide groups, 25wt% of propylene oxide groups, and a molecular weight of 12000 g mol^{-1} . This specific combination of hydrophilic and hydrophobic monomer groups ensures that, despite the rather large molecular weight, the polymer melt (no water in the solution) remains liquid at ambient temperature, with a Newtonian viscosity of order 40 Pa s . It also ensures that the polymer is soluble in water at all concentrations. This means that by properly choosing the mass fraction f of polymer in the solutions for the bath and the blob, we can experimentally access more than four decades of viscosity ratio. Additionally, the following characterizations (see §II.3) will show that the effective diffusion coefficient in the presence of water is of order $D \sim 10^{-11} - 10^{-10} \text{ m}^2 \text{ s}^{-1}$, which corresponds to a purely diffusive time $1 \text{ mm}^2 / D \sim 10^4 \text{ s}$. Last, the water-polymer solutions are transparent at all concentrations.

II.1.2 Viscosity ratio λ

The viscosity ratio, λ , is controlled by tuning the mass fraction of polymer f in the solutions for the bath and for the blob. Therefore, the viscosity dependence on f has to be characterized systematically. To this end, we prepare ten sample solutions, with f varying from 0 to 1 in steps of 0.1, which we characterize with the help of a small gap, cone-plate rheometer (Anton Paar MCR 501). The shear viscosity is measured for shear rates linearly ramped between $\dot{\gamma} \simeq 0.3 \text{ s}^{-1}$ and $\dot{\gamma} = 5 \text{ s}^{-1}$ and at a temperature of 22°C , which match the typical range of shear rates and the temperature in the mixing flow experiments.

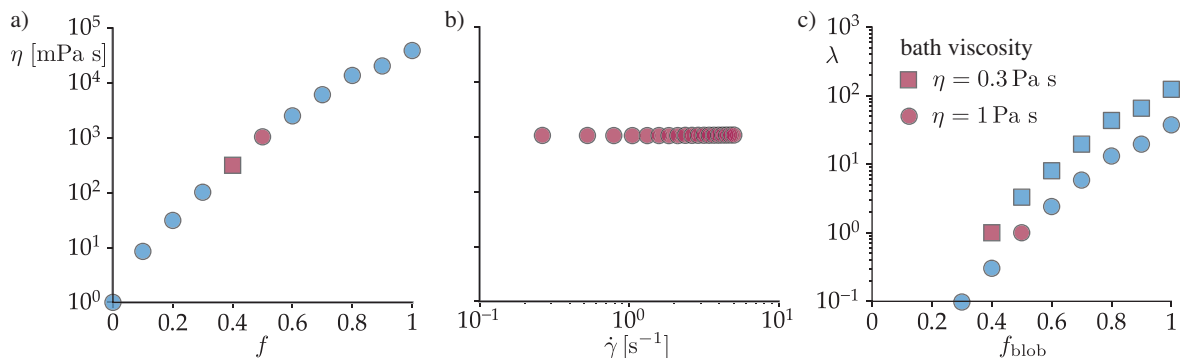


FIGURE II.1: *Viscosity of the water-polymer solutions.* (a) Viscosity η for different polymer mass fractions f at the temperature of the mixing flow experiments (22°C). The red circle and square highlight the two solutions used for the bath in the mixing flow experiments. (b) Viscosity η versus applied shear rate $\dot{\gamma}$ ($f = 0.5$). (c) Viscosity ratio λ obtained in the mixing flow experiments versus the polymer mass fraction in the blob f_{blob} for the two different baths.

As shown in figure II.1a, the viscosity increases regularly (close to exponentially) from $\eta \simeq 1 \text{ mPa s}$, for $f = 0$, to $\eta \simeq 39 \text{ Pa s}$, for $f = 1$. Importantly, the viscosity is found to be constant within $\pm 1\%$, over the whole range of the explored shear rates (see fig II.1b for $f = 0.5$), which shows that the liquids can be considered as Newtonian in the mixing flow experiments.

To explore large viscosity ratios ($\lambda \sim 10^2$), the bath viscosity must be kept small enough. Conversely, to ensure a purely viscous flow (small Reynolds number) and limit the effect of the small density mismatch (see also §II.1.3), the bath viscosity must remain fairly large. In practice, this tradeoff led us to use two different baths with viscosity $\eta = 0.3 \text{ Pa s}$ and $\eta = 1 \text{ Pa s}$, respectively. For each of them, figure II.1c indicates the viscosity ratio λ obtained as a function of the mass fraction f in the blob.

II.1.3 Density matching

Changing the mass fraction of the polymer also changes the density of the solutions. To limit creaming or settling of the blob due to a density mismatch with the bath, the density of the bath and the blob must be carefully matched. To this end, we first characterize the density of the polymer solutions. It is measured at the experiment temperature of 22°C , with the help of a densimeter, and is plotted versus the polymer mass fraction f in figure II.2a. The density is found to increase by typically 10% up to $f \approx 0.8$, beyond which it slightly decreases. To match the bath and the blob densities, we add salt either to the bath, when it is lighter (which corresponds to $\lambda > 1$), or to the blob when the bath is denser ($\lambda < 1$). Due to the large volume of solution needed for the bath, we use table salt (sodium chloride, with molecular mass $\simeq 58 \text{ g mol}^{-1}$) in the first case, and caesium chloride ($\simeq 168 \text{ g mol}^{-1}$) in the second.

Figure II.2b shows how the density of the two different baths increases with the mass fraction of added salt f_{salt} . In both cases, density goes beyond the maximal density without salt, which means that the density of the blob can be matched by adding salt to the bath for all viscosity ratios $\lambda \geq 1$. A similar calibration curve is obtained when adding salt to the blob solution ($\lambda < 1$, not shown). In practice, we use a linear interpolation through the calibration data to compute the exact quantity of salt to be used. This procedure leads to a density matching within typically $\pm 1 \text{ kg m}^{-3}$, which keeps the blob settling velocity below a few microns per second (*i.e.*, much smaller than the typical shear velocity $\dot{\gamma}b \sim 1 \text{ mm s}^{-1}$).

The addition of salt also shifts the viscosity of the solutions. For instance, adding 3% of salt to a solution with $f = 0.5$ decreases viscosity by typically 10%. The variation in η is close to linear with the added salt mass fraction. We measure and take into account this variation to determine the exact value of λ in all the experiments.

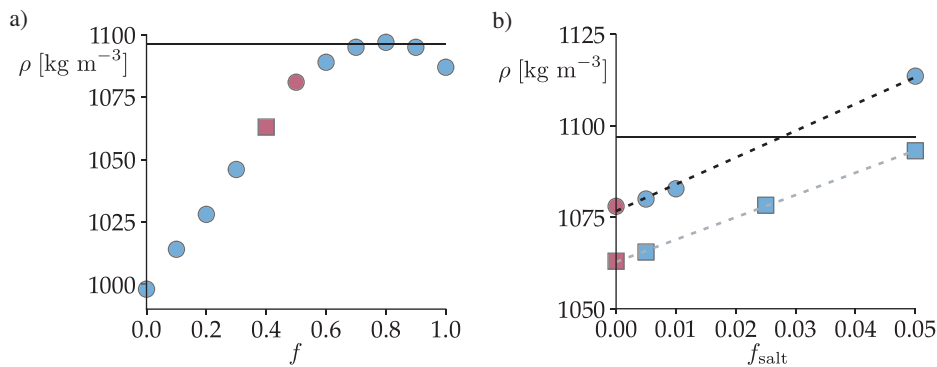


FIGURE II.2: Density matching of the water-polymer solutions. (a) Density ρ for different polymer mass fraction f (without salt). Red circle and square: the two different mass fractions used as bath in the mixing flow experiments. (b) Increase in the bath density with the mass fraction of added salt f_{salt} . Horizontal line: maximal density, without salt, measured for $f \approx 0.8$. Dashed lines: linear interpolation used to match the bath density with the blob density.

II.1.4 Preparation of the liquids

Each water-polymer solution is prepared by weighing the water mass m_{H_2O} and the polymer mass m_P to obtain the desired mass fraction

$$f = \frac{m_P}{m_{H_2O} + m_P}.$$

The solution is then mixed with either a magnetic stirrer, for the large volumes of the bath, or a fast-mixer (SpeedMixer FV2), for the smaller volumes used to prepare the blobs. In both cases, mixing leads to the nucleation or trapping of air bubbles, which are removed by letting the solutions rest overnight. For solutions with salt, the salt is dissolved in the needed amount of water using a magnetic stirrer, and the resulting solution is mixed with the polymer.

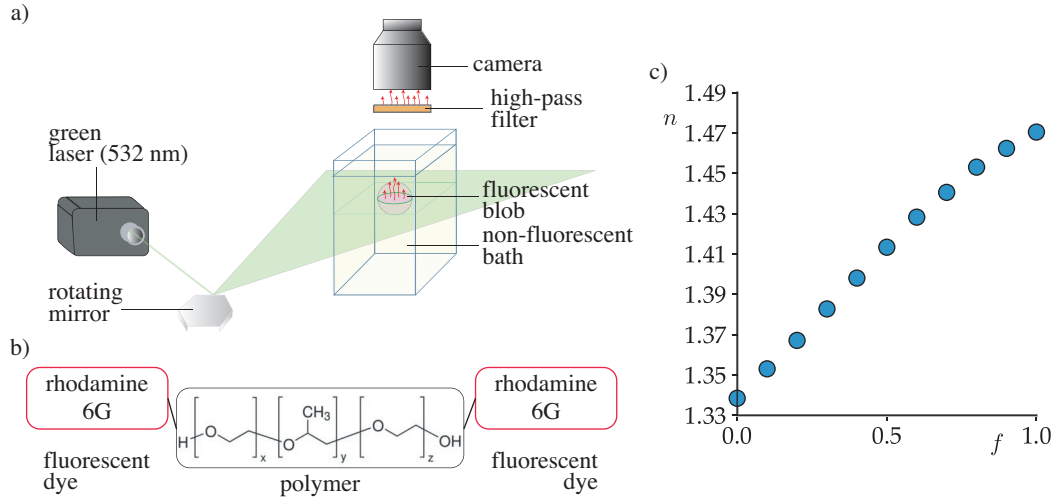


FIGURE II.3: *Visualization of the viscosity field.* (a) Principle of the Planar Laser-Induced Fluorescence technique used to track the blob in the flow experiment (and in the static setup to measure the diffusivities). (b) Schematics of the fluorescent polymer, designed and chemically synthesized for us by Prof. Eric Drockenmüller, by binding Rhodamine to the polymer. (c) Refraction index of the solution versus polymer mass fraction (at wavelength 470 nm), which will be used for the schlieren visualization method (see §II.3).

II.2 Principle of the visualization techniques

Characterizing mixing requires the quantification of a diffusive front in either a still or a moving liquid. We use the common visualization technique of Planar Laser-Induced Fluorescence (PLIF), which consists in diluting a fluorescent dye in a subpart of the liquid and obtaining the concentration field of the dye through measurements of the fluorescent intensity field (using a uniform illumination and sufficiently diluted concentration to keep fluorescence intensity proportional to concentration). However in the present study the liquids we mix are already binary solutions of molecules with very different size ($M_{H_2O} \simeq 18 \text{ g mol}^{-1}$, while $M_{\text{polymer}} \simeq 12 \text{ kg mol}^{-1}$). In order to avoid complex ternary diffusion problems [108, 109] due to the introduction of an additional fluorescent molecule, we choose to bind the fluorescent molecule to the polymer. This visualization technique will be used both to characterize the effective diffusivities (see §II.3), and to visualize and quantify the blob mixing in the shear and chaotic flow configurations (chapters III, IV).

Besides the fluorescence technique, we also use a schlieren technique which is sensitive to the refraction index gradient in the mixing front and gives direct access to the evolution of the viscosity field. By contrast with the fluorescence technique, the schlieren technique can be made quantitative only in a Hele-Shaw configuration. It will be used to better understand the non-trivial effective diffusion of the fluorescence signal (dyed polymers) between the two water-polymer solutions in order to interpret properly the PLIF measurements in the three-dimensional mixing flow configurations.

II.2.1 Fluorescence

The fluorescence visualization technique (PLIF) involves a laser sheet to excite a fluorescent dye and a camera to observe the fluorescent signal (see Figure II.3a). We use a 2 W green laser diode of wavelength 532 nm. To ensure a uniform light in the field of view, we use a rotating mirror to create the laser sheet, which is focalized down to a thickness of $60 \mu\text{m}$ [47] with a system of lenses (not shown in the schematics). The fluorophore is Rhodamine 6G. The molecule (that appears as a dark, red powder when it is pure) is soluble in water and its absorption spectrum (500 to 559 nm) has a peak close to the laser wavelength.

Light is re-emitted by fluorescence at larger wavelengths (between ≈ 550 and 650 nm). To collect only the fluorescent re-emission from the dye and block the reflected laser light, we use a high-pass filter which cuts off all wavelengths below 590 nm.

Binding of the fluorescent agent: As introduced above, the Rhodamine molecule is bound to the polymer to avoid complex ternary diffusion. The chemical design and synthesis of this fluorescent polymer was realized for us by our collaborator Prof. Eric Drockenmüller, who is a chemist at the University of Lyon. The fluorescent polymer is the same polymer molecule (Ucon 75-H-90000) with one rhodamine molecule bound at each end (see schematic in figure II.3b). Its molecular weight ($\approx 12800 \text{ g mol}^{-1}$) is close to that of the bare polymer ($\approx 12000 \text{ g mol}^{-1}$), which ensures that both polymers (fluorescent and non-fluorescent) have a similar mobility and diffuse similarly. In the experiments, a minute amount of the fluorescent polymer ($\approx 10^{-5}$ in mass fraction [64]) is added to the solution of the blob to make it fluorescent. The quantity is chosen to have a large emission response while keeping the absorption across the blob small enough (typically less than 5% over 3 mm), to ensure that laser excitation remains close to uniform. In this case, the re-emitted light intensity is proportional to the dye concentration. However, we will see below that this proportionality does not apply when the amount of water in the blob solution is too small.

Photobleaching: A common experimental difficulty when using PLIF is that a continuous illumination of the fluorescent dye over a long time may lead to a permanent degradation of its emission efficiency called photobleaching. The magnitude of this photobleaching effect depends on the laser fluence and on the duration of the exposure. To limit the effect in the mixing flow experiments, we use an attenuation filter mounted on a actuated arm synchronized with the camera, which strongly dims the laser intensity (by typically a factor 10^{-2}) between image captures (see also §III.1.2). In the static experiment presented in the next section, the laser light is even switched off between image captures. This allows to keep the effect of photobleaching on re-emitted light intensity below 8%.

Fluorescence yield: Last, we encountered an effect most specific to our experiment. For a fixed dye concentration, we find that the re-emitted light intensity strongly decreases for very viscous solutions, *i.e.*, those solutions which contain a small amount of water. As shown in figure II.4, the re-emitted light intensity, for a fixed laser intensity, is almost constant for f between 0.1 and ≈ 0.6 . However, for larger values of f ($\gtrsim 0.6$) it drops significantly, presumably because the quantum efficiency of the dye decreases when the amount of water in the solution is decreased. This leads to a non-trivial interpretation of the relation between the fluorescence intensity and the concentration fields for more viscous blobs, which will need to be considered when analyzing the data.

This feature can also be considered positively, in the sense that the fluorescent polymers therefore act as a sensitive tracer for the presence of water. We will indeed see that when the blob is prepared with pure polymer (without water), fluorescence provides a very contrasted signal of the diffusion of water into the blob. Such a sensitivity could also be interesting in other contexts to detect the presence of water, for instance, in experiments involving drying or chemical reactions.

II.2.2 Index of refraction

Fluorescence is not the only method for observing and quantifying the homogenization of our water-polymer solutions. The index of refraction of the solution, n , also changes with the polymer mass fraction f . This means that it can be used to infer the viscosity field. We will see in the next section how this can be done in a simple configuration of a Hele-Shaw cell using a schlieren technique. As a calibration for this

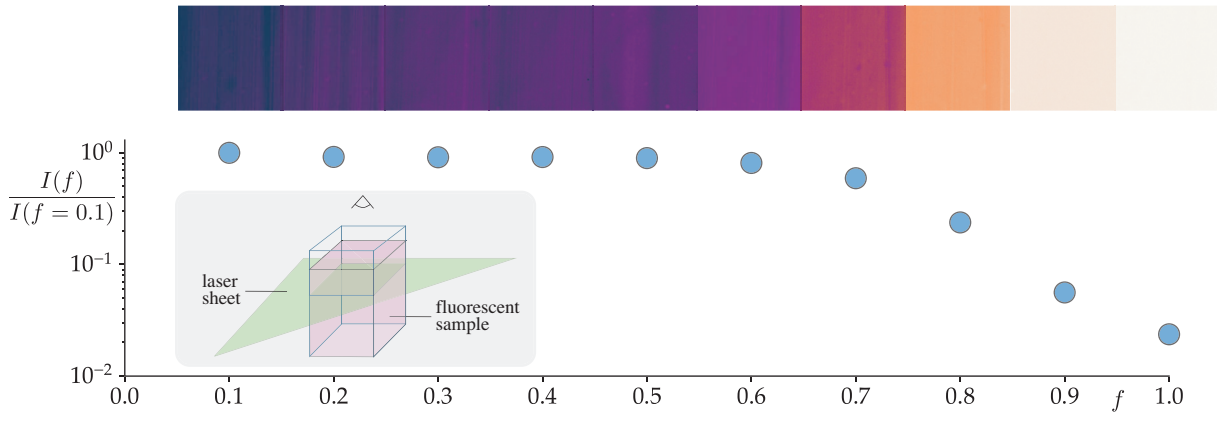


FIGURE II.4: *Variation of the fluorescence yield.* (Top) Snapshots of a $2.5 \times 2.5 \text{ mm}^2$ portion of sample fluorescent baths showing the intensity of the re-emitted light for a fixed amount of *fluorescent* polymer ($\simeq 10^{-5}$ of mass fraction), but different *total* mass fraction of polymer (f). Snapshots are obtained by keeping the laser intensity and the exposure time of the camera fixed. (Bottom) Re-emitted light intensity relative to the case $f = 0.1$. (Insert) Schematics of the measurements configuration. Visualization is from the top of the sample.

technique, we systematically measure the index of refraction of the water-polymer solutions as a function of f . The measurements are made with a refractometer at the experiment temperature of 22°C . The light supplied to the refractometer is a blue LED with a wavelength of 470 nm (the same light that will be used to apply the schlieren technique in the Hele-Shaw cell). As shown in figure II.3c, the refraction index increases monotonically with f , by approximately 10% over the full range of variation ($f = 0$ to $f = 1$). Since schlieren techniques can be made highly sensitive to gradients of the refraction index [110, 111], this increase provides a sufficient dynamics to obtain accurate measurements of the polymer mass fraction f from the index of refraction.

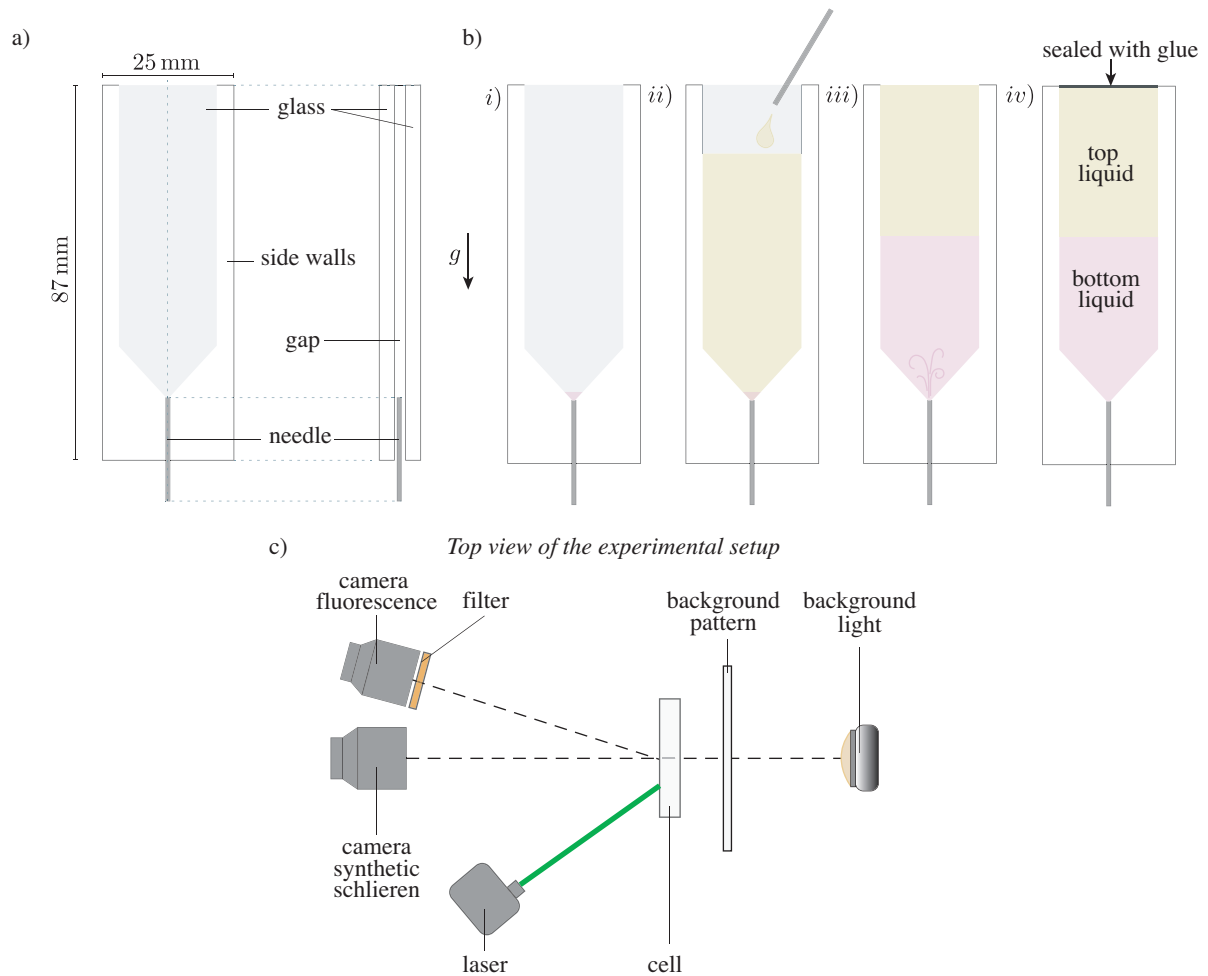


FIGURE II.5: *Static experimental setup used to characterize the effective diffusivities.* (a) Schematics of the Hele-Shaw cell. (b) Four-step protocol to obtain a sharp initial front between the two liquids, see text. (c) Schematics (top view) of the general layout allowing to use the two visualization techniques at the same time.

II.3 Effective diffusivities

To control the Péclet number and to interpret and model the mixing flow experiments we need to clarify the diffusion process between our solutions and characterize the effective diffusivities. To do so, we use a Hele-Shaw configuration to observe the diffusion front between non-moving solutions with different mass fraction and to quantify the unidimensional purely diffusive process. This characterization is done using the fluorescence method (tracking the fluorescent polymers) and the schlieren method (tracking both fluorescent and non-fluorescent polymers). These complementary observations will allow us to interpret the non-trivial diffusion process between the water-polymer solutions.

II.3.1 Experimental setup

Figure II.5a shows the Hele-Shaw cell. It consists of two glass plates sandwiching plastic side walls. The thickness of the side walls (digitally designed and laser-cut) set the uniform gap separating the glass plates, $\ell = 0.5$ mm, and allows to host a needle at the bottom for liquid injection. The characterization of the diffusion coefficient is performed by placing the Hele-Shaw cell vertically, which stabilizes against any convection currents the front between the more viscous (denser) solution, placed at the bottom, and the less viscous (lighter) solution, placed at the top. The cell-filling protocol, sketched in figure II.5b is as

follows:

- i) the injection needle is filled with the more viscous solution and inserted at the bottom of the cell,
- ii) the cell is filled with the less viscous (less dense) solution from the top of the cell. A reference image is captured for the schlieren technique that will be described in the next section,
- iii) the more viscous solution is slowly infused (from below) until the front between the two solutions reaches the cell half-height,
- iv) the cell is cleaned and sealed with glue at the top to avoid evaporation.

We monitor the diffusive mixing between the two solutions for typically 20 h, by acquiring images quadratically spaced in time. The process was initially done by hand and then automatized via remote control of the components (laser and cameras). Importantly the characterization by the two techniques (fluorescence and schlieren) is done simultaneously, by taking images with the two camera at the same times.

II.3.2 The two measurements techniques

In the following we investigate the diffusion of the front between the two solutions and compare the results obtained from the fluorescence and the schlieren techniques. To do so, we detail the two techniques and present a typical experiment in which the top side of the cell is filled with a non fluorescent solution with polymer mass fraction $f = 0.3$ ($\eta \simeq 0.1$ Pa s), and the bottom side with a fluorescent solution with $f = 0.7$ ($\eta \simeq 6$ Pa s).

II.3.2.a Fluorescence technique

In the present Hele-Shaw cell configuration, the laser sheet is placed vertically to illuminate a slab of liquid along the long side of the cell, in the direction where the diffusion front spreads (see figure II.6a). Figure II.6b shows a typical image of the light intensity re-emitted by the fluorescent polymer. The dark strip corresponds to the side of the illuminated slab where the dye concentration is large (to facilitate the visualization and lecture of the images, colors are inverted showing as dark the re-emitted light and as

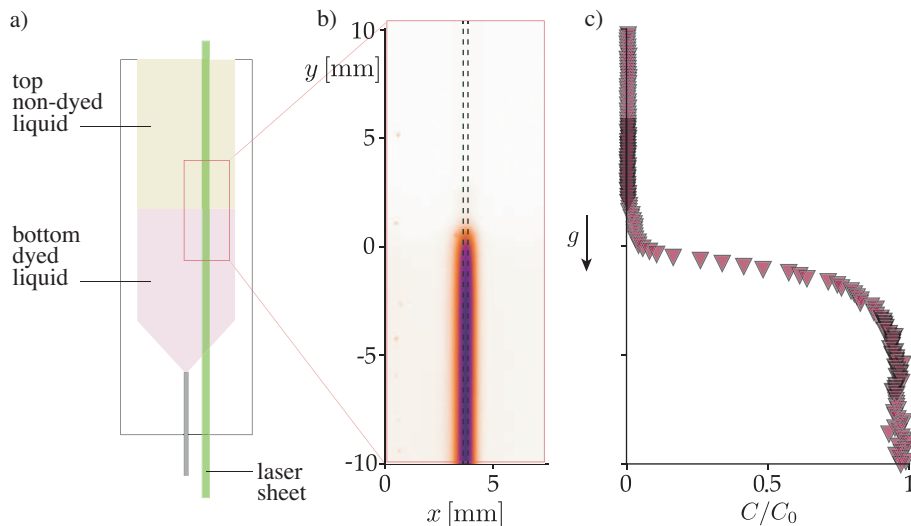


FIGURE II.6: *Fluorescence technique (characterization of the diffusivities)*. (a) Schematics of the cell illustrating the vertical slice of the liquid which is illuminated by the laser sheet. (b) Snapshot of the portion of the cell highlighted by the red frame in (a), (taken $t \simeq 12500$ s after the injection). The dark line is the light re-emitted by the fluorescent polymer (the white background corresponds to zero re-emitted light). (c) Concentration profile of the fluorescent polymer along the y -axes obtained from (b). Markers show 1 every 10 datapoints.

bright the zero intensity background). Figure II.6c shows the corresponding concentration profile, which is obtained by averaging the light intensity profile over 20 pixels along the x -axis direction (the averaging width is indicated by dashed lines in figure II.6b) and by defining

$$\frac{C(y)}{C_0} = \frac{\langle I(y) \rangle - I_b}{I_M - I_b}, \quad (\text{II.1})$$

where C_0 is the maximal initial dye concentration, $\langle I(y) \rangle$ is the (x -averaged) intensity profile along the vertical light sheet, I_b is the background light intensity and I_M is the maximum light intensity (maximum of $\langle I(y) \rangle$ at $t = 0$ immediately after the cell is filled).

II.3.2.b Synthetic schlieren technique

The synthetic schlieren technique uses the characterization of the refraction index described in the previous section (§II.2). The technique is used in the same fashion as in [112]. A background pattern is observed through the transparent Hele-Shaw cell containing the mixing solutions. By quantifying the optical distortion of the background pattern due to the refraction index gradients in the cell, we reconstruct the spatial profile of the index of refraction. As an illustration, figure II.7b shows a snapshot of a human-friendly background pattern observed through the cell when the liquid is uniform (constant refraction index n , image A), and its distortion by the diffusive front between two water-polymer solutions (finite index refraction gradient, image B).

In practice we do not use the human friendly pattern for quantification, we use a random background pattern which allows to obtain accurate measurements of the apparent distortion by an image correlation analysis. The random pattern is a semi-transparent sand-blasted glass plate, which is backlit with a monochromatic light source (blue LED, 470 nm). It is positioned between the cell and the light, at a distance $L_p \simeq 18.2$ mm from the cell (see figure II.5c). The camera is placed at a distance $L_0 = 55$ cm from the cell and is coupled with a macroscope lens (Sigma MACRO 180 mm DG HSM). The coupling gives a resolution of $13 \mu\text{m pix}^{-1}$, and with a reasonable aperture of the lens, both the cell and the pattern are within the depth of field. In the reference experiment, the refraction index varies continuously in the cell from the value $n(f = 0.3)$ at the top, to the value $n(f = 0.7)$ at the bottom. During the diffusion of the two liquids we observe an apparent displacement of the pattern ΔY that can be measured (see below) and related to the refraction index gradient inside the cell. This variation of $n(y)$ is then used to recover the mass fraction profile $f(y)$ in the cell.

Figure II.7a shows the schematics of the light path, used to relate the apparent displacement of the background pattern to the refraction index gradient in the cell, across the setup (not in scale). The blue line indicates the reference light path from a point of the background pattern at height Y_A through a uniform liquid ($\partial n / \partial y = 0$). The solid red-green line indicates the light path in the presence of a negative refraction index gradient ($\partial n / \partial y < 0$), in which case light is deflected towards the large n , *i.e.*, towards the bottom of the cell. The green dashed line is the virtual path from a point of the background pattern at height Y_B , which defines the apparent displacement of the pattern $\Delta Y = Y_B - Y_A$.

From figure II.7a, we can quantify and relate the paths. In the absence of refraction index gradient, the light path across the interfaces is given by the Snell law, $n_i \sin(\vartheta_i) = \text{constant}$, *i.e.*, $n_i \vartheta_i = \text{constant}$ in the limit of small angles, from which we have:

$$\vartheta_i = n_g \vartheta_1 = n \vartheta_2, \quad n \vartheta_3 = n_g \vartheta_4 = \vartheta_5, \quad (\text{II.2})$$

where the index of refraction of air is put to 1. Inside the cell, the presence of a vertical refraction index

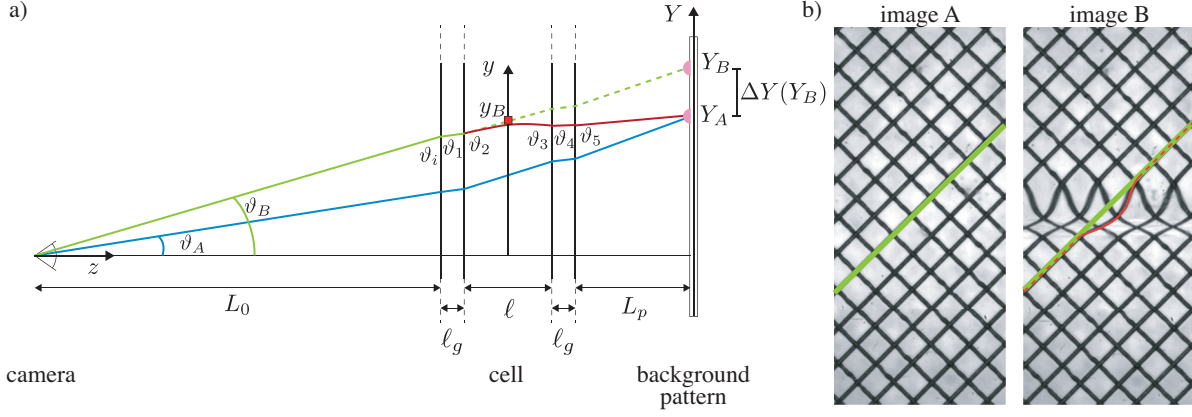


FIGURE II.7: *Synthetic schlieren technique (characterization of the diffusivities)*. (a) Sketch of the light path used to relate the apparent displacement of the background pattern to the refraction index gradient in the cell. The blue line indicates the reference light path (from the background pattern at height Y_A) through a uniform liquid (no gradient). The red and green lines indicate the light path in the presence of a refraction index gradient ($\partial n/\partial y < 0$). The dashed green line is the virtual path defining the apparent displacement of the background pattern ΔY . (b) Snapshots of the human-friendly background pattern observed through the cell. (Left) Reference image (no gradient). (Right) Background distorted by the diffusive front between two water-polymer solutions ($\partial n/\partial y < 0$).

gradient is equivalent to a continuum of *horizontal* interfaces, across which $n \cos \vartheta = \text{constant}$. By differentiating along the close-to-horizontal light path we obtain $\frac{\partial n}{\partial y} - n \frac{d\vartheta}{dz} = 0$, which gives a relation between the angles ϑ_3 and ϑ_2 in the liquid immediately next to the glass plates (see Figure II.7a):

$$\vartheta_3 = \vartheta_2 + \frac{\partial n}{\partial y} \ell. \quad (\text{II.3})$$

For an arbitrary point at height Y on the background pattern, the height is related to the path angles and setup lengths through (see schematic in figure II.7a),

$$Y = L_0 \vartheta_i + \ell_g \vartheta_1 + \frac{\ell}{2} \vartheta_2 + \frac{\ell}{2} \vartheta_3 + \ell_g \vartheta_4 + L_p \vartheta_5,$$

which can be recasted into

$$Y = (\mathcal{L}_0 + \mathcal{L}_p) \vartheta_i + \mathcal{L}_p \ell \frac{\partial n}{\partial y}, \quad (\text{II.4})$$

$$\text{with } \mathcal{L}_0 = L_0 + \frac{\ell_g}{n_g} + \frac{1}{2} \frac{\ell}{n}, \quad \text{and } \mathcal{L}_p = \frac{1}{2} \frac{\ell}{n} + \frac{\ell_g}{n_g} + L_p. \quad (\text{II.5})$$

From equation II.4 we can now relate the reference and deflected paths. For the reference path we have $Y = Y_A$, $\vartheta_i = \vartheta_A$ and $\partial n/\partial y = 0$. For the deflected path we have also $Y = Y_A$, but a different angle at the camera $\vartheta_i = \vartheta_B$, and $\partial n/\partial y \neq 0$, with $\partial n/\partial y$ the unknown gradient we want to express. Equating the expressions for Y_A in both cases we obtain

$$\vartheta_B = \vartheta_A - \frac{\mathcal{L}_p}{\mathcal{L}_0 + \mathcal{L}_p} \ell \frac{\partial n}{\partial y}. \quad (\text{II.6})$$

Considering now equation II.4 for the virtual path setting the apparent position Y_B (green dashed line), we have $Y = Y_B$, $\vartheta_i = \vartheta_B$ and $\partial n/\partial y = 0$, so that

$$\Delta Y = Y_B - Y_A = (\mathcal{L}_0 + \mathcal{L}_p) (\vartheta_B - \vartheta_A). \quad (\text{II.7})$$

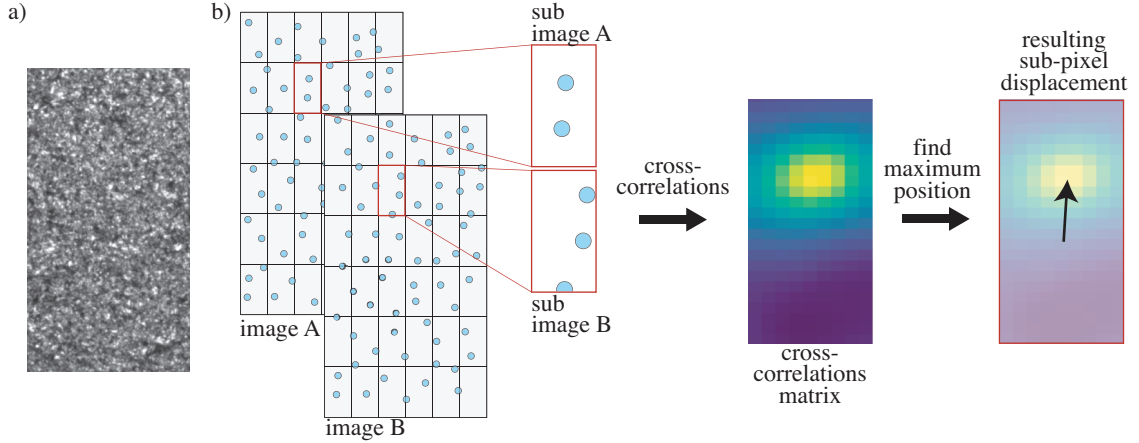


FIGURE II.8: Principles of the (PIV) algorithm used to compute the apparent displacement field. (a) Sample portion of the random background pattern (backlit sand-blasted glass plate). (b) Diagram of cross-correlation processing between the current sub-image and its reference ($\partial n/\partial y = 0$). The sub-pixel estimate of the maximum value of the cross-correlation matrix gives the local displacement vector.

Last, combining equations II.6 and II.7, we obtain the final expression:

$$\frac{\partial n}{\partial y} = -\frac{1}{\mathcal{L}_p \ell} \Delta Y, \quad (\text{II.8})$$

which relates the index of refraction gradient $\frac{\partial n}{\partial y}(y_B)$, at the height $y_B = -\frac{\mathcal{L}_p}{\mathcal{L}_0 + \mathcal{L}_p} Y_B$ in the cell, to the apparent displacement $\Delta Y(Y_B)$, at height Y_B in the background pattern.

To obtain $\frac{\partial n}{\partial y}$ we need to measure ΔY precisely, which is done with the same image correlation technique as for Particle Image Velocimetry (PIV). The method consists in comparing the reference and the current images of the pattern, dividing each of them into a grid of sub-images and finding the relative displacement that maximizes the correlation between each pair of sub-images (see Figure II.8). To this end, a cross-correlation matrix is computed for each pair of sub-images and a parabolic fit to the peak of the matrix is used to obtain the displacement with a sub-pixel precision. Since the displacement is essentially vertical (there is no horizontal gradient), we choose sub-images with a large horizontal width and

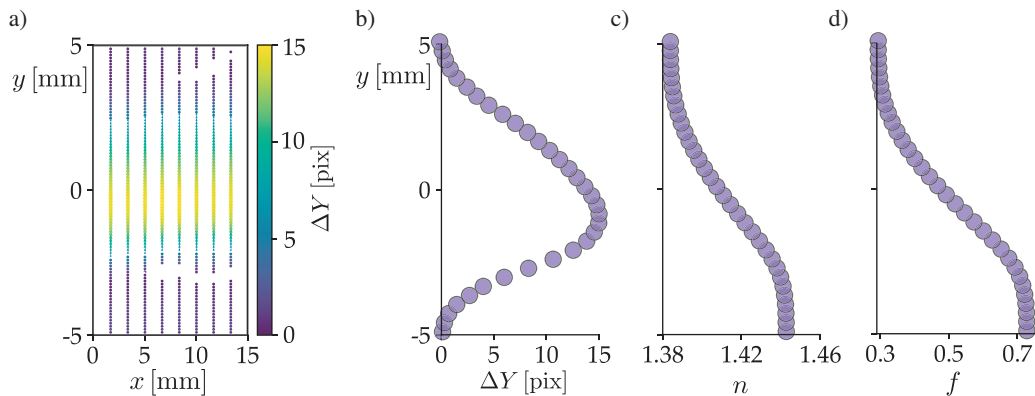


FIGURE II.9: Reconstruction of the polymer mass fraction profile from the apparent displacement. (a) Vertical displacement field $\Delta Y(x, y)$ obtained from the PIV algorithm. Color indicates the magnitude of the displacement in *pixel*. (b) Displacement profile along the y -axes (average over the x -direction). (c) Index of refraction profile inferred from (b). (d) Mass fraction profile inferred from (c). Markers in (b) to (d) display 1 every 3 datapoints.

a short vertical height to keep a good correlation signal while resolving accurately the short-time front where $\partial n / \partial y$ is large.

A typical displacement field is illustrated in figure II.9a for a snapshot obtained at time $t = 12500$ s after the filling of the cell. The color code represents the magnitude of the apparent displacement ΔY . Panel (b) shows the displacement profile across the front $\Delta Y(y)$ (averaged over the transverse direction x). By integrating equation II.8, which relates ΔY to $\partial n / \partial y(y)$ (with boundary condition $n = n(f = 0.3)$ at the top of the cell), we obtain the refraction index profile $n(y)$, shown in panel (c), and finally (using the calibration curve $n(f)$, see §II.2.2, Figure II.3c) the mass fraction profile $f(y)$, shown in panel (d). With this procedure we overshoot the value of $f = 0.7$ by less than 8%, which indicates the accuracy of the method.

II.3.3 Comparison between the fluorescence profile and the mass fraction profile & interpretation

Figure II.10 shows the comparison between the dyed polymer concentration profile obtained with the fluorescence technique and the total polymer mass fraction profile obtained via synthetic schlieren. Panels a and b show the raw data for the experiment involving a non-dyed liquid with polymer mass fraction $f = 0.3$ at the top of the cell and a dyed liquid with $f = 0.7$ at the bottom, at $t = 12500$ s after the creation of the front. Figure II.10c shows the comparison between the two experimental profiles and highlights an evident mismatch. Indeed, the polymer mass fraction front (circles) is significantly broader than the one obtained with fluorescence (triangles). Yet, both profiles are actually reasonably well fitted, at all times, by the relevant solution of the diffusive equation, *i.e.*, the error function:

$$C(y, t) = \frac{C_0}{2} \left[1 + \operatorname{erf} \left(\frac{y - y_0}{\sqrt{2}\sigma} \right) \right], \quad (\text{II.9})$$

where C stands for C or f , which yields the two different evolutions of the gradient variance σ^2 (for C and f) reported in figure II.10d. Both variances increase linearly with time, and can be fitted by $\sigma^2 = \sigma_0^2 + 2Dt$,

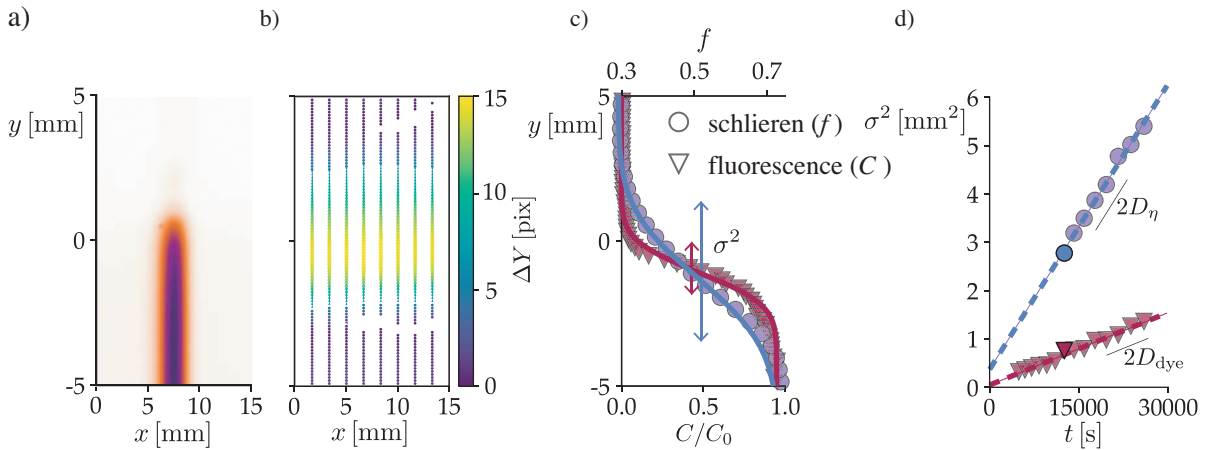


FIGURE II.10: Comparison between the diffusion coefficients obtained from the fluorescence and the mass fraction profiles. (a) Snapshot from the fluorescence technique. (b) Displacement field obtained from the synthetic schlieren technique. (c) Comparison between the two reconstructed profiles (dye concentration C for the fluorescence and mass fraction f for the synthetic schlieren) obtained at time $t = 12500$ s. (d) Time evolution of the corresponding variances. Blue and red dashed lines: linear fit with $\sigma^2 = \sigma_0^2 + 2Dt$ yielding $D_{\text{dye}} \simeq 10^{-11} \text{ m}^2 \text{ s}^{-1}$ for the fluorescent dye profile, and

$$D_{\eta} \simeq 2 \times 10^{-10} \text{ m}^2 \text{ s}^{-1} \text{ for the mass fraction profile.}$$

to determine the respective (effective) diffusion coefficients D characterizing the evolution of the two profiles.

The above results raise two important points. Firstly, the fit of the profiles by an error function, at all times, and the linear increase of the variances with time indicate that the two diffusion coefficients are constant and not much dependent on the viscosity. Secondly, the effective diffusion coefficient of the dye obtained with the fluorescent technique, $D_{\text{dye}} \simeq 2.5 \times 10^{-11} \text{ m}^2 \text{ s}^{-1}$, is typically one order of magnitude smaller than the binary diffusion coefficient obtained with the schlieren technique, $D_{\eta} \simeq 10^{-10} \text{ m}^2 \text{ s}^{-1}$. But why is it?

Interpretation of the diffusion process

We interpret the above diffusion process as follows. For sake of simplicity, we neglect here the minor contribution of the fluorescent yield dependence on the total polymer mass fraction f (see §II.2.1) and consider that the fluorescence intensity is proportional to the dye concentration. Figure II.11a sketches the initial condition, when a sharp front separates two water-polymer solutions with different initial mass fractions f . The water concentration profile (blue line) is complementary to that of the polymer mass fraction, and only the more viscous solution (larger f) contains fluorescent polymers (red line). In these concentrated mixtures of water and polymer, the small water molecules have presumably a much larger mobility than the long polymer molecules. Therefore, the broadening of the front is mainly driven by the passive swelling of the ‘almost frozen arrangement’ of the low mobility polymers by the rapidly diffusing water molecules, which tends to equilibrate the water content, *i.e.*, the *total* mass fraction of polymer. This fast diffusion swells and dilutes the dyed and non-dyed polymer almost equally, but the front between the dyed and non-dyed polymers remains sharp because of the low mobility of the polymers.

As shown in figure II.11b, this process leads to a broad profile for the total polymer mass fraction f (yellow dashed line), and a two-piece and much sharper profile for the dyed polymer concentration C (red line). Since the schlieren technique gives access to the overall polymer mass fraction profile, it naturally yields a diffusion coefficient D_{η} (the real binary diffusion coefficient between polymers and water) much larger than the effective diffusion coefficient D_{dye} obtained with the fluorescence technique.

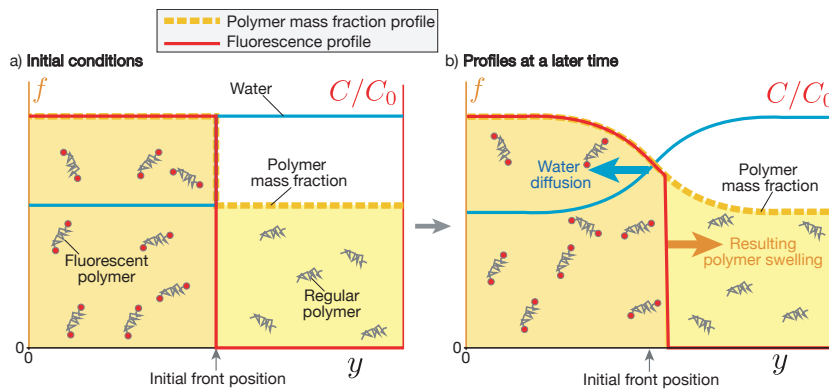


FIGURE II.11: Qualitative sketch for the difference between the fluorescence profile and the mass fraction profile. (a) Initial profiles for the concentrations of polymer $f(y)$, and dye $C(y)/C_0$. The two profiles are not proportional to each other. (b) The ‘large’ mobility of the ‘small’ water molecules (relative to the ‘low’ mobility of the ‘large’ polymer molecules) drives the profile evolution. The net water flux (right to left) swells and dilutes equally the dyed and non-dyed polymers (towards the right), but the front between dyed and non-dyed polymers remains sharp because of the low mobility of the polymers. This leads to a broad profile for the polymer mass fraction f (yellow line), and a two-piece and much sharper profile for the fluorescent dye concentration C/C_0 (red line, the position of the sharp front shifts to the right to keep the area enclosed by the red line constant). The relative size of the two pieces of the profile depends on the ratio between the initial mass fraction on the right and on the left.

The latter (D_{dye}) actually depends on the ratio of the initial mass fraction between the dyed and non-dyed polymer in the two solutions, because the relative size of the two pieces of the dye profile (see figure II.11) depends on this ratio.

To validate the above scenario, we perform two complementary experiments:

- one experiment, called proportional case, where the dye concentration is adjusted to be proportional to the polymer concentration in both polymer solutions,
- a second experiment of self-diffusion, called iso-water case, with the same polymer mass fraction f (same water quantity) in both solutions, to measure the binary diffusion coefficient between the dyed and non-dyed polymers in the solution (with no influence of the swelling by water).

Verification in the proportional case: The experiment is repeated with dyed polymers in the two solutions, with a quantity of dyed polymer which is proportional to the total polymer mass fraction f in each solution (C/f uniform in the whole cell). In this case, the fluorescence profile and the mass fraction profile are expected to remain identical at all time, as sketched in the insert of figure II.12a.

Figure II.12a shows the comparison between the profiles of f and C obtained from the two techniques at three different times. It confirms that when f and C are initially proportional, the two profiles remain almost identical at all times. Moreover, the variances is found to follow the same linear increase with time ($D_{\text{dye}} \simeq D_{\eta} \simeq 1.3 \times 10^{-10} \text{m}^2 \text{s}^{-1}$, see figure II.12b), which indicates that, in this case, the effective diffusivity of the dye is very close to the binary diffusion coefficient $D_{\eta} \approx 2 \times 10^{-10} \text{m}^2 \text{s}^{-1}$.

Verification in the iso-water case: To further validate the non-trivial effective diffusion of the dye described above, we perform the second experiment with a uniform water content ($f = 0.5$) and dyed polymer only on one side, in which we measure the self-diffusion coefficient of the polymer molecules in the solution.

Figure II.13a, shows the rescaled dye concentration profiles at three different times and the evolution of the variance (insert). In this iso-water case, the measured self-diffusion coefficient of the polymer $D_{\text{self,polymer}} \simeq 0.7 \times 10^{-11} \text{m}^2 \text{s}^{-1}$ is indeed much smaller than the binary diffusivity between polymer and water D_{η} and comparable with the effective diffusivity $D_{\text{dye}} \approx 10^{-11} \text{m}^2 \text{s}^{-1}$ found previously when tracking the dye concentration profile in the non-proportional case (Fig. II.10).

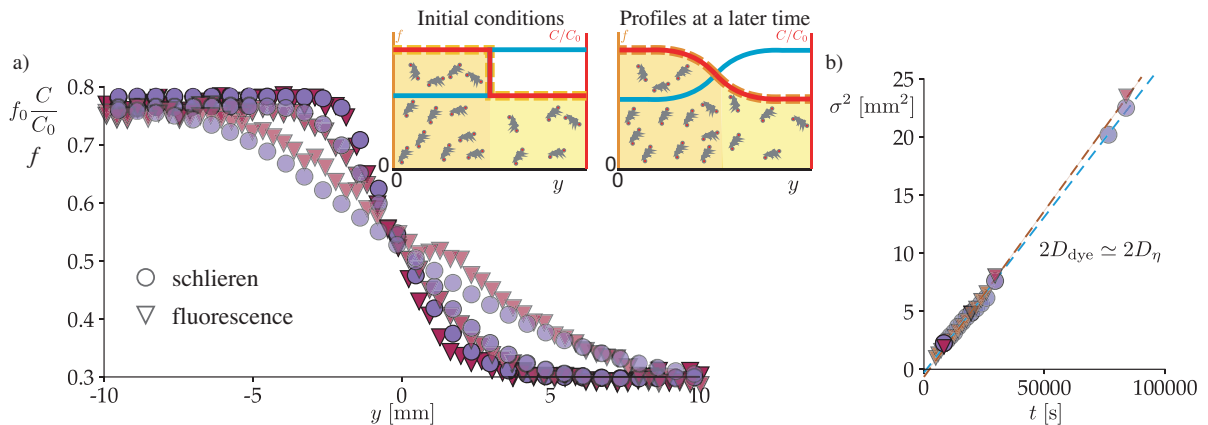


FIGURE II.12: Identity of the fluorescence and the mass fraction diffusion in the proportional case. (a) Comparison of the two profiles, at three different times ($t \simeq 8100\text{s}$, 19800s and 82800s after the creation of the front, $f_0 \simeq 0.77$ and C_0 respectively stand for the initial mass fraction and the initial concentration on the left-hand side). Insert: sketch of the overall diffusive process in the proportional case ($C/f = \text{constant}$ in both solutions). (b) The variances of the profile gradient for the two quantities follow the same linear increase in time, showing that the two quantities diffuse at the same rate.

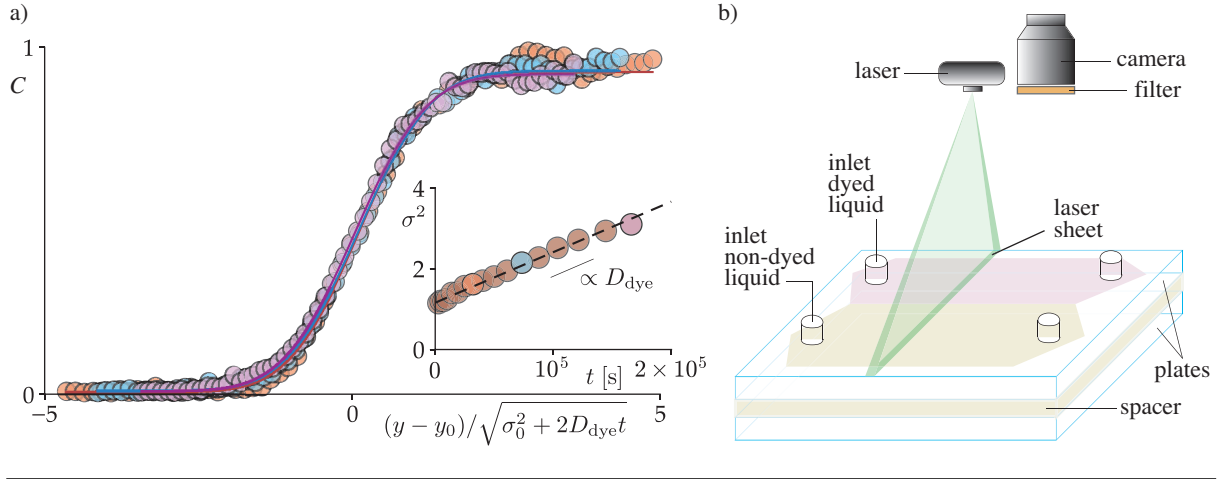


FIGURE II.13: *Independent characterization of the self-diffusion coefficient of the polymer.* Diffusion between dyed and non-dyed polymer for a uniform total polymer concentration (no net water flux, $f = 0.5$). (a) Time-rescaled dye concentration profiles at three different times ($t \simeq 32400$ s, 72900 s and 165600 s after the creation of the front). Insert: time evolution of the variance giving the self diffusion coefficient of the polymer molecules $D_{\text{self, polymer}} \simeq 0.7 \times 10^{-11} \text{ m}^2 \text{ s}^{-1}$, which matches the effective value $D_{\text{dye}} \simeq 10^{-11} \text{ m}^2 \text{ s}^{-1}$ obtained in the non-proportional case (Fig. II.10). (b) Modified injection setup used for the present case, where the two solutions have the same density. The sharp initial front is obtained by forcing the two solutions to flow parallel and rapidly in the Hele-Shaw cell. The flow is stopped before the diffusion process is observed.

Note that to perform this experiment, we cannot use gravity to prepare a sharp front since the density of the solutions are equal. We thus use a slightly different Hele-Shaw cell, shown in figure II.13b. The cell has two adjacent canals with no separation wall, but a separated inlet and outlet for each. It is placed horizontally. The two channels are filled with the two solutions, at the same flow rate and with the help of gravity, to obtain a sharp initial front, after which the inlets and outlets are closed, and measurements are taken according to the procedure explained for the fluorescence technique (§II.3.2).

II.3.4 Diffusion coefficients: summary of the results

Now that we have clarified why and in which case the effective diffusivity of the dye D_{dye} differs from the binary diffusion coefficient between the water-polymer solutions D_{η} , we need to strengthen our dataset and measure systematically the two values as a function of the viscosity ratio λ between the two solutions. The value of D_{η} is obtained with the schlieren technique. The value of D_{dye} is obtained from the fluorescence signal, either in the proportional case (between dyed and non-dyed polymer) or in the non-proportional case (dye only in the more viscous liquid). The viscosity ratio is ranged from $\lambda = 1$ to $\sim 10^4$ using three different low-viscosity solutions: $\eta = 1 \text{ mPa s}$ (pure water, squares), $\eta = 0.1 \text{ Pa s}$ ($f = 0.3$, diamonds), and $\eta = 1 \text{ Pa s}$ ($f = 0.5$, circles). The measurements are summarized in figure II.14. The purple symbols represent D_{η} . The hollow orange symbols indicate the effective dye diffusivity D_{dye} in the proportional case. The solid orange symbols indicate D_{dye} in the non-proportional case (the value for $\lambda = 1$ is the measured self-diffusivity of the polymer $D_{\text{self, polymer}}$).

Overall, we find that diffusion coefficient between the water-polymer solutions D_{η} , which determines the diffusivity of the viscosity field, has a value $D_{\eta} \simeq 1.65 \times 10^{-10} \text{ m}^2 \text{ s}^{-1}$, which does not vary much with viscosity over the two decades of viscosity ratio investigated ($\lambda \simeq 60$ to 6000). Regarding the dye, for the non-proportional case (dye only on one side, solid yellow symbols) that will be used to interpret the mixing flow experiments, the dye effective diffusion coefficient D_{dye} remains close to the self-diffusion coefficient of the polymer in a uniform solution $D_{\text{self, polymer}}$, with a value $D_{\text{dye}} \simeq 10^{-11} \text{ m}^2 \text{ s}^{-1}$, which is

also not varying much over the two decades of viscosity ratio investigated ($\lambda = 1$ to 60). This is consistent with the idea of a diffusion process driven by the large mobility of water and of a lower effective diffusivity of the dye due to the initial condition imposed by the visualization protocol for the mixing flow experiments (see below).

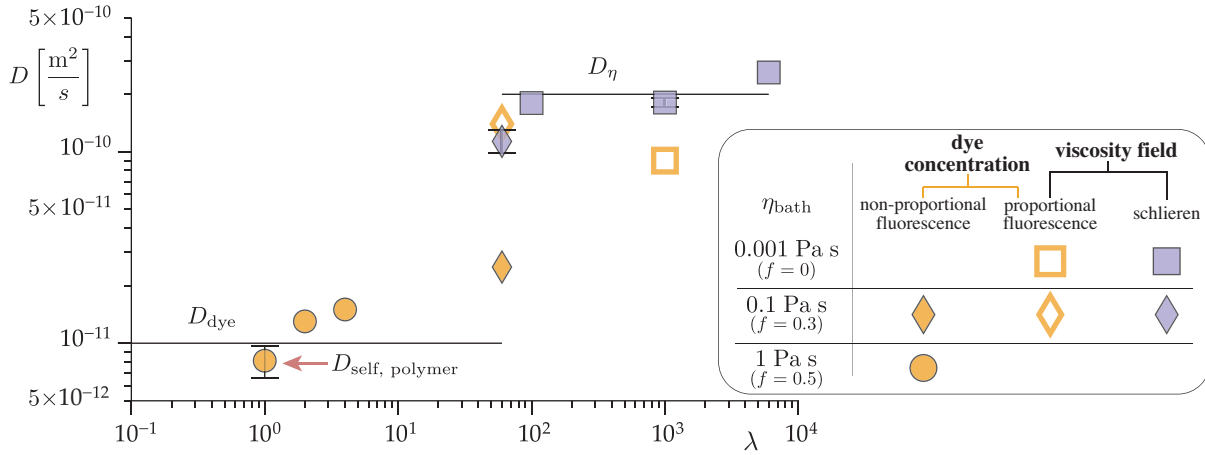


FIGURE II.14: *Final map for the value of the diffusivities.* Diffusion coefficients as a function of the viscosity ratio for different viscosity of the bath. The symbol shape indicates the bath viscosity. The purple symbols indicate the diffusivity of the viscosity field $D_\eta \approx 1.65 \times 10^{-10} \text{ m}^2 \text{ s}^{-1}$. The orange solid symbols indicate the effective diffusivity of the dye in the non-proportional case $D_{\text{dye}} \approx 10^{-11} \text{ m}^2 \text{ s}^{-1}$, which will be used for the mixing flow experiments in the next chapters (the orange hollow symbols show the dye effective diffusivity in the proportional case, where it matches D_η).

The values we obtain for the diffusivities can be compared with those reported in the literature. Though we could not find data for our water-polymer solutions, data exist for other systems of long polymers, whether in pure melts or in solutions with shorter polymers or small molecule solvents. The first relevant comparison is to a study by Paul [80], who measured by interferometric technique the diffusive front between solutions of a very long-chain polymer (acrylonitrile-vinyl acetate copolymer, $M_w \simeq 200 \text{ k g/mol}$) in small molecule solvents (dimethylacetamide with $M_w \simeq 200 \text{ g/mol}$, dimethylformamide with $M_w \simeq 73 \text{ g/mol}$, or dimethyl sulfoxide $M_w \simeq 78 \text{ g/mol}$) at mass fraction comparable to ours ($f = 0.25$). He reports binary diffusion coefficients $D \sim 0.9\text{-}1.5 \times 10^{-10} \text{ m}^2 \text{ s}^{-1}$ in the same range as the value $D_\eta \simeq 1.65 \times 10^{-10} \text{ m}^2 \text{ s}^{-1}$ we obtain. Second, a study by Wang and Meerwall [113] for melts containing both short polymers ($M_w \simeq 0.7 \text{ k g/mol}$) and long polymers ($M_w \simeq 12 \text{ k g/mol}$), confirms that the self-diffusivity of two species with different molecule size (measured by nuclear molecular resonance techniques for a uniform mass fraction) can differ by large factors ($\gtrsim 10$). The value they, as well as other study [73], report for the self-diffusivity of the long polymers, $D \sim 10^{-12} \text{ m}^2 \text{ s}^{-1}$, is about 10 times smaller than the dye diffusivity $D_{\text{dye}} \simeq 2 \times 10^{-11} \text{ m}^2 \text{ s}^{-1}$ we find. This is presumably because in our case the long polymers diffuse in a solution of very small molecules (water), whereas in their case, the long polymers diffuse in a melt where all molecules are large.

Last, it is important at this point to stress that in the mixing flow experiments presented in the next chapters, we will only be able to use the fluorescence technique with dyed polymer in the blob only. Indeed the non-trivial tridimensional shape of the blob prevents from obtaining quantitative data from the schlieren technique. On the other hand, to obtain a good image contrast, dyed polymer cannot be added to the bath, which prevent us from respecting the proportionality between the dyed and non-dyed polymer. This means that the fluorescence profile, which tracks the initially dyed polymer, will not give access directly to the viscosity field. We will see that depending on the viscosity ratio between the blob

and the shearing bath, it will actually be relevant to use either the dye diffusion coefficient D_{dye} or the mass fraction diffusion coefficient D_{η} to properly address the mixing problem.

II.4 Initial shape of the viscous blob

To complete the description of the main experimental methods and characterizations, we present the technique we had to develop to obtain a reproducible and controlled initial condition in the mixing flow experiments. Indeed, as will be seen in the next chapters, the initial shape of the blob strongly influences its subsequent deformation, but the absence of surface tension between the blob and the bath prevents controlling the blob shape by simply injecting one solution into the other. It was thus crucial to find an alternative way to control the initial shape of the blob.

After several attempts, trying to mold the initial shape of the blob or freeze it on a glass plate (which all proved unsatisfactory), we finally found an efficient protocol to produce quasi-spherical blob, based on the inverse Leidenfrost effect [114]. Figure II.15 illustrates the steps of the preparation:

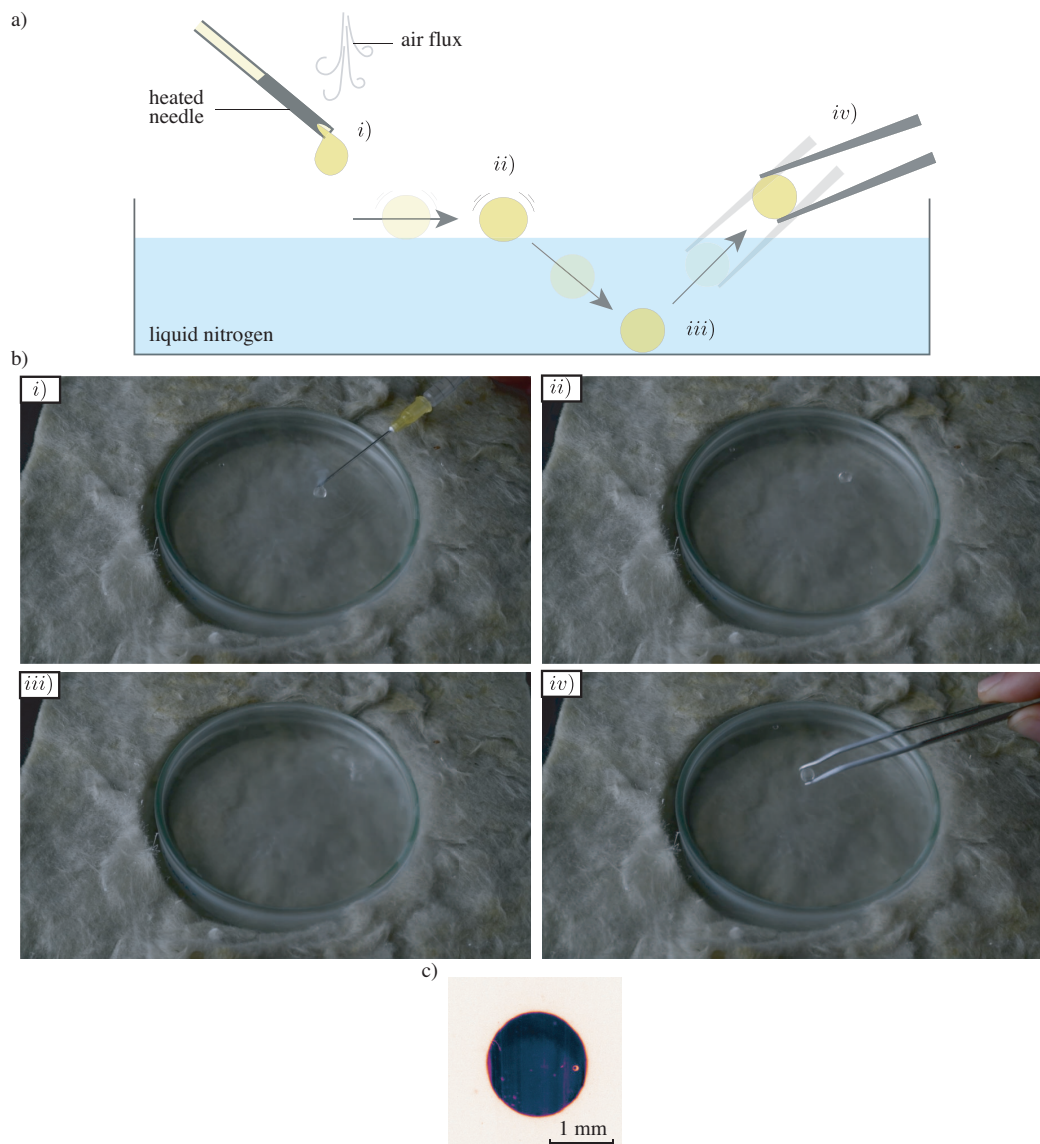


FIGURE II.15: Protocol to obtain an initially spherical blob. (a) The four steps of the protocol. *i*) A drop of the blob liquid is gently deposited onto a liquid nitrogen bath, with the help of a small air jet to detach the drop from the needle when it is small ($b_0 \lesssim 1$ mm). *ii*) While being levitated and rotated by nitrogen vaporization, the blob slowly freezes into a sphere. *iii*) Once it is frozen, it sinks in the bath. *iv*) The sphere is collected with cold tweezers and immersed into the bath of the experiment. (b) Snapshots of the four steps for a large ($b_0 \gtrsim 1$ mm) blob size. (c) Typical initial shape obtained for $\lambda = 8$ in a bath of viscosity $\eta = 1$ Pa s ($f = 0.5$).

- i) a drop of the blob liquid is gently deposited on the surface of a liquid nitrogen bath,
- ii) while being levitated and rotated by nitrogen vaporization, the blob slowly freezes in a quasi-spherical shape thanks to the air/solution surface tension,
- iii) once frozen, it sinks into the bath,
- iv) the frozen sphere is collected with cold tweezers and rapidly immersed in the bath,
- v) last, it is left to melt and equilibrate in temperature with the bath before the experiment is started.

The deposition of the drop on the nitrogen bath is done with the help of a syringe. For the largest drops (radius of 1 mm to 2 mm), the drop is detached from the needle by gravity. For smaller drops (radius below 1 mm), the drop is detached by flushing air. When the blob is highly viscous or small, the needle is preheated to decrease viscosity, such that the levitating drop relaxes to a sphere before freezing. The immersion in the bath requires care to avoid to trap air bubbles at the blob surface which would subsequently deform the blob once it has melt. We therefore place the blob at the bath surface and sink it by covering it with some of the bath liquid while it is still frozen. The subsequent melting of the blob and temperature equilibration takes a few tens of a seconds during which there is no significant mass diffusion between the blob and the bath since mass diffusivity is several orders of magnitude lower than thermal diffusivity.

With this technique we are able to prepare blobs which are highly spherical and have a sharp contour (see *e.g.*, figure II.15c for $\lambda = 8$) for all viscosity ratios. The radius can be tuned between 0.7 and 2 mm, and the typical asphericity of the blob $1 - b_0/a_0$ is kept below 0.08, where a_0 and b_0 are the maximal and minimal radii in the observation plane, respectively.

II.5 Conclusion

In this chapter, we have presented the miscible liquids we will use for the mixing flow experiments in the next chapters. The liquids are water-polymer solutions, of different polymer mass fraction f , which allows us to vary the viscosity ratio between the blob and the bath over a wide range ($0.1 \leq \lambda \leq 124$). We have also investigated in detail the diffusion between these liquids in the absence of flow. This investigation was done both with a schlieren technique, which tracks the total polymer mass fraction (*i.e.*, the viscosity field), and with the fluorescence technique we will use for the mixing flow experiments, which tracks only the small fraction of the polymers that are fluorescent and initially concentrated in the blob. The following observations have been made:

- Although the diffusive process leads to a viscosity field that varies in space and time, the experimental profiles, both for the polymer mass fraction f and the fluorescent concentration C , are well-fitted at all times by error functions with a characteristic length σ varying diffusively like $\sqrt{\sigma_0^2 + 2Dt}$.
- The fitted diffusion coefficients D remain nearly constant when the viscosity ratio is varied over two decades.
- Although the investigated liquids are highly viscous (with viscosities up to 40 Pa s), the observed diffusivities are rather large ($D \sim 10^{-10}$ - $10^{-11} \text{ m}^2 \text{ s}^{-1}$).
- The inter-diffusion coefficient between the water and the polymer molecules, which determines how fast the viscosity field diffuses, is found to be $D_\eta \simeq 1.65 \times 10^{-10} \text{ m}^2 \text{ s}^{-1}$.
- The inter-diffusion coefficient between the fluorescent and non-fluorescent polymer molecules, which determines how fast the fluorescent concentration diffuses (in the case when dye is added only to one of the two solutions), is found to be typically one decade lower, at $D_{\text{dye}} \simeq 10^{-11} \text{ m}^2 \text{ s}^{-1}$.

These observations have several consequences for the mixing flow experiments of next chapters and their interpretation. First, large diffusion coefficients mean that experiments can be kept reasonably long (typically less than an hour), while observing diffusion effects at the millimeter scale of the blob. Their weak dependence on the viscosity field will strongly simplify the description of the mixing process. The fluorescent signal from which we will track the deformation and the diffusion of the blob, will not exactly reflect the viscosity field (since the fluorescent polymer fraction cannot be made proportional to the total polymer fraction f to avoid light absorption and contrast issues). However, we will see that depending on the viscosity contrast and the flow conditions (and in particular whether the viscosity field still matters or not by the time when the diffusive mixing actually takes place), it will be relevant to use either the diffusivity D_η , which controls the viscosity field, or the diffusivity D_{dye} , which sets the fluorescence field.

Last, to obtain a good control on the initial shape of the blob, an original technique based on the inverse Leidenfrost effect was developed. With these tools at hand, we are now ready to tackle the main problem and investigate how liquids of unequal viscosity mix *in a flow*.

Chapter III

Mixing in a simple shear flow

The aim of this chapter is to study how an initially spherical blob of viscosity $\lambda\eta$ mixes when strained in a simple shear flow of viscosity η . The control parameters are the viscosity ratio λ , varied between 10^{-1} and $\sim 10^2$, and the Péclet number Pe , varied between $\sim 10^2$ and $\sim 10^5$, mainly by changing the shear rate $\dot{\gamma}$. Our strategy to understand this mixing process is to tackle, first, the stretching kinematics of the blob in the limit of an infinite Péclet number, before addressing the mixing *per se*. The chapter is organized as follows.

We introduce the shear cell and the experimental methods to control the flow and track the blob. To study the infinite Pe kinematics, a first set of experiments is performed at a large Péclet number, $Pe \approx 3 \times 10^5$, focusing on times before diffusion effects become important. These experiments reveal a remarkable transition from an endless stretching to an endless rolling of the blob, as the viscosity ratio λ is increased. We develop a kinematic model, based on Eshelby's framework [105], which quantitatively captures this transition and the kinematics of the two deformation regimes. These results on the kinematics at infinite Péclet are presented in the form of an article published in *Physical Review Letters*, which is preceded by a summary of its results. In the second part of the chapter we investigate mixing, by tracking the evolution of the blob concentration over longer times, for systematically varied viscosity ratios and Péclet numbers. We show how the characterization of the infinite Pe kinematics, allow us to predict the blob mixing time for finite Pe over the whole range of viscosity ratios and Péclet numbers investigated.

III.1 Simple shear setup	43
III.1.1 Principle of the shear cell	43
III.1.2 Additional features of the shear cell	44
III.1.3 Quantification of the blob deformation & mixing	46
III.2 Kinematics of deformation of the blob (infinite Pe limit)	48
III.2.1 General observations	48
III.2.2 Model for the blob deformation kinematics	49
III.2.3 Comparison between model & experiments	51
III.2.4 Copy of the letter	52
III.2.5 Additional informations	68
III.2.5.a Folding regime	68
III.2.5.b Flow reversibility	69
III.3 Mixing of the blob	70
III.3.1 General observations	70
III.3.2 Mixing in the <i>stretching regime</i>	70
III.3.2.a Phenomenology & quantification	71

III.3.2.b	Mixing model including the stretch shift factor β	71
III.3.2.c	Model versus experimental results	72
III.3.3	Mixing in the <i>rolling regime</i>	74
III.3.3.a	Phenomenology & quantification	74
III.3.3.b	Mixing model: a 'dissolving' rolling sphere	77
III.3.3.c	Model versus experimental results	78
III.4	Conclusion	82

III.1 Simple shear setup

In order to characterize the blob deformation and subsequent mixing, we design and build from scratch an experimental setup, which achieves high-quality visualizations of the blob in a controlled and stable laminar shear flow over long times and large strains. This section presents the setup and associated experimental methods.

III.1.1 Principle of the shear cell

Figure III.1 shows a schematics of the principal components of the setup. The configuration we choose is a cylindrical Couette cell, made of two co-axial cylinders of radii $R_{\text{in}} = 36 \text{ mm}$ and $R_{\text{out}} = 60 \text{ mm}$. The rotation of the two cylinders is set by two independent precision rotation stages (PI M061PD MicroMotor), so that the cylinders can rotate in the same direction (co-rotation) or in opposite direction (counter-rotation). The counter-rotation setting allows to position the neutral velocity line at the center of the blob, which maintains the blob in the field of view during the shear. In the gap between the two cylinders the rotation stages impose the desired shear rate $\dot{\gamma}$, varied between 0.05 and 5 s^{-1} . This sets a Reynolds number at the cell scale, $\rho\dot{\gamma}(R_{\text{out}} - R_{\text{in}})^2/\eta$, between ~ 0.02 and 2 (with ρ the bath liquid density and η its viscosity), and a Reynolds number at the blob scale, $\rho\dot{\gamma}b_0^2/\eta$, between $\sim 10^{-4}$ and 10^{-2} , which ensures inertial effects are small. To reach the desired shear rate, we set a slow initial acceleration ($\ddot{\gamma}/\dot{\gamma} = 0.1 \text{ s}^{-1}$), such that the flow is quasi-steady at all time.

The gap between the two cylinders is filled with the bath liquid of viscosity η , which is floated over a layer of high-density, low-viscosity and non miscible oil (Fluorinert FC43) to ensure quasi stress-free boundary conditions at the bottom of the cell. The fluorescent blob, of viscosity $\lambda\eta$, is placed frozen in the bath as explained in the previous chapter (§II.4), and is illuminated at its equator with the laser sheet (PLIF experimental technique detailed in the previous chapter). The cross-section of the blob is observed from the top, with a camera coupled to a macroscope lens (Leica Z16 APO). The camera field of view includes a small portion of the inner and outer walls, which allows us to locate the blob initial position

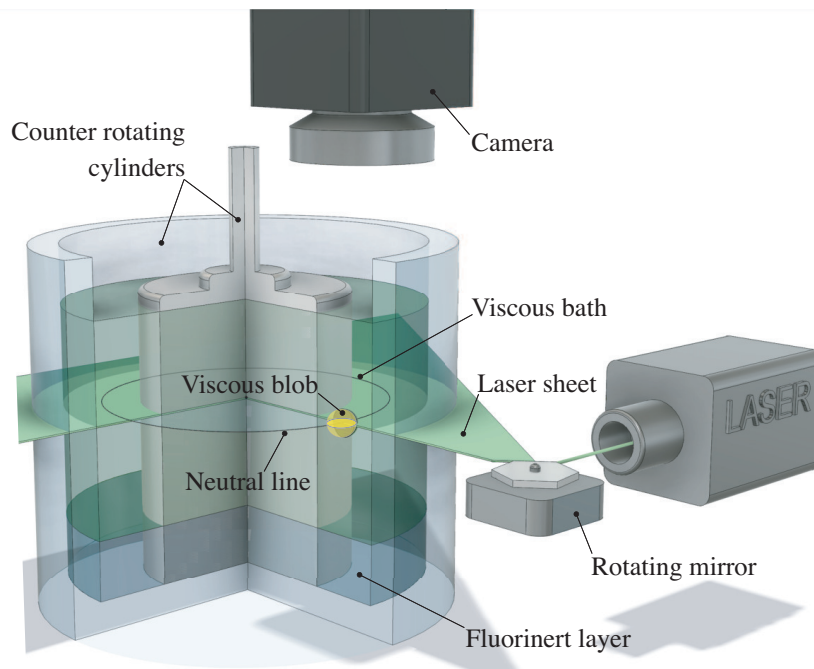


FIGURE III.1: Schematics of the simple shear flow setup.

across the gap (see also §III.1.2). The resolution of the images in the experiments dedicated to the large Pe kinematics of the blob (§III.2) is of $12\ \mu\text{m}/\text{pix}$. For the mixing experiments, the image resolution is doubled to $6\ \mu\text{m}/\text{pix}$ to resolve the mixing length scale ($\sim 20\ \mu\text{m}$ in the isoviscous case) as needed to properly characterize the mixing process [47]. We use two different bath viscosities, $\eta = 0.3\ \text{Pa s}$ and $\eta = 1\ \text{Pa s}$, which allow us to explore a wide range of viscosity ratios $\lambda \in [0.1, 90]$. With a blob initial diameter $2b_0$ varied between 1 and 3 mm, we vary the Péclet number over three orders of magnitude, from $Pe \sim 10^2$ to $Pe \sim 10^6$ (with a Reynolds number kept small).

III.1.2 Additional features of the shear cell

The experiment is remotely controlled with a Python script. In particular, we control and synchronize the rotation stages that move the cell walls, the camera, the laser and the laser beam shutter. The experimental setup has also additional features, which are shown in figure III.2 and described separately in the following paragraphs.

Placement of the blob in the bath. Once the blob is frozen (as described in §II.4), it is picked up with a pair of tweezers positioned precisely above the middle of the gap (see figure III.2.i). The frozen blob is then released from the tweezers to fall onto the surface of the bath and is quickly covered and immersed by injecting some of the bath liquid on top of it. This immersion is achieved about 90° away from the field of view. We thus co-rotate the walls (without shear) to bring the blob in the field of view.

Control of the Péclet number. Since the blob size varies slightly from one preparation to another, we use the following protocol to control precisely the Péclet number. We detect the blob with a software, immediately after it is placed in the bath. After binarizing, thresholding and fitting the blob contour with an ellipse, we obtain the initial blob radius b_0 and its radial position R_b in the gap, see figure III.3a. The

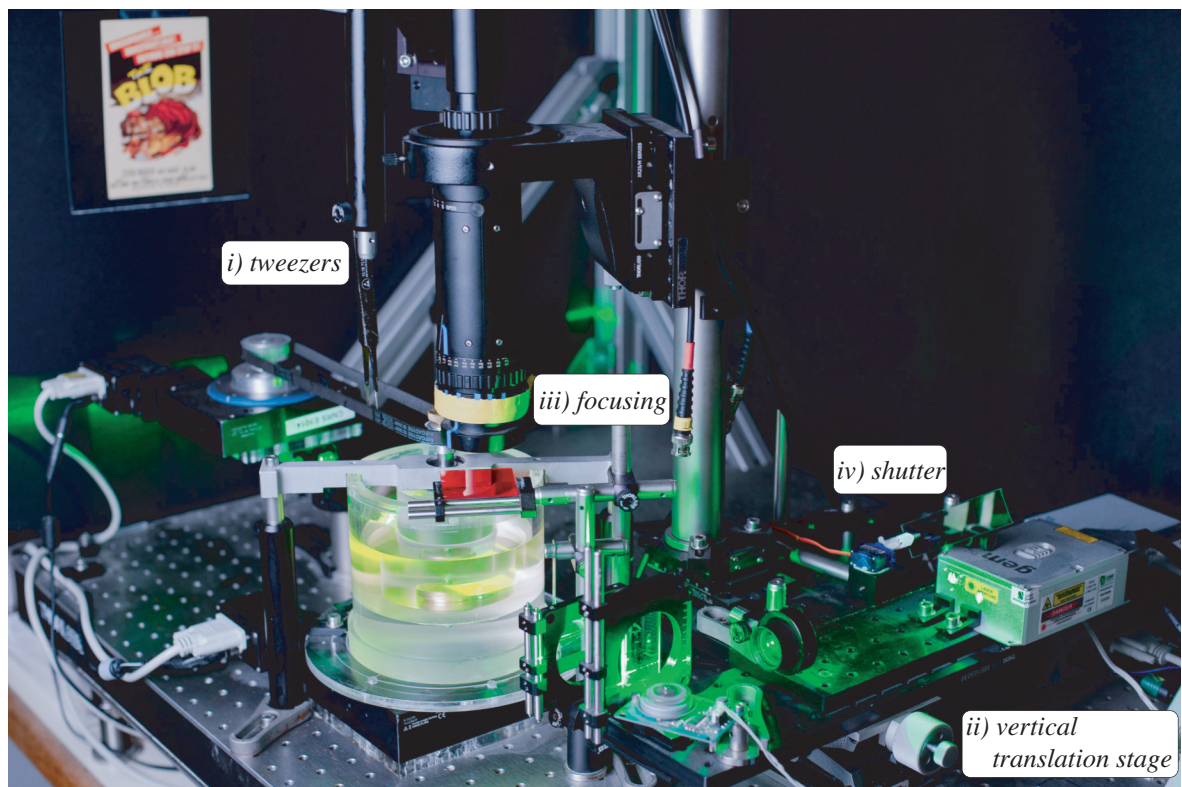


FIGURE III.2: Picture of the simple shear flow setup.

blob size is used to compute the shear rate, $\dot{\gamma} = DPe/b_0^2$, required to achieve the desired Péclet number. The angular velocities of the walls are set to

$$\omega_{\text{in}} = \frac{\dot{\gamma}}{2} \left(\frac{R_b^2}{R_{\text{in}}^2} - 1 \right), \quad \omega_{\text{out}} = \frac{\dot{\gamma}}{2} \left(1 - \frac{R_b^2}{R_{\text{out}}^2} \right), \quad (\text{III.1})$$

which ensures both the required shear rate and the position of the neutral velocity line at the center of the blob.

For mixing experiments, when the blob evolves towards a very thin lamella, we found that counter-rotating the cylinders could induce small flow perturbations, which could bias the measurements of the blob thickness. Although we did not fully understand the origin of these perturbations, we found that adding some co-rotation yielded a more stable flow, which solved the problem and allowed us to track the lamella width over longer times. In this case, the inner wall velocity is set to $\omega_{\text{in}} = \omega_{\text{max}} Pe/Pe_{\text{max}}$, where ω_{max} is the maximal velocity of the rotating stage and Pe_{max} is the maximal value of the Péclet number achievable with the setup. The velocity of the outer wall is then computed from $\omega_{\text{out}} = \omega_{\text{in}} + \dot{\gamma}(R_{\text{in}}^{-2} - R_{\text{out}}^{-2})R_b^2/2$.

Keeping the blob in the field of view. Once the shear is started, the blob sometimes drifts very slowly in the radial direction. This drift, probably due to small convection currents, is problematic under counter-rotation because the blob is then slowly advected out of the field of view. In this case, we slightly shift the position of the neutral velocity line to the new position of the blob by adjusting the wall velocities, while keeping the shear rate at the blob center constant. This tuning is done with a joystick interface programmed in our software, which allows us to set rapidly the direction and magnitude of the shift. Figure III.3b shows a schematic of the procedure. To avoid transient inertial effects, these adjustments are made at rates much smaller than the inverse viscous diffusion time across the cell gap.

Limiting the blob sedimentation. In the experiments for the large Péclet kinematics, the bath liquid has a viscosity $\eta = 1 \text{ Pa s}$ and a density $\rho = 1079 \text{ kg m}^{-3}$. The largest density contrast with the blob (below 3.5%) is thus obtained for $\lambda = 0.1$ (see figure II.2a). In this worst case, the creaming velocity of the blob $\sim (2/9)\Delta\rho g b_0^2/\eta \sim 10^{-4} \text{ m s}^{-1}$ remains much smaller than the typical shear velocity $\dot{\gamma} b_0 \simeq 1.5 \times 10^{-3} \text{ m s}^{-1}$. Since these experiments for the large Péclet kinematics experiments are rather short (typically 5 min), there was no need to match the density.

Conversely, for the mixing experiments, which last much longer (≈ 10 to 60 min), the two densities are matched. In practice, we use salt to match the bath and blob density with the largest density of the

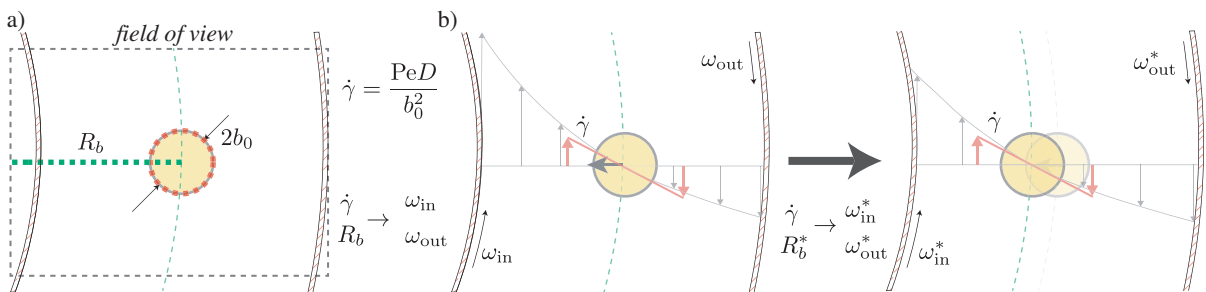


FIGURE III.3: Control of the Péclet number and of the blob position in the field of view. (a) Schematics of the camera field of view. The software detects the size of the blob (red dotted line) and its radial position R_b across the gap (green dotted line), which are used to compute the exact shear rate for the target Péclet number and the position of the neutral velocity line. (b) If the blob drifts radially, the neutral line is shifted to the new blob center position (R_b^*) by updating the velocities ω_{in} and ω_{out} of both walls according to Eq. III.1, which keeps the shear rate at the blob center constant.

(non-salted) water/polymer solutions (reached for $f = 0.8$, see §II.1.3). This allows us to use the same salted bath for all viscosity ratios. Doing so, all liquids are iso-dense in all mixing experiments.

Control of the focus during measurements. Despite the efforts to adjust densities, a slow residual vertical motion of the blob is sometimes observed. This is problematic because the blob drifts away from the laser sheet and it also becomes out of focus as the optical path length to the camera changes. To solve these problems, we mount the laser (together with the system of lenses, shutter and mirror producing the laser sheet) on a vertical translation stage (Figure III.2.ii), which is manually activated to keep the laser sheet at the blob equator. In parallel, we adjust the focus of the camera, using a pre-calibration of how the focus must be adjusted for each position of the laser sheet (Fig. III.2.ii). This calibration is done prior to the experiments, by placing a minute amount of small fluorescent tracers (PS-FluoRed-Particle, of size $2.99 \mu\text{m}$) in the bath with no flow, and fine tuning the focus for each laser position.

Limiting photobleaching. The long experiments for studying mixing require to limit photobleaching (see also §II.2.1). To this end, we use a light filter mounted on a small activated arm (Fig. III.2.iv). During image acquisition the arm is risen and all the laser light goes into the sheet ($\approx 1 \text{ W}$). Between the acquisition of the images, the filter intercepts the laser beam, which reduces the sheet intensity by about two orders of magnitude. This drastically limits photobleaching, while keeping enough light to visualize the blob at all time and to adjust the neutral velocity line position with the joystick (to keep the blob in the field of view). The movement of the filter is controlled by the software and synchronized with the camera. This limited exposure of the blob to the laser light keeps photobleaching effects below 8% over the whole experiment.

III.1.3 Quantification of the blob deformation & mixing

For small blob deformation, *i.e.*, when the blob shape is close to ellipsoidal, the maximal and minimal radii, a and b , and the orientation, φ , of the blob are simply quantified by fitting an ellipse to the thresholded image, as shown in figure III.4a. When the blob deforms further and reaches the shape of a lamella, the field of view only shows the central part of the lamella (see Fig. III.4b). To quantify the evolution of the lamella, we define an angular sector (between the two red crosses in Fig. III.4b), over which we extract radial intensity profiles. This region is manually identified for each frame, and the azimuthal distance between the top and bottom crosses determines the number of intensity profiles analyzed for each (typically 100). The intensity profiles are then converted into concentration profiles using $\frac{C(x)}{C_0} = \frac{I(x) - I_b}{I_M - I_b}$. Each of these radial concentration profile is then fitted by the following error function:

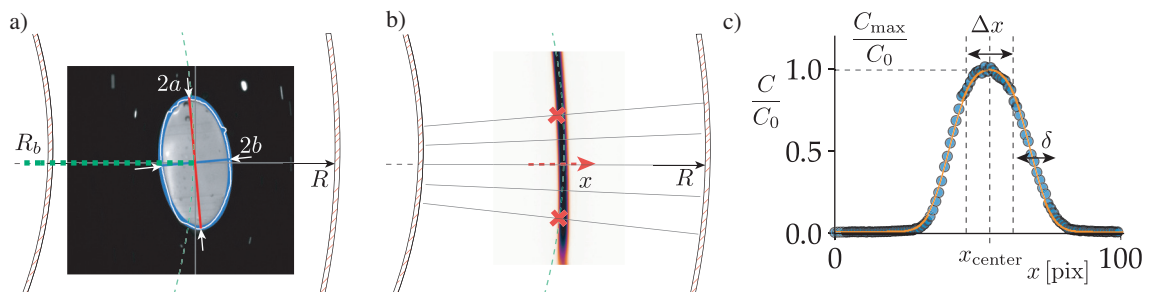


FIGURE III.4: Quantification of the blob deformation and mixing. (a) For small blob deformation, the blob contour (white) is fitted by an ellipse (blue) to determine the blob principal dimensions, a and b , and its orientation φ . (b) At large blob deformation, the lamella is characterized by analyzing all radial concentration profiles between the two red crosses.

(c) Typical concentration profile (black symbols) fitted by the error function (orange solid line) given in Eq. III.2.

$$C(x, x_{\text{center}}, \Delta x, \delta, C_{\text{max}}, C_{\text{noise}}) = \frac{\operatorname{erf}\left(\frac{x + \Delta x/2 - x_{\text{center}}}{\delta}\right) - \operatorname{erf}\left(\frac{x - \Delta x/2 - x_{\text{center}}}{\delta}\right)}{2} C_{\text{max}} + C_{\text{noise}}, \quad (\text{III.2})$$

where x_{center} , Δx , δ , and C_{max} are represented in figure III.4c, and C_{noise} accounts for the background noise of the image. These parameters are used to compute the width $b = \sqrt{\langle (x - x_{\text{center}})^2 \rangle} = \sqrt{\Delta x^2/3 + \delta^2}$ of the lamella, which takes into account both the kinematic compression and the diffusive broadening, and to obtain the maximal concentration C_{max} of the blob. These two quantities are then averaged over all the radial profiles analyzed. Last, from the angular evolution of the radial position of the lamella x_{center} between the profiles, we extract an accurate measurement of the lamella orientation φ .

For the large viscosity ratios λ obtained with large mass fractions f of polymer, the fluorescent yield effect mentioned in §II.2.1 (dependence of the ratio between fluorescent intensity and dye concentration on f) becomes significant. In practice, for $f \gtrsim 0.6$ this effect biases the intensity profiles as shown in figure III.5 for a blob of viscosity ratio $\lambda = 30$ and mass fraction $f \approx 0.7$. Although the fluorescent dye concentration is monotonically decreasing from the blob center outwards, the intensity pattern shows a marked intensity peak at the mixing front with the bath, where the fluorescence yield increases by a large factor because the mass fraction f decreases. We have tried to deconvolute the yield effect, in order to recover the polymer concentration profiles from the intensity profiles. However, the magnitude of the yield effect (biasing intensity by orders of magnitudes), its dependence on both the dyed polymer and total polymer concentration, and the steep intensity gradients at the blob boundary, made this deconvolution unsuccessful. It was, therefore, not possible to extract quantitative concentration profiles from the blobs with large viscosity ratios. However, we will see below that these blobs do not stretch in practice and that their mixing can actually be followed and characterized from the evolution of their width b (obtained by fitting an ellipse as explained above).

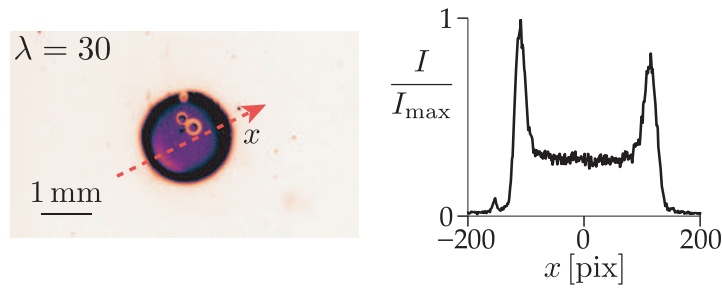


FIGURE III.5: Bias due to the fluorescence yield effect. Blob with a large viscosity ratio $\lambda = 30$ obtained with a large polymer mass fraction ($f \approx 0.7$) and corresponding intensity profile, largely biased by the fluorescence yield effect.

III.2 Kinematics of deformation of the blob (infinite Pe limit)

This section is devoted to the characterization of the kinematics of deformation of the blob before diffusive effects become significant. To be able to observe this infinite Péclet limit of the kinematics for significant deformations, we perform experiments at a large Péclet number ($\approx 10^5$) and we systematically vary the viscosity ratio from $\lambda = 0.1$ to $\lambda = 40$. The experiments have a duration of about 4 min, during which the blob is constantly visualized while being illuminated with the laser sheet. We provide below a summary of the main results concerning the infinite Péclet kinematics. The detailed results are then presented in the form of a Letter included in the manuscript.

III.2.1 General observations

When the viscosity ratio λ of the blob is varied, three highly different regimes of deformation are observed (see Fig. III.6).

- At low viscosity ratio ($\lambda \lesssim 4$), the kinematics is qualitatively close to the canonical isoviscous case. The blob stretches into an endlessly thinning lamella, which progressively aligns with the flow direction. We call this first regime ‘*stretching regime*’.
- As the viscosity ratio is increased to large values ($\lambda \gtrsim 4$), the kinematics drastically changes. Instead of stretching, the blob adopts a periodic motion, which is close to rolling and with only a little periodic stretch of the blob. We call this regime ‘*rolling regime*’.
- For intermediate viscosity ratio ($\lambda \approx 4$), an initial transient is observed when the blob stretches significantly but slower than the isoviscous case (what we call ‘*substretching*’), after which the elongated blob eventually destabilizes by folding and swirling. We call this last regime ‘*folding regime*’.

These observations are very interesting and central to this thesis because they highlight the way by which changing the viscosity of the blob deeply modifies its deformation kinematics and eventual mixing. For instance, figure III.6 clearly shows that the low viscosity blob, which has rapidly stretched into a thin lamella, is close to being mixed at a strain $\gamma \equiv \dot{\gamma}t = 100$. Conversely, at the same strain, the rolling (highly viscous) blob is barely deformed and we therefore expect its mixing time to be largely delayed by the different kinematics.

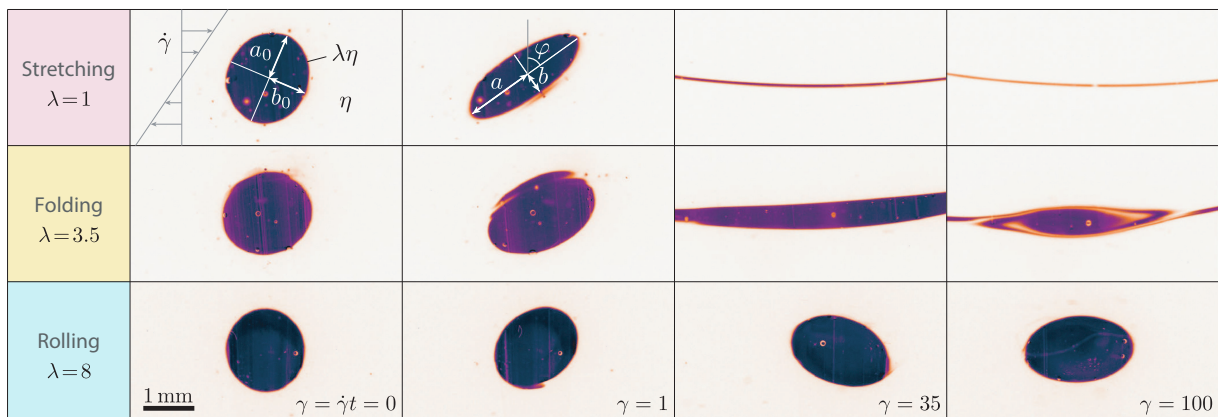


FIGURE III.6: Deformation of the initially spherical blob in a simple shear flow for different viscosity ratios λ . Stretching regime ($\lambda = 1$): the blob stretches into an endlessly thinning lamella which aligns with the flow direction. Folding regime ($\lambda = 3.5$): the blob stretches and aligns significantly slower with the flow (substretching), and eventually destabilizes by folding. Rolling regime ($\lambda = 8$): the blob essentially rolls, with only a small periodic stretch.

III.2.2 Model for the blob deformation kinematics

To gain insight on the above kinematics, we build a model based on the formally analogous elastic problem solved by Eshelby in 1957 [105]. This original work solves for the deformation of an elastic solid inclusion embedded in an elastic solid matrix with a different elastic modulus. For a linear deformation imposed to the matrix and an ellipsoidal inclusion, Eshelby's formalism gives exact solutions for the deformation of the inclusion in the form of elliptic integrals. The idea of transposing this framework (relative elastic deformation for a modulus contrast) to purely viscous flows (relative deformation rate for a viscosity contrast) was originated by Eshelby himself [104, 105], and further adopted by others [115, 116], including us. The crucial point why the formalism is particularly suited to our case, is that for an ellipsoid, the deformation (rate) field inside the ellipsoid is *uniform*, which means that an ellipsoid deforms into another ellipsoids. Starting from our initially spherical blob, which is ellipsoidal, we can therefore obtain the exact evolution of the shape, by time integrating Eshelby's solution for the current deformation rate inside the blob.

The model is valid for an isolated ellipsoidal blob of viscosity $\lambda\eta$, sheared in an infinite bath of viscosity η , considering Newtonian incompressible liquids, under conditions of no inertia ($Re = 0$), no diffusion ($Pe = \infty$), and no surface tension between the blob and the bath. The far-field flow in the bath is a simple shear ($u = \dot{\gamma}y, v = 0$). The main radii of the blob are noted a, b and c and its orientation in the shear plane (xy) is noted φ (see Fig. III.5i). In the coordinate system aligned with the main axis directions (e_a, e_b, e_c),

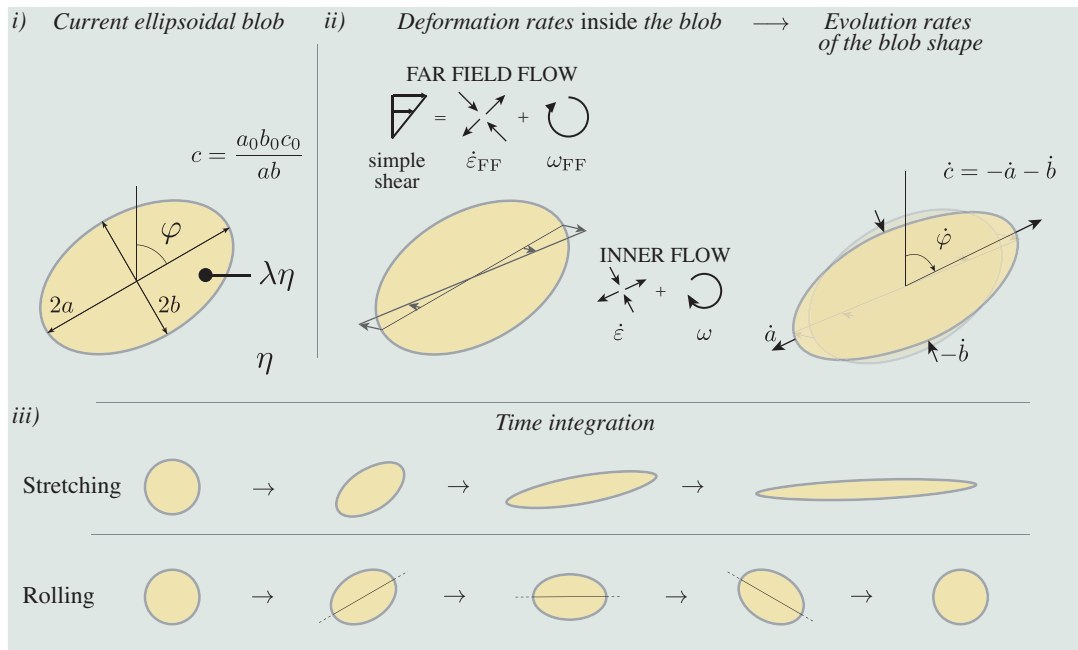


FIGURE III.7: Analytic model for the blob deformation kinematics in a simple shear flow. (i) The blob of viscosity $\lambda\eta$ (in an infinite bath of viscosity η) has a current arbitrary ellipsoidal shape, with dimensions a, b, c and orientation φ . (ii) For a linear far-field flow in the bath (FF), the deformation rate inside the ellipsoidal blob is uniform [105], which exactly deforms the blob into a new ellipsoid and gives the evolution rate of the blob ($\dot{a}, \dot{b}, \dot{c}$ and $\dot{\varphi}$ given by Eq. III.5). (iii) The deformation history is obtained by time-integrating the evolution equations for $\dot{a}, \dot{b}, \dot{c}$ and $\dot{\varphi}$, which recovers both the stretching regime and the rolling regime (sketched in the top and bottom, respectively).

the far field (FF) strain rate and rotation rate are

$$\dot{\epsilon}_{\text{FF}} = \begin{pmatrix} \sin 2\varphi & -\cos 2\varphi & 0 \\ -\cos 2\varphi & -\sin 2\varphi & 0 \\ 0 & 0 & 0 \end{pmatrix}_{(e_a, e_b, e_c)} \frac{\dot{\gamma}}{2}, \quad \omega_{\text{FF}} = -\frac{\dot{\gamma}}{2}. \quad (\text{III.3})$$

From Eshelby's solution, the strain rates and vorticity *inside* the ellipsoid, $\dot{\epsilon}_{aa}$, $\dot{\epsilon}_{bb}$, $\dot{\epsilon}_{cc}$ and ω , are uniform and function of the current blob geometry, far field flow (Eq. III.3) and viscosity ratio λ according to

$$\begin{aligned} \dot{\epsilon}_{aa} &= \mathcal{A}\left(\frac{a}{b}, \frac{b}{c}, \lambda\right) \sin 2\varphi \frac{\dot{\gamma}}{2}, & \dot{\epsilon}_{bb} &= -\mathcal{B}\left(\frac{a}{b}, \frac{b}{c}, \lambda\right) \sin 2\varphi \frac{\dot{\gamma}}{2}, & \dot{\epsilon}_{cc} &= -\dot{\epsilon}_{aa} - \dot{\epsilon}_{bb}, \\ \dot{\epsilon}_{ab} &= -\mathcal{S}\left(\frac{a}{b}, \frac{b}{c}, \lambda\right) \cos 2\varphi \frac{\dot{\gamma}}{2}, & \omega &= \frac{\dot{\gamma}}{2} + \mathcal{R}\left(\frac{a}{b}, \frac{b}{c}, \lambda\right) \cos 2\varphi \frac{\dot{\gamma}}{2}. \end{aligned} \quad (\text{III.4})$$

From simple geometrical considerations, these strain and rotation rates set the evolution rates of the ellipsoid shape, $\frac{\dot{a}}{a} = \dot{\epsilon}_{aa}$, $\frac{\dot{b}}{b} = \dot{\epsilon}_{bb}$, $\frac{\dot{c}}{c} = \dot{\epsilon}_{cc}$ and $\dot{\varphi} = -\omega - \frac{a^2+b^2}{a^2-b^2} \dot{\epsilon}_{ab}$, which take the final form

$$\begin{aligned} \frac{1}{\dot{\gamma}} \frac{\dot{a}}{a} &= \mathcal{A}\left(\frac{a}{b}, \frac{b}{c}, \lambda\right) \frac{\sin 2\varphi}{2}, & \frac{1}{\dot{\gamma}} \frac{\dot{b}}{b} &= -\mathcal{B}\left(\frac{a}{b}, \frac{b}{c}, \lambda\right) \frac{\sin 2\varphi}{2}, \\ \frac{\dot{c}}{c} &= -\frac{\dot{a}}{a} - \frac{\dot{b}}{b}, & \frac{1}{\dot{\gamma}} \dot{\varphi} &= \frac{1}{2} + \mathcal{F}\left(\frac{a}{b}, \frac{b}{c}, \lambda\right) \frac{\cos 2\varphi}{2}, \end{aligned} \quad (\text{III.5})$$

The functions \mathcal{A} , \mathcal{B} and \mathcal{F} embed the dependance of the blob deformation rates on the viscosity ratio and current shape of the blob. In the isoviscous case they are simply $\mathcal{A} = \mathcal{B} = 1$ and $\mathcal{F} = \frac{a^2+b^2}{a^2-b^2}$. For an arbitrary viscosity ratio, they involve elliptic integrals and their complete expressions are provided in the supplemental material of the letter, together with their derivation.

The evolution of the blob shape is obtained by time-integrating equations III.5 from the spherical initial shape $a = b = c = a_0$ and $\varphi = \pi/4$. Figure III.7 summarizes the steps of the computation and sketches how it recovers the stretching and rolling regimes of deformation of the blob observed experimentally.

The strength of the above framework is that it provides predictions of the (infinite Péclet) deformation kinematics for ellipsoidal blobs of arbitrary aspect ratios a/b , b/c and viscosity ratio λ . As emphasized in figure III.8, this framework therefore generalizes the known solutions for the isoviscous case ($\lambda = 1$, arbitrary a/b , b/c), for the solid ellipsoid case solved by Jeffery ($\lambda = \infty$, arbitrary a/b , b/c [86]), for the close to spherical case solved by Taylor (arbitrary λ , $a/b \approx b/c \approx 1$ [87]) to the whole parameter space

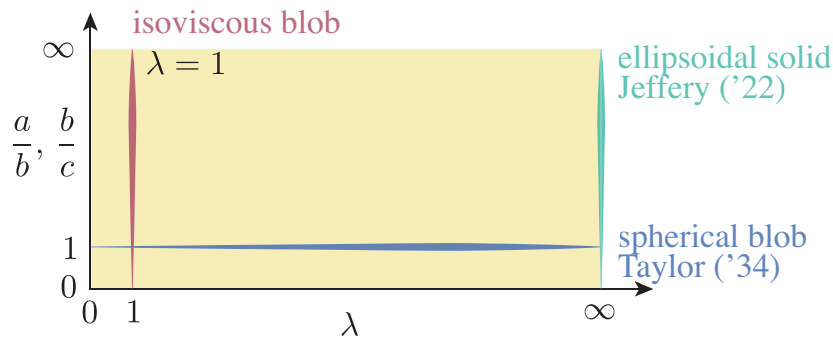


FIGURE III.8: Sketch of the parameter space covered by the model. The parameter space of Eq. III.5 (arbitrary λ and arbitrary a/b , b/c , in yellow) encompasses the isoviscous case ($\lambda = 1$, arbitrary a/b , b/c), Jeffery's orbits for a solid ellipsoid ($\lambda = \infty$, arbitrary a/b , b/c) [86] and Taylor's solution for nearly spherical blobs (arbitrary λ , $a/b \approx b/c \approx 1$, [87]).

(arbitrary a/b , b/c and arbitrary λ). It is worth noticing that it can also be readily extended to other two-dimensional flows (see Chapter IV) as well as to arbitrary three-dimensional flows (not studied in this thesis).

III.2.3 Comparison between model & experiments

Figure III.9 compares the model (solid lines) with the experimental measurements (symbols) for the range of viscosity ratio λ investigated. The overall agreement is good. The list below summarizes the main points.

- Isoviscous case ($\lambda = 1$): the blob width follows the canonical long time linear compression $b/b_0 \rightarrow \gamma^{-1}$ (see panel a), and asymptotically aligns with the flow direction (see panel b).
- Stretching regime ($0.1 < \lambda \leq 2$): at long time the blob eventually thins down similarly to an isoviscous blob (i.e. proportionally with γ^{-1}) but with a shifted law $b/b_0 \rightarrow \beta(\lambda)\gamma^{-1}$. This means that at long time the viscosity of the blob does not affect the thinning any more (the blob is so slender that it cannot slow down the far field flow). The stretch shift factor β is a function of λ , which embeds the initially slower ($\lambda > 1$) or faster ($\lambda < 1$) thinning of the blob relative to the isoviscous case and varies only mildly with λ (the model gives $\beta \simeq 0.431$ for $\lambda = 0$ and $\beta \simeq 1.99$ for $\lambda = 2$). The model quantitatively captures both the linear thinning and the shift β (see panel c).
- Rolling regime ($\lambda \gtrsim 4$): the model recovers the rolling-like motion of the blob, with a small periodic stretch. The features of this periodic oscillation of the blob size and orientation are quantitatively captured by the model (see panel (d) for the evolution of the orientation φ and the width b/b_0 and panel (e) for the period and the amplitude of the oscillation versus λ).
- Folding regime ($\lambda \simeq 4$): the model predicts a critical viscosity ratio $\lambda_c \simeq 3.975$ separating the *stretching* and the *rolling* regimes, for which the blob is endlessly substretched with a different power law, $b/b_0 \sim \gamma^{-1/2}$. The experiments for $\lambda = 3$ and $\lambda = 3.5$ are found to closely follow this sub-stretching regime before they eventually fold. This folding is not predicted by the model, which suggests that the sub-stretching flow is unstable, when λ is sufficiently close to λ_c (see further discussions in §III.2.5.a).

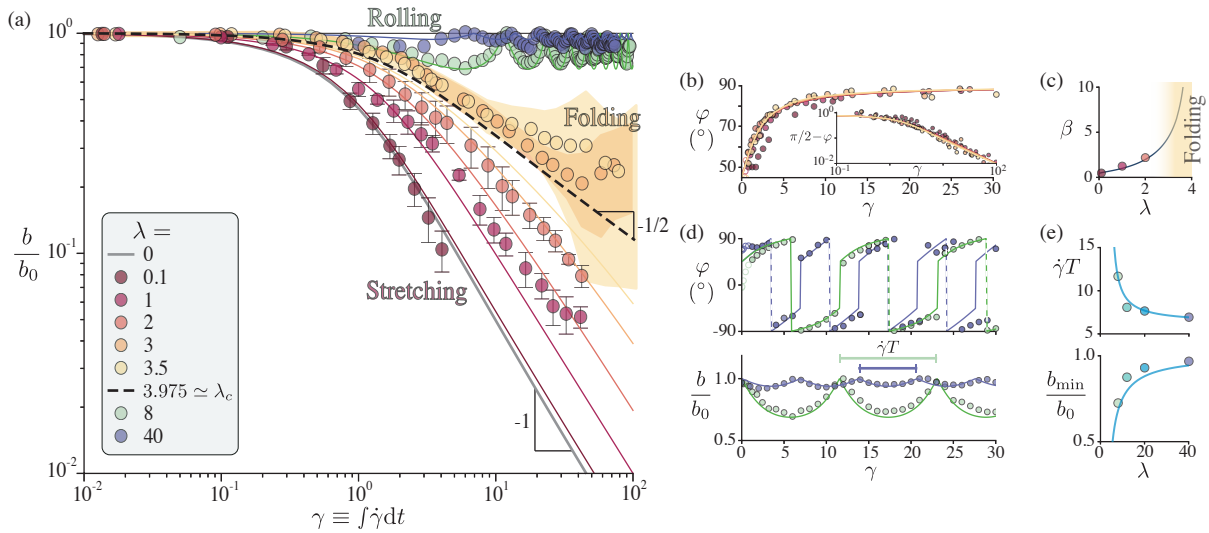


FIGURE III.9: Kinematics of deformation (infinite Péclet limit): model versus experiments. (a) Normalized blob width b/b_0 versus accumulated shear strain γ for different viscosity ratio λ . Error-bars: standard deviation between runs. Shaded-area (*folding regime*): extremal values highlighting the large dispersion of the width when the destabilization occurs (see also §III.2.5.a). (b-d) Blob orientation φ and width b/b_0 vs strain. (c) Stretch shift factor β vs λ . (e) Period γT and amplitude of the oscillations b_{\min}/b_0 vs λ . Symbols: experiments (average over 2 runs). Solid lines: model.

The above experimental and theoretical results provide a complete characterization of the blob deformation kinematics before diffusive effects occur, for the whole map of viscosity ratios. The identified kinematic transition, at $\lambda \approx \lambda_c = 3.975$, between unbounded stretching and rolling is of particular relevance to the mixing problem, because one anticipates a dramatic impact on the blob mixing time. In the Letter presented below, we have proposed simple predictions for this impact on the mixing. These predictions will be detailed and compared to experiments in §III.3, which is devoted to mixing.

III.2.4 Copy of the letter

Shearing Liquids of Unequal Viscosity: Can Mixing be Independent of Stirring Rate at a Large Viscosity Ratio?

I. Castaldi¹, B. Metzger², and H. Lhuissier^{1*}
¹Aix-Marseille Université, ²CNRS, IUSTI, Marseille, France

(Received 22 January 2024; revised 16 May 2024; accepted 10 September 2024; published 8 October 2024)

Mixing liquids with unequal viscosity involves complex flows and a nontrivial diffusive feedback. As an insightful reference case, we study the deformation of a spherical blob with viscosity $\lambda\eta$, sheared in a miscible bath with viscosity η . Experiments resolve the transition from unbounded stretching, at low λ , to rollinglike motion, at large λ . In between the blob is transiently substretched before destabilizing into swirling structures. Exact solutions of the flow recover all three regimes and predict a transition ratio $\lambda_c \simeq 3.975$. We discuss the dramatic impact of the flow transition on mixing and propose scaling laws for the blob mixing time in the limit of large Péclet numbers, suggesting mixing could be independent of shear rate at large λ .

DOI: 10.1103/PhysRevLett.133.154001

The fate of a localized heterogeneity of viscosity in a liquid depends on its dispersion, small-scale deformation, and possible dilution by the stirring flow. Besides the limiting case of solid inclusions, much attention has been devoted to immiscible liquid heterogeneities, i.e., droplet emulsions, which are spherical at rest and deform or break up when flow stresses overcome capillary cohesion [1–12]. Nonetheless, many natural and industrial processes (e.g., mixing in the Earth mantle [13–17] or dilution of polymer melts [18,19]) involve fully miscible heterogeneous blends, which are not segregated by capillarity and will eventually mix, i.e., homogenize by molecular diffusion at long time. This route to homogenization highly depends on the deformation kinematics of the heterogeneities, which may increase mixing surfaces and steepen concentration gradients, or not [20–22]. For viscous flows, such kinematics depend on the applied flow and on the heterogeneity field. They are generally complex, but we show in this Letter that important fundamental results can be obtained by studying the case of an isolated and initially localized heterogeneity.

More particularly, we consider the deformation of an initially spherical blob of viscosity $\lambda\eta$, subjected to a simple shear in a bath of a different viscosity η . We perform experiments in the limit of a purely viscous flow (low Reynolds number) and slow mass diffusion (large Péclet, i.e., large Schmidt, numbers). Such experiments are challenging and scarce [23], since the deformation history depends highly on the initial blob shape, whereas capillarity cannot be used to form an initially spherical blob. Measurements are compared and complemented with an analytical modeling of the flow, based on integral solutions of the analogous elastic problem [24]. Altogether they

reveal three highly different regimes of deformation, as well as their critical dependence on the viscosity ratio λ and on the initial blob shape, of which we discuss the dramatic consequences on the mixing of the blob.

The setup is sketched in Fig. 1(a). The simple shear flow is set in a viscous bath in a cylindrical Couette cell with counterrotating walls (with radii of 36 and 60 mm). The blob is prepared with a spherical shape (see below) and sheared at the zero-velocity radius in the middle of the gap. The bath and blob liquids are Newtonian, aqueous solutions of a fully miscible organic copolymer (Ucon

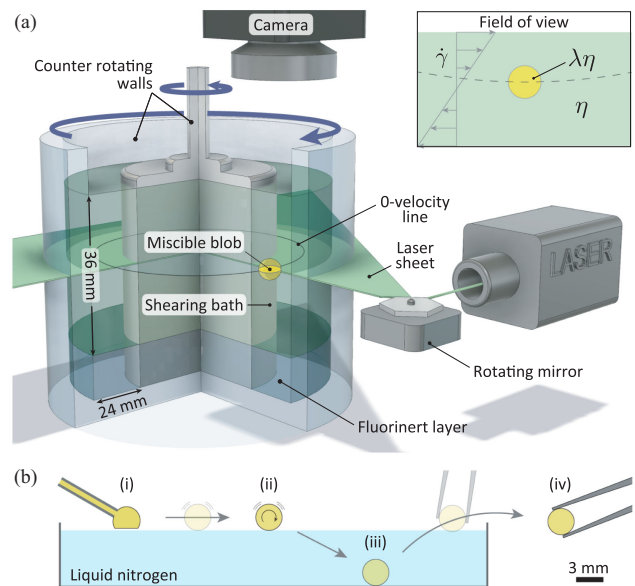


FIG. 1. Setup and protocol. (a) Sketch of the shear cell. (b) Blob preparation: (i) drop deposition, (ii) rotation and slow freezing during calefaction, (iii) sinking, (iv) collection of the solid sphere to be placed in the shear cell.

*Contact author: henri.lhuissier@univ-amu.fr

75-H-90000 by Dow, see Supplemental Material (SM), Sec. 2 [25]) prepared at different mass fraction f . The viscosity ratio λ between the blob and the bath is varied by fixing the bath viscosity, $\eta = 1$ Pa s ($f = 50$ wt%), and adjusting the blob viscosity $\lambda\eta$ between 0.1 and 40 Pa s ($30 \text{ wt}\% \leq f \leq 100 \text{ wt}\%$). A minute amount of fluorescent dye (Rhodamine 6G at 3×10^{-5} g/mL) is chemically bound to the blob polymers for visualization. Viscosities are measured with a cone-plate rheometer. The blob is illuminated with a thin horizontal laser sheet of wavelength 532 nm [26] and observed from the top with a camera. To ensure a parallel flow, the bath is floated on top of a high-density, immiscible, and low-viscosity layer of oil (Fluorinert FC43).

To obtain a spherical blob without interfacial tension we use the protocol sketched in Fig. 1(b). A drop of the blob liquid is deposited onto a liquid nitrogen bath. While being levitated and rotated by nitrogen vaporization, the blob slowly freezes into a sphere. The sphere is collected and immersed in the shear cell, where it rapidly melts and reaches thermal equilibrium before shear start. The technique yields a smooth blob, with radius $\sqrt{a_0 b_0} = 1.72 \pm 0.06$ mm and asphericity $1 - b_0/a_0 < 0.08$ (with a_0 and b_0 the maximal and minimal blob radii in the observation plane, respectively). The shear rate ($\dot{\gamma} = 1 \text{ s}^{-1}$) sets a low Reynolds number $\rho\dot{\gamma}a_0^2/\eta \approx 10^{-3} \ll 1$ (with $\rho \approx 1080 \text{ kg/m}^3$ the blob density) and a large Péclet number $\text{Pe} \equiv a_0^2\dot{\gamma}/D \sim 10^5$ (with $D \approx 10^{-11} \text{ m}^2 \text{ s}^{-1}$ the effective diffusion coefficient of the dye between the blob and bath mixtures), which ensures negligible effects of diffusion before a strain $\gamma \equiv \int \dot{\gamma} dt \sim 10^2$ (see final discussion). Last, the blob is kept in the field of view, by constantly adjusting the rotation speed of the walls (keeping $\dot{\gamma}$ unchanged, see SM, Sec. 2 [25]).

The blob deformation is found to depend critically on the viscosity ratio λ with the bath. Three qualitatively different regimes are observed, which are illustrated in Fig. 2

(see also SM movies [25]). In the isoviscous case ($\lambda = 1$), representative of the conventional *stretching* regime, the blob elongates monotonically and unboundedly into a thin lamella, which progressively aligns with the flow. In contrast, for the largest viscosity ratio ($\lambda = 8$), typical of the *rolling* regime already reported for highly viscous drops and blobs [2–5,23], the blob does not align with the flow. It actually follows a periodic orbital motion with little stretch and endless rotation. Last, for the intermediate ratio ($\lambda = 3.5$) a third kinematic regime, which we call *folding* regime, is observed. The blob elongates at short times, though significantly less than in the isoviscous case, and eventually destabilizes by folding into swirling structures.

To quantify the three regimes, we measure the blob relative width b/b_0 and orientation relative to the flow gradient direction φ for λ between 0.1 and 40. As shown in Figs. 3(a) and 3(b), in the stretching regime ($\lambda \leq 2$), the short-time decay of the blob width b/b_0 is slower for $\lambda > 1$ and, conversely, faster for $\lambda < 1$. However, at long time the blob aligns with the flow and recovers the stretching rate of an isoviscous blob. The orientation φ follows $90^\circ - \varphi \sim \gamma^{-1}$ [Fig. 3(b), inset], whereas the width decreases asymptotically as $b/b_0 = \beta/\gamma$, with β a stretch shift factor, quantifying the longtime deviation to the isoviscous case ($b/b_0 = \gamma^{-1}$) due to the different short-time kinematics, which increases with increasing λ . In the rolling regime ($\lambda \geq 8$), the blob deformation is periodic. The elongation amplitude and the period of oscillations both decrease with increasing λ toward the values expected for an almost solid drop, i.e., $\Delta b \equiv b_0 - b_{\min} = 0$ and $\gamma T = 2\pi$. Last, in the folding regime ($\lambda = 3$ and 3.5), the decrease in b/b_0 deviates strongly from both previous trends. A long initial transient, called *substretching* transient, is observed, where the (maximal) width decreases slowly like $b/b_0 \sim \gamma^{-1/2}$ for significant strains ($\gamma \gtrsim 10$), until it plateaus as the blob eventually folds and swirls, before rolling with little stretch.

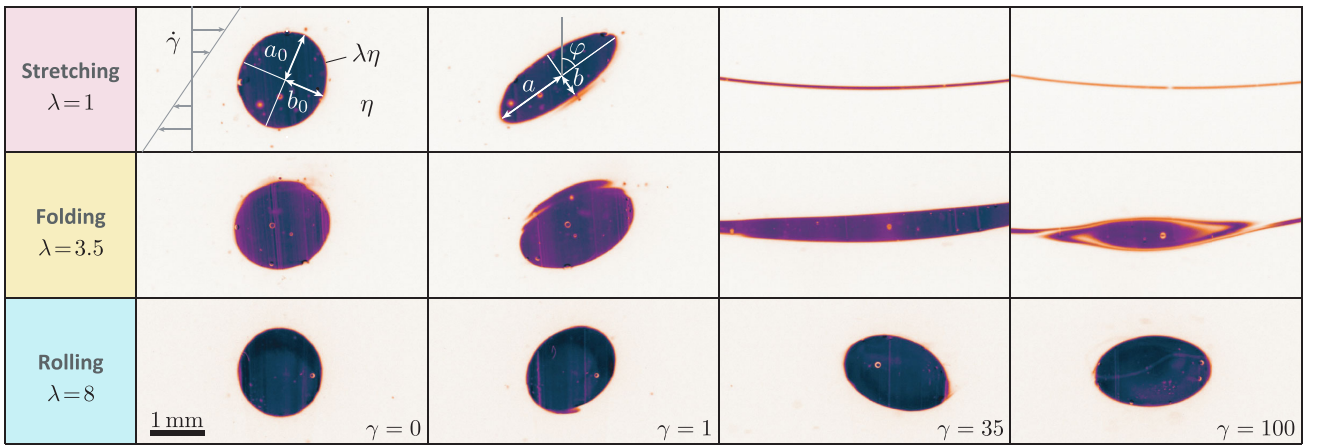


FIG. 2. Snapshots of the three deformation regimes observed for increasing viscosity ratio λ ($\gamma \equiv \int \dot{\gamma} dt$, see also SM movies [25]).

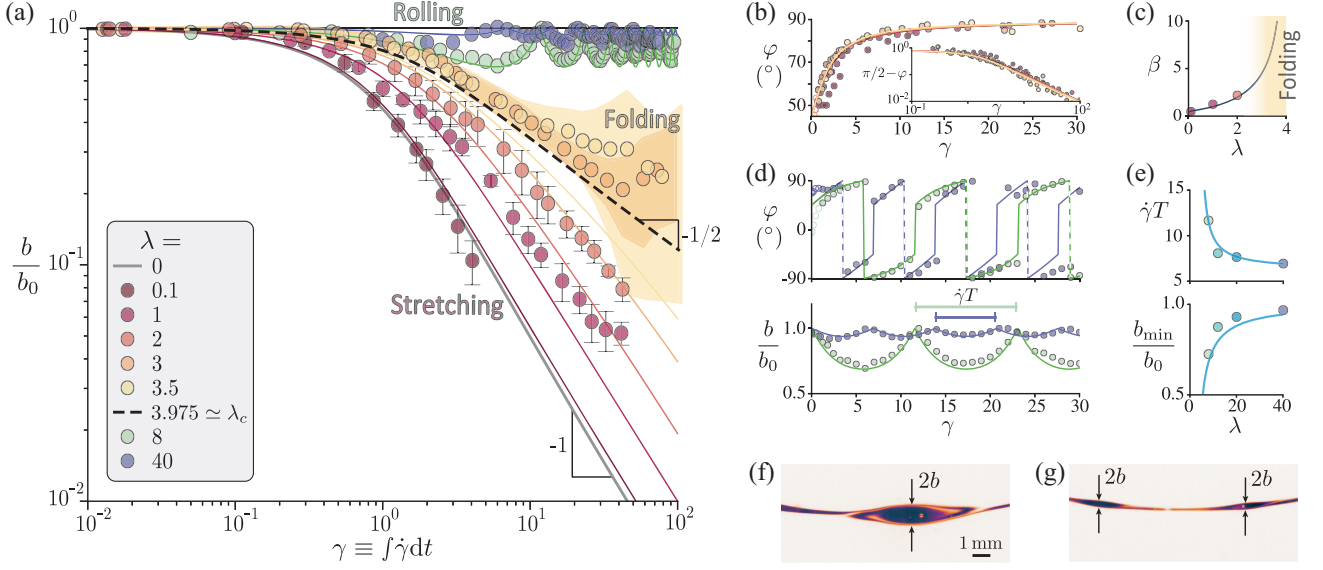


FIG. 3. Stretch laws. (a) Normalized blob width vs accumulated shear strain for different viscosity ratio λ . Error bars: standard deviation between runs (over 4, 6, and 1 run for $\lambda \leq 2$, $\lambda = 3-3.5$, and $\lambda \geq 8$, respectively). Shaded-area (folding): extremal values. (b), (d) Blob orientation and width vs strain. (c) Stretch shift factor, $\beta \equiv \lim_{\gamma \gg 1} \gamma b/b_0$, vs λ . (e) Period and amplitude of the oscillations vs λ . Symbols: experiments (average over 2 runs). Solid lines: Eq. (1). (f),(g) Typical patterns observed in the folding regime ($2b$ is the maximal width measured at the swirling structures).

The onset of folding and the number of swirling structures are found to vary between experiments, as highlighted by the envelope of the extremal values observed for b/b_0 [Fig. 3(a)], and by the two typical patterns of swirling structures presented in Figs. 3(f) and 3(g). The longtime (maximal) width is distributed between $b/b_0 \approx 0.08$ and ≈ 0.4 , which indicates the kinematics in the folding regime is highly sensitive to small changes in the initial conditions or in the flow.

To gain insight on these kinematics, we model the blob deformation in the limit of a purely viscous, incompressible, simple shear flow, $\mathbf{u} = \dot{\gamma}y\mathbf{e}_x$, and no mass diffusion.

$$\begin{aligned} \frac{1}{\dot{\gamma}} \frac{\dot{a}}{a} &= \mathcal{A}\left(\frac{a}{b}, \frac{b}{c}, \lambda\right) \frac{\sin 2\varphi}{2}, & \frac{1}{\dot{\gamma}} \frac{\dot{b}}{b} &= -\mathcal{B}\left(\frac{a}{b}, \frac{b}{c}, \lambda\right) \frac{\sin 2\varphi}{2}, \\ \frac{\dot{c}}{c} &= -\frac{\dot{a}}{a} - \frac{\dot{b}}{b}, & \frac{1}{\dot{\gamma}} \dot{\varphi} &= \frac{1}{2} + \mathcal{F}\left(\frac{a}{b}, \frac{b}{c}, \lambda\right) \frac{\cos 2\varphi}{2}, \end{aligned} \quad (1)$$

where \mathcal{A} , \mathcal{B} , and \mathcal{F} are analytical functions of the blob aspect ratios and of λ (see SM, Sec. 3 [25]). Remarkably, the above formalism extends Jeffery's results [28] for a solid ellipsoid ($\lambda^{-1} = 0$), and those of Taylor [2] and followers for a close to spherical drop ($a_0 \simeq b_0 \simeq c_0$), to the whole parameter space, by providing the blob evolution for all initial ellipsoid and viscosity ratio.

As shown in Fig. 3, Eq. (1) recovers the stretching and rolling regimes observed experimentally at low and high λ , respectively. Specifically, for λ below a critical value

Following [27] we use exact analytical solutions of the instantaneous viscous flow, derived by Eshelby for the analogous elastic problem [24]. This approach is relevant since for a linear flow, such as the simple shear considered here, the strain rates inside an ellipsoidal blob are *uniform*. This implies an initially spherical blob remains ellipsoidal at all times, with a shape given by time-integrating Eshelby's solution for the instantaneous deformation rates. In the present case, the stretching rates of the three main axes a , b , c of the ellipsoid and its orientation φ relative to the flow gradient direction follow

$\lambda_c \simeq 3.975$, the theory predicts the blob ultimately aligns with the flow and stretches according to $b/b_0 \rightarrow \beta\gamma^{-1}$ (see SM, Sec. 4 [25]). The stretch shift factor is only mildly lower than 1 ($\beta \simeq 0.431$) for an inviscid blob ($\lambda = 0$) and diverges like $\beta \sim (\lambda_c - \lambda)^{-1/2}$ in λ_c , which agrees with experimental observations for the stretching regime [$\lambda \leq 2$, see Fig. 3(c)]. For $\lambda > \lambda_c$, Eq. (1) recovers the periodic rotation and oscillations of the rolling regime, with an amplitude $\Delta b/b_0 \sim 5/2\lambda$ and period $\dot{\gamma}T/2\pi \sim 1 + 15/4\lambda$ (see SM, Sec. 6 [25] for derivation), in good agreement

with observations. For λ close to λ_c , the theoretical kinematics eventually converge to one of the two previous asymptotics (stretching or rolling). However the latter are only reached after a large strain, which diverges like $\gamma \sim (\lambda_c - \lambda)^{-1}$, and before which the blob experiences a long transient substretching regime with a different power law, $b/b_0 \sim \gamma^{-1/2}$ (see SM, Sec. 5 [25]). This critical substretching regime (dashed line in Fig. 3) is found to be close to the transient substretching actually observed for $\lambda = 3$ and 3.5, before the blob eventually folds. However, Eq. (1) does not capture the folding nor the subsequent kinematics, which suggests folding actually stems from an instability of the transient substretching flow, when λ is sufficiently close to λ_c . This noninertial shear instability bears a similarity with the swirling instability reported for a viscous liquid stream sheared by a less viscous liquid in a channel [29], and might be related with the purely viscous mechanism uncovered by Yih [30,31].

The measurements and analyses above regard the limit when material diffusion has negligible effects. Nonetheless, they allow us to discuss how, and how fast, the two miscible liquids will eventually mix at long time. Indeed, at large Pe , mixing strongly depends on how much the concentration gradients and the contact area between the blob and the bath are increased. Such enhancement by the flow is well documented for the reference case of an isoviscous blob ($\lambda = 1$), which stretches as $b/b_0 = \gamma^{-1}$ at long time. In this case, diffusion proceeds essentially across the blob smallest dimension b , where gradients are large [32]. At first order in Pe^{-1} , the advection-diffusion equation $c_t + \mathbf{u} \cdot \nabla c = D\Delta c$, with c the concentration and D the molecular diffusivity, becomes the purely diffusive equation $c_\tau = c_{\xi\xi}$, in terms of the relative transverse coordinate $\xi \equiv y'/b$ and dimensionless time $\tau \equiv \int (b_0/b)^2 d\gamma / Pe \approx \gamma^3 / Pe$ [20,22,32]. Mixing occurs for $\tau \approx 1$, at a time $Dt_{\text{mix}}/b_0^2 \approx Pe^{-2/3}$ [21] (which is Schmidt number independent in the present limit of very high Schmidt numbers).

For other viscosity ratios in the stretching regime, the longtime kinematics depend only on λ through the stretch shift factor, $\beta \equiv \lim_{\gamma \gg 1} \gamma b/b_0$. Hence, the same formalism as for $\lambda = 1$ is expected to apply. This yields

$$\frac{Dt_{\text{mix}}}{b_0^2} \approx \beta^{2/3} Pe^{-2/3}, \quad (2)$$

for $Pe \gg 1$, and implies that the mixing time should vary only mildly with λ ; decreasing by $\approx 40\%$ for an inviscid blob ($\lambda \ll 1$), and increasing by $\approx 60\%$ for $\lambda = 2$, relative to $\lambda = 1$ [see Fig. 4(a)]. Importantly, for $Pe \gg 1$, mixing proceeds at a time when the kinematics has become independent of the viscosity field, which implies that the diffusion coefficient to use in (2) is not necessarily that between water and polymer molecules (setting viscosity), but that of the scalar which is actually tracked (e.g., dye, ...). By contrast, a dramatic effect is expected in the

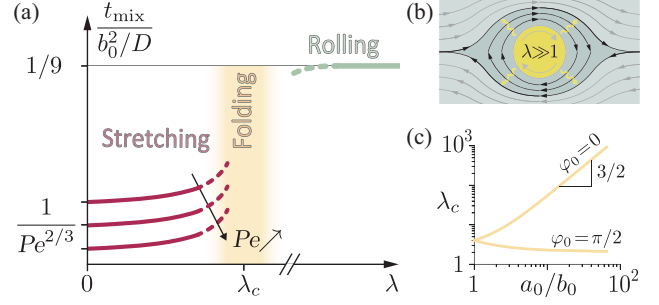


FIG. 4. (a) Expected dependence of the mixing time on λ at large Péclet number. (b) Sketch of the closed streamlines region expected for $\lambda \gg 1$. (c) Theoretical dependence of λ_c on the initial aspect ratio a_0/b_0 for an initial orientation $\varphi_0 = 0$ or $\pi/2$ (and $c_0 = \sqrt{a_0 b_0}$).

rolling regime. Indeed, for $\lambda \gg 1$, the nondiffusive kinematics converge to a solid body rotation, in the blob, and to the steady flow around a solid sphere, in the bath. Crucially, the latter features a recirculating region, with closed streamlines and a typical extension $\sim a = b$ around the sphere (see [33], Fig. 4) across which the long term radial transport is essentially diffusive at $Pe \gg 1$. In this limit the mass transfer, $-D \int_S \nabla c \cdot \mathbf{ds}$ with $S = 4\pi b^2$ the sphere surface, is quasisteady and only $\approx 9/2$ faster, asymptotically, than for a nonmoving sphere in a nonmoving bath [34–38]. From this scaling, the blob is expected to dilute slowly as it rolls, with a sphere radius decreasing like $b/b_0 \approx \sqrt{1 - t/t_{\text{mix}}}$, until it is fully mixed at a time

$$\frac{Dt_{\text{mix}}}{b_0^2} \approx \frac{1}{9}, \quad (3)$$

which is independent of shear rate and all the more long relative to the stretching regime so that Pe is large. By contrast with the stretching regime, the rolling kinematics depend on the viscosity field until mixing proceeds, which implies that the effective diffusivity to use in (3) is that of the viscosity field (i.e., of the polymer concentration). For intermediate ratios ($\lambda \approx 2-4$), the long initial substretching regime ($b/b_0 \sim \gamma^{-1/2}$) would lead to $\tau \sim \gamma^2/Pe$, hence $Dt_{\text{mix}}/b_0^2 \approx Pe^{-1/2}$. However, the folding of the blob interrupts stretching and forms rolling sub-blobs, for which a similar scaling as in the rolling regime [with an effectively reduced initial size $b_0 \rightarrow \{0.08-0.4\}b_0$] can be expected. All these trends are summarized in Fig. 4(a).

As a conclusion, observations and modeling provide a complete picture of the deformation of a localized heterogeneity of viscosity, for the reference case of a spherical blob in a viscous simple shear flow. The transition between unbounded stretching at low blob viscosity and periodic rolling at large blob viscosity occurs close to a critical

viscosity ratio $\lambda_c \approx 3.975$, and involves, experimentally, an intermediate regime, in which the blob is substretched and folded by the flow. For a miscible heterogeneity, this transition is expected to impact dramatically the homogenization of the flow. From the nondiffusive kinematics one anticipates a mixing time at large Pe changing from $t_{\text{mix}} \propto \text{Pe}^{-2/3}$, for a subviscous or close to isoviscous blob, to $t_{\text{mix}} \propto \text{Pe}^0$, in the limit $\lambda \gg 1$, i.e., to a mixing time which is insensitive to the velocity of the stirring flow. Theoretically, the transition has a strong dependence on the initial shape and orientation of the blob, which suggests that for an elongated heterogeneity mixing may be slowed down only for rather large viscosity ratios ($\lambda \gtrsim (a_0/b_0)^{3/2}$, for a blob initially perpendicular to flow, see Fig. 4(c) and SM, Sec. 5 [25]).

These trends concern an idealized flow and asymptotic limits of mixing. Yet, they provide clear guiding laws for the complex and nonlinear process of mixing highly viscous liquids with nonuniform viscosity. Indeed, although the blob deformation depends on the flow imposed to the bath—e.g., in a purely extensional flow, a blob eventually stretches after a transient $\sim \lambda/\dot{\gamma}$, however, large λ is [39], see also SM, Sec. 7 [25]—the transition, or the existence of a long initial delay, between a stretching and rollinglike blob is presumably relevant to many realistic flows, including chaotic ones, provided vorticity is nonzero and Lagrangian persistence time short enough. As for the nonlinearity of the mixing problem, it relates to the feedback of the viscosity field on the flow. One facet is the initial blob shape and viscosity ratio λ , which have been addressed above. The other one relates to the evolution of the viscosity field by molecular diffusion, which implies that *the flow is a priori* not independent of mixing, i.e., not Pe independent, in contrast to most mixing processes. On this second facet, the present work also brings clarifications. In the stretching regime ($\lambda < \lambda_c$), the blob passively follows the flow after a short transient of order γ^{-1} , which means the nonlinearity is entirely embedded in the longtime stretch shift factor β , while the flow independence to diffusivity at high Pe is recovered. In the rolling regime ($\lambda > \lambda_c$), the situation is more intricate. As diffusion proceeds, the viscosity profile in the recirculating region around and inside a highly viscous blob will evolve, possibly affecting the periodic motion and the asymptotic prediction $t_{\text{mix}} \propto \text{Pe}^0$. Yet, observation indicates rolling persists for many rotations, and flow dependence to Pe is presumably confined near the boundary between closed and open streamlines, which would resemble the passive transport case [34–38], inertial vortex stripping [40], or stripping of particle clouds [41]. Clarifying this feedback of diffusion on the flow will demand further investigations through longtime experiments resolving mixing. The benchmark results obtained here for a localized heterogeneity will also need to be extended to more complex viscosity fields in order to bridge the gap with

the case of solid particulate suspensions [26,42] or porous media [43–45] and to offer a complete picture of mixing between liquids with unequal viscosity.

Acknowledgments—This project has received funding from the European Union’s Horizon 2020 research and innovation programme under the Marie Skłodowska-Curie grant agreement No. 956457.

- [1] G. Taylor, The viscosity of a fluid containing small drops of another fluid, *Proc. R. Soc. A* **138**, 41 (1932).
- [2] G. Taylor, The formation of emulsions in definable fields of flow, *Proc. R. Soc.* **146**, 501 (1934).
- [3] F. Rumscheidt and S. Mason, Particle motions in sheared suspensions. Deformation & burst of fluid drops in shear and hyperbolic flow, *J. Colloid Sci.* **16**, 238 (1961).
- [4] S. Torza, R. Cox, and S. Mason, Particle motions in sheared suspensions XXVII. Transient and steady deformation and burst of liquid drops, *J. Colloid Interface Sci.* **38**, 395 (1972).
- [5] H. Grace, Dispersion phenomena in high viscosity immiscible fluid systems and application of static mixers as dispersion devices in such systems, *Chem. Eng. Commun.* **14**, 225 (1982).
- [6] B. Bentley and L. Leal, An experimental investigation of drop deformation and breakup in steady, 2-dimensional linear flows, *J. Fluid Mech.* **167**, 241 (1986).
- [7] H. Stone, B. Bentley, and L. Leal, An experimental study of transient effects in the breakup of viscous drops, *J. Fluid Mech.* **173**, 131 (1986).
- [8] M. Tjahjadi and J. Ottino, Stretching and breakup of droplets in chaotic flows, *J. Fluid Mech.* **232**, 191 (1991).
- [9] H. Stone, Dynamics of drop deformation and breakup in viscous fluids, *Annu. Rev. Fluid Mech.* **26**, 65 (1994).
- [10] P. Elemans, J. Van Wunnik, and R. Van Dam, Development of morphology in blends of immiscible polymers, *AIChE J.* **43**, 1649 (1997).
- [11] V. Sibillo, G. Pasquariello, M. Simeone, V. Cristini, and S. Guido, Drop deformation in microconfined shear flow, *Phys. Rev. Lett.* **97**, 054502 (2006).
- [12] J. Gounley, G. Boedec, M. Jaeger, and M. Leonetti, Influence of surface viscosity on droplets in shear flow, *J. Fluid Mech.* **791**, 464 (2016).
- [13] D. Spence, J. Ockendon, P. Wilmott, D. Turcotte, and L. Kellogg, Convective mixing in the mantle: The role of viscosity differences, *Geophys. J. Int.* **95**, 79 (1988).
- [14] M. Manga, Mixing of heterogeneities in the mantle: Effect of viscosity differences, *Geophys. Res. Lett.* **23**, 403 (1996).
- [15] N. Du Vignaux and L. Fleitout, Stretching and mixing of viscous blobs in earth’s mantle, *J. Geophys. Res.* **106**, 30893 (2001).
- [16] P. van Keken, E. Hauri, and C. Ballentine, Mantle mixing: The generation, preservation, and destruction of chemical heterogeneity, *Annu. Rev. Earth Planet Sci.* **30**, 493 (2002).
- [17] J. Woodhead, Mixing it up in the mantle, *Nature (London)* **517**, 275 (2015).
- [18] D. Paul and J. Barlow, Polymer blends, *J. Macromol. Sci., Phys.* **18**, 109 (1980).

- [19] C. Roland, Rheology of a miscible polymer blend, *J. Polym. Sci., Part B* **26**, 839 (1988).
- [20] W. Ranz, Application of a stretch model to mixing, diffusion, and reaction in laminar and turbulent flows, *AIChE J.* **25**, 41 (1979).
- [21] M. Souzy, I. Zaier, H. Lhuissier, T. Le Borgne, and B. Metzger, Mixing lamellae in a shear flow, *J. Fluid Mech.* **838**, R3 (2018).
- [22] E. Villermaux, Mixing versus stirring, *Annu. Rev. Fluid Mech.* **51**, 245 (2019).
- [23] S. Comas-Cardona and C. Tucker III, Measurements of droplet deformation in simple shear flow with zero interfacial tension, *J. Rheol.* **45**, 259 (2001).
- [24] J. Eshelby, The determination of the elastic field of an ellipsoidal inclusion, and related problems, *Proc. R. Soc.* **241**, 376 (1957).
- [25] See Supplemental Material at <http://link.aps.org/supplemental/10.1103/PhysRevLett.133.154001> for movies of experiments, additional information on the setup and the derivation of equations.
- [26] M. Souzy, H. Lhuissier, E. Villermaux, and B. Metzger, Stretching and mixing in sheared particulate suspensions, *J. Fluid Mech.* **812**, 611 (2017).
- [27] E. Wetzel and C. Tucker, Droplet deformation in dispersions with unequal viscosities and zero interfacial tension, *J. Fluid Mech.* **426**, 199 (2001).
- [28] G. Jeffery, The motion of ellipsoidal particles immersed in a viscous fluid, *Proc. R. Soc.* **102**, 161 (1922).
- [29] T. Cubaud and T.G. Mason, Swirling of viscous fluid threads in channels, *Phys. Rev. Lett.* **98**, 264501 (2007).
- [30] C.-S. Yih, Stability of liquid flow down an inclined plane, *Phys. Fluids* **6**, 321 (1963).
- [31] C.-S. Yih, Instability due to viscosity stratification, *J. Fluid Mech.* **27**, 337 (1967).
- [32] G. I. Taylor, Conditions under which dispersion of a solute in a stream of solvent can be used to measure molecular diffusion, *Proc. R. Soc.* **225**, 473 (1954).
- [33] R. Cox, I. Zia, and S. Mason, Particle motions in sheared suspensions XXV. Streamlines around cylinders and spheres, *J. Colloid Interface Sci.* **27**, 7 (1968).
- [34] A. Acrivos, Heat transfer at high Péclet number from a small sphere freely rotating in a simple shear field, *J. Fluid Mech.* **46**, 233 (1971).
- [35] G. Poe and A. Acrivos, Closed streamline flows past small rotating particles: Heat transfer at high Péclet numbers, *Int. J. Multiphase Flow* **2**, 365 (1976).
- [36] G. Batchelor, Mass transfer from a particle suspended in fluid with a steady linear ambient velocity distribution, *J. Fluid Mech.* **95**, 369 (1979).
- [37] C. Bielinski, L. Xia, G. Helbecque, and B. Kaoui, Mass transfer from a sheared spherical rigid capsule, *Phys. Fluids* **34** (2022).
- [38] Y. Wang, D. Vazquez Alvarez, H. Wan, R. Gonzalez Pizarro, and F. Shu, Advection-enhanced heat and mass transport from neutrally suspended droplet in simple shear flow, *Phys. Fluids* **35**, 063317 (2023).
- [39] C. Florek and C. Tucker, Stretching distributions in chaotic mixing of droplet dispersions with unequal viscosities, *Phys. Fluids* **17**, 053101 (2005).
- [40] A. Mariotti, B. Legras, and D. Dritschel, Vortex stripping and the erosion of coherent structures in two-dimensional flows, *Phys. Fluids* **6**, 3954 (1994).
- [41] B. Metzger and J. Butler, Clouds of particles in a periodic shear flow, *Phys. Fluids* **24** (2012).
- [42] R. Turuban, H. Lhuissier, and B. Metzger, Mixing in a sheared particulate suspension, *J. Fluid Mech.* **916**, R4 (2021).
- [43] J. Heyman, D. Lester, R. Turuban, Y. Méheust, and T. Le Borgne, Stretching and folding sustain microscale chemical gradients in porous media, *Proc. Natl. Acad. Sci. U.S.A.* **117**, 13359 (2020).
- [44] M. Souzy, H. Lhuissier, Y. Méheust, T. Le Borgne, and B. Metzger, Velocity distributions, dispersion and stretching in three-dimensional porous media, *J. Fluid Mech.* **891**, A16 (2020).
- [45] J. Heyman, D.R. Lester, and T. Le Borgne, Scalar signatures of chaotic mixing in porous media, *Phys. Rev. Lett.* **126**, 034505 (2021).

Supplemental Material for ‘Shearing liquids of unequal viscosity: can mixing be independent of stirring rate at a large viscosity ratio?’

I. Castaldi, B. Metzger, and H. Lhuissier*
Aix Marseille Univ, CNRS, IUSTI, Marseille, France
(Dated: October 3, 2024)

Contents of this file

- SM1. Description of the experimental movies
- SM2. Additional information on the experimental setup
- SM3. Theory - Derivation of the blob deformation rates (Eq. 1)
- SM4. Theory - Long-time limit of the stretching and substretching kinematics
- SM5. Theory - Critical viscosity ratio and dependance to initial shape
- SM6. Theory - Amplitudes and period of oscillation for $\lambda \gg 1$
- SM7. Theory - Stretching delay in an extensional flow for $\lambda \gg 1$

SM1. Description of the experimental movies

The movies show the deformation of an initially spherical blob for different viscosity ratio λ between the blob and the shearing bath. They correspond to the image sequences provided in Fig. 2 of the main body of the paper. The blob appears as dark. The Péclet number is $\sim 10^5$.

Movie 1: Stretching regime ($\lambda = 1$, Fig. 2 top).

Movie 2: Folding regime ($\lambda = 3.5$, Fig. 2 middle).

Movie 3: Rolling regime ($\lambda = 8$, Fig. 2 bottom).

All three movies are speed up 10 times. The length scale is indicated by a scale bar.

SM2. Additional information on the experimental setup

The bath and blob liquids are aqueous solutions of Ucon 75-H-90000 by Dow (linear polymers with 75wt% ethylene oxide groups, 25wt% propylene oxide groups and a molar mass ≈ 12 kg/mol). Varying the mass fraction of the polymer in the blob relative to the bath slightly changes the blob buoyancy. The largest density difference (below 3.5%) is obtained for $\lambda = 0.1$. This small density mismatch does not perturb the flow significantly (the typical creaming velocity $(2/9)\Delta\rho gb_0^2/\eta$, with $\eta = 1$ Pa/s the bath viscosity, is below 10^{-4} m/s, i.e., much below the typical shear velocity $\dot{\gamma}b_0 \simeq 1.5 \cdot 10^{-3}$ m/s.).

Viscosities are measured at the experiment temperature (22°C) with a cone-plate rheometer (Aanton Paar MCR 501). The shear rate is imposed with values logarithmically ramped between 0.1 s^{-1} and 10 s^{-1} . For all liquids, viscosity is constant, within $\pm 1\%$, over the range of applied shear rates.

The laser sheet is obtained from a cylindrical laser beam of wavelength 532 nm, a cylindrical plano-convex lens, and a rapidly rotating mirror with 6 flat faces (see Fig.1(a) of the main body of the paper). The lens focuses the beam in the vertical direction to obtain a thin sheet at the intersection with the blob. The rotating mirror expands the beam horizontally to form a sheet with uniform thickness and uniform light intensity. A low-pass filter is positioned between the blob and the long-distance macroscope (Leica Z16 APO) of the camera (achieving a spatial resolution of $12 \mu\text{m}/\text{px}$) to block the laser light while letting the fluorescent light from the dye pass.

* henri.lhuissier@univ-amu.fr

The Reynolds number at the scale of the shear cell is low ($\rho\dot{\gamma}\Delta r^2/\eta \sim 10^{-1}$, with $\Delta r = 24$ mm the gap between the inner and outer walls, and η the bath viscosity). The initial acceleration time of the walls is much longer ($\dot{\gamma}/\ddot{\gamma} \sim 10$ s) than momentum diffusion across the gap ($\rho\Delta r^2/8\eta \lesssim 0.1$ s). The rotation speeds ω_{in} and ω_{out} of the two walls are controlled by two independent rotation stages to ensure both the desired shear rate (only set by the difference $\omega_{\text{out}} - \omega_{\text{in}}$) and a vanishing velocity at the blob center in the reference frame of the laboratory (set by adjusting independently the sum $\omega_{\text{in}} + \omega_{\text{out}}$). To avoid that the blob would drift slowly over very long times in the azimuthal direction, the co-rotation speed $(\omega_{\text{in}} + \omega_{\text{out}})/2$ is constantly and slowly adjusted while keeping the counter rotation $\omega_{\text{in}} - \omega_{\text{out}}$ exactly unchanged. To ensure that the shear rate remains very close to constant at all time in the shear cell, these adjustments are also done with change rates much lower than the inverse viscous diffusive time across the cell gap.

The initial asphericity of the blob in the vorticity direction is not quantified directly. However, the frozen blob is immersed in the bath with a random orientation. Therefore, the average and variations between runs of the initial value of c_0 are expected to be the same as those of a_0 and b_0 (i.e. 1.72 ± 0.06 mm).

SM3. Theory - Derivation of the blob deformation rates (Eq. 1)

This section provides the derivation of the expressions for the deformation rates of the blob (Eq. 1 of the main body of the paper) based on Eshelby's solution for the formally analogous problem of the elastic deformation of a matrix containing an inclusion of a different stiffness [1].

We consider a viscous blob, with viscosity $\lambda\eta$, which is sheared in a viscous liquid bath, with viscosity η . Both liquids are Newtonian and incompressible. The inertia of the flow is neglected. The bath is considered infinite and a simple shear flow $\mathbf{u}^{FF} = \dot{\gamma}y\mathbf{e}_x$ is imposed in the far-field. To describe the kinematics of an initially spherical blob at all time, it is enough to consider an ellipsoidal blob, with main radii $a, b < a$ and c aligned with directions $\mathbf{e}_a, \mathbf{e}_b$ and \mathbf{e}_c , in the particular case when \mathbf{e}_c is also the vorticity direction. In such case, the orientation of the ellipsoid is fully determined by the angle φ between the velocity gradient direction, \mathbf{e}_y , and \mathbf{e}_a (for $\varphi = 0$, the length a is normal to the flow, for $\varphi = \pi/2$, it is along the flow). In such case, also, Eshelby established that the deformation rate inside the ellipsoid is *uniform* and related to the far-field flow and viscosity ratio λ , through a linear operator.

Strain rates of the inner fluid

In the ellipsoid coordinate system $(\mathbf{e}_a, \mathbf{e}_b, \mathbf{e}_c)$ the far-field strain rates and rotation rate are, respectively,

$$\dot{\boldsymbol{\varepsilon}}^{FF} = \begin{pmatrix} \sin 2\varphi & -\cos 2\varphi & 0 \\ -\cos 2\varphi & -\sin 2\varphi & 0 \\ 0 & 0 & 0 \end{pmatrix} \frac{\dot{\gamma}}{2}, \quad \omega^{FF} = -\frac{\dot{\gamma}}{2}.$$

From Eshelby's solution, the uniform rates inside the ellipsoid, $\dot{\boldsymbol{\varepsilon}}$ and ω , follow

$$[\mathcal{I} + \lambda'\mathcal{S}]\dot{\boldsymbol{\varepsilon}} = \dot{\boldsymbol{\varepsilon}}^{FF}, \quad \omega = \omega^{FF} - 2\lambda'\mathcal{R}\dot{\boldsymbol{\varepsilon}}_{ab}, \quad (\text{SM.1})$$

where $\lambda' \equiv \lambda - 1$, \mathcal{I} is the identity matrix and $\mathcal{S}(\frac{a}{b}, \frac{b}{c})$ and $\mathcal{R}(\frac{a}{b}, \frac{b}{c})$ are, respectively, a fourth order linear operator and a coefficient, depending on the ellipsoid aspect ratios only.

The operator \mathcal{S} is such that $(\mathcal{S}\dot{\boldsymbol{\varepsilon}})_{ij} = \mathcal{S}_{ijkl}\dot{\boldsymbol{\varepsilon}}_{kl}^P$ (where summation has to be performed on the kl indexes). It does not couple the shears from perpendicular directions nor does it couple extensions with shears. This means that each coefficient \mathcal{S}_{ijkl} for which any of the i, j, k, l appears an odd number of times vanishes. The other coefficients are [1]

$$\begin{aligned} \mathcal{S}_{aaaa} &= a^2 I_{aa}, & \mathcal{S}_{bbbb} &= b^2 I_{bb} \\ \mathcal{S}_{aabb} &= b^2 I_{ab}, & \mathcal{S}_{bbba} &= a^2 I_{ab}, & \mathcal{S}_{aacc} &= c^2 I_{ac}, & \mathcal{S}_{bbcc} &= c^2 I_{bc}, \\ \mathcal{S}_{abab} &= \mathcal{S}_{abba} = \frac{a^2 + b^2}{2} I_{ab}, & \mathcal{R} &= \frac{I_a - I_b}{6}, \end{aligned}$$

which involve the following moments of a, b and c

$$\begin{aligned}
I_a &= \frac{3}{2}abc \int_0^\infty \frac{\Delta^{-1}}{a^2 + u} du, & I_b &= \frac{3}{2}abc \int_0^\infty \frac{\Delta^{-1}}{b^2 + u} du, & I_c &= 3 - I_a - I_b, \\
I_{ab} &= \frac{I_b - I_a}{3(a^2 - b^2)}, & I_{ac} &= \frac{I_c - I_a}{3(a^2 - c^2)}, & I_{bc} &= \frac{I_c - I_b}{3(b^2 - c^2)}, \\
I_{aa} &= \frac{1}{a^2} - I_{ab} - I_{ac}, & I_{bb} &= \frac{1}{b^2} - I_{ab} - I_{bc}, & I_{cc} &= \frac{1}{c^2} - I_{ac} - I_{bc},
\end{aligned} \tag{SM.2}$$

with $\Delta = \sqrt{(a^2 + u)(b^2 + u)(c^2 + u)}$. All these moments express in terms of I_a and I_b , only, which can themselves be expressed as

$$I_a = -\frac{3c^2}{a^2 - c^2} \left(1 - \frac{a}{c} \frac{E\left[\arccos\left(\frac{a}{b}\right), \frac{c^2 - b^2}{a^2 - b^2}\right]}{\sqrt{1 - a^2/b^2}} \right),$$

where E is the elliptic integral of the second kind, and the expression for I_b is found by substituting a for b .

In our particular case, the solution of (SM.1) for the extension components is

$$\begin{aligned}
\frac{\dot{\epsilon}_{aa}}{\dot{\gamma}} &= \frac{1 + [(I_{ab} + I_{bb})b^2 - (I_{ac} + I_{bc})c^2]\lambda'}{N} \frac{\sin 2\varphi}{2}, \\
\frac{\dot{\epsilon}_{bb}}{\dot{\gamma}} &= -\frac{1 + [(I_{aa} + I_{ab})a^2 - (I_{ac} + I_{bc})c^2]\lambda'}{N} \frac{\sin 2\varphi}{2},
\end{aligned} \tag{SM.3}$$

with

$$\begin{aligned}
N &= 1 + [I_{aa}a^2 + I_{bb}b^2 - (I_{ac} + I_{bc})c^2]\lambda' \\
&\quad + [(I_{aa}I_{bb} - I_{ab}^2)a^2b^2 + (I_{ab}I_{ac} - I_{aa}I_{bc})a^2c^2 + (I_{ab}I_{bc} - I_{ac}I_{bb})b^2c^2]\lambda'^2.
\end{aligned} \tag{SM.4}$$

The shear component is

$$\frac{\dot{\epsilon}_{ab}}{\dot{\gamma}} = -\frac{1}{1 + (a^2 + b^2)I_{ab}\lambda'} \frac{\cos 2\varphi}{2}, \tag{SM.5}$$

while the rotation rate inside the ellipsoid is

$$\frac{\omega}{\dot{\gamma}} = -\frac{1}{2} + \frac{\frac{I_a - I_b}{3}\lambda'}{1 + (a^2 + b^2)I_{ab}\lambda'} \frac{\cos 2\varphi}{2}. \tag{SM.6}$$

Relation between inner fluid strain and ellipsoid deformation

The inner liquid deformation rates ($\dot{\epsilon}_{aa}$, $\dot{\epsilon}_{bb}$, $\dot{\epsilon}_{ab}$ and ω) allow us to compute the deformation of the ellipsoid itself, i.e., the stretching rates of its main axes, \dot{a}/a , \dot{b}/b , \dot{c}/c , and its rotation rate in the $\mathbf{e}_a, \mathbf{e}_b$ plan, $\dot{\varphi}$, as follows.

The rotation rate of the ellipsoid $\dot{\varphi}$, i.e., the rotation rate of \mathbf{e}_a , has actually two components. The first one is the rotation rate of the line of inner fluid, which is parallel with \mathbf{e}_a at a given time

$$\dot{\varphi}_{\text{line}} = -\omega - \dot{\epsilon}_{ab}.$$

The second one is the rotation rate of \mathbf{e}_a relative to the line of inner fluid, due to the ellipsoid deformation. This latter contribution can be derived as follows (not considering the rotation rate of the flow, which is already considered in $\dot{\varphi}_{\text{line}}$). The equation of the ellipse contained in the $\mathbf{e}_a, \mathbf{e}_b$ plane is

$$\frac{r}{b} = \frac{\sqrt{2}a}{\sqrt{a^2 + b^2 - (a^2 - b^2)\cos 2(\phi - \varphi)}}, \tag{SM.7}$$

with r the local ellipse radius and ϕ the polar angle relative to the gradient direction \mathbf{e}_y . In the neighborhood of the main axis, the radius r evolves, at lowest order, with time t as

$$r(\varphi + d\phi, t + dt) = r + r''d\phi^2/2 + (\dot{r} + \dot{r}'d\phi)dt, \tag{SM.8}$$

where $'$ and $\dot{}$ stand for derivation relative to ϕ and t , respectively, evaluated at $\phi = \varphi$. The new orientation of the ellipse is given by $\frac{dr}{d\phi} = r''d\phi + \dot{r}'dt = 0$, which means that the ellipse main axes rotate at a rate

$$\dot{\varphi}_{\text{shape}} \equiv \frac{d\phi}{dt} = -\frac{\dot{r}'}{r''}.$$

From (SM.7), the denominator can be expressed as

$$r'' = -a(a^2/b^2 - 1).$$

As for the numerator, one has

$$\dot{r}' = a\dot{c}' = a[\cos^2(\phi - \varphi)\dot{\varepsilon}_{aa} - 2\cos(\phi - \varphi)\sin(\phi - \varphi)\dot{\varepsilon}_{ab} + \sin^2(\phi - \varphi)\dot{\varepsilon}_{bb}]' = -2\dot{\varepsilon}_{ab}.$$

Combining the previous equations yields the expression for the rotation rate $\dot{\varphi} = \dot{\varphi}_{\text{line}} + \dot{\varphi}_{\text{shape}}$ of the ellipse

$$\dot{\varphi} = -\omega - \frac{a^2 + b^2}{a^2 - b^2}\dot{\varepsilon}_{ab},$$

while, from the first order terms in (SM.8), one has simply

$$\dot{a} = a\dot{\varepsilon}_{aa}, \quad \dot{b} = b\dot{\varepsilon}_{bb}, \quad \dot{c} = c\dot{\varepsilon}_{cc}.$$

General expressions for the ellipsoid deformation rates

Finally, making use of (SM.3,SM.5,SM.6) we recover Eq. 1 of the main body of the paper:

$$\begin{aligned} \frac{1}{\dot{\gamma}} \frac{\dot{a}}{a} &= \mathcal{A}\left(\frac{a}{b}, \frac{b}{c}, \lambda\right) \frac{\sin 2\varphi}{2}, & \mathcal{A} &= \frac{1 + [(I_{ab} + I_{bb})b^2 - (I_{ac} + I_{bc})c^2]\lambda'}{N}, \\ \frac{1}{\dot{\gamma}} \frac{\dot{b}}{b} &= -\mathcal{B}\left(\frac{a}{b}, \frac{b}{c}, \lambda\right) \frac{\sin 2\varphi}{2}, & \mathcal{B} &= \frac{1 + [(I_{aa} + I_{ab})a^2 - (I_{ac} + I_{bc})c^2]\lambda'}{N}, \end{aligned} \quad (\text{SM.9})$$

$$\frac{\dot{c}}{c} = -\frac{\dot{a}}{a} - \frac{\dot{b}}{b},$$

$$\frac{\dot{\varphi}}{\dot{\gamma}} = \frac{1}{2} + \mathcal{F}\left(\frac{a}{b}, \frac{b}{c}, \lambda\right) \frac{\cos 2\varphi}{2}, \quad \mathcal{F} = \frac{\frac{a^2+b^2}{a^2-b^2} + \frac{I_b - I_a}{3}\lambda'}{1 + \frac{a^2+b^2}{a^2-b^2} \frac{I_b - I_a}{3}\lambda'}, \quad (\text{SM.10})$$

which have to be complemented with (SM.4,SM.2) for the expression of N and of the moments $I_a, I_{ab} \dots$ in terms of a, b and c , respectively.

SM4. Theory - Long-time limit of the stretching and substretching kinematics

This section presents a derivation for the asymptotics of the long-time stretching regime ($\lambda < \lambda_c$) and of the long transient substretching regime when $\lambda \approx \lambda_c$.

For sufficiently low viscosity ratio, or sufficiently elongated initial shape, the ellipsoid lengthens forever and asymptotically aligns with the flow direction. As the ellipsoid lengthens, its *stretching* is increasingly slaved to that of the far-field flow, because the typical drag of the bath $\sim \eta(\dot{\varepsilon}_{aa}^{FF} - \dot{a}/a)a^2$ balances the viscous tension in the ellipsoid $\sim \lambda\eta(\dot{a}/a)bc$, which imposes that the stretching rate difference $\dot{\varepsilon}_{aa}^{FF}/(\dot{a}/a) - 1 \sim \lambda bc/a^2 = \lambda r_{\text{eq}}^3/a^3$ decreases strongly with increasing length (with $r_{\text{eq}} \equiv (abc)^{1/3}$, the constant sphere-equivalent radius of the ellipsoid). However, although in most of the cases the *alignment*, or rotation, of the ellipsoid is also slaved to that of the far-field flow, there exist cases where the viscosity contrast affects the alignment even for an infinitely elongated shape, leading to a different asymptotics of alignment, with the consequence of a different long-term elongation of the ellipsoid.

In both cases one has to consider the limit $a \gg r_{\text{eq}}, b \ll r_{\text{eq}}, c \sim r_{\text{eq}}$ and $\delta\varphi = \pi/2 - \varphi \ll 1$. The asymptotics of (SM.9,SM.10) are obtained by noting that $\mathcal{A} \rightarrow 1, \mathcal{B} \rightarrow 1, \frac{a^2+b^2}{a^2-b^2} \rightarrow 1 + 2\frac{b^2}{a^2}$ and $\frac{I_b - I_a}{3} \rightarrow \frac{1}{1+ab^2/r_{\text{eq}}^3}$, which confirms

that the ellipsoid stretches at the same rate as the far-field flow parallel with its long axis (e_a) and that the actual elongation is determined by the kinematics of alignment according to

$$\frac{1}{\dot{\gamma}} \frac{\dot{a}}{a} \simeq -\frac{1}{\dot{\gamma}} \frac{\dot{b}}{b} \simeq \delta\varphi, \quad \frac{1}{\dot{\gamma}} \frac{\dot{c}}{c} \simeq 0, \quad \frac{\dot{\varphi}}{\dot{\gamma}} = -\frac{\delta\dot{\varphi}}{\dot{\gamma}} \simeq \frac{\lambda}{\lambda-2} \frac{b^2}{a^2} + \delta\varphi^2. \quad (\text{SM.11})$$

Inspection of the last equation shows that the angle $\delta\varphi \equiv \pi/2 - \varphi$ has to decay like γ^{-1} , i.e., $\delta\varphi = \varphi_1 \gamma^{-1}$, while the stretching rate is given by the prefactor φ_1 .

'Regular' alignment and stretching regime

If the term $\frac{\lambda}{\lambda-2} \frac{b^2}{a^2}$ is subdominant, one obtains $\delta\dot{\varphi} = -\dot{\gamma} \delta\varphi^2$, i.e. $\delta\varphi = \gamma^{-1}$ or $\varphi_1 = 1$, like in the isoviscous case. Not only the current stretching rate but also the alignment rate is the same as that of the outer fluid. As a consequence the long-term elongation has to follow the isoviscous scaling

$$\frac{a}{r_{\text{eq}}} \rightarrow \alpha\gamma, \quad \frac{b}{r_{\text{eq}}} \rightarrow \beta\gamma^{-1}, \quad \text{with} \quad \varphi \rightarrow \gamma^{-1},$$

and the viscosity mismatch merely leads to a lag, or anticipation, in the kinematics relative to the isoviscous case ($\alpha, \beta \neq 1$).

Overalignment or substretching regime

However, the term $\frac{\lambda}{\lambda-2} \frac{b^2}{a^2}$ is not necessarily subdominant. For some kinematics of alignment (see Fig. SM.1), it can actually be of the same order as $\delta\varphi^2$ ($\sim \gamma^{-2}$). Since at long time $c \propto \gamma^0$, one has $a/r_{\text{eq}} \sim (b/r_{\text{eq}})^{-1}$, which implies $a \rightarrow r_{\text{eq}} a_1 \gamma^{-1/2}$. Therefore, the first two equations of (SM.11) impose $\delta\varphi = (2\gamma)^{-1}$, i.e.,

$$\frac{a}{r_{\text{eq}}} \rightarrow a_1 \gamma^{1/2}, \quad \frac{b}{r_{\text{eq}}} \rightarrow b_1 \gamma^{-1/2}, \quad \text{with} \quad \varphi \rightarrow \frac{1}{2} \gamma^{-1},$$

while the last one imposes the following relation between the prefactors a_1 and b_1

$$\frac{a_1^2}{b_1^2} = \frac{\lambda}{\lambda-2}.$$

The actual value of a_1 (or alternatively b_1) is not prescribed by the present asymptotic analyses (it is set by the short-time kinematics before alignment).

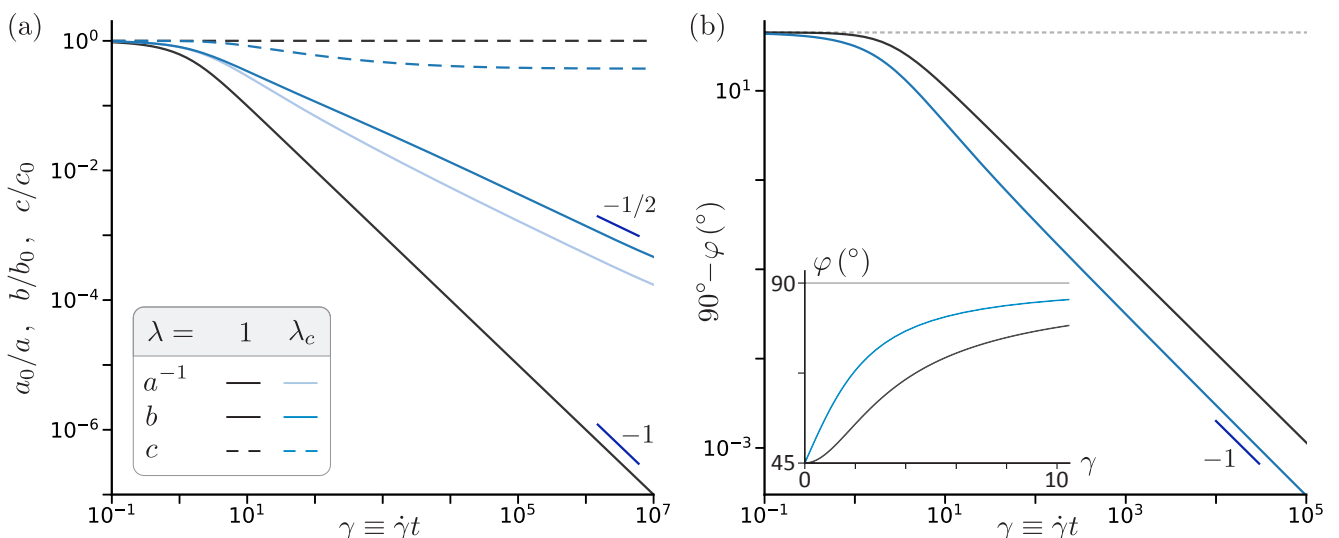


Figure SM.1. Deformation kinematics of an initially spherical blob ($a_0 = b_0 = c_0$), in the isoviscous case ($\lambda = 1$, black) and for the critical viscosity ratio ($\lambda = \lambda_c \simeq 3.975$, blue). (a) Main blob lengths vs accumulated shear strain. (b) Blob orientation vs accumulated shear strain. Inset: short time.

SM5. Theory - Critical viscosity ratio and dependence to initial shape

This section presents the critical deformation kinematics, which separates the stretching from the rolling regimes, for an initially spherical blob. It also presents typical critical kinematics for an initially ellipsoidal blob with different initial orientations relative to the flow, as well as the dependence of the critical viscosity ratio on the blob initial aspect ratio and orientation.

Fig. SM.1 presents the critical deformation kinematics for an initially spherical blob ($\lambda = \lambda_c \simeq 3.975$) up to an accumulated shear strain $\gamma \equiv \dot{\gamma}t = 10^7$. The kinematics is compared to the isoviscous case ($\lambda = 1$). Fig. SM.2a compares the critical deformation kinematics of an initially ellipsoidal blob with a fixed initial aspect ratio $a_0/b_0 = 4$, for different initial orientations $\varphi_0 = 0, 45, 70, 80, 85$ and 90° relative to the velocity gradient direction. Fig. SM.2b shows the dependence of the critical viscosity ratio λ_c on the initial aspect ratio a_0/b_0 and orientation φ_0 of the blob. The critical viscosity ratio is obtained by a shooting method as the viscosity ratio for which the angle $\pi/2 - \varphi$ decays like γ^{-1} at long time (the trend is verified up to the largest computed deformation $\gamma = 10^7$).

SM6. Theory - Amplitudes and period of oscillation for $\lambda \gg 1$

This section provides the derivation for the amplitudes and period of the shape oscillations of the blob, in the case of a large viscosity ratio ($\lambda \gg 1$).

For sufficiently large viscosity ratio and sufficiently compact initial shape, the ellipsoid does not align with the flow direction but keeps rotating while it undergoes stretching and compression cycles. In the strict absence of inertia ($Re = 0$) the orbiting motion is periodic, as a consequence of the reversibility and symmetry of the flow (the kinematics is unchanged under a $(t, \varphi) \rightarrow (-t, \pi/2 - \varphi)$ transformation). For large amplitude orbits, one has to rely on numerical integration of (SM.9, SM.10). However, for large viscosity ratios ($\lambda \gg 1$), the blob experiences only small amplitude oscillatory deformations around the steady solution of a solid rotating sphere ($a = b = c = r_{\text{eq}}$, $\dot{\varphi} = \dot{\gamma}/2$), of which the amplitude and period can be derived.

In the latter limit ($\lambda \gg 1$), the angle φ is of order 1 (it increases from $\pi/4$ to $3\pi/4$ over the period), whereas the deformations are of order $|a - 1| \sim |b - 1| \sim \lambda^{-1}$. However, the deviation of the period from $2\pi/\dot{\gamma}$ actually involves the next order in λ^{-1} . We therefore seek for the orientation and small deformations in the form:

$$\frac{a}{r_{\text{eq}}} - 1 = \frac{a_1}{\lambda} + \frac{a_2}{\lambda^2}, \quad \frac{b}{r_{\text{eq}}} - 1 = \frac{b_1}{\lambda} + \frac{b_2}{\lambda^2}, \quad 2\varphi = \frac{\pi}{2} + 2\varphi_0 + \frac{2\varphi_1}{\lambda}, \quad (\text{SM.12})$$

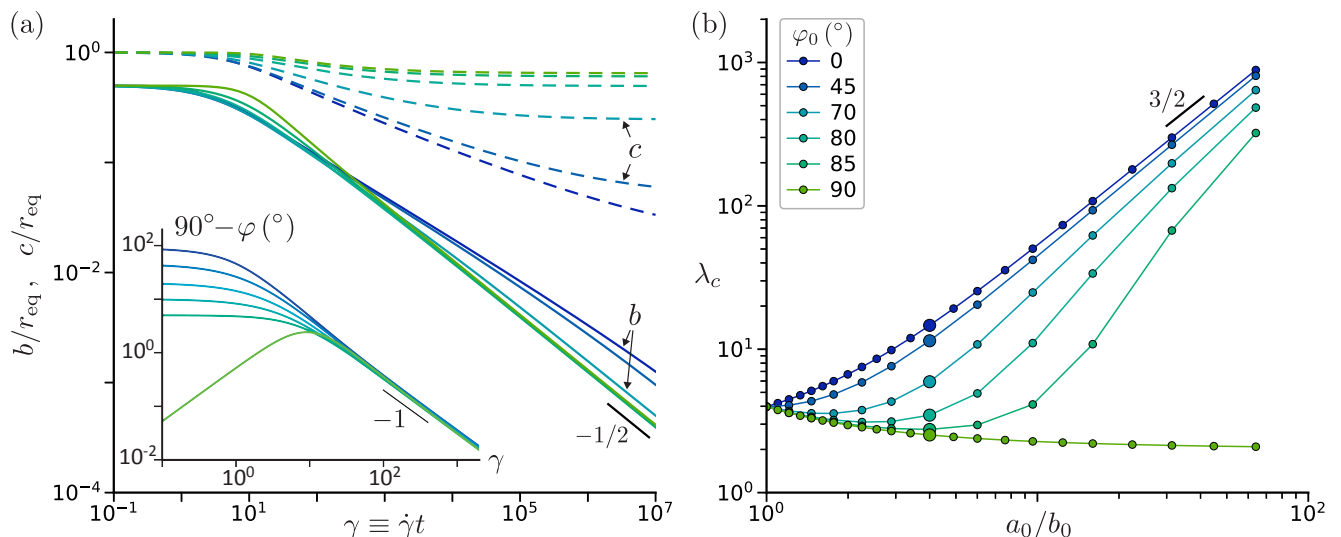


Figure SM.2. Critical deformation kinematics for an initially ellipsoidal blob with different initial aspect ratios and orientations. (a) Critical kinematics for a fixed initial aspect ratio $a_0/b_0 = 4$ (with $c_0 = r_{\text{eq}} \equiv (a_0 b_0 c_0)^{1/3}$) and different initial orientations $\varphi_0 = 0, 45, 70, 80, 85$ and 90° relative to the velocity gradient direction. (b) Critical viscosity ratio vs initial aspect ratio for the same initial orientations. Large symbols correspond to the kinematics shown in (a).

with $a_1, a_2, b_1, b_2, \varphi_0$ and φ_1 unknown functions of the shear strain γ only. Developing the system (SM.9,SM.10) in series of the small parameter λ^{-1} yields:

$$\begin{aligned} \frac{1}{\dot{\gamma}} \left(\frac{\dot{a}_1}{\lambda} + \frac{\dot{a}_2}{\lambda^2} \right) &= \left[\frac{\mathcal{A}_1}{\lambda} + \frac{\mathcal{A}_2}{\lambda^2} \right] \cos(2\varphi_0 + \frac{2\varphi_1}{\lambda}), \\ \frac{1}{\dot{\gamma}} \left(\frac{\dot{b}_1}{\lambda} + \frac{\dot{b}_2}{\lambda^2} \right) &= - \left[\frac{\mathcal{B}_1}{\lambda} + \frac{\mathcal{B}_2}{\lambda^2} \right] \cos(2\varphi_0 + \frac{2\varphi_1}{\lambda}), \\ \frac{1}{\dot{\gamma}} \left(2\dot{\varphi}_0 + \frac{2\dot{\varphi}_1}{\lambda} \right) &= 1 - \left[\mathcal{F}_0 + \frac{\mathcal{F}_1}{\lambda} \right] \sin(2\varphi_0 + \frac{2\varphi_1}{\lambda}), \end{aligned} \quad (\text{SM.13})$$

where

$$\begin{aligned} \mathcal{A}_1 &= \frac{5}{2}, & \mathcal{A}_2 &= -\frac{25}{4} \left(1 - \frac{22a_1 + 4b_1}{35} \right), \\ \mathcal{B}_1 &= \frac{5}{2}, & \mathcal{B}_2 &= -\frac{25}{4} \left(1 - \frac{4a_1 + 22b_1}{35} \right), \\ \mathcal{F}_0 &= \frac{5}{2} \frac{1}{a_1 - b_1}, & \mathcal{F}_1 &= -\frac{5}{2} \frac{a_2 - b_2}{(a_1 - b_1)^2} - \frac{175 - 65(a_1 + b_1) - 28(a_1 - b_1)^2}{28(a_1 - b_1)}, \end{aligned}$$

are the serie coefficients in λ^{-1} of $\mathcal{A} \equiv a\mathcal{A}$, $\mathcal{B} \equiv b\mathcal{B}$, and \mathcal{F} , depending on a_1, a_2, b_1, b_2 only. At first order, the system (SM.13) becomes

$$\frac{\dot{a}_1 + \dot{b}_1}{\dot{\gamma}} = 0, \quad \frac{\dot{a}_1 - \dot{b}_1}{\dot{\gamma}} = \frac{5}{2} \cos 2\varphi_0, \quad \frac{2\dot{\varphi}_0}{\dot{\gamma}} = 1 - \frac{5 \cos 2\varphi_0}{2(a_1 - b_1)},$$

which is solved by

$$a_1 + b_1 = 0, \quad a_1 - b_1 = 5 \sin \frac{\gamma}{2}, \quad 2\varphi_0 = \frac{\gamma}{2}. \quad (\text{SM.14})$$

The second order is

$$\begin{aligned} \frac{\dot{a}_2 + \dot{b}_2}{\dot{\gamma}} &= (\mathcal{A}_2 - \mathcal{B}_2) \frac{\cos 2\varphi_0}{2} = \frac{225}{56} \sin \gamma, \\ \frac{\dot{a}_2 - \dot{b}_2}{\dot{\gamma}} &= -2\mathcal{A}_1 \frac{\sin 2\varphi_0}{2} 2\varphi_1 + (\mathcal{A}_2 + \mathcal{B}_2) \frac{\cos 2\varphi_0}{2} = -\frac{5}{2} \sin \frac{\gamma}{2} 2\varphi_1 - \frac{25}{4} \cos \frac{\gamma}{2}, \\ \frac{2\dot{\varphi}_1}{\dot{\gamma}} &= -\mathcal{F}_0 \cos 2\varphi_0 2\varphi_1 - \mathcal{F}_1 \sin 2\varphi_0 = -\frac{1}{2} \frac{2\varphi_1}{\tan \frac{\gamma}{2}} + \frac{1}{10} \frac{a_2 - b_2}{\sin \frac{\gamma}{2}} + \frac{5}{2} \cos \gamma - \frac{5}{4}, \end{aligned}$$

which yields

$$a_2 + b_2 = -\frac{225}{56} \sin \gamma, \quad a_2 - b_2 = \frac{25}{8} (\sin \gamma - 3\gamma) \cos \frac{\gamma}{2}, \quad 2\varphi_1 = \frac{15}{8} (\sin \gamma - \gamma). \quad (\text{SM.15})$$

Using (SM.14,SM.15) in the expression for φ (SM.12), we obtain the period of the oscillations as the strain $\gamma = \dot{\gamma}T$ at which $2\varphi = \pi/2 + \gamma/2 + \frac{15}{8\lambda} (\sin \gamma - \gamma) = 3\pi/2$, i.e.,

$$\frac{\dot{\gamma}T}{2\pi} = 1 + \frac{15}{4\lambda},$$

at first order in λ^{-1} , as stated in the main body of the paper.

SM7. Theory - Stretching delay in an extensional flow for $\lambda \gg 1$

This section presents the derivation for the typical time delay $\sim \lambda/\dot{\gamma}$ before a highly viscous blob strained by a purely extensional flow stretches as fast as the far-field flow.

We consider a blob with a viscosity ratio λ relative to the suspending bath, which is strained in a two-dimensional extensional flow $\mathbf{u}^{FF} = \dot{\gamma}x'\mathbf{e}_{x'} - \dot{\gamma}y'\mathbf{e}_{y'}$. For an initially spherical blob, the longest axis a is parallel with the main extensional direction $\mathbf{e}_{x'}$ at all times. Therefore, simplifying (SM.9) for $\omega = 0$, $\varphi = \pi/4$ and $\dot{\gamma}/2 \rightarrow \dot{\gamma}$ yields the relevant evolution equations for the blob dimensions:

$$\frac{1}{\dot{\gamma}} \frac{\dot{a}}{a} = \mathcal{A}\left(\frac{a}{b}, \frac{b}{c}, \lambda\right), \quad \frac{1}{\dot{\gamma}} \frac{\dot{b}}{b} = -\mathcal{B}\left(\frac{a}{b}, \frac{b}{c}, \lambda\right), \quad \frac{\dot{c}}{c} = -\frac{\dot{a}}{a} - \frac{\dot{b}}{b}. \quad (\text{SM.16})$$

As the blob deforms, the aspect ratios a/b and b/c change, and the stretching rates \dot{a}/a , \dot{b}/b and \dot{c}/c follow successively three different regimes, as illustrated in Fig. SM.3 for a viscosity ratio $\lambda = 100$. At short time, the blob is close to spherical and stretches at a low rate set by the blob viscosity:

$$\frac{1}{\dot{\gamma}} \frac{\dot{a}}{a} \simeq \frac{1}{1 + 2(\lambda - 1)/5} \simeq \frac{5}{2\lambda}, \quad \frac{\dot{b}}{b} \simeq -\frac{\dot{a}}{a}, \quad \frac{\dot{c}}{c} \simeq 0,$$

as given by the limit of (SM.16) for $a \simeq b \simeq c$, in agreement with Taylor's result [2]. This first transient lasts until the blob shape has significantly deviated from a sphere, which takes a typical time

$$t_a \sim \frac{2\lambda}{5\dot{\gamma}}. \quad (\text{SM.17})$$

After t_a , the stretching rate \dot{a}/a of the long axis rapidly increases up to the far-field rate $\dot{\gamma}$, but the blob does not deform like an isoviscous blob, yet. For an intermediate transient regime the blob undergoes a close to biaxial extension, with $a \gg b \simeq c$, for which (SM.16) becomes

$$\frac{1}{\dot{\gamma}} \frac{\dot{a}}{a} \simeq 1, \quad \frac{1}{\dot{\gamma}} \frac{\dot{b}}{b} \simeq -\frac{1 + \lambda/2}{1 + \lambda}, \quad \frac{1}{\dot{\gamma}} \frac{\dot{c}}{c} \simeq -\frac{\lambda/2}{1 + \lambda}.$$

For $\lambda \gg 1$, the stretching rates of b and c are both close to $-\dot{\gamma}/2$, but they are not equal. The third axis c is compressed with a rate about $\dot{\gamma}/\lambda$ faster than b , which means that after an additional time

$$t_b - t_a \sim \frac{\lambda}{\dot{\gamma}}, \quad (\text{SM.18})$$

the aspect ratio b/c becomes much larger than 1 and the kinematics enter the long-time regime.

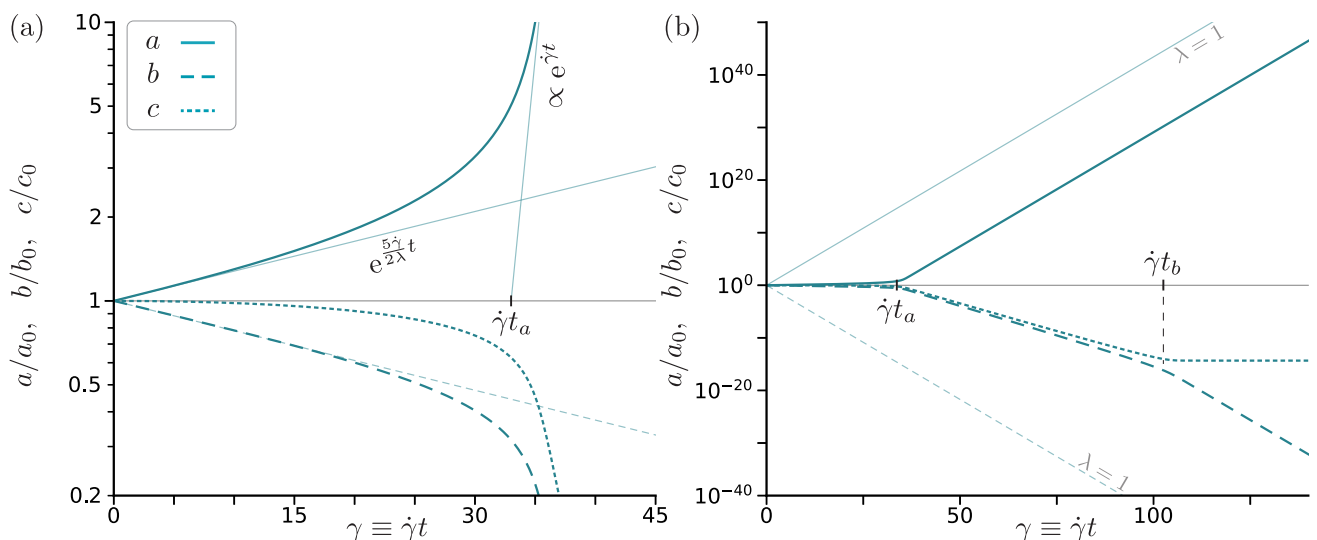


Figure SM.3. Time evolution of the blob dimensions for an initially spherical blob with viscosity ratio $\lambda = 100$ in a two-dimensional extensional flow (time-integration of (SM.16)). (a) Close-up on the initial transient ($\gamma \lesssim \dot{\gamma}t_a$), with a slow stretching limited by the blob viscosity. (b) Whole kinematics, showing also the intermediate transient ($\dot{\gamma}t_a \lesssim \gamma \lesssim \dot{\gamma}t_b$), and the long time regime ($\gamma \gtrsim \dot{\gamma}t_b$), when the blob width is compressed as fast as the far-field flow.

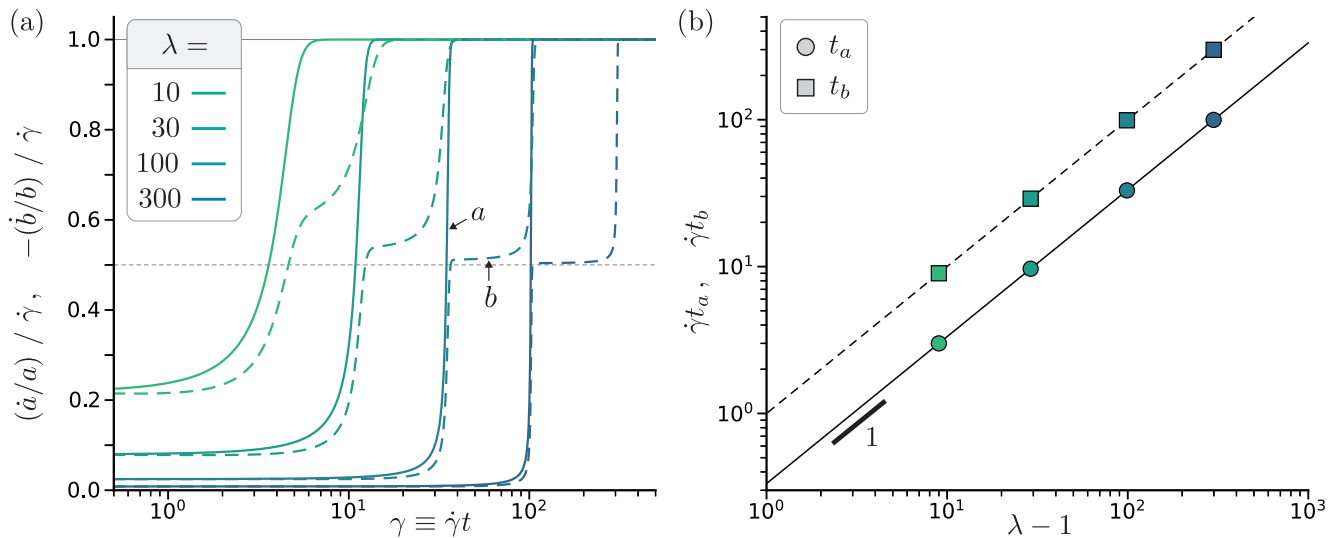


Figure SM.4. (a) Time evolution of the blob extremal stretching rates for different λ . (b) Transition times between the three successive stretching regimes vs λ . Symbols: values obtained from the time-integration (t_a and t_b are obtained by evaluating $\dot{\gamma}^{-1} \lim_{\gamma \gg \lambda} [\gamma - \ln(a/a_0)]$ and $\dot{\gamma}^{-1} \lim_{\gamma \gg \lambda} [\gamma + \ln(b/c)]$, respectively). Plain and dashed lines: (SM.19) for t_a and t_b , respectively.

At long time, the blob is so slender that it passively follows the far-field flow with stretching rates

$$\frac{1}{\dot{\gamma}} \frac{\dot{a}}{a} \simeq 1, \quad \frac{\dot{b}}{b} \simeq -\frac{\dot{a}}{a}, \quad \frac{\dot{c}}{c} \simeq 0,$$

given by the limit $a \gg c \gg b$ of (SM.16), which are independent of the blob viscosity.

Fig. SM.4a presents the extension rate \dot{a}/a and the compression rate $-\dot{b}/b$ obtained by time-integrating (SM.16) for λ ranging from 10 to 300. The three stretching regimes are recovered. They are all the more distinct so that λ is high. Fig. SM.4b shows the times t_a and t_b separating the three regimes. They are found to follow

$$t_a \simeq \frac{1}{\dot{\gamma}} \frac{\lambda - 1}{3}, \quad \text{and} \quad t_b \simeq \frac{1}{\dot{\gamma}} (\lambda - 1), \quad (\text{SM.19})$$

in agreement with (SM.17), and (SM.18), and as stated in the discussion in the main body of the paper.

-
- [1] J. Eshelby, The determination of the elastic field of an ellipsoidal inclusion, and related problems, Proc. R. Soc. Lond. **241**, 376 (1957).
 [2] G. Taylor, The formation of emulsions in definable fields of flow, Proc. R. Soc. Lond. **146**, 501 (1934).

III.2.5 Additional informations

Before addressing mixing, we provide additional information about two specific aspects of the flow, which have not been discussed much in the letter. First, about the folding instability observed for a viscosity ratio close to the critical value λ_c , and second, regarding the reversibility of the flow.

III.2.5.a Folding regime

When the viscosity ratio is close to λ_c , the blob deviates from the predicted substretching and eventually folds. We did not systematically investigate this instability, however, it presents a rich phenomenology and some of our observations deserve to be reported. In figure III.10a, we show that for two experiments starting from the same initial conditions ($\lambda = 3.5$), the blob either destabilizes into one large folding swirl (top), or into a series of smaller evenly-spaced swirls (bottom). This result suggests that the folding instability is, in practice, very sensitive to small changes in the initial shape or orientation of the blob. We also observe that the duration of the sub-stretching transient, before the blob eventually folds, depends on the viscosity ratio: the closest to the critical viscosity, the earlier the destabilization. The exact sequence of the folding kinematics and the actual number of rolling structures is found to vary from one repetition of the experiment to the other, however, the destabilization is robustly observed.

A similar phenomenology, reported by Cubaud and Mason, [117], occurs when a viscous liquid thread flowing in a channel is sheared by a less viscous liquid co-flowing in the same channel (see Fig. III.10b). The authors report a viscous swirling instability, which becomes more pronounced when the thread is off-centered in regions of larger shear. The authors do not provide a detailed mechanism, but their swirling instability and the folding instability we report might be related with the purely viscous mechanism uncovered by Yih [118, 119].

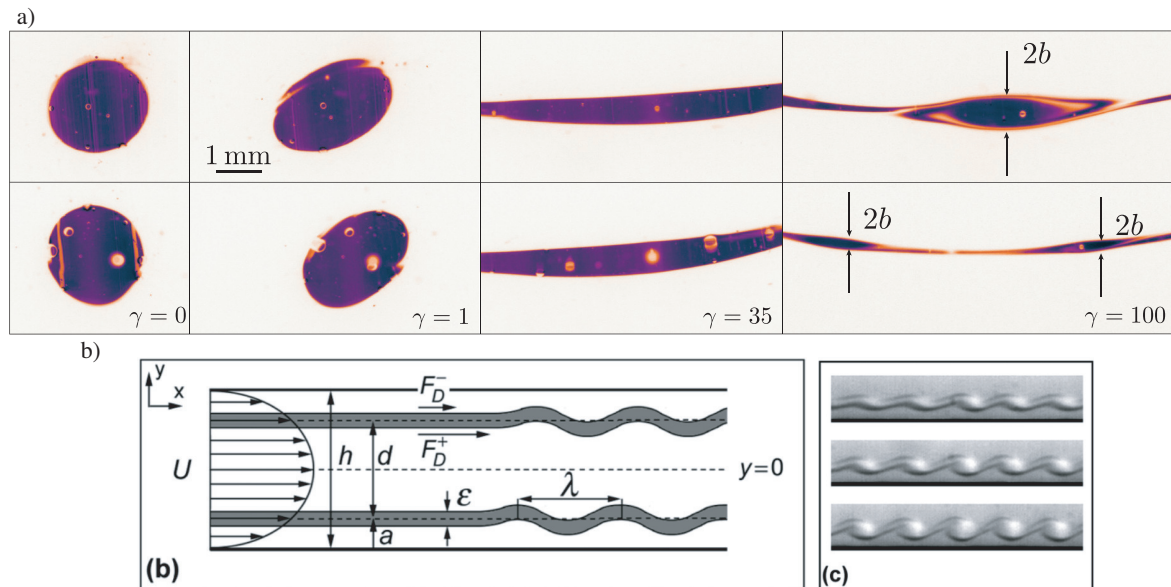


FIGURE III.10: *Variability of the folding regime and similarity with reported flows.* (a) Detail of the folding observed for two experiments with $\lambda = 3.5$. Both blobs stretch while aligning with the flow direction, until they destabilize and *fold* into a different pattern: (top) a single large swirl, (bottom) multiple small swirls. (b) Reproduction of Fig. 3b and Fig. 4c of [117], showing off-centered viscous threads co-flowing with a less viscous liquid in a small channel and destabilizing into a series of viscous swirls.

III.2.5.b Flow reversibility

The various kinematics of deformations observed when varying the viscosity ratio naturally raise the question of the flow reversibility. In 1966, Taylor illustrated the reversibility of certain Stokes flows, with a celebrated experiment with a Couette flow [120]. A blob of dye sheared in a viscous liquid recovers its initial shape when the shear direction is reversed (except for the blurring due to molecular diffusion). Taylor's demonstration concerns the isoviscous blob case. But what about reversibility when the blob viscosity is not equal to the bath viscosity?

Just like for the isoviscous case, equations III.5 we derived for the flow with a non-isoviscous blob are time reversible (at $Re = 0$ and $Pe = \infty$). However, just like for the isoviscous case, this reversibility of the equations tells nothing about the actual stability of the flow relative to small perturbations. We therefore performed preliminary experiments to investigate the deformation of an initially spherical blob, of varied viscosity, over a back and forth shear cycle with a strain amplitude of $\gamma = 12$. Pictures of the mid-cycle and end-cycle shapes are reported in figure III.11. For the isoviscous benchmark ($\lambda = 1$, top panel) the blob is stretched in a thin lamella and eventually recovers its initial shape, mildly blurred by molecular diffusion. For a blob in the rolling regime ($\lambda = 8$, bottom panel), the blob also returns to its initial condition after the flow is reversed. By contrast, for a non-isoviscous stretching blob ($\lambda = 2$, middle panel) reversibility breaks down. The blob stretches into a fairly elongated lamella but, as shear is reversed the lamella seems to buckle and eventually folds. This instability might bear similarity with viscous buckling, because when the shear is reversed, the viscous stresses in the more viscous blob switch from tensile to compressive along its long axis a . It would be interesting to further investigate this instability and, in particular, to determine the relation between the critical elongation to trigger the instability and the viscosity ratio. Indeed, the rolling regime (which probes reversibility since, without shear reversal, the second part of the periodic motion is already the symmetric of the first one) shows that for large λ and sufficiently small deformations, the flow is stable, hence reversible.

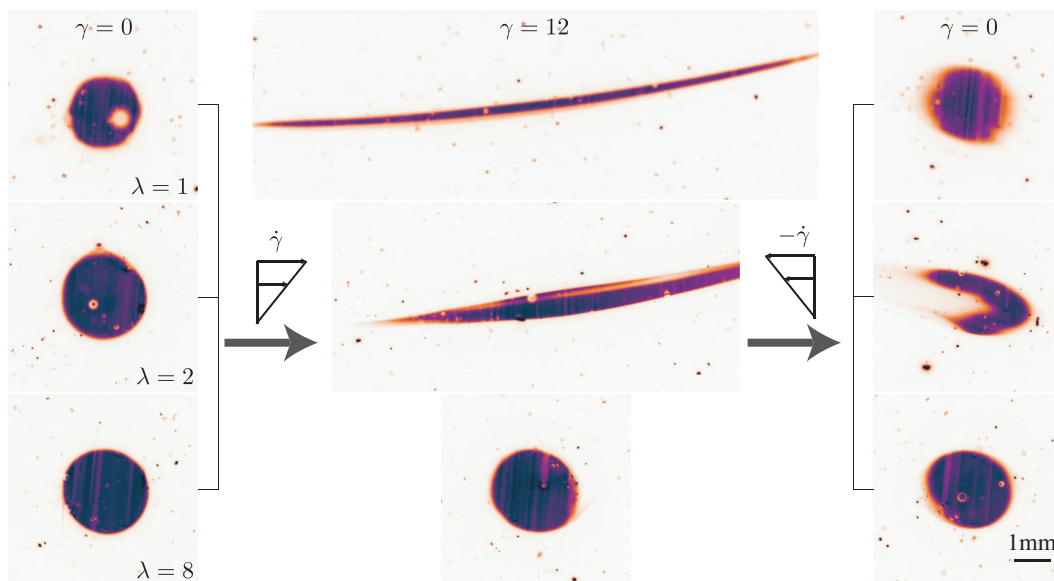


FIGURE III.11: Extending Taylor's reversibility experiment to non-isoviscous blobs. The blobs are submitted to a back and forth cycle of shear of strain $\gamma \simeq 12$. (Top) Benchmark isoviscous case ($\lambda = 1$). (Middle) Non-isoviscous stretching blob ($\lambda = 2$). (Bottom) Rolling blob ($\lambda = 8$).

III.3 Mixing of the blob

The experiments conducted to examine the kinematics of deformation at high Péclet numbers revealed the existence of three distinct regimes depending on the viscosity ratio λ . In this section, we will focus on the two extreme regimes, the *stretching* regime ($\lambda \leq 2$) and the *rolling* regime ($\lambda \gtrsim \lambda_c \simeq 4$), to investigate how the qualitative change in kinematics influences the mixing time of the blob. We will leave aside the intermediate *substretching* regime, for which mixing depends on the details of the complex folding instability and of the variability of the swirling sub-blob size it produces. The following mixing investigation requires additional, longer and more resolved, experiments where, besides varying the viscosity ratio, we will also vary the Péclet number.

III.3.1 General observations

Figure III.12 illustrates the typical evolution towards mixing in the stretching regime ($\lambda = 2$) and the rolling regime ($\lambda = 30$), at similar Péclet numbers $Pe \approx 10^4$. For $\lambda = 2$ (top), the blob follows a canonical stretching-enhanced mixing. It is rapidly thinned down into a lamella by the shear. After some minutes its concentration decays, and it is eventually mixed completely within 20 minutes. For $\lambda = 30$, the blob rolls and adopts a close to self-similar ovoidal shape, whose size decreases very slowly. After 20 minutes, the rolling blob is still far from mixed and its core concentration is almost unchanged relative to the initial blob. This comparison illustrates how the kinematic transition from stretching to rolling, due to the increase in the viscosity ratio λ , qualitatively changes the mixing process and dramatically affects the blob mixing time.

In the following, we model the mixing in the two regimes, and present additional systematic experiments to measure the mixing time dependence to the viscosity ratio and the Péclet number, which will allow us to test the model.

III.3.2 Mixing in the *stretching regime*

We first address the *stretching regime* by performing long experiments with a viscosity ratio λ between 0.1 and 2 and a Péclet number Pe between 6×10^3 and 6×10^5 . The experiments are conducted by adjusting the shear velocity in accordance with the size of the blob to achieve the exact desired Péclet number (see §III.1.2). Some co-rotation is added to the cell walls counter-rotation to obtain a cleaner flow (see §III.1.2),

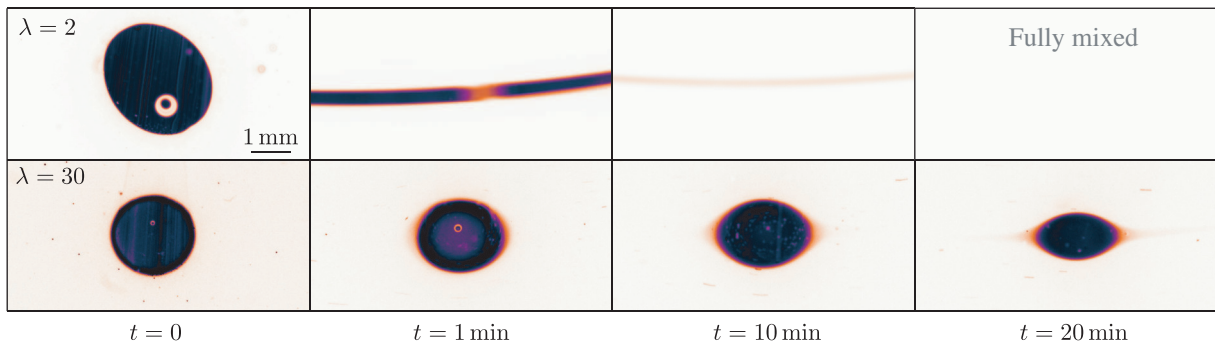


FIGURE III.12: *Dramatic impact of the stretching to rolling transition on the mixing of the blob.* Evolution of the mixing process in a simple shear flow at $Pe \approx 10^4$ ($\dot{\gamma} \simeq 0.3 \text{ s}^{-1}$) for a low viscosity stretching blob ($\lambda = 2$, top) and a large viscosity rolling blob ($\lambda = 30$, bottom).

which allows us to track quantitatively the evolution of very thin lamellae with decaying concentration levels. Images are captured at approximately one frame per second.

III.3.2.a Phenomenology & quantification

Figure III.13a shows the blob at four successive strains for $\lambda = 2$ and $Pe = 6 \times 10^4$. The corresponding concentration profiles measured across the blob width and their fit with an error function are shown in figure III.13b. In this stretching regime, the mixing of the blob is qualitatively similar to the isoviscous case presented in the introduction (§I.2.3.a). The mixing process is only shifted by the kinematic stretch shift factor $\beta(\lambda)$ (investigated and understood in §III.2.2 and §III.2.4), which quantifies how much the long term thinning of the more viscous blob, $b/b_0 \rightarrow \beta\gamma^{-1}$, is shifted relative to the isoviscous case, $b/b_0 \rightarrow \gamma^{-1}$. In the following, we show how the Ranz lamellar approach can be extended to include this shift factor β and predict the mixing process over the whole stretching regime.

III.3.2.b Mixing model including the stretch shift factor β

In the stretching regime, the kinematic evolution of the blob width is asymptotically given by $b/b_0 = 1/\sqrt{1 + (\dot{\gamma}t/\beta)^2}$. The Ranz dimensionless warped time, $\mathcal{T} = \int_0^t \frac{D}{b(t')^2} dt'$, is thus readily expressed as $\mathcal{T} = \frac{1}{Pe}(\dot{\gamma}t + \frac{(\dot{\gamma}t)^3}{3\beta^2}) \simeq \frac{1}{Pe} \frac{(\dot{\gamma}t)^3}{3\beta^2}$, from which we obtain the expressions for the diffusive evolution of the

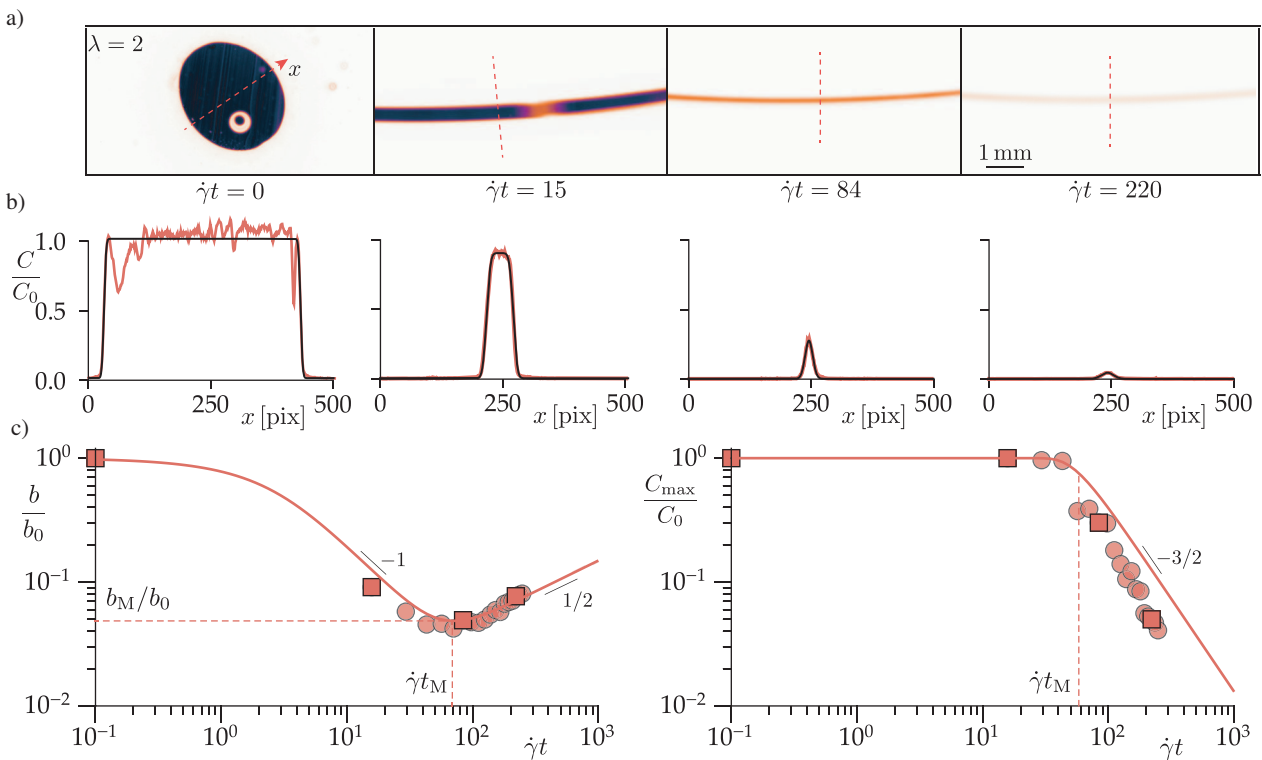


FIGURE III.13: *Mixing in the stretching regime – Quantification.* (a) Image sequence of the mixing process for $\lambda = 2$ and $Pe = 6 \times 10^4$ ($\dot{\gamma} \simeq 0.2$). (b) Concentration profiles measured along the dotted lines in (a) and fitted with an error function (black solid line). (c) Resulting normalized blob width b/b_0 and maximal concentration C_{\max}/C_0 vs strain.

Solid lines: extended Ranz lamellar framework accounting for the stretch shift factor β (Eqs. III.6 and III.8).

blob width and maximal concentration

$$\begin{aligned} \frac{b}{b_0} &= \frac{\sqrt{1 + \frac{2}{Pe} \frac{(\dot{\gamma}t)^3}{3\beta^2}}}{\sqrt{1 + \frac{(\dot{\gamma}t)^2}{\beta^2}}} \xrightarrow{t \gg t_M} \sqrt{\frac{2}{3} \frac{\dot{\gamma}t}{Pe}}, \\ \frac{C_{\max}}{C_0} &= \frac{1}{\sqrt{1 + \frac{2}{Pe} \frac{(\dot{\gamma}t)^3}{3\beta^2}}} \xrightarrow{t \gg t_M} \sqrt{\frac{3\beta^2}{2} \frac{Pe}{(\dot{\gamma}t)^3}}. \end{aligned} \quad (\text{III.6})$$

The onset mixing time t_M and the minimal width of the blob at the onset of mixing b_M are obtained for $\mathcal{T} = 1$, which gives

$$\frac{t_M}{b_0^2/D} \simeq \left(\frac{Pe}{\sqrt{3}\beta} \right)^{-2/3}, \quad \text{and} \quad \frac{b_M}{b_0} \simeq \left(\frac{Pe}{\sqrt{3}\beta} \right)^{-1/3}. \quad (\text{III.7})$$

Equations III.6 and III.7 give all the dependance of the mixing process on the viscosity ratio λ through the stretch shift factor $\beta(\lambda)$. To explicit this dependance on λ we provide the following approximation of the function β

$$\beta(\lambda) \simeq 1 + (\lambda - 1)(1 - \beta_0 - 0.1\lambda + 0.16\lambda^2), \quad \text{with} \quad \beta_0 = \beta(0) \simeq 0.431, \quad \text{for} \quad 0 \leq \lambda \leq 3, \quad (\text{III.8})$$

which is valid within 5% over the range $0 \leq \lambda \leq 3$ and gives the exact value for both the inviscid case ($\lambda = 0$) and the isoviscous case ($\lambda = 1$; for value close to $\lambda_c \approx 4$, the function β diverges like $(\lambda_c - \lambda)^{-1/2}$ but it is not relevant anymore since the blob folds, see Fig. III.9c).

The above expressions deserve comments. First, the stretching regime is limited to viscosity ratio λ below ~ 2 (because of the folding instability), for which the stretch shift factor varies between ≈ 0.4 and ≈ 2 . The mixing time is thus expected to vary only mildly with λ , decreasing by $\approx 40\%$ for an inviscid blob ($\lambda \ll 1$) and increasing by $\approx 60\%$ for $\lambda = 2$, relative to the iso-viscous case. As for the Péclet dependence, it is the same as in the iso-viscous case. Second, in the long time diffusing regime ($t \gg t_M$) although the maximal concentration $C_{\max} \propto \beta$ keeps a dependance to λ , the width of the blob $b \propto \beta^0$ does not (conservation of the dye is ensured by the increase in the blob other dimensions $ac \propto 1/\beta$). For experiments at different viscosity ratio at fixed Péclet number, we therefore expect a collapse of the blob widths after the mixing time.

Relevant diffusivity. Last, and importantly, in the stretching regime and for the large Péclet numbers we consider, mixing occurs at a time when the viscosity field does not influence the flow anymore. Although the blob is thicker or thinner by the factor β (which embeds the early history of deformation), the current thinning rate $-\dot{b}/b = t^{-1}$ is independent of β , hence of the blob viscosity. This implies that equations III.6 to III.8 describe not only the mixing of the viscosity field (if one uses $D = D_\eta$ to compute Pe), but also the mixing of a dye that would diffuse slower (using $D = D_{\text{dye}}$), or the mixing of any other diffusive scalar initially concentrated in the blob and advected by the liquids (using the diffusivity coefficient of this scalar). The only condition is that the corresponding Péclet number be large compared to 1.

III.3.2.c Model versus experimental results

The above predictions are tested by performing two sets of experiment. One varying the Péclet number between 6×10^3 and 6×10^5 , at fixed viscosity ratio $\lambda = 2$, the other varying the viscosity ratio between

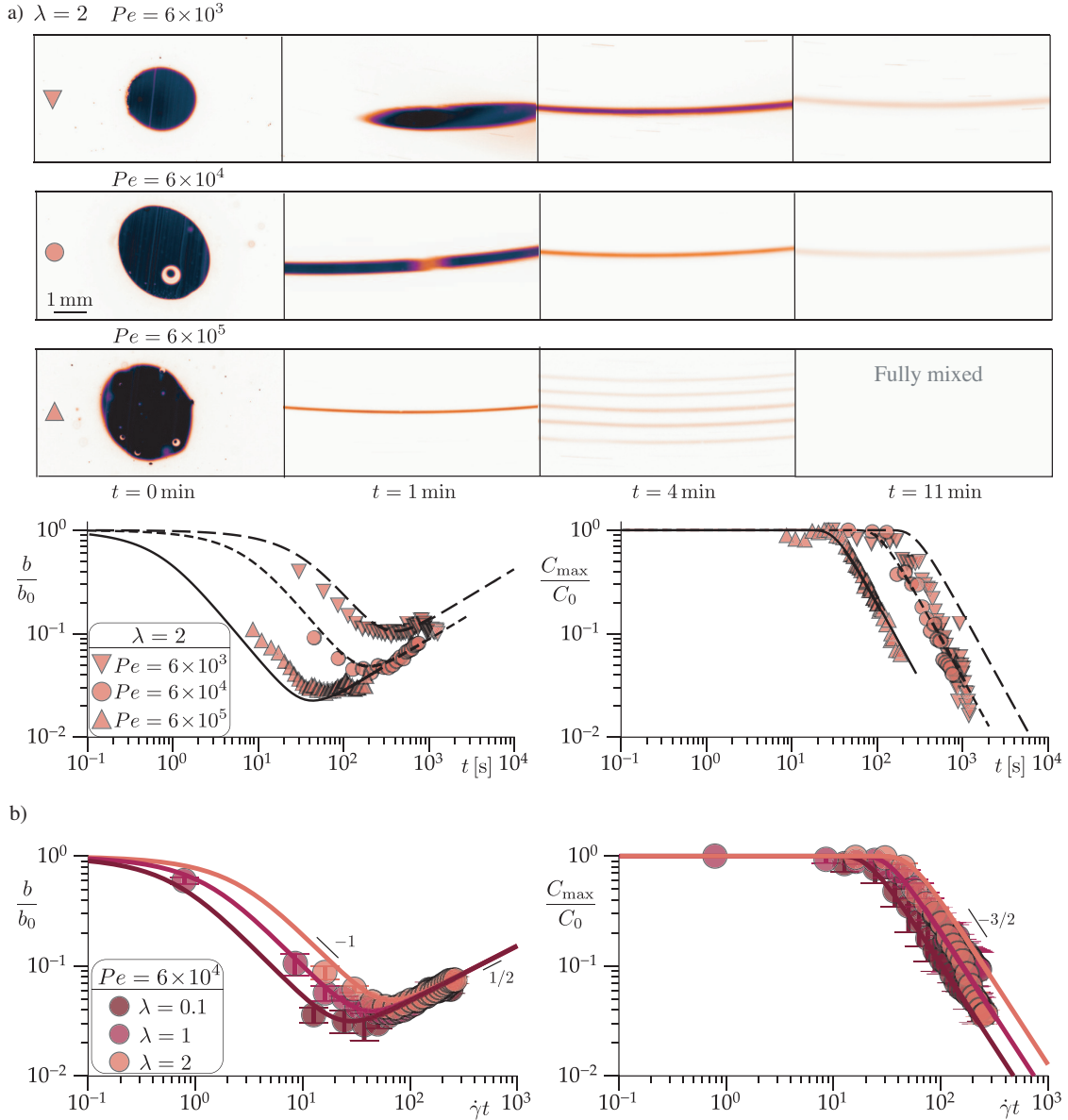


FIGURE III.14: *Mixing in the stretching regime – Model versus experiments.* (a) Experiments varying the Péclet number ($6 \times 10^3 \leq Pe \leq 6 \times 10^6$) at fixed viscosity ratio ($\lambda = 2$). Top: Image sequence of the mixing process (the many stripes observed for $Pe = 6 \times 10^5$ are pieces of the same highly stretched blob, spiraling in the shear cell). Bottom: Evolution of the blob width and maximal concentration vs strain. (b) Experiments varying the viscosity ratio ($0.1 \leq \lambda \leq 2$) at fixed Péclet number ($Pe = 6 \times 10^4$). Black and solid lines: extended Ranz lamellar framework accounting for the stretch shift factor β (Eqs. III.6 and III.8).

0.1 and 2, at a fixed Péclet, $Pe = 6 \times 10^4$. Given the weak dependence on λ , these experiments are challenging and had to be improved by all the techniques listed in §III.1.1 before resolving the trends. In practice, each experimental curve is an average over typically 3 individual runs, and error bars represent the standard deviation between runs. The viscosity ratios being close to 1, the dye diffusion is dominated by the low mobility of the polymer molecules $D_{\text{dye}} \simeq 10^{-11} \text{ m}^2/\text{s}$ (see Chapter II), and the Péclet number $Pe = b_0^2 \dot{\gamma} / D_{\text{dye}}$ is computed with this value.

Figure III.14a shows the results obtained when varying Pe , together with image sequences of the typical evolutions. As for the iso-viscous case, shearing faster accelerates mixing. At $t = 11$ min the lamella has been mixed at the largest Péclet (6×10^5), whereas it is still visible at the lower Péclet numbers. The

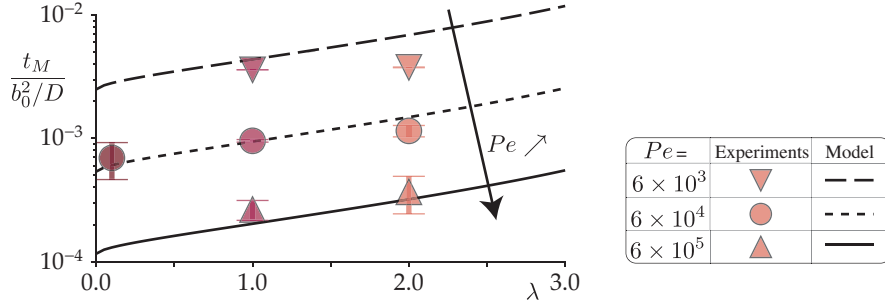


FIGURE III.15: *Mixing in the stretching regime – Mixing time.* Normalized mixing time Dt_M/b_0^2 versus λ for the different Péclet numbers investigated ($D = D_{\text{dye}} = 10^{-11} \text{ m}^2/\text{s}$ and $Pe = b_0^2 \dot{\gamma}/D_{\text{dye}}$). Black lines: extended Ranz lamellar framework accounting for the stretch shift factor β (Eqs. III.7 and III.8).

evolution of the blob width b/b_0 and of the maximal concentration C_{max}/C_0 show a significant influence of the imposed Péclet number, and the measurements are well captured by the model (Eq. III.6).

Figure III.14b shows the results obtained when varying λ . Here, as expected, the influence of λ is mild but still appreciable, both for the width and for the concentration. Blobs with a larger viscosity mix at a later time and the shift between different curves is typically captured by the model including the stretch shift factor β . As anticipated, we observe that the widths of blobs of different viscosity ratio collapse onto a single curve after the mixing scale.

Figure III.15 summarizes the results of this section devoted to understanding and quantifying mixing in the *stretching* regime, by presenting the normalized mixing time Dt_M/b_0^2 obtained for all the viscosity ratio and Péclet numbers investigated. Measurements show a strong dependence of the mixing time on the Péclet number, and a mild dependence on the viscosity ratio. They agree with the description proposed above. The extended Ranz lamellar framework (Eqs. III.6 and III.8), which include the stretch shift factor β , is found to capture quantitatively the observed experimental trends over the whole range of viscosity ratio and Péclet number investigated. It is worth stressing that the model is plotted without fitting parameters. Indeed, the blob size and experimental shear rate are set by the experimental conditions, the dependence of the stretch shift factor β on the viscosity ratio λ was determined analytically in the previous section dedicated to the kinematics at infinite Péclet, and the diffusion coefficient $D = D_{\text{dye}}$ was measured independently in the static diffusion experiment presented in chapter 2.

III.3.3 Mixing in the *rolling regime*

We now move to the *rolling regime* observed for large viscosity ratios. Here, the blob no longer stretches, but rolls, and a lamellar description is no longer relevant. In what follows, we perform experiments dedicated to this *rolling regime* by varying the viscosity ratio $\lambda \in [5, 90]$ and the Péclet number $Pe \in [2 \times 10^2, 2 \times 10^4]$ in order to interpret the mixing process at play and provide a model for the blob mixing time. For these experiments, the shear cell is counter-rotating to keep the blob in the field of view, and we use the laser shutter to mitigate photobleaching (see §III.1.2).

III.3.3.a Phenomenology & quantification

Figure III.16a highlights the typical long-time mixing phenomenology in the rolling regime (here for $\lambda = 30$ and $Pe = 2 \times 10^3$). The salient features, which are robustly observed for $\lambda \in [5 - 90]$, are the following:

- i-iii)* The blob rolls, while undergoing small amplitude stretching-compression cycles. The amplitude of these oscillations, which have been discussed in the section devoted to the kinematics (see Fig. III.9a),

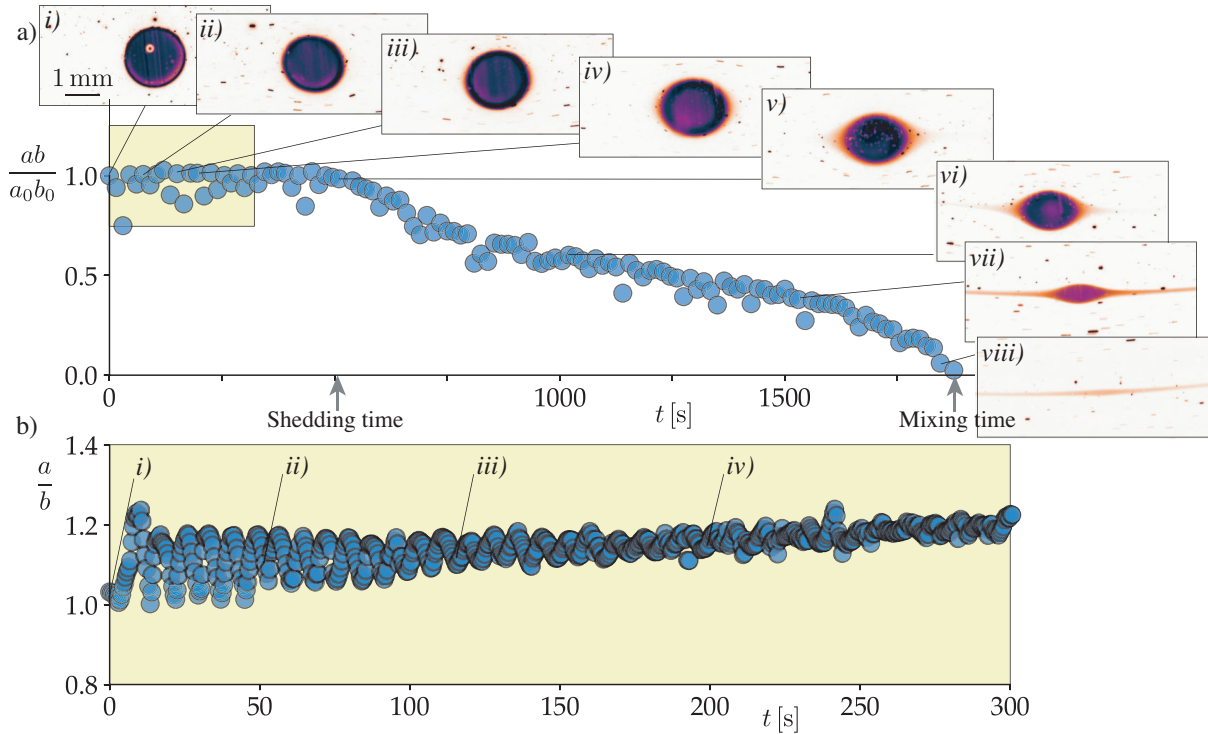


FIGURE III.16: *Mixing in the rolling regime – Phenomenology and quantification.* (a) Evolution of the cross-sectional area of the blob versus time and corresponding snapshots of the blob, emphasizing the slow and close to self-similar shrinkage of the blob, at long time. (b) Short-time evolution of the blob aspect ratio a/b , showing the rapid damping of the oscillations of the rolling motion and the convergence to the quasi-steady self-similar shape.

is shown in panel b, which focuses on the early evolution of the blob aspect ratio.

iv) The blob oscillations are progressively damped, and the blob relaxes to a quasi-steady ellipsoidal shape with its long dimension a aligned with the flow direction.

v) After a time t_{shed} , the dyed liquid start to be shed in the outer bath, in the form of two thin diffuse lamellae aligned with the flow, at each side of the blob.

vi-vii) The shedding process continues, while the blob dimensions decrease close to self-similarly by keeping a roughly constant aspect ratio a/b .

viii) The core of the blob, dissolving between the shed lamellae, eventually disappears at a time t_M , which we call the mixing time.

This definition of the mixing time is chosen because we are mostly interested in the mixing process by which the rolling blob progressively ‘dissolves’ into the bath. The subsequent mixing of the shed lamella left in image (*viii*) can simply be described with the standard Ranz formalism.

We now provide more information on the three dimensional evolution of the blob. Figure III.17a shows the vertical thickness profile of a blob measured at $t = 500$ s ($\lambda = 30$, $Pe = 2 \times 10^3$) and obtained by vertically scanning the blob with the laser sheet (see corresponding cross-sections of the blob). We observe that the blob significantly departs from its initial isotropic spherical shape and elongates in the vorticity direction (e_z), reaching an aspect ratio $c/b \approx 2.5$. By performing this scan at 4 different times over the mixing process, we find that this aspect ratio is relatively constant and independent of the viscosity ratio. We can also compare the typical evolution of the cross-sectional area (ab/a_0b_0), which decreases rapidly, to that of the blob volume ($abc/a_0b_0c_0$), which increases first, before decreasing after the shedding time (see Fig. III.17b). We will come back to this observation and provide an explanation after we have

presented the model.

Last, we discuss the close to self-similar ellipsoidal shape of the blob observed over most of the process. This shape results from a damping of the periodic stretching component of the rolling motion and it is essentially maintained as mixing proceeds. We did not study the damping itself (which might be a consequence of a minute diffusion of the viscosity field or of the small but finite Reynolds number of the flow), but we notice that the self-similar shape depends on the viscosity ratio. The lower λ the more slender the blob in the shear plane (the larger a/b , see Fig. III.17c). This trend can actually be understood from the infinite Péclet kinematics of the blob.

Indeed, inspection of the equations III.5 for the blob kinematics at infinite Péclet shows that there are steady solutions of the flow ($\dot{a} = \dot{b} = \dot{c} = \dot{\varphi}$) only for $\varphi = \pi/2$, *i.e.*, only when the blob is aligned with the flow direction (e_x). The condition on $\dot{\varphi} = 0$ therefore imposes $\mathcal{F}\left(\frac{a}{b}, \frac{b}{c}, \lambda\right) = 1$, which is equivalent to (see expression for \mathcal{F} provided in the supplemental material of the letter in §III.2.4)

$$\frac{a_S b_S c_S}{2} \int_0^\infty \frac{a_S^2 - b_S^2}{(a_S^2 + u)^{3/2} (b_S^2 + u)^{3/2} (c_S^2 + u)^{1/2}} du = \lambda, \quad (\text{III.9})$$

with a_S, b_S, c_S the steady dimensions. Equation III.9 defines the dependence of the steady shapes on the viscosity ratio λ . For a given λ there is actually a family of steady shapes a_S/b_S parametrized by the third dimension c_S/b_S . This means that for the observed transverse aspect ratio $c_S/b_S \simeq 2.5$, there is a single steady solution for each viscosity ratio. This analytical steady solution is compared to measured shapes in figure III.17c. The analytically derived cross-sectional aspect ratio a_S/b_S is found to match closely the measurements over the whole range of viscosity ratio investigated. This indicates that, in spite of

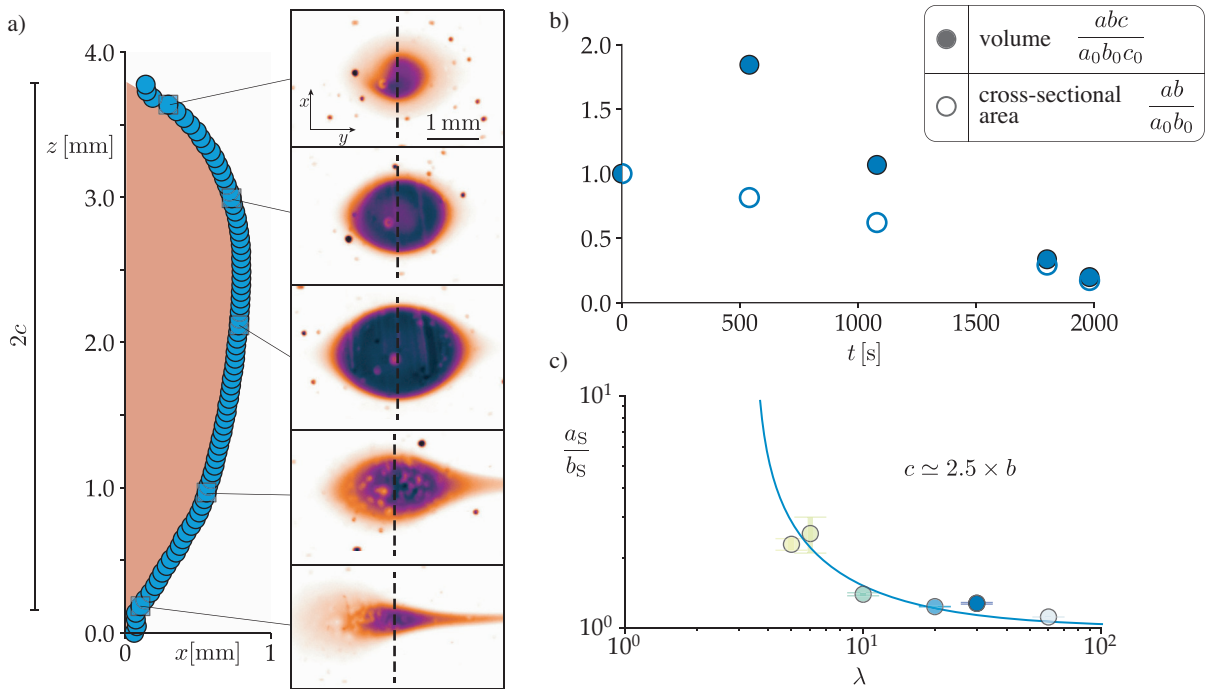


FIGURE III.17: *Mixing in the rolling regime – 3D shape of the blob.* (a) Vertical thickness profile of the blob (measured at $t = 500$ s, $\lambda = 30$, $Pe = 2 \times 10^3$) and some snapshots (corresponding to horizontal cross-sections). (b) Evolution of the blob cross-sectional area ab/a_0b_0 (hollow circles) and blob volume $abc/a_0b_0c_0$ (circles) versus time. (c) Aspect ratio a_S/b_S of the close to self-similar quasi-steady shape observed over most of the mixing process versus viscosity ratio λ (measurements are done at times close to the shedding time). Blue line: analytical steady solution for a non-diffusing blob (Eq. III.9 with $c_S/b_S = 2.5$). Error-bars: Standard deviation over 3 run.

the diffusion of the viscosity field, the flow remains not too far from that of a non-diffusing blob. This observation suggests that the core of the blob does not dilute significantly over most of the slow shrinkage of the blob. We will come back to this point below.

III.3.3.b Mixing model: a ‘dissolving’ rolling sphere

The longer mixing time in the *rolling regime* reported in figure III.12 is, obviously, a consequence of the rolling motion preventing the thinning of the blob observed at low viscosity ratios. To provide a quantitative prediction, we consider the limit of a highly viscous blob ($\lambda \gg 1$), for which the nondiffusive kinematics converge to a solid body rotation, in the blob, and to the steady flow around a solid sphere, in the bath. Crucially, the latter features a recirculating region, with closed streamlines and a typical extension $\lesssim a = b$ around the sphere. This recirculating region is illustrated in figure III.19 with a schematics of the closed streamlines and a beautiful image from an experiments by Cox, Zia & Mason [90]. These closed streamlines play a crucial role since they drastically limit the mass transfer from the sphere to the outer fluid. Indeed, in the limit of large Péclet numbers we are interested in, the long term radial transport is limited by the diffusion across the locally parallel streamlines and it is of an essentially diffusive nature. In this limit, the mass transfer rate is quasi-steady and its asymptotic value derived by Acrivos [121–125] for a solid sphere in a simple shear

$$q = -D \int_{\Sigma} \nabla C \, ds \approx 18\pi DC_0 \times b, \quad \text{with } \Sigma = 4\pi b^2 \text{ the sphere surface,} \quad (\text{III.10})$$

is only about $9/2$ faster than for a sphere diffusing in a static bath. Importantly, the rate q in the simple shear also scales with the sphere size b . From mass conservation, $\frac{d}{dt} \frac{4\pi}{3} b^3 = -q$, applying this scaling to a highly viscous blob implies that the blob would ‘dissolve’ slowly as it rolls, with a radius following

$$\frac{b}{b_0} \simeq \sqrt{1 - \frac{t}{t_M}}, \quad (\text{III.11})$$

until it the blob is fully mixed at a time

$$\frac{t_M}{b_0^2/D} \simeq \frac{1}{9}. \quad (\text{III.12})$$

This result is remarkable and may seem counterintuitive, at first sight, since it indicates that the mixing of a fairly viscous blob should be independent of the flow strength. Shearing faster is not expected to mix faster! To our knowledge, there is no experimental evidence of this odd behavior in literature.

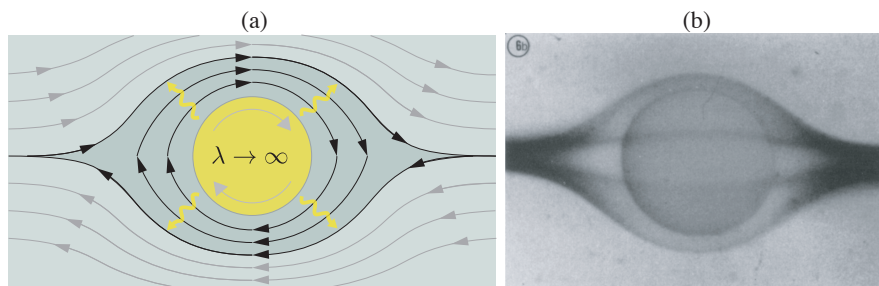


FIGURE III.18: *Recirculating region around a solid sphere in a simple shear flow.* (a) Schematics illustrating the closed streamlines in the recirculating region. (b) Picture of an experiment by Cox, Zia & Mason [90], highlighting the recirculation region with a dye released by the sphere.

Relevant diffusivity. Importantly, in this scenario, the slow rate of mixing of the blob is set by the rolling motion, which requires that the viscosity contrast with the bath be maintained. This means that the evolution of the blob given by equations III.11 and III.12 depends on the evolution of the viscosity field. Therefore, even if we track the mixing of a dye that does not diffuse as fast as the viscosity field, the relevant diffusivity to use in these equations is $D = D_\eta$ (it would be $D = D_{\text{dye}}$ only if the dye diffusivity D_{dye} was larger than D_η , see final discussion in Chapter V). Indeed, if viscosity has equilibrated, the liquid is stretched and any content, including dye, will mix rapidly.

In the following we address whether the above limit, of a highly viscous blob diffusing without significantly changing the flow around, could describe the mixing process observed in the *rolling regime*. In particular: is there actually a recirculating region around the blob, given the finite viscosity ratio and the self-similar ellipsoidal shape? If this recirculating region exists, can it explain the various features mentioned above (long mixing time, finite shedding time, etc..) and capture the blob mixing time over the range of viscosity ratios and Péclet numbers investigated?

III.3.3.c Model versus experimental results

To investigate the presence of a recirculating region around the blob, we perform a dedicated experiment with small fluorescent tracers in the bath (PS-FluoRed-Particle of size $2.99 \mu\text{m}$) and a blob of a fairly large viscosity ($\lambda = 30$). We monitor the flow, once the blob has reached the quasi-steady ellipsoidal shape and before shedding occurs. A stack of 100 images is acquired at a large frame rate (5 fps), which are corrected for the minute drifts of the blob to be exactly centered on the blob. By superimposing the images, the assembly of tracers draws the streamlines of the flow in the reference frame of the blob shown in figure III.19a. One clearly observes a recirculating region (highlighted in green), which is very similar, qualitatively, with the recirculation region computed by Cox [90] for solid sphere (see Fig. III.19b).

This experiment validates the presence of a recirculating region around the rolling blob. We now investigate to what extent this region controls the mass transfer rate and the mixing time of the blob. To do so, we follow the mixing of the blob for different Péclet numbers $Pe \in [2 \times 10^2 - 2 \times 10^4]$ for a fairly large viscosity ratio ($\lambda = 30$). The experiments, reported in figure III.20, are performed with blobs of very similar size. This means that the Péclet number is varied by changing only the shear rate and allows

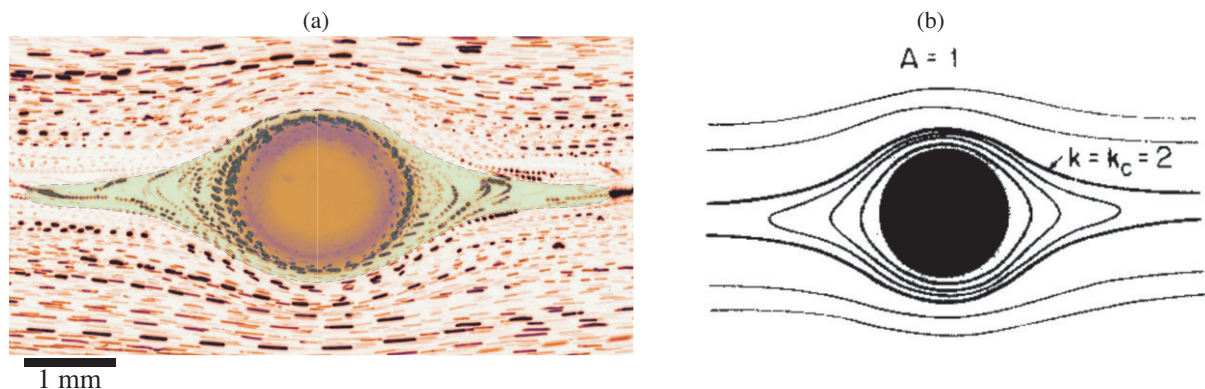


FIGURE III.19: *Mixing in the rolling regime – Evidence of a recirculating region around the blob.* (a) Streamlines around a viscous blob for $\lambda = 30$ obtained by the superimposition of 100 frames when the blob has reached its quasi-steady self-similar shape (before t_{shed}). The recirculating region is highlighted in transparent green. (b) For comparison, theoretical streamlines around a solid sphere in a simple shear flow [122].

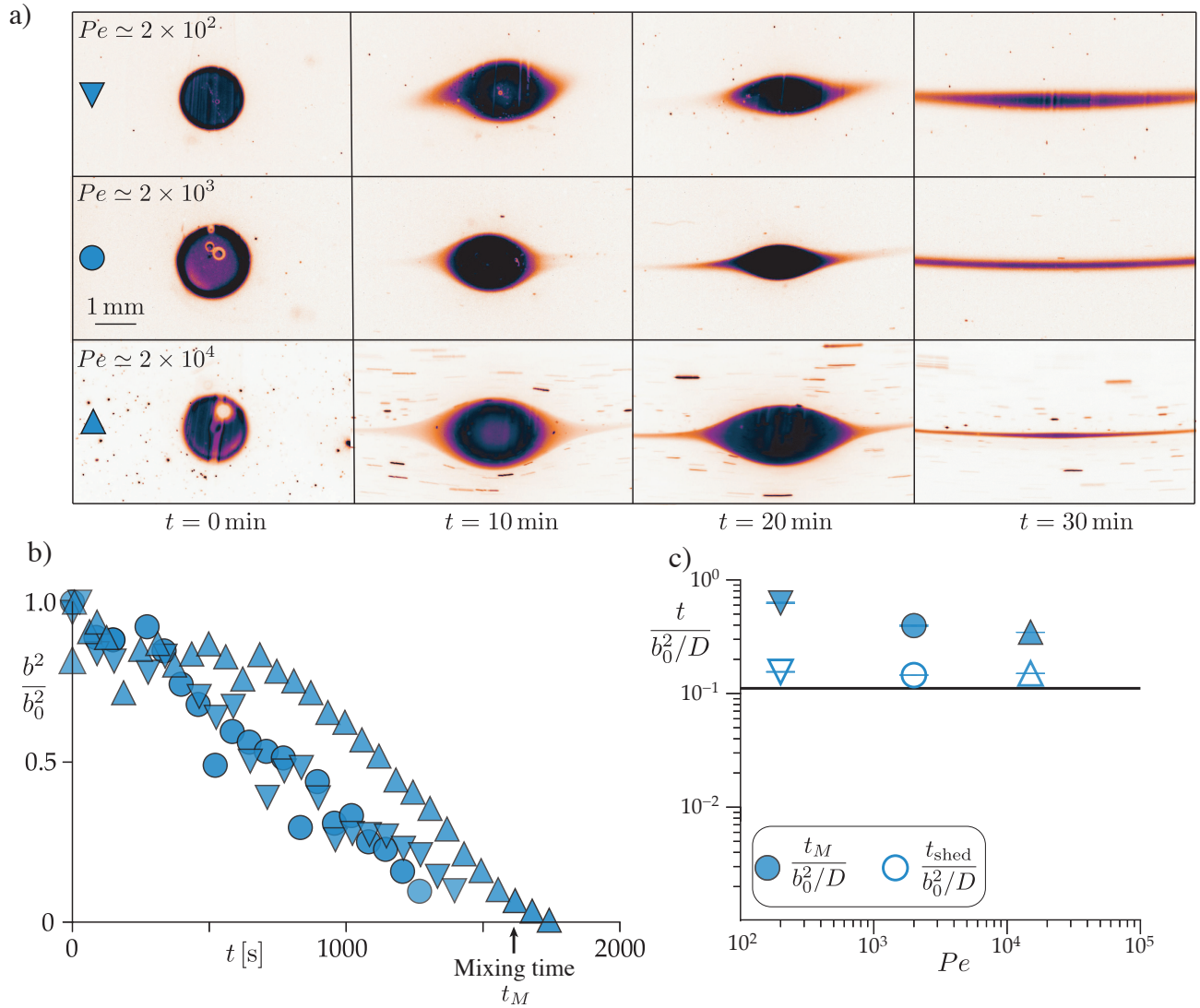


FIGURE III.20: *Mixing in the rolling regime – Shear rate (in-)dependence*. Experiments for different shear rates ($0.03 \text{ s}^{-1} \leq \dot{\gamma} \leq 2.3 \text{ s}^{-1}$) at a fixed viscosity ratio $\lambda = 30$ and similar blob size $b_0 \approx 0.75 \text{ mm}$. (a) Image sequences illustrating the mixing process at different shear rates. (b) Evolution of the squared blob width b^2/b_0^2 versus time, in agreement with the linear decay predicted by Eq. III.11. (c) Normalized mixing time (solid symbols) and shedding time (hollow symbols) versus Pe . Black line: prediction of the mixing time from (Eq. III.12 with $D = D_\eta = 1.65 \times 10^{-10} \text{ m}^2/\text{s}$).

us to test directly the dependence of the mixing time on the stirring strength. The illustrated comparison in figure III.20a is striking. Although the shear rate is varied over two decades, the rate of mixing is found to be similar, and the last bulge formed by the blob disappears almost at the same time for all three experiments. More quantitatively, figure III.20b shows that for all three experiments the squared width b^2/b_0 decays close to linearly with time and that the decay rate is independent of the shear rate, in agreement with the prediction of Eqs. III.11 and III.12. Figure III.20c confirms that the resulting mixing times are essentially independent of the shear rate (with a maximal variation of a factor 2 over the two decades of variation in $\dot{\gamma}$). We however notice a significant offset. The measured mixing time is longer than predicted by the model by a factor 3 to 6. Although we do not fully understand it, two effects could contribute to this offset. First, an overestimation of the diffusion coefficient of the viscosity field, D_η . A measurement of D_η for the same viscosity ratio $\lambda = 30$ would help to confirm that the normalization is correct or not. A second, more interesting, possibility is that the longer mixing time is the signature of an

additional feedback of the diffusion of the viscosity field on the kinematics. When the viscous liquid of the blob diffuses inside the recirculation region, one expects that the flow is updated by the new viscosity field and that the recirculation region would extend slightly further outwards, which would increase the diffusion time across the region and the mixing time of the blob. These hypotheses remain to be tested quantitatively.

We also measured the shedding time t_{shed} , which is reported as hollow symbols in figure III.20c. It is found to be a significant fraction ($\approx \frac{1}{4}$ to $\frac{1}{2}$) of the mixing time and almost independent of the shear rate. This is qualitatively consistent with the general mixing mechanism given above. Shedding is expected once the dye has filled the recirculating region and reached the separatrix with the open-streamlines flow. Since the thickness of the recirculating region is a fraction of the initial blob size b_0 , the onset of shedding is expected at a certain fraction of b_0^2/D , independent of the shear rate and smaller than the mixing time.

We now examine the influence of the viscosity ratio $\lambda \in [5 - 90]$ at a fixed Péclet $Pe = 2 \times 10^3$ (see Fig. III.21). As λ is decreased, the blob shape and internal flow depart more and more from the limit of a solid sphere, and mixing should deviate from the model. In particular, we have seen that the lower λ , the more slender the blob (see a_S/b_S versus λ in Fig. III.17c). This is qualitatively expected to increase the area of the blob, to steepen the concentration gradients across the recirculation region, and, therefore, to shorten the mixing slightly. This picture is qualitatively consistent with the data reported in figure III.21a.

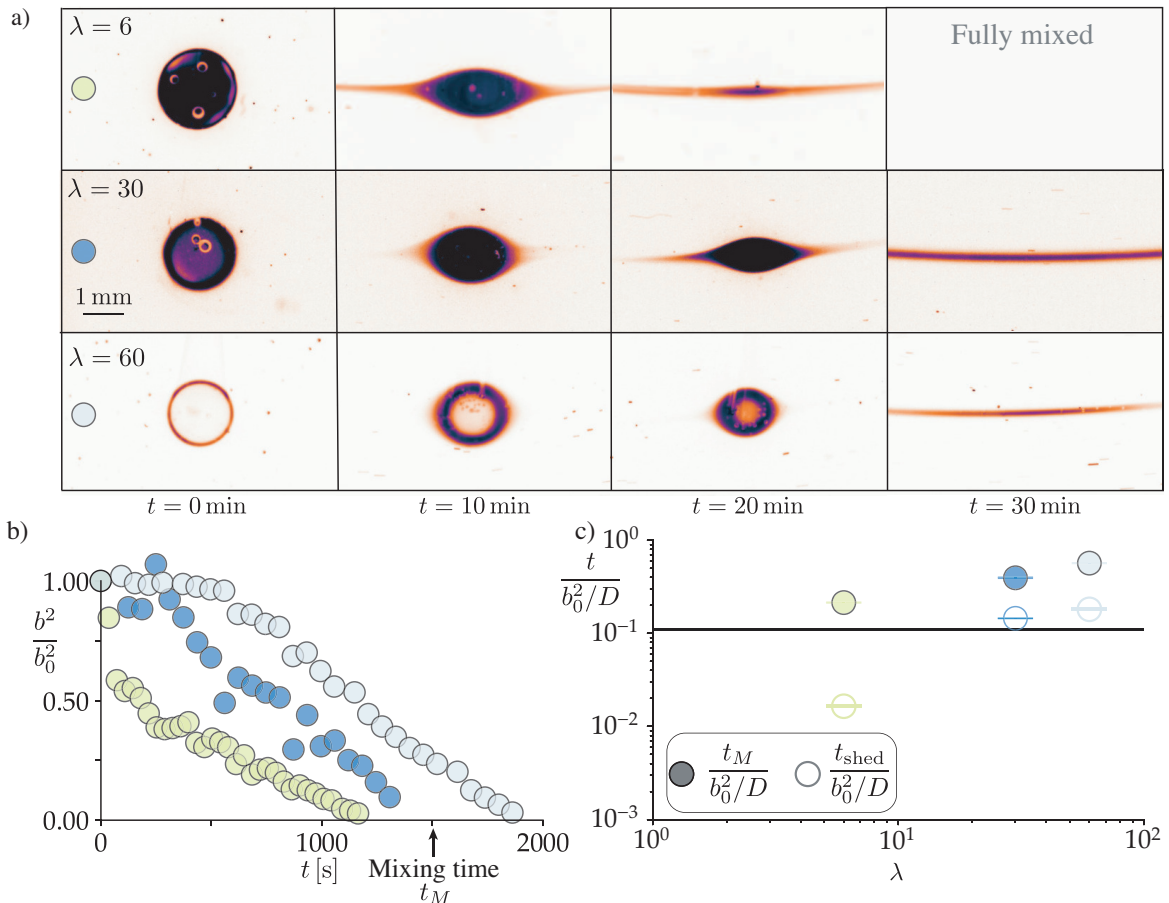


FIGURE III.21: *Mixing in the rolling regime – Viscosity ratio dependence.* Experiments for $\lambda \in [6 - 60]$ at a fixed Péclet $Pe = 2 \times 10^3$. (a) Image sequences illustrating the mixing process for different viscosity ratio λ . (b) Evolution of the squared blob width b^2/b_0^2 versus time, in agreement with the linear decay predicted by Eq. III.11. (c) Normalized mixing time (solid symbols) and shedding time (hollow symbols) versus λ . Red line: prediction of the mixing time from (Eq. III.12 with $D = D_\eta = 1.65 \times 10^{-10} \text{m}^2/\text{s}$).

The blob of viscosity ratio $\lambda = 6$ mixes roughly 3 times faster than the more viscous blobs. Consistently, we see in figure III.21b, that for this low viscosity, b^2/b_0^2 drops rapidly and significantly to the quasi-steady thickness b_S^2/b_0^2 , before decreasing much more slowly with the diffuse linear decay predicted by the model. Altogether, the resulting mixing times shown in III.21c (filled symbols) show only a mild dependence on λ in fair agreement with the model, but with an offset similar to that observed in figure III.20c and already discussed above.

The shedding time, by contrast, shows a much stronger dependence on λ . It becomes shorter than a tenth of the mixing time at $\lambda = 6$ (see hollow symbols in Fig. III.21c). This might be related with the more elongated self-similar shape of the blob (larger a_S/b_S for lower λ), which would tend to decrease the volume of the closed-streamlines region, but this hypothesis has not been tested experimentally.

A last interesting observation can be made for the case $\lambda = 60$ shown in figure III.21a. If the fluorescence yield effect caused difficulties for interpreting the fluorescence signal, it is here particularly useful. For this highly viscous blob, which initially contains a very small amount of water, the fluorescence can be used, thanks to the yield effect, as a *proxi* to indicate how far water molecules from the bath have diffused into the blob. At $t = 0$, the highly viscous core of the blob does not fluoresce (because of the yield effect) and the mixing front, seen as a ring of intense fluorescence, is very thin. As time passes, water diffuses into the blob and the fluorescent ring becomes thicker. However, the core of the blob maintains a very low fluorescence intensity almost until the blob disappears, indicating that not much water has reached the blob center. The core of the blob therefore keeps a large viscosity until the very end of the mixing process and evolves, qualitatively, as a slowly dissolving solid sphere.

III.4 Conclusion

In the present chapter, we have examined experimentally and theoretically the deformation kinematics and the mixing process of a viscous blob in a simple shear flow, for a wide range of viscosity ratios $\lambda \in [0.1 - 90]$ and Péclet numbers $Pe \in [2 \times 10^2 - 6 \times 10^5]$.

Concerning the non-diffusive kinematics ($Pe = \infty$), the transition to a rolling-like motion could be anticipated from the behavior of highly viscous droplets (equivalent to vanishing surface tension), and had been reported for two dimensional [10] and three dimensional [115] viscous blobs. However, we have performed controlled experiments and provided exact analytical results which have allowed us to characterize quantitatively the non-diffusive kinematics over the whole range of viscosity ratio. Three regimes have been identified: the *stretching regime*, where the blob thickness follows $b/b_0 \simeq \beta\gamma^{-1}$ for $\lambda \lesssim 2$, an intermediate *folding regime*, where $b/b_0 \approx \gamma^{-1/2}$ for $\lambda \approx \lambda_c \approx 4$, and the *rolling regime*, where $b/b_0 \approx 1$ for $\lambda \gtrsim \lambda_c$. Based on Eshleby's framework, we have rationalized the dependence to λ of the stretch shift factor β , which determines the long-term thinning in the *stretching regime*, predicted the period and magnitude of the blob oscillations in the *rolling regime*, and determined the precise value of the critical viscosity ratio $\lambda_c \simeq 3.975$ of the kinematic transition. Overall, these observations and modeling provide a complete characterization of the non-diffusive deformation kinematics of an initially spherical blob strained in a simple shear flow.

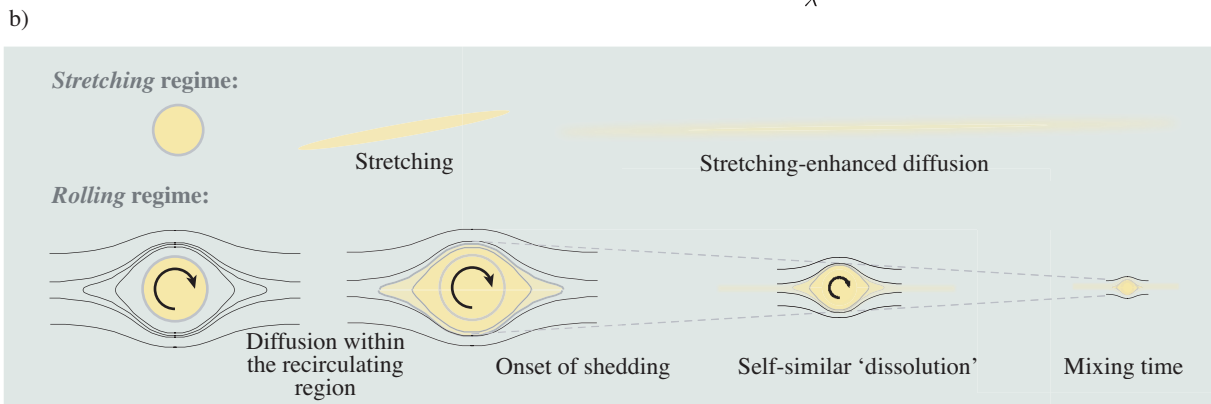
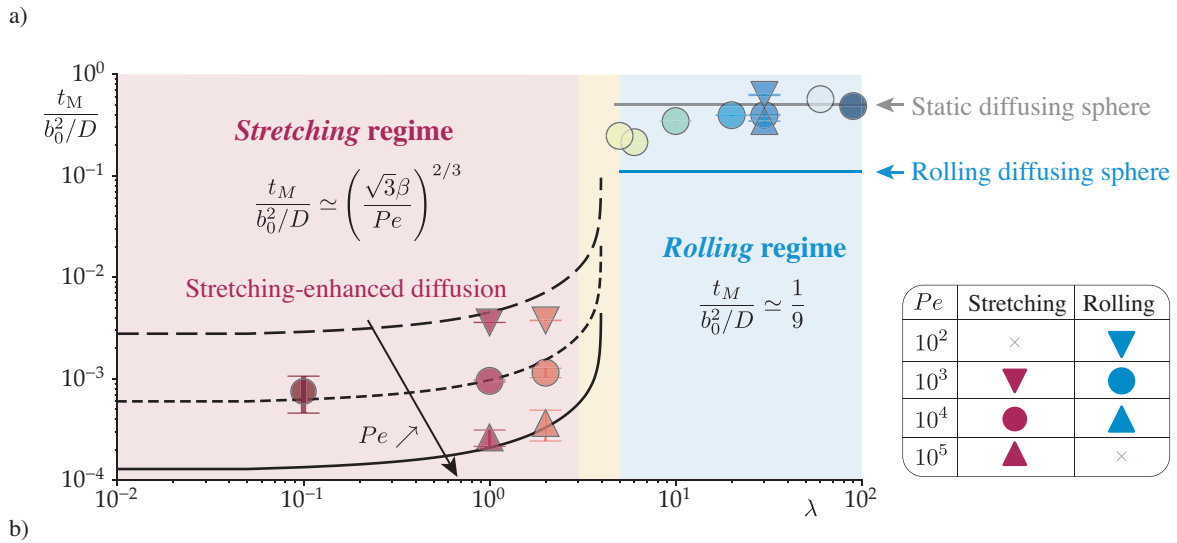


FIGURE III.22: *Mixing in a simple shear flow – Summary of the results.* (a) Normalized mixing time Dt_M/b_0^2 versus viscosity ratio λ for different Péclet numbers (in the stretching regime $D = D_{dye}$, in the rolling regime $D = D_\eta$). (b) Sketch of the mixing processes in the *stretching* and *rolling* regimes.

With this clear kinematics limit at hand, we have tackled the mixing problem. On the ground of systematic experiments for a wide range of viscosity ratios and Péclet numbers, we have documented and modeled the dramatic impact of the viscosity ratio λ on the phenomenology of the mixing process and on the mixing time t_M of the blob. A graphical summary of the main results is presented in figure III.22a. It illustrates how the stretching-to-rolling transition results in a very sharp increase in the mixing time, which is all the more pronounced so that the Péclet number of the flow is large. The large increase in mixing time is the signature of two different mixing processes, which are sketched in figure III.22b:

- In the *stretching* regime, the blob undergoes the classical *stretching-enhanced* diffusion process, which is well captured by extending the Ranz lamellar framework to include the effect of the stretch shift factor β . As shown in figure III.22a the predicted mixing time $Dt_M/b_0^2 = (\sqrt{3}\beta/Pe)^{2/3}$ agrees well with the measurements, in trend and magnitude, for the dependence on both the viscosity ratio and the Péclet number.
- In the *rolling* regime, the rotating blob is surrounded by a recirculating region, which imposes a purely diffusive mass transfer from the blob to the bath. This feature leads to a somehow counterintuitive behavior: the blob mixing time becomes independent of the stirring strength! We have been able to confirm this remarkable property experimentally: as shown in figure III.22a, varying the shear rate over 2 decades (for a fixed blob size) gives a virtually constant mixing time. The temporal evolution of the mixing process in this regime is sketched in figure III.22b. Initially, no shedding is observed and the volume of the blob increases until the dye has filled the recirculating region. From this time on ($t > t_{\text{shed}}$) the content of the blob is slowly shed away and diluted in the bath. Accordingly, the viscous core of the blob decreases in size while maintaining a close to self-similar shape, until it disappears. This phenomenology is similar to the slow dissolution of a solid sphere. By considering a highly viscous blob core ($\lambda \gg 1$) and building on a solution for the quasi-steady transfer rate around a solid sphere in a shear flow by Acrivos [121], we could model the slow diffusive decay of the blob size $b^2/b_0^2 \propto 1 - t/t_M$, with a mixing time $t_M \simeq b_0^2/9D$ independent of the shear rate. Surprisingly, this ‘dissolving sphere’ description holds down to a viscosity ratio $\lambda = 5$ fairly close to the critical value λ_c (see III.22b), which means the transition of the mixing time between the stretching and rolling regimes is very sharp.

What needs to be further explored. The global picture drawn above could be refined in many ways. First, in the rolling regime, the ‘dissolving sphere’ model predicts a normalized mixing time $t_M = b_0^2/9D$. We have experimentally confirmed the independence to the shear rate and captured the magnitude. However, more experiments would be needed to confirm independently the scaling dependance b_0^2 to the blob size. Although smaller spherical blobs are challenging to prepare and manipulate, whereas larger blobs cause sedimentation issues, we believe these experiments could be envisaged. Second, deeper investigations would be required to explore the details of the feedback between diffusion and flow kinematics. This would ideally require a fluorescent tracer that is not biased by the yield effect. Measurements of the intensity field could then be used to study the evolution of the viscosity field inside and around the rolling blob. Also, further exploration of the *folding* regime would be interesting and would require to understand the destabilization of the blob in the substretching regime and the size of the formed sub-blobs.

The results summarized above provide guiding laws to understand mixing of a viscous liquid with nonuniform viscosity. In the strict sense, they apply to a rather idealized flow: that of a simple shear. However, as will be stressed in the final conclusion (Chapter V), it turns out that they are qualitatively relevant for a large class of laminar steady flows (except those which are too close from purely extensional). Naturally, one may wonder about the fate of a viscous blob strained in even more realistic or complex situations, like chaotic flows for instance, which are frequently used to achieve mixing of highly

viscous fluids in industrial applications. In these flows, the direction of stretching is permanently changing and the stretching of material lines is on average exponential [126]. In such flows, would the rolling transition at large viscosity ratios still occur? Would the blob mixing time be significantly delayed when increasing λ as well? What about the recirculating region around the blob observed in a simple shear? Would it be observed too and control the mixing time of the blob? In the following chapter, we propose to address these questions by investigating the kinematics of deformation and the resulting mixing process of viscous blobs in a chaotic laminar flow.

Chapter IV

Mixing in a chaotic flow

This chapter extends the study on the mixing of a spherical blob of a more viscous liquid to the case of a chaotic two-dimensional laminar flow, *i.e.*, when the flow in the bath is varying essentially randomly in space and time around the blob. The control parameters are the same as for the steady simple shear flow investigated in the previous chapters: the viscosity ratio λ , varied between 1 and 124, and the Péclet number Pe , varied between $\sim 10^2$ and $\sim 10^4$. This study has benefited from the huge experimental contribution of Bruno Weber, who has performed the experiments during his 5 month internship at IUSTI. The chapter is organized as follows.

We first introduce the setup and characterize the experimental chaotic flow, in particular, the Lagrangian statistics for the local and instantaneous strain and rotation rates, but also their Lagrangian persistence time and the Lyapounov exponent for a liquid volume advected by the flow. We present experiments for the reference case of an isoviscous blob ($\lambda = 1$), in which the blob is rapidly stretched and mixed, which we validate against the expected mixing behavior for an isoviscous chaotic flow presented in chapter I. We then extend the experiments to viscosity ratios above one. These experiments reveal a kinematics of deformation of the blob with two very different phases: a long initial transient, in which the blob stretches much slower than an isoviscous blob, followed by a fast acceleration of the stretching, which rapidly mixes the blob with the bath. We will see how this two-phase kinematics can be understood from a simple model inspired by the deformation of a viscous blob in a steady extensional flow and how this allows to understand the mixing time and its dependence on the viscosity ratio in the case of moderate to large Péclet numbers. We will also see that, besides the simplification, the model can be legitimized by a more refined stochastic analysis of the average deformation of a viscous blob in a random linear flow with a finite correlation time.

IV.1	Chaotic flow setup	87
IV.2	Base flow characterization & reference isoviscous case	89
IV.2.1	Flow field	89
IV.2.2	Flow statistics	90
IV.2.3	Stretching statistics	91
IV.2.4	The reference isoviscous mixing case	92
IV.3	Kinematics & mixing of a more viscous blob	94
IV.3.1	General observations	94
IV.3.2	Influence of the viscosity ratio	95
IV.3.3	Model of the slow-stretching initial transient (large Pe limit)	96
IV.3.3.a	Large Pe kinematics in a steady extensional flow	96
IV.3.3.b	Heuristic model of the large Pe kinematics in a chaotic flow	98

IV.3.3.c	A more refined stochastic model of the large Pe kinematics in a chaotic flow	98
IV.4	Dependence on Pe & mixing time of the blob	101
IV.4.1	Dependence of the kinematics on Pe	101
IV.4.2	Mixing time of the blob	102
IV.5	Conclusion	104

IV.1 Chaotic flow setup

The experimental setup is sketched in figure IV.1. The bath consists of a 15 mm thick layer of water/polymer solution with a viscosity of $\eta = 0.3 \text{ Pa s}$, which is floated on a thinner layer of an inviscid immiscible oil (Fluorinert) in a square PMMA container with a width of 20 mm. The walls of the container around the Fluorinert layer are coated with a hydrophobic tape to obtain a flat meniscus between the oil and the bath. Like for the shear flow setup, this configuration ensures a two-dimensional flow in the bath. The flow is set by the cyclic stirring motion of a 6 mm cylindrical rod made of PMMA and placed vertically across the bath. The rod rotates with a constant speed about its axis while translating horizontally along a modified '8-shaped' cyclic path (see below). A spherical blob of a different viscosity is prepared and inserted in the bath with the same techniques as in the previous chapters. The flow in the bath and the deformation of the blob are visualized with the same PLIF technique. The horizontal uniform laser sheet is obtained with a 2.5 W laser beam of wavelength 532 nm (MGL-F-532) passing through a Powell lens (a laser-line-generating lens from ThorLabs), which is focussed vertically with a semicircular lens to achieve a sheet thickness of $\approx 24 \mu\text{m}$. Images are taken from the bottom of the cell through the same high-pass filter used in the shear cell to block direct reflections of the laser light. The coupling of camera (Hamamatsu ORCA-Flash4.0 C11440) and lens (Sigma MACRO 180 mm DG HSM) gives a resolution of $15 \mu\text{m}/\text{pix}$. The setup is mounted on a vertical translation stage (not shown in the schematics) to allow manual control of the laser sheet height in the bath.

The cyclic stirring motion of the rod is sketched in figure IV.1(b). It essentially consists of two 8-shape paths, at right angle to each other, which are stretched towards the corners of the container to follow the walls. This particular stirring motion has been chosen because the path intersects itself repeatedly, which is known to yield an efficient chaotic stirring [42, 43]. A small rotation of the rod is added to avoid a direct contact between the rod and the bob. The minimal distance between the rod and the wall ($\approx 8b_0$) is chosen to ensure that the blob is not squeezed between the rod and the wall, nor trapped for a long time in a corner of the container with low deformation rates. The same stirring motion can be realized at different rates by changing the translation and rotation speeds proportionally. Importantly, since the Reynolds number of the flow is kept much below one ($\rho[V + D\Omega]D/\eta \lesssim 0.02$, with V , Ω and D the velocity, rotation rate and diameter of the rod, respectively), the flow is expected to be the same at all rates, *i.e.*, with the same chaoticity, patterns, correlations, statistics of deformation etc... All deformation

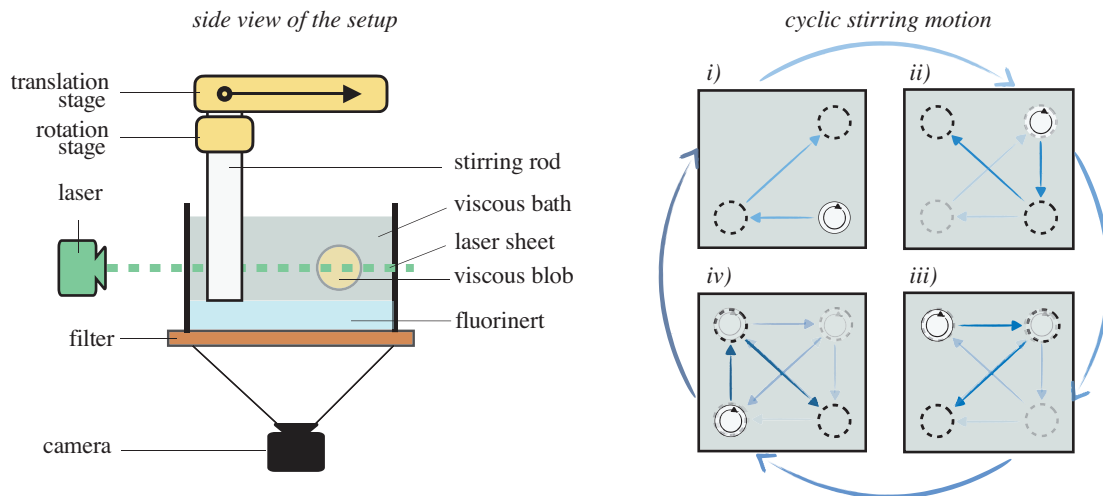


FIGURE IV.1: *Experimental setup and stirring protocol of the chaotic flow.* (a) Side view schematics of the setup. (b) Top view schematics of the cyclic motion of the rod in the bath, producing the chaotic laminar flow.

rates are expected to vary proportionally with the average strain rate $\langle \dot{\epsilon} \rangle$, which can be varied between 0.04 and 2.2 s^{-1} (see §IV.2 for further characterizations), while all flow times will vary like $\langle \dot{\epsilon} \rangle^{-1}$.

IV.2 Base flow characterization & reference isoviscous case

Before addressing the mixing problem, we need to characterize the chaotic flow obtained with our experimental setup. We follow the same approach as in Souzy *et al.* [68]. We measure the chaotic velocity field from particle image velocimetry techniques and obtain the relevant features and statistics of the flow from the numerical advection of virtual tracer particles in the experimental velocity field. In particular, we will characterize the Lagrangian statistics of the deformation rates, as well as the persistence time of the deformation, the stretching statistics and the Lyapunov exponent for a piece of material line advected by the flow.

IV.2.1 Flow field

The two-dimensional velocity field $\{u(x, y, t), v(x, y, t)\}$ is characterized with particle imaging velocimetry (PIV) in the mid-plane of the bath and for one specific stirring rate (rod velocity) corresponding to $\langle \dot{\epsilon} \rangle \simeq 0.087 \text{ s}^{-1}$. For this characterization, the bath is replaced by a different fluid (Triton X, a hydrophilic surfactant), which has the same viscosity as the bath used for the mixing experiment ($\eta = 0.3 \text{ Pa s}$) and the same refractive index as the stirring rod ($n = 1.49$). The index matching avoids shadow effects by the rod and allows us to visualize the whole flow, including next to the rod, at all times. The bath is seeded with a minute quantity of micrometer-sized fluorescent particles (PS-FluoRed-particles with diameter $\simeq 2.99 \mu\text{m}$), which are passively advected by the flow. The PIV routine is adapted from a Matlab script developed by Meunier & Leweke [127], which obtains the velocity field by iterative runs of image cross-correlation (see also §II.3.2.b). One velocity field with a spatial resolution of $\approx 0.3 \text{ mm}$ is obtained every 0.05 s, which corresponds to ≈ 4400 velocity fields over the whole cycle of the rod motion. A small sample of a typical velocity field is shown in figure IV.2b. Only one fourth of the whole cycle is actually characterized, since the whole cycle is the repetition of sub-cycles (labeled i, ii, iii and iv in Fig. IV.1b), which are identical within a simple symmetry transformation.

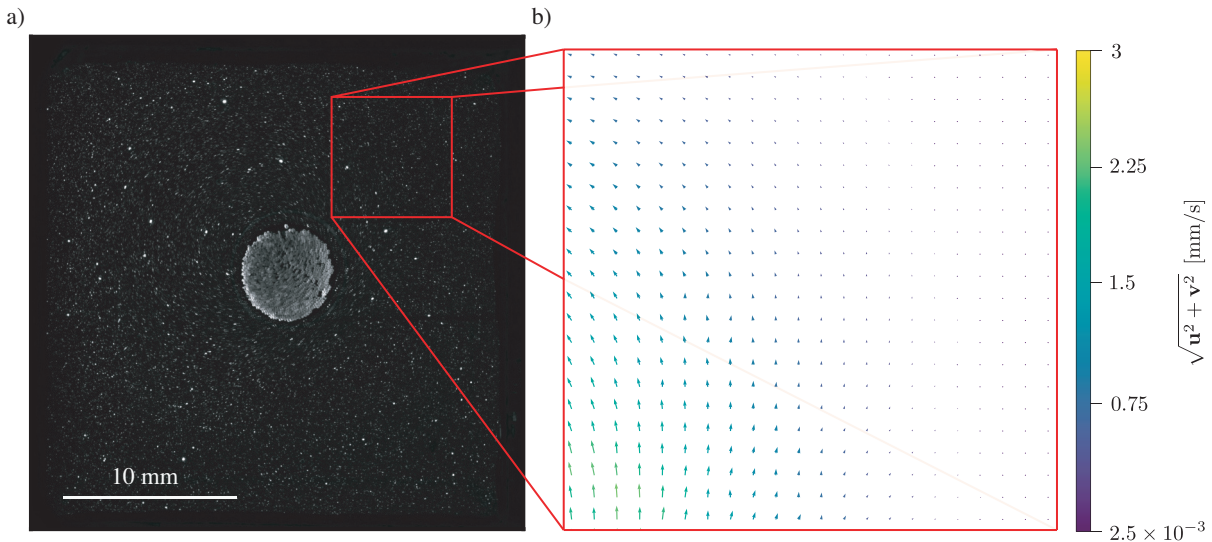


FIGURE IV.2: *Characterization of the flow field.* (a) Picture of the liquid slice illuminated by the laser sheet. The bright spots are the seeding particles used to track the flow, the bright disk in the center is the stirring rod. (b) A small portion of the instantaneous velocity field obtained from the PIV ($\langle \dot{\epsilon} \rangle = 0.087 \text{ s}^{-1}$).

IV.2.2 Flow statistics

To obtain the Lagrangian statistics of the experimental flow field we numerically advect nine virtual particles initially placed at random positions $\{x_p, y_p\}$ in the plane. Each particle is advected according to the local velocity of the flow as

$$\dot{x}_p(t) = u(x_p(t), y_p(t), t), \quad \dot{y}_p(t) = v(x_p(t), y_p(t), t).$$

Figure IV.3a shows the trajectory of the particles, whose initial condition is marked with a circle, computed over 5 cycles. Each of the trajectories explores and therefore samples the entire flow domain.

At each time and for each particle we compute the local velocity gradient, from which we extract the local (positive) strain rate, the local rotation rate and the orientation of the main strain direction defined, respectively, by

$$\dot{\epsilon} = \sqrt{-\frac{\partial u}{\partial x} \frac{\partial v}{\partial y} + \frac{1}{4} \left(\frac{\partial u}{\partial y} + \frac{\partial v}{\partial x} \right)^2}, \quad \omega = \frac{1}{2} \left(\frac{\partial v}{\partial x} - \frac{\partial u}{\partial y} \right), \quad \text{and} \quad \varphi = \arctan \frac{\mathbf{e} \cdot \mathbf{e}_y}{\mathbf{e} \cdot \mathbf{e}_x},$$

with \mathbf{e} the eigen vector for the main (positive) strain. The probability distribution functions of these quantities are plotted in figure IV.3b-d. We systematically compute their average, $\langle \chi \rangle$, and standard deviation, $\sigma_\chi = \sqrt{\langle \chi^2 \rangle - \langle \chi \rangle^2}$, where χ represents one of the three variables. These correspond to time averages since the sampling is performed with a fixed time interval.

The strain rate $\dot{\epsilon}$, which is always positive with our definition, is taken as the reference for the rate of the flow and all other quantities will be discussed relative to its average value $\langle \dot{\epsilon} \rangle$ ($= 0.087 \text{ s}^{-1}$ for the stirring velocity used for characterizing the flow). Its relative standard deviation $\sigma_{\dot{\epsilon}} / \langle \dot{\epsilon} \rangle \simeq 1.11$ is close to 1, which indicates that $\dot{\epsilon}$ does not have an abnormally large tail distribution. The distribution for the vorticity is found to be close to symmetric relative to $\omega = 0$ ($\langle \omega \rangle / \langle \dot{\epsilon} \rangle \simeq 0.14$), indicating that

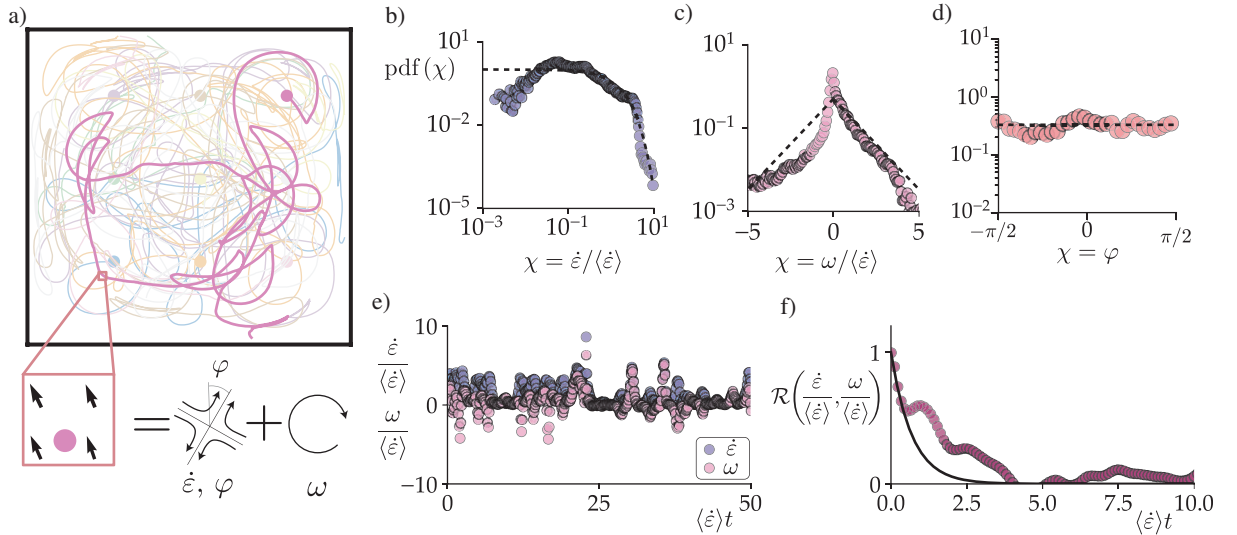


FIGURE IV.3: *Lagrangian one-point statistics.* (a) Typical Lagrangian trajectories computed from the experimental velocity field. Circles: initial position of the advected particles. Solid lines: trajectories over 5 cycles, see text. (b-c-d) Lagrangian probability distribution functions for the strain rate $\dot{\epsilon}$, the rotation rate ω and the orientation of the main strain axis φ . Circles: data. Dashed line: model distributions used for the simulation of the blob deformation in a random flow: $\text{pdf}(\dot{\epsilon}/\langle \dot{\epsilon} \rangle) = e^{-\dot{\epsilon}/\langle \dot{\epsilon} \rangle}$, $\text{pdf}(\omega/\langle \dot{\epsilon} \rangle) = e^{-|\omega|/\langle \dot{\epsilon} \rangle}/2$, $\text{pdf}(\varphi) = 1/\pi$ (see §IV.2.2 and Appendix A). (e) Typical temporal evolution of the strain and rotation rates experienced by an advected particle. (f) Lagrangian cross-correlation function between the local strain rate and the rotation rate indicating a correlation time $\langle \dot{\epsilon} \rangle \tau \approx 0.7$.

positive and negative rotation direction are close to equally likely. The magnitude of the vorticity is therefore essentially given by the relative value $\sigma_\omega / \langle \dot{\epsilon} \rangle \simeq 1.12$, which is close to the value for σ_ϵ . Last, the distribution of φ is found to be flat indicating that orientation is fully random between $-\pi/2$ and $\pi/2$. Given the symmetry, the relative magnitudes and the relative variances of $\dot{\epsilon}$, ω and φ , the distribution of these three quantities is actually well approximated by the simple exponential and flat functions plotted in Fig. IV.3b-d. These approximate distributions will be used below to model the stochastic deformation of a viscous blob in a random flow.

Besides the magnitudes and amplitudes of variation of the strain and vorticity, a crucial quantity of the chaotic flow is the persistence time of the local flow experienced by an advected particle, in particular the Lagrangian persistence times of $\dot{\epsilon}$, ω and φ , which express how fast the local flow around the particle varies. Figure IV.3e shows a typical temporal evolution of the strain rate magnitude $\dot{\epsilon}$ and vorticity ω experienced by an advected particle. The persistence time can be estimated from the cross-correlation function between $\dot{\epsilon}$ and ω , which is represented in Figure IV.3f. The relative decorrelation time (obtained by fitting an exponential decay) is found to be of the order of the inverse mean strain rate ($\langle \dot{\epsilon} \rangle \tau \simeq 0.7$). This quantity will turn to be important to model the stochastic deformation of the blob.

IV.2.3 Stretching statistics

To summarize the global effects of the variability, coupling, and persistence of the local flow around an advected fluid particle, we compute the stretching history of a fluid line in the chaotic flow. In practice we advect numerically very short segments (pairs of close particles) of initial length $\ell(0)$ in the velocity field and monitor their stretching in the limit when the segments remain short enough to probe the actual stretching of a continuous line in the flow [68, 70, 128]. Each pair has an initially random position and orientation in the flow and the advection is performed over height full stirring cycles. To ensure that the segments remain short enough, they are split in two each time their length has doubled, and one half is discarded to keep the total number of advected segments constants. This refinement method allows us to keep track of the entire strain history without overburdening the computation. By counting the number j of divisions, the actual elongation of the segment is recovered from $\rho(t) = 2^j \ell(t) / \ell(0)$ (see figure IV.4b). Each segment experiences a different stretching history depending on its initial position and orientation. To probe the whole flow and obtain statistically converged distributions, the advection is performed for 10^3 segments.

Figure IV.4c-d presents the time evolution of the statistics of the elongation. Since the lengths typically grow exponentially, we actually use the logarithm of the elongation $\ln \rho$. The average and variance of $\ln \rho$ are plotted in Fig. IV.4c. They both grow linearly with time (with a variance typically twice as large as the mean), as expected for a chaotic flow. The long time evolution of the mean $\langle \ln \rho \rangle$ defines the dimensionless Lyapounov exponent of the flow

$$\kappa \equiv \frac{\langle \ln(\rho) \rangle}{\langle \dot{\epsilon} \rangle t} \simeq 0.17. \quad (\text{IV.1})$$

This dimensionless Lyapounov exponent represents the effective stretching rate $\langle \dot{\rho} / \rho \rangle$ in the chaotic flow relative to the mean strain rate $\langle \dot{\epsilon} \rangle$, which sets the long time average $\langle \ln(\rho) \rangle = e^{\kappa \langle \dot{\epsilon} \rangle t}$. It can be seen as a measurement of the asymmetry between the amplitude of the stretching events ($\dot{\rho} / \rho > 0$) and of the compressive events ($\dot{\rho} / \rho < 0$) for a line advected in the chaotic flow. The value $\kappa \simeq 0.17$ is consistent with the fairly long persistence time and indicates that the flow is highly chaotic.

Besides the mean value and variance, the distribution of $\langle \ln(\rho) \rangle$ is found to converge to normal distributions (see Fig. IV.4d). This confirms that the chaotic flow actually achieves a random multiplicative process for the length of material lines, where the current elongation ρ is the product of the uncorrelated

elongation factors ρ_i accumulated over the sequence of uncorrelated stretching or compression events (with typical duration τ) the line has gone through.

All these characterizations refers to the chaotic flow in the absence of blob. They are, of course, directly useful to understand the stretching of an isoviscous blob, which does not change the flow, but they will also be crucial to understand the evolution of the local ‘outer’ flow that a viscous blob experiences as it is stirred in the chaotic setup.

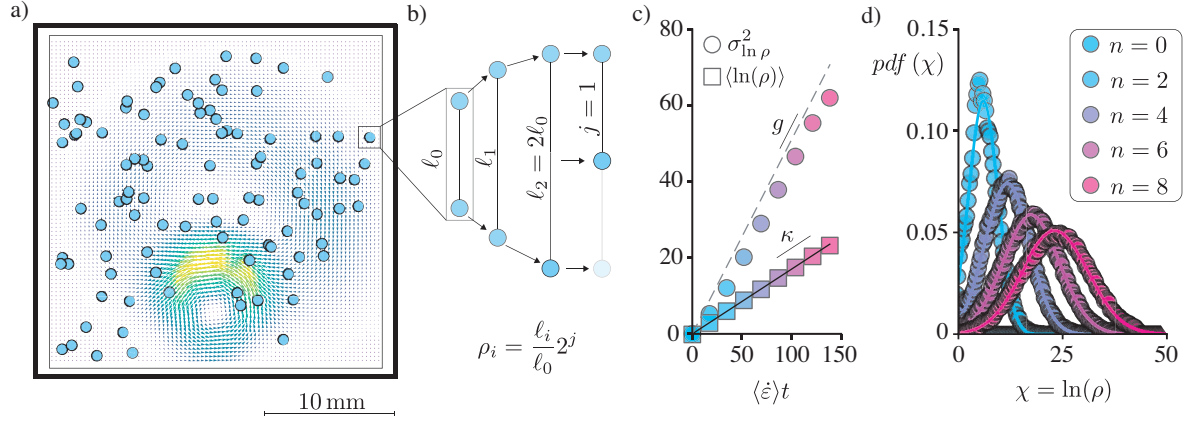


FIGURE IV.4: *Lagrangian stretching statistics*. (a) Typical velocity field showing the pairs of advected particles (circles). (b) Schematics of the refinement method allowing to resolve the stretching factor ρ of infinitely short segments, see text. (c) Variance (circles) and mean (squares) of $\ln(\rho)$ versus strain. Solid line: linear fit of $\langle \ln(\rho) \rangle$ defining the Lyapunov exponent $\kappa = \langle \ln(\rho) \rangle / \langle \dot{\epsilon} \rangle t$. Dashed line: linear fit of the variance. (d) Probability distribution function of $\ln(\rho)$ (the color indicates the number n of cycles that have been completed).

IV.2.4 The reference isoviscous mixing case

As a reference case for the mixing of a more viscous blob, we consider, first, the mixing of a dyed isoviscous blob in the chaotic flow. We use the freezing and melting protocol to prepare a quasi-spherical blob of size $b_0 = 0.85$ mm, which we randomly position in the bath, and we select the stirring velocity to obtain a fairly large Péclet number $Pe = b_0^2 \langle \dot{\epsilon} \rangle / D_{\text{dye}} = 3.1 \times 10^4$. The typical evolution of the blob is illustrated in figure IV.5a. As the rod stirs the bath, the blob is advected and stretched by the flow into a longer and longer (thinner and thinner) lamella, which is eventually mixed with the bath by molecular diffusion to yield a uniform mixture, as can be appreciated from the uniform dye concentration displayed in the last panel.

Figures IV.5b-c present the evolution of the blob maximal width and of the maximal dye concentration during the mixing process (they are obtained as the average value between the two thickest portion of the lamella observed at each time, as illustrated in Fig. IV.5a.ii). On average, the blob is found to thin down with a rate close to the isoviscous mean stretching rate $\kappa \langle \dot{\epsilon} \rangle$, which is indicated with a black dashed line. By contrast, the maximal concentration is found to remain fairly constant for a few tens of seconds until it decays very rapidly when molecular diffusion actually homogenizes the concentration. The decay is found to be close to the expected onset of mixing (indicated by a vertical line in Fig. IV.5b-c)

$$t_{M,\text{iso}} \simeq \frac{\ln(2\kappa Pe)}{2\kappa \langle \dot{\epsilon} \rangle} \simeq 63 \text{ s}, \quad (\text{IV.2})$$

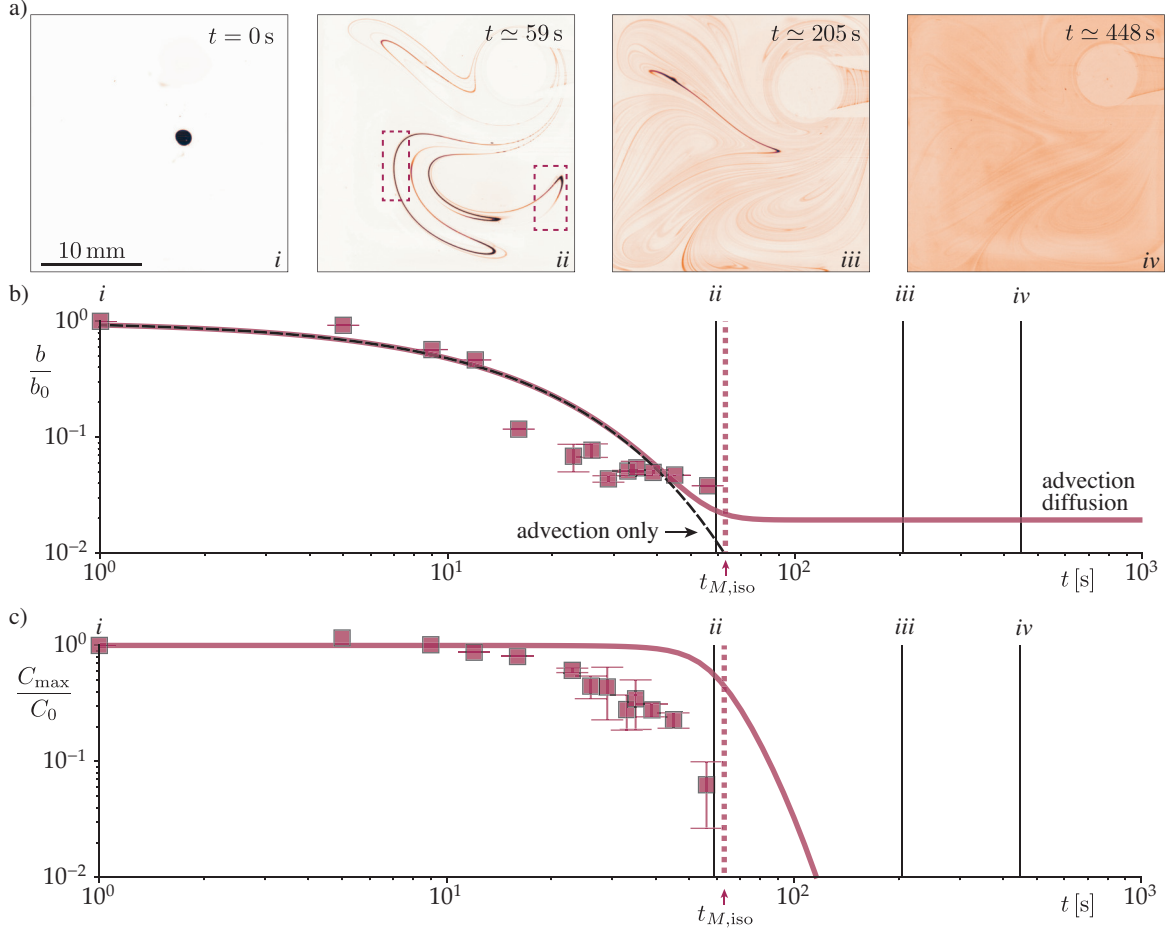


FIGURE IV.5: Reference case of an isoviscous blob. (a) Snapshots illustrating the typical evolution of the mixing process in the isoviscous case ($\lambda = 1$, $\langle \dot{\epsilon} \rangle \simeq 0.43 \text{ s}^{-1}$, $Pe = b_0^2 \langle \dot{\epsilon} \rangle / D_{\text{dye}} \simeq 3.1 \times 10^4$). Dashed rectangles: portions of the blob where the maximal width and maximal concentration are measured. (b) Normalized blob width versus time. (c) Normalized maximal concentration versus time. Symbols indicate the average over the 2 thickest portions of the lamella. Solid red line: expectation based on the quantitative characterization of the flow (Eq. IV.3, the black dashed line indicates the purely advective evolution $b/b_0 = e^{-\kappa \langle \dot{\epsilon} \rangle t}$). Dashed red line: expected mixing time $t_{M,\text{iso}} = \ln(2\kappa Pe) / (2\kappa \langle \dot{\epsilon} \rangle)$.

which has been derived in the introduction (§I.2.3.c, Eq. I.26) for a mean-field lamella stretched with a constant exponential rate $\kappa \langle \dot{\epsilon} \rangle$. The complete mean-field solution for the evolution of b and C_{max} (considering both advection and diffusion)

$$\frac{b}{b_0} = \frac{\sqrt{1+2\mathcal{T}}}{e^{\kappa \langle \dot{\epsilon} \rangle t}}, \quad \frac{C_{\text{max}}}{C_0} = \frac{1}{\sqrt{1+2\mathcal{T}}}, \quad \text{with } \mathcal{T} = \frac{e^{2\kappa \langle \dot{\epsilon} \rangle t} - 1}{2\kappa Pe}, \quad (\text{IV.3})$$

is also shown in figure IV.5b-c, where it is found to capture the evolution of the two quantities.

This agreement confirms that the mixing process for an isoviscous blob is typically well described by the mean-field approximation of a lamella that is stretched with a constant rate equal to the Lyapounov exponent $\kappa \langle \dot{\epsilon} \rangle$.

IV.3 Kinematics & mixing of a more viscous blob

We now consider the case when the blob is more viscous than the bath. Before varying the viscosity contrast with the bath systematically, we will present observations for a large viscosity ratio ($\lambda \sim 10^2$), which highlights the very different phenomenology by which mixing proceeds when the blob is highly viscous. These observations will motivate a simple model for the deformation kinematics of the blob, which will be legitimated against a more refined stochastic model and used to interpret the observed dependence of the mixing time on the viscosity ratio and on the Péclet number.

IV.3.1 General observations

We start with an experiment at the largest viscosity ratio investigated $\lambda = 124$, for the same stirring velocity as in the isoviscous case presented above (the mean strain rate is $\langle \dot{\epsilon} \rangle \simeq 0.43 \text{ s}^{-1}$). The typical phenomenology of deformation and mixing of the blob is illustrated in figure IV.6a. The first obvious difference with the isoviscous case is that the mixing of the more viscous blob is largely delayed. Whereas the isoviscous blob has been dramatically stretched and is almost entirely mixed within 3 min (panel *iv* in Fig. IV.5a), the more viscous blob has not stretched much and is still far from being mixed after more than 10 min of stirring (panel *iii* in Fig. IV.6a). However, at longer times the evolution of the blob seems to be much faster: only 4 min later (panel *v*) the blob has dramatically stretched and is almost entirely mixed. This suggests that the deformation kinematics for the more viscous blob is not only quantitatively different from the isoviscous case, but also *qualitatively* different.

To precise the above observations, we report in figure IV.6b the evolution of the maximal width b of the blob versus time. For comparison, we also indicate the effective thinning kinematics for the isoviscous

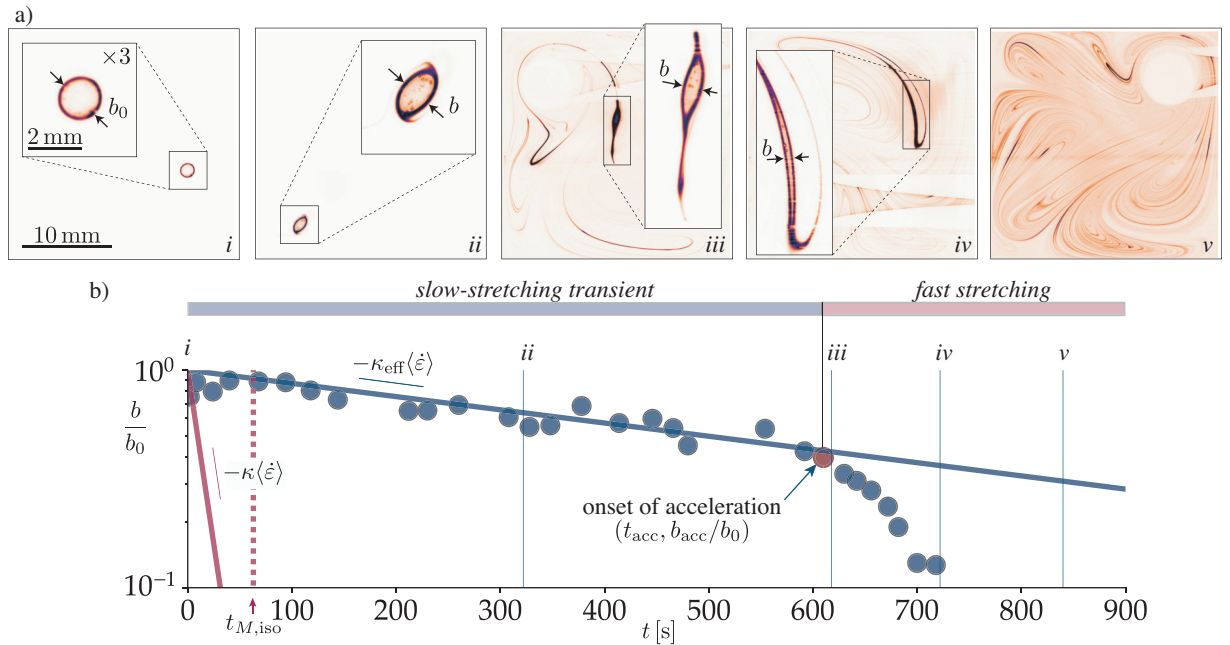


FIGURE IV.6: *Phenomenology of the mixing for an highly viscous blob.* (a) Snapshots illustrating the typical evolution of the mixing process for $\lambda = 124$ (same stirring rate as in the isoviscous case (Fig. IV.5): $\langle \dot{\epsilon} \rangle \simeq 0.43 \text{ s}^{-1}$, $Pe = b_0^2 \langle \dot{\epsilon} \rangle / D_\eta = 1.7 \times 10^3$). Inserts: close-up view of the blob. (b) Normalized blob width versus time. Symbols: measurements. The red circle indicates the onset of the acceleration between the initial *slow-stretching transient*, when the blob stretches much slower than an isoviscous liquid, and the late *fast stretching*, when the isoviscous stretching rate is recovered. Red lines: isoviscous stretching kinematics (solid) and isoviscous mixing time (dashed). Solid line: exponential fit over the slow-stretching transient defining κ_{eff} .

case, $b/b_0 = e^{-\kappa\langle\dot{\epsilon}\rangle t}$, and the isoviscous mixing time, $t_{M,iso}$. The measurements confirm the qualitatively different kinematics. By contrast with the isoviscous case, where the blob is stretched with a close to constant and fast effective rate, the more viscous blob is found to experience successively two highly different stretching kinematics:

- First, an initial *slow-stretching transient* (panels *i* to *iii*), when the blob thins only very little and with an effective rate $\kappa_{eff}\langle\dot{\epsilon}\rangle$ much lower than the isoviscous blob (in the present case $\kappa_{eff}\langle\dot{\epsilon}\rangle \simeq 1.2 \times 10^{-3}$, whereas $\kappa\langle\dot{\epsilon}\rangle \simeq 0.07$). Over this initial transient, which lasts much longer than the isoviscous mixing time $t_{M,iso}$ (over 600 s in the present case, versus $t_{M,iso} \sim 60$ s), no significant mixing of the blob is observed.
- Second, a subsequent *fast stretching* (panels *iv* to *v*), when the thinning of the blob accelerates dramatically towards rates much closer to the isoviscous rate $\kappa\langle\dot{\epsilon}\rangle$. In this last stage, the blob stretches very significantly, which rapidly achieves a complete mixing with the bath.

As illustrated in figure IV.7a, this two-phase kinematics is robustly observed when the experiment is repeated. The blob systematically experiences a slow stretching initial transient and a fast stretching late stage. Moreover, in spite of the slightly different initial conditions and the slightly different history of stretching of each blob, which are inherent to the chaotic flow, the initial effective thinning rate, $\kappa_{eff}\langle\dot{\epsilon}\rangle$, and the time t_{acc} and blob width b_{acc} , at the onset of the fast stretching, are found to keep similar values between the different repetitions of the experiment.

IV.3.2 Influence of the viscosity ratio

The two-phase kinematics is also observed for a lower viscosity ratio. Figure IV.7b presents the thinning kinematics measured for blobs with $\lambda = 8, 20, 50$ and 124. The distinction between a slow early transient and a much faster thinning at large times is observed systematically. However, the onset time of the fast stretching t_{acc} is significantly reduced as λ is decreased, whereas the blob width b_{acc} at this onset time is found to be changed much less, which suggests that the initial thinning rate decreases significantly with decreasing λ .

These trends can be made quantitative by extracting systematically the effective thinning rate, $\kappa_{eff}\langle\dot{\epsilon}\rangle$, as well as the time, t_{acc} , and maximal width of the blob, b_{acc} , at the onset of the fast stretching. The measurements are reported in figure IV.8. The effective thinning rate is indeed decreasing with increasing value of λ , down to typically a hundredth of the isoviscous rate at $\lambda = 124$. The blob width at the onset of the acceleration b_{acc}/b_0 is not varying much with λ , remaining between approximately 0.7 and 0.8 over

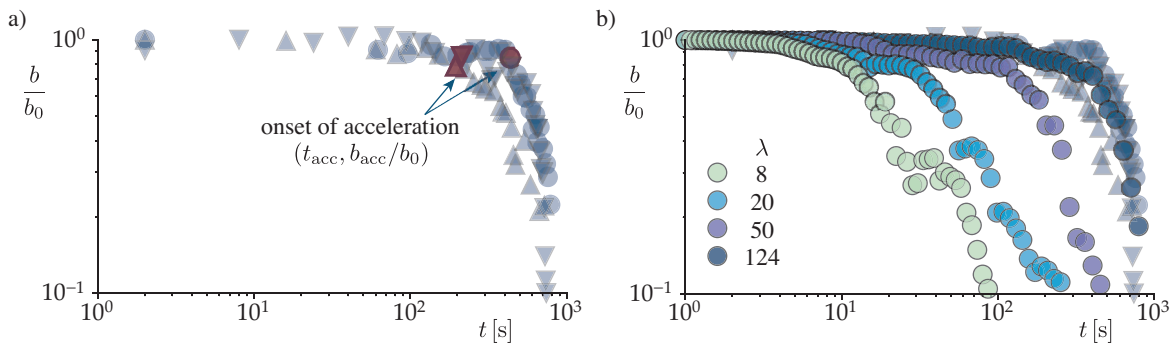


FIGURE IV.7: *Stretching kinematics of a viscous blob.* (a) Normalized blob width b/b_0 versus time for three different realization of the experiment ($\lambda = 124$, $\langle\dot{\epsilon}\rangle \simeq 0.43 \text{ s}^{-1}$, each run has a different symbol shape). The red symbols indicate the onset of the acceleration defining t_{acc} and b_{acc} . (b) Evolution of the blob width for different viscosity ratio λ . Symbols represent the geometric mean over 2 runs ($\lambda = 8$), 3 runs ($\lambda = 20$ and 124), or 5 runs ($\lambda = 50$).

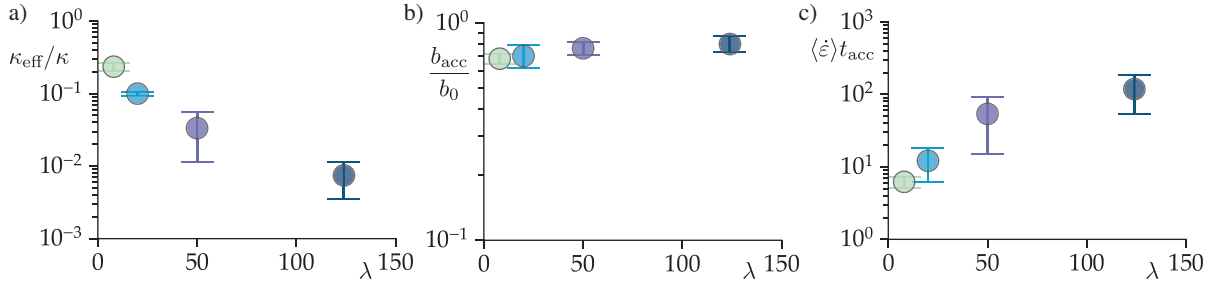


FIGURE IV.8: *Initial thinning rate and onset of the fast stretching.* (a) Thinning rate of the blob in the slow-stretching transient versus viscosity ratio λ (the value $\kappa_{\text{eff}}(\dot{\epsilon})$ is normalized by the isoviscous thinning rate $\kappa(\dot{\epsilon})$, $Pe = 1.7 \times 10^3$, $\langle \dot{\epsilon} \rangle \simeq 0.43 \text{ s}^{-1}$). (b) Blob width at the onset of the fast stretching versus λ . (c) Onset time of the fast stretching versus λ . Errorbars: standard deviation over realizations.

the range investigated. Last, the onset time of the acceleration increases significantly with the viscosity ratio, from $\langle \dot{\epsilon} \rangle t_{\text{acc}} \approx 6$ at $\lambda = 8$ to $\langle \dot{\epsilon} \rangle t_{\text{acc}} \approx 120$ at $\lambda = 124$.

The observations detailed above indicate that the eventual mixing of the blob is strongly delayed when the blob viscosity is increased, and that the delay is directly related with the initial slow-stretching transient, during which the blob does not mix significantly with the bath. This means, first, that to understand the actual mixing time, the slow-stretching transient and its duration have to be understood. Second, this suggests that the slow-stretching transient is actually an intrinsically kinematic transient, which is not set by the diffusion between the blob and the bath (in the limit when the Péclet number is large enough). The next step is, therefore, to model the slow-stretching transient and to understand its dependence on the viscosity ratio.

IV.3.3 Model of the slow-stretching initial transient (large Pe limit)

To describe the slow initial transient we need to model the deformation kinematics of a viscous blob ($\lambda > 1$) in the chaotic flow in the limit when the Péclet number is very large. This kinematics depends on the characteristics of the flow, and it is stochastic by essence, since the flow is chaotic. Of course, it also depends on both the viscosity and the current shape of the blob, which determine, together, how and how fast the blob is deformed by the current velocity field in the bath. The exact kinematics depends subtly on the coupling between these two aspects (variability of the flow and deformation response of the blob). However, it turns out that if the stirring flow around the blob is considered as a (random) sequence of arbitrary linear two-dimensional flows, the two aspects decouple. Indeed, in this case, the blob always evolves through the exact same family of shapes, which is the same it would experience in a steady extensional flow, whereas the details of the flow history only determines how fast and how much ‘back and forth’ the blob evolves through the family of shapes.

This observation allows a tremendous simplification of the modeling and it indicates that the reference case of the stretching in a steady extensional flow should be analyzed first. Once this reference kinematics is understood, we will see that a simple heuristic model capturing most trends of the kinematics can be easily established. We will then present a more involved stochastic model, which supports the simple heuristic argument and precises the dependence on the flow characteristics in the limit of sufficiently short correlation times and sufficiently large viscosity of the blob.

IV.3.3.a Large Pe kinematics in a steady extensional flow

We consider, for now, the deformation of an initially spherical viscous blob ($\lambda > 1$) in a steady extensional flow with strain rate $\dot{\epsilon}$. The kinematics is set by the exact same viscous formalism as used in §III.2.2.

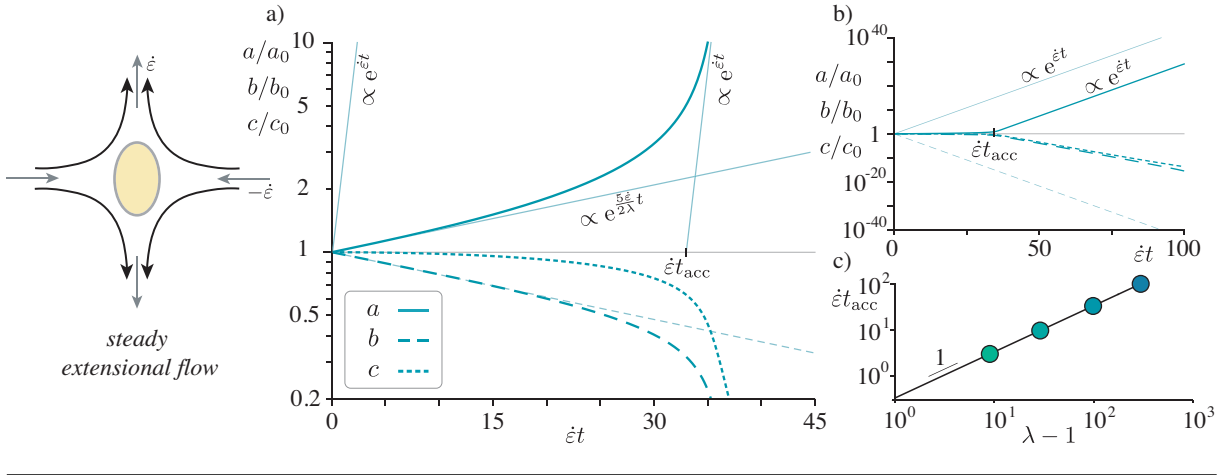


FIGURE IV.9: The stretching kinematics of a viscous blob in a steady extensional flow gives the key to the fast stretching onset in a chaotic flow. (a-b) Time evolution of the three dimensions of the blob for a viscosity ratio $\lambda = 100$. Thick lines: numerical integration of Eq. IV.4. Thin lines: initial stretching rate given by the limit case of a sphere (Eq. IV.4). (c) Onset time of the stretching acceleration as a function of the viscosity ratio. The solid line is Eq. IV.6.

Starting from the equations for the simple shear case, those for the extensional case are obtained by replacing the strain rate $\dot{\gamma}/2$ by $\dot{\epsilon}$, the rotation rate $\dot{\gamma}/2$ by 0, and by realizing that the blob is initially aligned with the extensional direction (since it is a sphere) and, therefore, remains aligned at all times. This yields:

$$\frac{\dot{a}}{a} = \mathcal{A}\left(\frac{a}{b}, \frac{b}{c}, \lambda\right) \dot{\epsilon}, \quad \frac{\dot{b}}{b} = -\mathcal{B}\left(\frac{a}{b}, \frac{b}{c}, \lambda\right) \dot{\epsilon}, \quad \frac{\dot{c}}{c} = -\frac{\dot{a}}{a} - \frac{\dot{b}}{b}, \quad (\text{IV.4})$$

with \mathcal{A} and \mathcal{B} the functions already defined in Eq. III.5. In the isoviscous case one has $\mathcal{A} = \mathcal{B} = 1$ and the blob width follows $b/b_0 = e^{-\dot{\epsilon}t}$. This is also the behavior recovered for a viscous blob which is sufficiently slender ($\mathcal{A}, \mathcal{B}\left(\frac{a}{b}, \frac{b}{c}, \lambda\right) \xrightarrow{a/b, b/c \gg 1} 1$), which means that a viscous blob will eventually thin down with the isoviscous rate $\dot{\epsilon}$ at long time.

However, for a viscous blob ($\lambda > 1$) the initial evolution is much slower. As long as the blob shape is close to spherical, the deformation rate remains close to the limit for a sphere $\mathcal{A} = \mathcal{B} = \Lambda^{-1}$ derived by Taylor [87], which means that the blob width initially follows:

$$\frac{\dot{b}}{b_0} \simeq e^{-\frac{1}{\Lambda}\dot{\epsilon}t}, \quad \text{with } \Lambda = 1 + \frac{2}{5}(\lambda - 1), \quad \text{for } t \lesssim t_{\text{acc,steady}}. \quad (\text{IV.5})$$

This initial thinning rate is typically slower than the long term rate by a factor Λ , which scales with the viscosity ratio λ for large values of λ . This low rate persists until the blob shape has significantly deviated from a sphere, which occurs after a typical time $t_{\text{acc,steady}} \sim \Lambda \dot{\epsilon}^{-1}$, which defines the onset of the acceleration to the long time (isoviscous) rate.

A more precise estimate of $t_{\text{acc,steady}}$ can be obtained by numerically integrating the system IV.4. The evolution of the blob dimensions a, b, c is represented in figure IV.9a, for a viscosity ratio $\lambda = 100$. The onset time $t_{\text{acc,steady}}$ is obtained from the time shift of the long time stretching stage (see Fig. IV.9b). Figure IV.9c presents the evolution of $t_{\text{acc,steady}}$ with λ , which is found to be very close to

$$t_{\text{acc,steady}} \simeq \frac{1}{\dot{\epsilon}} \frac{\lambda - 1}{3}. \quad (\text{IV.6})$$

At this time the blob width is found to be close to

$$b_{\text{acc,steady}} \approx e^{-1}. \quad (\text{IV.7})$$

IV.3.3.b Heuristic model of the large Pe kinematics in a chaotic flow

From the above understanding of the deformation kinematics in a steady extensional flow, we can propose a simple heuristic model for the initial slow transient stage in a chaotic flow.

The model is based on the idea that for a given local flow in the bath, a viscous blob thins down slower than an isoviscous blob by a certain factor $\mathcal{B}(\lambda, \frac{a}{b}, \frac{b}{c})$ (see Eq. IV.4), which only depends on the viscosity and the current aspect ratios of the blob. This is true, not only for a steady extensional flow, but for all linear flows. So, by seeing our chaotic flow as a random sequence of linear flows (with a certain persistence time), we can expect that the effective thinning rate of a viscous blob in the chaotic flow, $\kappa_{\text{eff}}\langle\dot{\epsilon}\rangle$, is related to the thinning rate for an isoviscous blob in the same flow, $\kappa\langle\dot{\epsilon}\rangle$, through a factor which is also close to $\mathcal{B}(\lambda, \frac{a}{b}, \frac{b}{c})$. From the picture of the kinematics in the extensional flow given by Eqs. IV.5 to IV.7, this implies that the blob in the chaotic flow will initially thins down as

$$\frac{b}{b_0} \approx e^{-\kappa_{\text{eff}}\langle\dot{\epsilon}\rangle t}, \quad \text{with} \quad \kappa_{\text{eff}} = \frac{\kappa}{\Lambda} \sim \frac{5}{2} \frac{\kappa}{\lambda}, \quad (\text{IV.8})$$

until the blob width has typically decreased to

$$b_{\text{acc}} \approx e^{-1}, \quad (\text{IV.9})$$

at a time close to

$$t_{\text{acc}} \approx \frac{1}{\kappa\langle\dot{\epsilon}\rangle} \frac{\lambda - 1}{3}, \quad (\text{IV.10})$$

which defines the onset of the fast stretching.

Before justifying better this heuristic model and discussing some of its limitations in the next section, it is worth comparing it to the experimental observations. Figure IV.10 compares the predictions of Eqs. IV.8-IV.10 to the set of data obtained for the different viscosity ratios ($\lambda = 8, 20, 50$ and 124). As shown in panels (a) and (b), the model captures well the initial thinning rate of the blob and in particular its strong decrease when λ is increased, although the observed thinning rate seems to be slightly lower than predicted for very large values of λ . The model is also consistent with the experimental observation that the blob width at the onset of the stretching acceleration does not vary much with λ (Fig. IV.10c). Last, the model recovers both the magnitude of the onset time of the fast stretching, and its large dependence on the blob viscosity (Fig. IV.10d).

IV.3.3.c A more refined stochastic model of the large Pe kinematics in a chaotic flow

To legitimate the heuristic model, discuss its limitations, but also explicit the dependence to the characteristics of the flow, we present now a more refined model of the blob kinematics in a chaotic flow, which resolves the stochastic nature of the process.

The idea of the model is to consider that as the viscous blob is advected by and through the chaotic flow, it experiences rapidly changing flow conditions (see Fig. IV.11). In the close neighborhood of the blob, these changing flow conditions can be considered as a continuous and randomly varying succession of linear flows, with statistics given by the statistics of the chaotic flow. For the sake of keeping the discussion simple without losing generality, we model these continuous change as sketched in figure

IV.11b, i.e., as a sequence of short random linear flow periods, with a fixed duration τ , no correlation between successive periods, and full correlation within each of them. For each period i the strain rate in the bath, $\dot{\epsilon}_i$, the rotation rate in the bath, ω_i , and initial orientation of the strain direction, φ_i , are randomly sorted from the model distribution of $\dot{\epsilon}$, ω and θ obtained from the isoviscous flow characterization (see Fig. IV.11c). This implies that during each period the blob deformation and orientation evolves through

$$\begin{aligned} \frac{\dot{a}}{a} &= \mathcal{A}\left(\frac{a}{b}, \frac{b}{c}, \lambda\right) \cos 2\varphi \dot{\epsilon}_i, & \frac{\dot{b}}{b} &= -\mathcal{B}\left(\frac{a}{b}, \frac{b}{c}, \lambda\right) \cos 2\varphi \dot{\epsilon}_i, \\ \frac{\dot{c}}{b} &= -\frac{\dot{a}}{a} - \frac{\dot{b}}{b}, & \dot{\varphi} &= \omega_i - \mathcal{F}\left(\frac{a}{b}, \frac{b}{c}, \lambda\right) \sin 2\varphi \dot{\epsilon}_i, \end{aligned} \quad (\text{IV.11})$$

which generalizes the system for a purely extensional flow to the arbitrary linear flow set by $\dot{\epsilon}_i$, ω_i and the evolving orientation of the blob relative to the main strain direction φ .

The system IV.11 couples non trivially, the blob viscosity (λ), the current flow ($\dot{\epsilon}_i$, ω_i), with its variability ($\text{pdf}(\dot{\epsilon}_i)$, $\text{pdf}(\omega_i)$) and its persistence time (τ), as well as the current shape and orientation of the blob (a/b , b/c , φ). Yet, in the limit we are interested in, where the correlation strain scale of the blob $\sim \dot{\epsilon}\tau/\lambda$ is small, the problem becomes much simpler. By averaging over the statistics of $\dot{\epsilon}_i$ and ω_i , the initial orientations of the blob φ_i , and over the duration τ of each period, the system IV.11 can be recasted at first order into the following mean field evolution equations (see derivation in Appendix A)

$$\frac{1}{a} \frac{\partial a}{\partial T} = \mathcal{A}\left(\frac{a}{b}, \frac{b}{c}, \lambda\right), \quad \frac{1}{b} \frac{\partial b}{\partial T} = -\mathcal{B}\left(\frac{a}{b}, \frac{b}{c}, \lambda\right), \quad (\text{IV.12})$$

which are exactly analog to those for a viscous blob in an extensional flow, except for the rate of evolution, which is set by the following relation between the real time t and the warped time T

$$\frac{\partial t}{\partial T} = \frac{2}{\langle \dot{\epsilon}^2 \rangle \tau} \frac{1}{\mathcal{F}\left(\frac{a}{b}, \frac{b}{c}, \lambda\right)}. \quad (\text{IV.13})$$

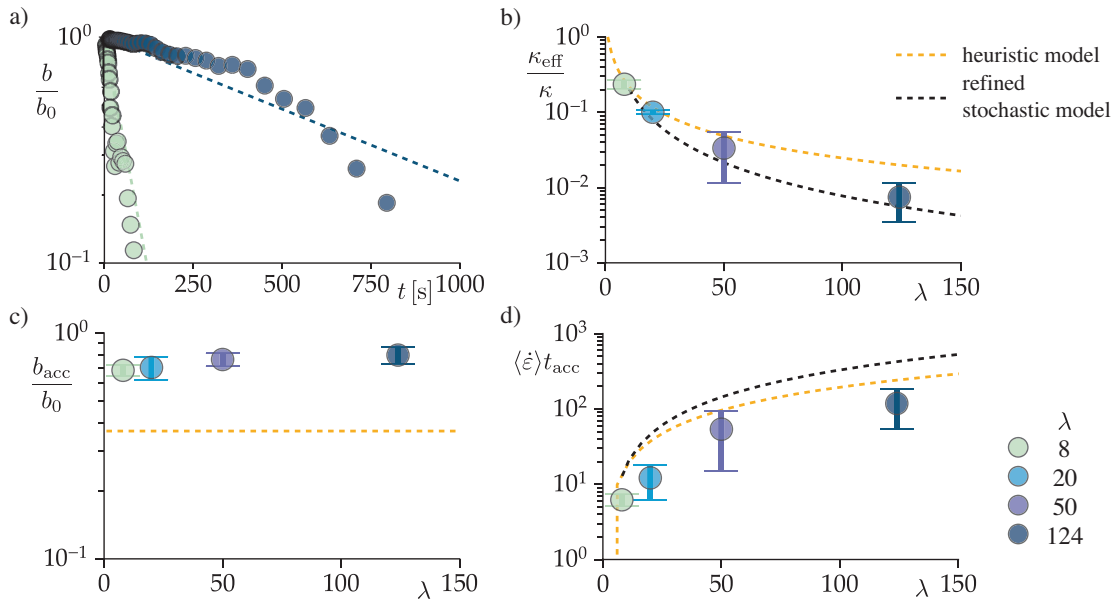


FIGURE IV.10: Comparison between model and experiments. (a) Normalized blob width versus time for $\lambda = 8$ and 124. (b) Initial thinning rate versus λ . (c,d) Blob width and time at the onset of the fast stretching versus λ . Symbols: measurements (same data as in Figs. IV.7 and IV.8). Orange dashed lines: heuristic model (Eqs. IV.8, IV.9 and IV.10). Black dashed lines: refined stochastic model (Eqs. IV.15 and IV.16).

The interest of Eqs. IV.12 and IV.13 is twofold. First, it stresses the separate influence of the slow-stretching transient obtained for a steady flow (given by IV.12) and of the additional slow down of the stretching due to the back and forth deformation imposed by the chaotic flow (given by IV.12, which also depends on the viscosity through the rate of re-alignment of the blob with the flow). Second, it makes an explicit link with the (isoviscous) Lyapounov exponent of the flow, which can be shown to be (see Appendix A)

$$\kappa = \frac{1}{2} \frac{\langle \dot{\epsilon}^2 \rangle \tau}{\langle \dot{\epsilon} \rangle}. \quad (\text{IV.14})$$

This relation is important because it provides additional predictive dependence to the characteristics of the chaotic flow.

Last, first order developments of Eqs. IV.12 and IV.13 valid for the case of large viscosity ratio (see Appendix A), show that the initial effective thinning rate is not exactly $\kappa_{\text{eff}} = \kappa/\Lambda$, as supposed heuristically, but is in fact closer to

$$\kappa_{\text{eff}} \simeq \frac{2\kappa}{\Lambda^{3/2}} \simeq \frac{5^{3/2}}{2^{3/2}} \frac{\langle \dot{\epsilon}^2 \rangle \tau}{\langle \dot{\epsilon} \rangle} \lambda^{-3/2}, \quad (\text{IV.15})$$

because of the subtle coupling between the shearing and reorientation of the blob (the \mathcal{F} term in Eq. IV.13). This refined expression for κ_{eff} is compared to the data in figure IV.10b, where it is found to fit the data better. However, the numerical resolution of Eqs. IV.12 and IV.13 (which is also validated against brute force simulations of the exact system IV.11 on a large number of random history and without assuming a short correlation time, see Appendix A) confirms that the onset time of the fast stretching, given by the following expression

$$t_{\text{acc}} \simeq \left(1 + \frac{3 \ln \frac{\Lambda}{4}}{10}\right) \frac{\lambda - 1}{3 \kappa \langle \dot{\epsilon} \rangle} \simeq \frac{1}{3} \frac{1}{\langle \dot{\epsilon}^2 \rangle \tau} \lambda, \quad (\text{IV.16})$$

is essentially equal to the expression obtained from the heuristic model (the logarithmic correction being very small in practice over the range of viscosity ratio investigated, see comparison in Fig. IV.10d).

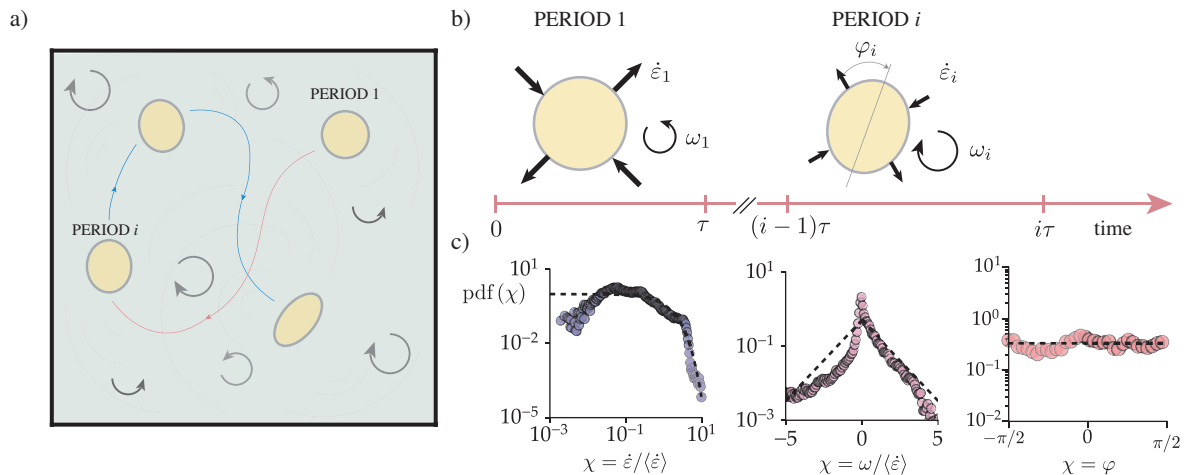


FIGURE IV.11: Modeling of the chaotic flow in the bath by a random sequence of linear flows. (a) Schematics of the blob advection by and through the chaotic flow. (b) The flow experienced by the blob is modeled as a sequence of random linear flow periods, with a fixed duration τ , no correlation between successive periods, and full correlation within each of them. (c) For each period i the strain rate in the bath, $\dot{\epsilon}_i$, the rotation rate in the bath, ω_i , and initial orientation of the strain direction, φ_i , are randomly sorted from the model distribution (dashed lines) of $\dot{\epsilon}$, ω and φ obtained from the isoviscous flow characterization (see §IV.2).

IV.4 Dependence on Pe & mixing time of the blob

So far, we have focussed much of the discussion on the blob deformation, for a fixed and large Péclet number $Pe = 1.7 \times 10^3$, and in particular on the initial slow-stretching transient observed for high viscosity ratios. But, of course, this specific two-phase kinematics has a direct consequence on the eventual mixing of the blob, and it may also be expected to be influenced, to some extent, by the mixing process itself.

IV.4.1 Dependence of the kinematics on Pe

To investigate these effects, we perform additional experiments where we vary systematically the Péclet number Pe between $\simeq 1.7 \times 10^2$ and $\simeq 8.4 \times 10^3$, by varying the stirring rate ($\langle \dot{\epsilon} \rangle$ varied between 0.04 s^{-1} and 2.2 s^{-1}), in the case when the viscosity ratio is large ($\lambda = 124$). Importantly, this variation is achieved with the exact same stirring protocol and keeping a low Reynolds number (see §IV.2), which means that the chaotic flow preserves the exact same features (in particular the value of κ), while all rates are simply scaled proportionally with $Pe \propto \langle \dot{\epsilon} \rangle$.

The evolution of the thinning of the blob for the different values of Pe is presented in figure IV.12a. It confirms that the two-phase kinematics, with an initial slow-stretching transient followed by a sharp acceleration toward the late fast stretching, is observed for all Péclet numbers. To characterize the slow-stretching transient, we report in panel (b) the initial effective thinning rate $\kappa_{\text{eff}}(\dot{\epsilon})$ relative to the isoviscous rate $\kappa(\dot{\epsilon})$. We see that the ratio $\kappa_{\text{eff}}/\kappa$ is not exactly constant, but actually accelerates, relative to the large Péclet number prediction (dashed line), for the smallest value of Pe . This suggests that small diffusive effects, which tend to decrease the viscosity in the blob, accelerates the stretching of the blob relative to the large Pe case.

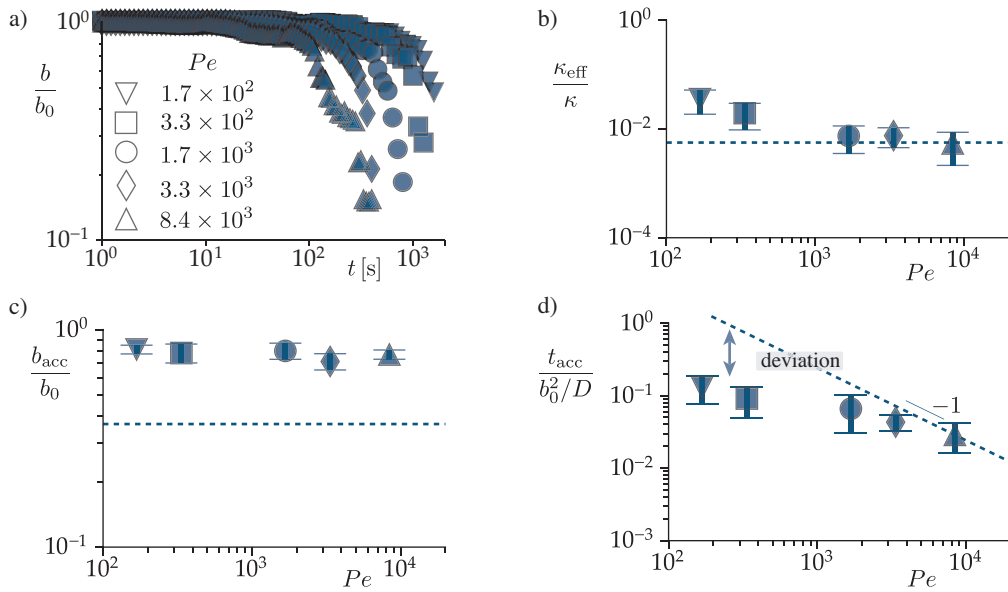


FIGURE IV.12: Comparison between model and experiments for different Péclet number ($\lambda = 124$). (a) Normalized blob width versus time. (b) Initial thinning rate versus Pe . (c,d) Blob width and time at the onset of the fast stretching versus Pe . Symbols: measurements (geometric mean between the runs, errorbars indicate the standard deviation). Blue dashed lines: refined stochastic model (Eqs. IV.15, IV.9 and IV.16).

Consistently, figure IV.12d shows that the onset time of the fast stretching t_{acc} is systematically shortened relative to the large Péclet limit $t_{\text{acc}} \simeq \frac{\lambda}{3\kappa\langle\dot{\epsilon}\rangle}$ (blue dashed line), whereas the value of b_{acc} is not found to vary much with Pe (Fig. IV.12c).

IV.4.2 Mixing time of the blob

The set of observations and characterizations presented above stress crucial points about the kinematics of the blob. The viscosity contrast between the blob and the bath is responsible for a delay before the chaotic stirring flow achieves a significant and very rapid thinning of the blob at a rate close to the isoviscous rate $\kappa\langle\dot{\epsilon}\rangle$. The more viscous the blob, the larger the delay ($t_{\text{acc}} \sim \lambda/\kappa\langle\dot{\epsilon}\rangle$) and the sharper the transition to the fast stretching. This means that, in the limit when the Péclet number is large enough so that the initial slow-stretching transient is not significantly influenced by Pe , one expects that the mixing time of the blob follows

$$t_{\text{M}} \approx t_{\text{acc}} + t_{M,\text{iso}} \simeq \frac{\lambda - 1}{3\kappa\langle\dot{\epsilon}\rangle} + \frac{\ln(2\kappa Pe)}{2\kappa\langle\dot{\epsilon}\rangle}, \quad \text{for } Pe \gg Pe_c, \quad (\text{IV.17})$$

because the stretch before t_{acc} is negligible at large Pe . The expression for Pe_c will be given below. Importantly, for a chaotic flow $t_{M,\text{iso}} = \frac{\ln(2\kappa Pe)}{2\kappa\langle\dot{\epsilon}\rangle}$ is only a few times the characteristic time scale $(\kappa\langle\dot{\epsilon}\rangle)^{-1}$, even at fairly large Péclet numbers, because of the exponential stretching of material lines. Therefore, even for moderate viscosity ratio ($\lambda \gtrsim \ln \kappa Pe$) the delay t_{acc} is in practice much longer than $t_{M,\text{iso}}$, which implies

$$t_{\text{M}} \approx t_{\text{acc}} \simeq \frac{\lambda - 1}{3\kappa\langle\dot{\epsilon}\rangle}, \quad \text{for } Pe \gg Pe_c, \quad \text{and } \lambda \gtrsim \frac{3}{2} \ln(2\kappa Pe). \quad (\text{IV.18})$$

Crucially, in this limit, which we call *delayed stretching regime of mixing*, the mixing time is virtually independent of the diffusivity D , because the latter only changes the duration of the very short terminal mixing time ($t_{M,\text{iso}}$).

As specified above, the limit of equation IV.18 is expected to be valid only if there is no significant effects of diffusion during the slow-stretching transient, otherwise the viscosity in the blob is decreased before t_{acc} and the delay t_{acc} is decreased relative to the large Péclet limit (as observed in practice for the smallest Péclet numbers investigated experimentally, see §IV.4.1). The transition between the two regimes of mixing is expected to occur typically when the large Péclet limit of t_{acc} compares with the mixing time of an essentially unstretched blob in the flow $t_{M,\text{unstretched}}$. Assuming, as a crude estimate, that this latter time is similar to the mixing time of a rolling blob in a simple shear flow, the transition is expected for

$$t_{M,\text{unstretched}} \simeq \frac{b_0^2}{9D} \approx t_{\text{acc}} \simeq \frac{\lambda - 1}{3\kappa\langle\dot{\epsilon}\rangle},$$

which give the critical Péclet number between the two regimes

$$Pe_c \approx \frac{3(\lambda - 1)}{\kappa}, \quad (\text{IV.19})$$

below which the mixing time is expected to follow the mixing time for an hardly stretched blob

$$t_{\text{M}} \approx t_{M,\text{unstretched}} \approx \frac{b_0^2}{9D}, \quad \text{for } Pe \ll Pe_c. \quad (\text{IV.20})$$

We call, this latter regime *unstretched regime of mixing*.

These two regimes of mixing are compared to all the experiments performed with the chaotic flow. Figure IV.13 reports the onset of the fast stretching t_{acc} , which is always a good proxy for the actual mixing

time for the range of viscosity ratios and Péclet numbers considered here ($\lambda \gtrsim \frac{3}{2} \ln(2\kappa Pe)$). The value of t_{acc} is non-dimensionalized by b_0^2/D , with $D = D_\eta$ the diffusivity of the viscosity field, which is relevant in the present case where the mixing of the blob is slaved to the evolution of the viscosity field. In these scales, the large Pe limit ($Pe \gg Pe_c$, Eq. IV.18) shows as $Dt_{\text{acc}}/b_0^2 \propto \lambda/Pe$ (dashed colored lines). The low Pe limit ($Pe \ll Pe_c$, Eq. IV.19) shows as a unique horizontal line (dashed grey). At large Péclet number ($Pe \sim 10^4$, $\lambda = 124$), t_{acc} is found to be close to the large Pe limit. At lower Péclet numbers ($Pe \lesssim 10^3$, $\lambda = 124$), it is found to deviate from the Pe^{-1} line, and get close to the $\frac{1}{9}$ of the low Pe limit. Last, as already discussed above, the measurements for the different λ at rather large Pe are found to follow the $t_M \propto \lambda$ trend predicted by the large Pe limit. This indicates that the simple two-limit model based on the detailed study of the kinematics (Eqs. IV.18-IV.19) captures both the magnitude and the trends of the observed mixing time with λ and Pe .

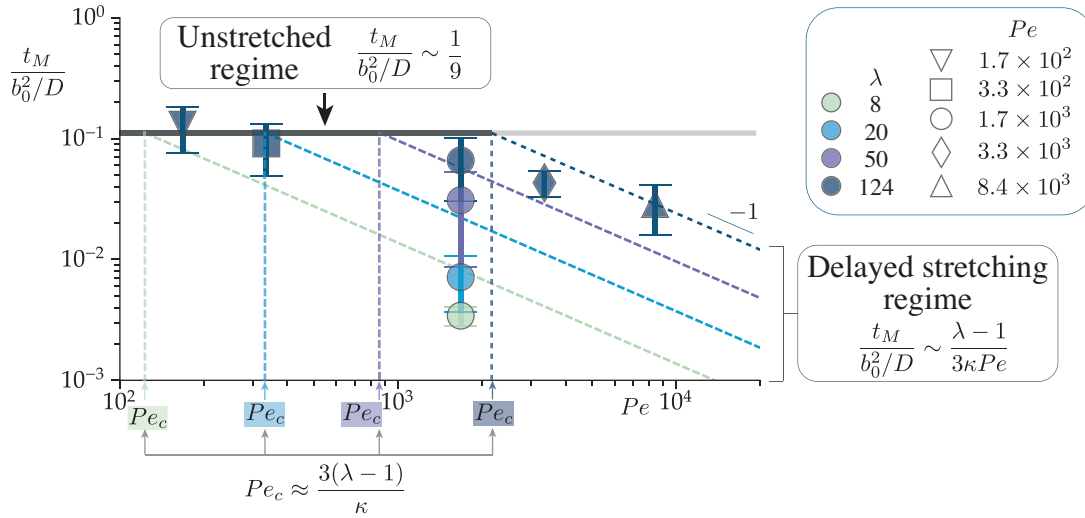


FIGURE IV.13: Global map of the dependence of the mixing time on λ and Pe . Symbols: measurements (geometric mean between the runs, errorbars indicate the standard deviation). Dashed colored lines: prediction for the *delayed stretching regime of mixing* expected in the limit of large Péclet ($Pe \gg Pe_c$, Eq. IV.18), when the mixing time is limited by the long delay t_{acc} before the blob stretches fast. Horizontal solid line: *unstretched regime of mixing* expected in the limit of low Pe ($Pe \ll Pe_c$, Eq. IV.19), when mixing occurs before the blob has significantly stretched.

IV.5 Conclusion

In the present chapter, we have extended our investigations to the case of a chaotic two-dimensional laminar stirring, where the flow in the bath is varying essentially randomly in space and time around the blob. We have presented experimental and theoretical results for the kinematics and the mixing of the blob, for a wide range of viscosity ratios $\lambda \in [1 - 124]$ and Péclet numbers $Pe \in [10^2 - 10^4]$.

We have seen that the phenomenology by which the blob mixes in such a chaotic flow is very different from that in a simple shear. In the chaotic flow, all blobs stretch and thin down, even those which are highly viscous. However, they stretch at a rate which depends strongly on the viscosity ratio with the bath and on how much the blob has already been stretched. Another crucial difference with the simple shear case, is that this stretching history is not deterministic anymore. It is by essence stochastic, with statistics set by those of the chaotic stirring flow, in particular, the mean stretching rate $\langle \dot{\epsilon} \rangle$ and the Lyapounov coefficient κ expressing the long term thinning of an isoviscous blob ($b_{\text{iso}}/b_0 \rightarrow e^{-\kappa \langle \dot{\epsilon} \rangle t}$).

On short times, when it is close to spherical, a more viscous blob thins down slower than an isoviscous one ($-\dot{b}/b \sim \kappa \langle \dot{\epsilon} \rangle / \lambda^{3/2}$). However, on longer times, when they are slender both blob stretch like the background chaotic flow ($-\dot{b}/b \rightarrow \kappa \langle \dot{\epsilon} \rangle$). In practice for a highly viscous blob, after a large delay needed to stretch the blob significantly ($t_{\text{acc}} \sim \lambda / \kappa \langle \dot{\epsilon} \rangle$), the blob is stretched very rapidly and mixed close to immediately by the chaotic flow. In this case, called *delayed stretching mixing regime* in figure IV.13, the blob is expected to be mixed in a time $t_M \sim \lambda / \kappa \langle \dot{\epsilon} \rangle$, which is purely set by the stirring intensity and the blob viscosity, with virtually no dependence on the diffusivity! This scaling in $\langle \dot{\epsilon} \rangle^{-1}$ is remarkable because it is the strongest possible dependence on the stirring intensity. It is also remarkable because it is at odd with the scaling $t_M \sim b_0^2 / D$ observed in the previous chapter for a simple shear (in the same limit of a large viscosity ratio and very large Péclet number), which has the lowest possible dependence $\dot{\gamma}^0$ on the stirring intensity!

The $t_M \propto \langle \dot{\epsilon} \rangle^{-1}$ scaling in a chaotic flow is only expected above a critical Péclet number ($Pe_c \sim \lambda / \kappa$), otherwise the blob mixes before it has hardly stretched, in a time $t_M \sim b_0^2 / D$ (called *unstretched regime of mixing* in figure IV.13). There is actually also an expected upper bound to the Péclet number for the scaling $t_M \propto \langle \dot{\epsilon} \rangle^{-1}$. But, this upper bound ($\ln \kappa Pe \sim \lambda$), set by the condition that the delay t_{acc} is much longer than the isoviscous mixing time, scales exponentially with the viscosity ratio λ , and is presumably not a concern in practice, for large λ .

This picture has been found to agree in magnitude, in trends and without fitting parameter, with the experiments, both for the dependence on the viscosity ratio and for the dependence on the Péclet number at large λ . It is rooted on an extension of the exact description of the non-diffusive kinematics introduced in the previous chapter to the case of a model chaotic flow. In particular, a stochastic approach of the problem has provided a powerful mean field description for the evolution of the average stretching over a large number of realizations. This has allowed us to relate the Lyapounov coefficient κ with the typical correlation strain scale of the chaotic flow $\langle \dot{\epsilon} \rangle \tau$, and therefore, to offer a prediction on how all the kinematics and the mixing regimes summarized above should depend on this correlation scale when it is small.

What needs to be further explored. As mentioned above, the stretching history of the blob is stochastic by essence. We have only documented the average evolution of the blob, which is close to sufficient when the correlation strain of the blob $\sim \langle \dot{\epsilon} \rangle \tau / \lambda$ is small and mixing only occurs after a very large number of correlation times ($t_M \gg \tau$). However, when the correlation strain of the blob is large, mixing should proceed within a few correlation times ($t_M \sim \tau$) and vary strongly from one realization to the other. In this case, documenting the variability would be interesting (though experimentally challenging) because it would bridge the gap between the picture of a steady flow described in the previous chapter and the

picture of a short correlation chaotic flow, described in this chapter. Last, the model chaotic flow we have considered is a *laminar* chaotic flow, in which the flow is not only changing rapidly in time but also slowly in space. It would therefore be particularly relevant to extend this study to the case when the smallest flow structures are smaller than the blob itself.

The detailed summary and the few perspectives given above are specific to this chapter on mixing in a chaotic flow. It is a step toward the global conclusion of this thesis that we will give in the next chapter.

Chapter V

Conclusion

We now reach the conclusion of this thesis. The goal was to investigate how two miscible liquids mix when their viscosities are unequal. We have chosen to study a single viscous and miscible heterogeneity, of spherical initial shape, mixed either by a simple shear or in a chaotic laminar flow, at low Reynolds and high Péclet numbers. Experiments have been conducted on three experimental setups; two for the two different types of flow, and one, without flow, to quantify the interdiffusion between liquids of different viscosity. A summary of the main results is presented in figure V.1, which highlights the different regimes of mixing identified for the two flows, specifying for each of them, the blob thinning kinematics, without diffusion ($Pe = \infty$) and with diffusion (finite Pe), the predicted mixing time and the relevant diffusion coefficient for the mixing of the dye.

Overall, the simple shear study has documented the remarkable *stretching-to-rolling* transition, when the viscosity ratio is increased above a critical value $\lambda_c \simeq 3.975$. Below this critical ratio, the blob stretches into a lamella, similarly to the isoviscous case. At large Péclet, mixing therefore occurs when the lamella is so thin that its thinning rate is not depending on the viscosity field anymore. This has allowed us to capture all details of the mixing process, by using the Ranz formalism with the stretch shift factor $\beta(\lambda)$ (see expression in Fig. V.1 caption), which embeds the short time overstretching ($\lambda < 1$) or substretching ($\lambda > 1$) of the blob relative to the isoviscous case. In this case, the blob mixing time follows $t_M \sim (\beta^2 Pe)^{1/3} \dot{\gamma}^{-1}$. For larger blob viscosities ($\lambda \gtrsim \lambda_c$), the mixing process is different. The blob motion converges to a quasi-steady rolling-like motion, which involves a recirculating region in the surrounding bath liquid, across which the mass transport to the far-field bath is essentially diffusive. This flow leads to a slow ‘dissolution-like’ process, with the somehow counterintuitive consequence that the mixing time, $t_M \sim b_0^2/D$, no longer depends on the stirring rate! In practice, this high viscosity ratio limit is found to persist down to viscosity ratios, $\lambda \sim 5$, which are very close to the critical value λ_c , indicating that the transition between the stretching and rolling regimes of mixing is very sharp. All these trends are supported by robust observations and a detailed modeling, which has been validated, without fitting parameters, against experiments covering wide ranges of viscosity ratios and Péclet numbers.

The picture in a chaotic laminar flow is very different. All blobs eventually stretch, whatever their viscosity, and once they have reached a significant aspect ratio ($a/b \gtrsim 1$), they all do so with essentially the same rate, which is the isoviscous stretching rate $\kappa \langle \dot{\epsilon} \rangle$, also called Lyapounov exponent of the flow. However, the time to reach such an aspect ratio, depends strongly on the viscosity ratio. The larger λ , the slower the initial stretching and, therefore, the longer the delay $\sim \lambda/\kappa \langle \dot{\epsilon} \rangle$ before the blob is rapidly stretched by the flow. In practice, for fairly viscous blobs ($\lambda \gtrsim \ln \kappa Pe$), the late stretching is so much faster than the initial one, that it mixes the blob completely within a time $\sim \ln(\kappa Pe)/\kappa \langle \dot{\epsilon} \rangle$ much shorter than the initial delay. In this limit, the mixing time is expected to be set by the initial delay $\sim \lambda/\kappa \langle \dot{\epsilon} \rangle$, which increases linearly with λ and is independent of diffusivity! This purely kinematic prediction provides a reasonable upper bound for the mixing times measured at large Péclet numbers ($Pe \gtrsim Pe_c \sim \lambda/\kappa$). At lower Péclet numbers ($Pe \lesssim Pe_c$), the blob is expected to start mixing during the slow initial stretching, which decreases its viscosity and shortens the delay before the blob is rapidly stretched. This means the

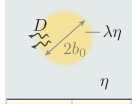
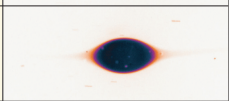
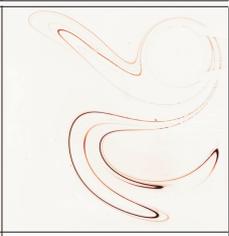
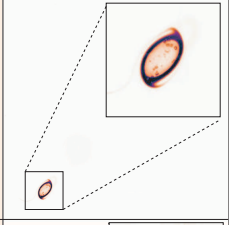
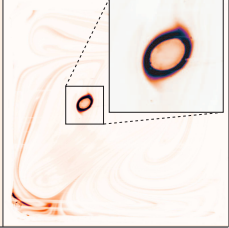
	Regime	Viscosity ratio	Blob width b/b_0		Mixing time for the dye t_M	Relevant diffusivity D	Typical observation
			No diffusion ($Pe = \infty$)	With diffusion (finite Pe)			
	Stretching	$\lambda \lesssim \lambda_c$	$\frac{\beta}{\dot{\gamma}t}$	$\frac{\beta}{\dot{\gamma}t} \sqrt{1 + \frac{2(\dot{\gamma}t)^3}{3\beta^2 Pe}}$	$\frac{\beta^{2/3}}{\dot{\gamma}} (3Pe)^{1/3}$	D_{dye}	
	Folding	$\lambda \sim \lambda_c$	$\frac{1}{\sqrt{\dot{\gamma}t}}$	\times	\times	\times	
	Rolling	$\lambda \gtrsim \lambda_c$	1	$\sqrt{1 - t/t_M}$	$\frac{b_0^2}{9D}$	D_η	
	Isoviscous-like stretching	$\lambda \gtrsim \frac{3}{2} \ln(2\kappa Pe)$	$\frac{1}{e^{\kappa\langle\dot{\epsilon}\rangle t}}$	$\frac{\sqrt{1 + \frac{e^{2\kappa\langle\dot{\epsilon}\rangle t}}{\kappa Pe}}}{e^{\kappa\langle\dot{\epsilon}\rangle t}}$	$\frac{\ln(2\kappa Pe)}{2\kappa\langle\dot{\epsilon}\rangle}$	D_{dye}	
	Delayed stretching	$Pe \gtrsim Pe_c$ & $\lambda \gtrsim \frac{3}{2} \ln(2\kappa Pe)$	At short time $e^{-\frac{\kappa\langle\dot{\epsilon}\rangle t}{(2\lambda/5)^{3/2}}}$ At long time $\frac{1}{e^{\kappa\langle\dot{\epsilon}\rangle t}}$	\times	$\frac{\lambda - 1}{3\kappa\langle\dot{\epsilon}\rangle}$	NO dependence	
	Unstretched	$Pe \lesssim Pe_c$ & $\lambda \gtrsim \frac{3}{2} \ln(2\kappa Pe)$	~ 1	\times	$\frac{b_0^2}{9D}$	D_η	

FIGURE V.1: *Summary of the results.* Evolution of the blob width b/b_0 , mixing time of the dye t_M , and typical observation, for the different regimes of mixing documented in a simple shear flow and a chaotic laminar flow, as a function of the two parameters of the problem: the viscosity ratio between the blob and the bath λ , and the Péclet number of the flow Pe . The other quantities are the critical viscosity ratio $\lambda_c \simeq 3.975$, the stretch-shift factor $\beta(\lambda) \simeq 1 + (\lambda - 1)(1 - \beta_0 - 0.1\lambda + 0.16\lambda^2)$, for $0 \leq \lambda \leq 3$, with $\beta_0 \simeq 0.431$, the critical Péclet number between the ‘delayed stretching’ and ‘unstretched’ mixing regimes $Pe_c \approx \frac{3(\lambda-1)}{\kappa}$, the dimensionless Lyapounov coefficient of the isoviscous flow κ , and the diffusivities of the dye D_{dye} and of the viscosity field D_η .

mixing time is equally shortened, and should asymptotically reach an upper bound $\sim b_0^2/D$, which is also found to be consistent, quantitatively, with measurements.

The above results deserve further comments.

On the type of flow and the mixing mechanisms: A first striking point is that mixing highly viscous blobs in a simple shear or in a chaotic laminar flow involves very different mechanisms, with opposite consequences. In a shear flow, the mixing time $t_M \sim b_0^2/D$ is only set by diffusion, with no dependence on the stirring rate, whereas in a chaotic laminar flow it follows $t_M \sim \lambda/\kappa\langle\dot{\epsilon}\rangle$, which is fully set by the flow speed and virtually independent of diffusivity. These trends are not only opposite but extreme (it is difficult to imagine dependences of t_M larger than $\langle\dot{\epsilon}\rangle^{-1}$ and D^{-1} , or smaller than $\dot{\gamma}^0$ and D^0). Nonetheless, they naturally emerge from the presence of a quasi-steady recirculating flow, in one case, and from the steep dependence of the creep of a viscous blob on its shape, for the other case.

On the *two* mixing problems in the mixing problem: It is crucial to realize that we have not monitored directly the homogenization of the viscosity field by the flow. We have tracked the homogenization of a dye, which diffusion is in practice only weakly correlated to that of the viscosity field (for the reasons, discussed in detail in Chapter II, related to how much dye we can put in each of the two liquids). Consistently, the mixing times t_M reported in figure V.1 are *those for the dye* concentration field. They depend on the dye diffusivity, D_{dye} , only when mixing occurs after a significant stretching of the blob ('stretching' regime in the shear flow and 'isoviscous-like stretching' in the chaotic flow). In this case, all mixing problems are independent, and the mixing time for the viscosity field (which we have not monitored) should also be set by its own diffusivity (D_η). The situation is different when mixing occurs *before* the blob has significantly stretched ('rolling' regime), or *while* it does so ('unstretched' regimes). In that case, the kinematics remain determined at all time by the viscosity field. Therefore, in the present study where the dye effectively diffuses slower than the viscosity field ($D_{\text{dye}} \ll D_\eta$), the mixing time of the *dye*, is set by the diffusivity of the *viscosity* D_η , because the latter controls when the blob will be stretched fast and mixed almost instantaneously.

More generally, this key remark stresses that two different questions can actually be addressed: how does the viscosity field mix? and how does another scalar initially segregated in one of the two liquids mix? Though the diffusion of the viscosity field and of the scalar can be partly correlated in some cases (like in our study where the dye is bound to some of the polymers), this is not necessarily true. For instance, if the viscosity contrast is due, not to a difference in composition, but to a difference in temperature in a bath with a strong temperature dependence of viscosity, viscosity diffuses as fast as heat ($D_\eta = D_T \sim 10^{-7} \text{ m}^2/\text{s}$), i.e., orders of magnitude faster than molecules of dye ($D_{\text{scalar}} = D_\eta \sim 10^{-11} \text{ m}^2/\text{s}$ or much less in some cases). The opposite situation is also possible. For viscosity contrasts due to a difference in composition and a negligible dependence of viscosity on temperature, the diffusivity of the viscosity field ($D_\eta \sim 10^{-10} \text{ m}^2/\text{s}$, or less), which follows, for instance, that of some polymers, would be much smaller than that of the scalar, i.e., heat ($D_{\text{scalar}} = D_T \sim 10^{-7} \text{ m}^2/\text{s}$). The first situation ($D_{\text{scalar}} \ll D_\eta$) corresponds to the one we have experimentally faced, and the mixing times of both the viscosity and the scalar have been discussed in the previous paragraph. In the latter case ($D_{\text{scalar}} \gg D_\eta$), one would expect the same scalings in all the regimes of mixing reported in figure V.1, except that the relevant diffusivity should be the (fast) scalar diffusivity $D = D_{\text{scalar}}$ in all cases, because even if the blob keeps rolling, for instance, the scalar will have homogenized before the viscosity.

On diffusion and the feedback on advection: At the beginning of this thesis, two major specificities have been anticipated, regarding the mixing of viscosity heterogeneities relative to the standard isoviscous case. The first one was that a non-uniform viscosity could induce a spatial variation of the diffusion coefficient. The second was that diffusion, by changing the fluid viscosity, could retroact on the flow kinematics. Interestingly, in practice, the experimental observations are well explained by models considering a constant diffusivity. This is related to the fact that for solutions of long chain polymers, the diffusivity is not inversely proportional to the viscosity, but is driven by the mobility of the water molecules, which does not depend too strongly on the mass fraction of polymers within the range we have used.

As for the feedback of diffusion on advection, this point relates to the two mixing problems discussed above. There is no feedback anytime the mixing of the viscosity field occurs *after* the blob has significantly stretched (Stretching, Isoviscous-like stretching and Delayed stretching regimes), because by that time the blob is so slender that viscosity does not affect the flow anymore. There is a feedback in all other situations. This is explicit in figure V.1, where the relevant diffusivity is D_η , only in these last situations.

On the generality and relevance to other flows: Some last comments about the general relevance of the two flows we have studied. At first sight, the simple shear flow might seem a very specific flow and, indeed, the fact that the transition to a rolling-like motion occurs at such a low viscosity ratio ($\lambda_c \sim 4$) is

due to the large vorticity of this flow. However, from the Eshelby formalism we have used, we anticipate that, except for a purely extensional flow (having no vorticity), a sufficiently viscous blob will undergo a rolling motion in *all* steady linear flows. Theoretically, the critical viscosity ratio λ_c is simply shifted towards larger values, as the vorticity of the flow is decreased, but the stretching to rolling transition should persist as well as the $t_M \approx b_0^2/D$ scaling (only the prefactor $\frac{1}{9}$ should shift towards lower values).

As for chaotic flows, the experiments and rationalization we have provided concern flows for which the correlated stretch of the blob is small. But this can actually be realized even when the correlation strain scale of the chaotic flow itself $\sim \langle \dot{\epsilon} \rangle \tau$ is large, provided the blob is sufficiently viscous, such that its *own* correlation strain scale $\sim \langle \dot{\epsilon} \rangle \tau / \lambda$ is small. Our experiments and models also concern *laminar* chaotic flows, for which the flow is changing slowly in space, and it is possible that mixing follows a different phenomenology when flow structures are smaller than the blob (see also below).

Future research

In the short term

We list below some experiments that we would like to perform in the short term, to further explore the problem and strengthen certain of our conclusions.

- In the simple shear, we have clarified the stretching and rolling regimes. However, most of the *folding* regime has remained unexplored, in particular the destabilization of the substretched lamella, the possibility of a cascade mechanism, and the size and mixing time of the formed sub-blobs.
- In the rolling regime, we would like to perform additional experiments with varied blob size, in order to confirm the b_0^2 dependence of the mixing time.
- Performing experiments with a tracer that is not biased by the yield effect, i.e., which efficiency does not depend on the water concentration, would give access to the evolution of the viscosity field at large viscosity ratio and reveal the details of the mixing inside the rolling blob.

On a longer term

We also propose two possible extensions to the present thesis.

Mixing viscous heterogeneities in turbulent flows: Our study has focused on low Reynolds number flows. A natural extension would be to explore inertial flows, in particular highly inertial turbulent flows. Preliminary observations have been made in collaboration with Gautier Verhille from IRPHÉ laboratory, in Marseille. Highly viscous blobs have been injected in his ‘washing-machine’ generating a highly turbulent isotropic flow [129]. Figure V.2 shows the typical phenomenology for two blobs with viscosity ratios of $\lambda = 10^3$ (top) and $\lambda = 40 \times 10^3$ (bottom). In both cases, the blob is eventually stretched and mixed, but its ‘lifetime’ shows a strong dependence on the viscosity ratio. For the 40-fold increase in λ , the ‘lifetime’ is increased by a factor over 10, and for the large viscosity ratios considered, it is orders of magnitude larger than the typically 10 ms long timescale of the flow ($\ell_T / \sqrt{\langle \mathbf{u}^2 \rangle}$, see details in the caption).

The turbulent flow case is interesting, because it differs in several aspects from the situations investigated in this thesis. First, it involves an additional dimensionless number, the Reynolds number. Moreover, turbulence involves a distribution of stirring scales. This means that some of the flow structures can be smaller than the blob, which could lead to different mechanisms of mixing. We also note that our protocol for controlling the blob initial shape is certainly suited for this case too.

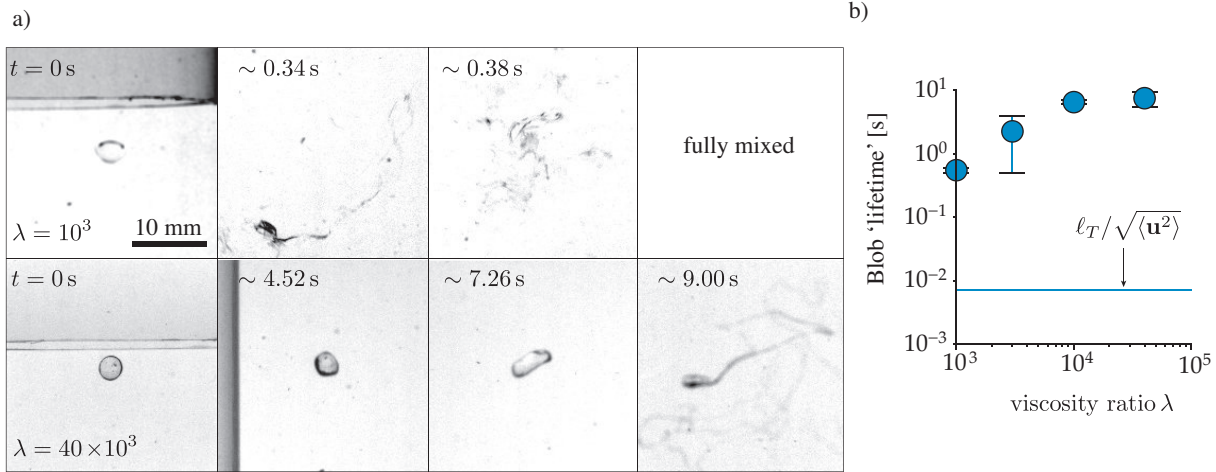


FIGURE V.2: *Perspectives – Mixing viscosity heterogeneities in a turbulent flow.* (a) Preliminary experiments with two viscous blobs of different viscosity ratio λ in a highly turbulent flow. The experiments have been done with Gautier Verhille, using his octaedron ‘washing machine’ device [129]. The blob size $2b_0 \approx 3$ mm is slightly larger than the Taylor scale $\ell_T = \sqrt{15\eta\langle u^2 \rangle / \varepsilon} \approx 1.40$ mm, with ε the rate of energy dissipation of the flow. The typical inverse shear rate of the flow $\ell_T / \sqrt{\langle u^2 \rangle}$, at the Taylor scale, is of order 10 ms (the flow is close to isotropic, the Reynolds number at the Taylor scale is $Re_T = \rho\sqrt{\langle u^2 \rangle}\ell_T / \eta \approx 470$, the Kolmogorov lengthscale and timescale are $(\eta^3 / \rho^3 \varepsilon)^{1/4} \approx 30$ μ m and $\sqrt{\eta / \rho \varepsilon} \approx 1$ ms, respectively). (b) Rough estimate of the blob ‘lifetime’, before it is entirely stretched and mixed by the flow, as a function of the viscosity ratio (same flow conditions as in (a)).

Towards ‘mixing’ granular suspensions: Last, the dispersion of a ‘cloud’ of particles immersed and sheared in a viscous fluid [130], which is illustrated in figure V.3, could be revisited and extended in light of the present study. In this problem, the heterogeneity in viscosity is not due to the composition of the liquid, but to the addition of solid particles. Beside its relevance to engineering applications where particulate systems are mixed (e.g. concrete, plaster,...), this problem has interesting connections with some of the phenomenologies reported in this thesis. In particular, one can wonder whether the dispersion time of the heterogeneity can be understood. Whether there is a critical volume fraction above which rolling and delayed dispersion would be observed. Whether the shear-induced dispersion of the particles in this athermal system could play a role similar to the molecular diffusion in the mixing problem.



FIGURE V.3: *Perspectives – ‘Mixing’ an heterogeneity in a particulate suspension.* Blob with a large volume fraction of solid particles sheared in a liquid bath. Left: initial condition. Right: after 10 ‘back and forth’ shear cycles with a strain amplitude $\gamma = 6$ (adapted from [130]).

Appendix A

Stochastic model of the blob kinematics in a chaotic flow in the large Pe limit

We detail here the stochastic model of the large Péclet deformation kinematics of an initially spherical blob in a laminar chaotic flow mentioned in chapter IV.

As discussed in chapter IV, the idea of the model is to consider that as the viscous blob is advected by and through the chaotic flow, it experiences rapidly changing flow conditions, which we model as a sequence of short random linear flow periods, with a fixed duration τ , no correlation between successive periods, and full correlation within each of them (see Fig. A.1). For each period i the strain rate in the bath, $\dot{\epsilon}_i$, the rotation rate in the bath, ω_i , and initial orientation of the strain direction, φ_i , are randomly sorted from the model distribution of $\dot{\epsilon}$, ω and φ obtained from the isoviscous flow characterization (see Fig. A.1c). This implies that during each period the blob dimensions (a , b , c) and orientation relative to the main strain direction φ evolve through

$$\begin{aligned} \frac{\dot{a}}{a} &= \mathcal{A}\left(\frac{a}{b}, \frac{b}{c}, \lambda\right) \cos 2\varphi \dot{\epsilon}_i, & \frac{\dot{b}}{b} &= -\mathcal{B}\left(\frac{a}{b}, \frac{b}{c}, \lambda\right) \cos 2\varphi \dot{\epsilon}_i, \\ \frac{\dot{c}}{c} &= -\frac{\dot{a}}{a} - \frac{\dot{b}}{b}, & \dot{\varphi} &= \omega_i - \mathcal{F}\left(\frac{a}{b}, \frac{b}{c}, \lambda\right) \sin 2\varphi \dot{\epsilon}_i, \end{aligned} \quad (\text{A.1})$$

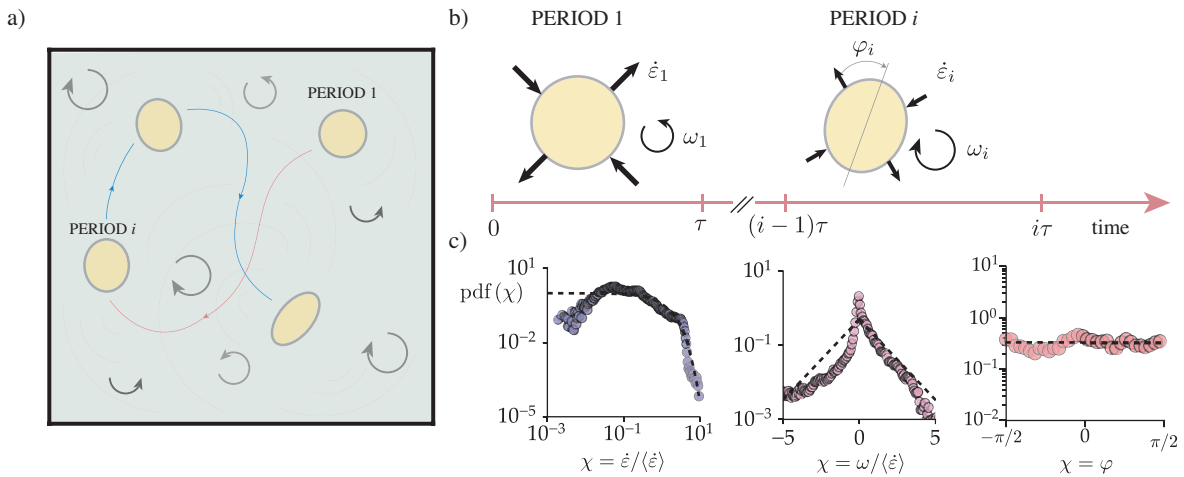


FIGURE A.1: (duplicate of Fig. IV.11). Modeling of the chaotic flow in the bath by a random sequence of linear flows. (a) Schematics of the blob advection by and through the chaotic flow. (b) The flow experienced by the blob is modeled as a sequence of random linear flow periods, with a fixed duration τ , no correlation between successive periods, and full correlation within each of them. (c) For each period i the strain rate in the bath, $\dot{\epsilon}_i$, the rotation rate in the bath, ω_i , and initial orientation of the strain direction, φ_i , are randomly sorted from the model distribution (dashed lines) of $\dot{\epsilon}$, ω and φ obtained from the isoviscous flow characterization (see §IV.2).

where the geometrical and viscosity dependent factors \mathcal{A} , \mathcal{B} and \mathcal{F} , which set the deformation rate *inside* the blob, are the same as those introduced in §III.2.2 to treat the simple shear case.

The system A.1 couples non trivially the blob viscosity (λ), the current flow ($\dot{\epsilon}_i, \omega_i$), with its variability (pdf($\dot{\epsilon}_i$), pdf(ω_i)) and its persistence time (τ), as well as the current shape and orientation of the blob ($a/b, b/c, \varphi$). It can be tackled by two different paths, that we will follow successively. First, a mean-field approximation, which can be made analytical in the limit we are interested in, when the correlation time of the chaotic flow is short. Second, a ‘brute force’ numerical resolution for a very large number of random flow sequences, which does not use any approximation and allows to validate the first approach.

A.1 Mean field approximation	114
A.1.1 Derivation	114
A.1.2 Isoviscous case & link with the Lyapounov exponent	115
A.1.3 Case of a highly viscous blob ($\lambda \gg 1$)	116
A.2 Brute force simulations	118

A.1 Mean field approximation

In the limit we are interested in, where the correlation strain scale of the blob $\sim \dot{\epsilon}\tau/\lambda$ is small, the system A.1 can be simplified into a much more tractable mean-field system for the evolution of the mean field variables (ensemble averages) $\langle a \rangle$, $\langle b \rangle$ and $\langle c \rangle$, by averaging successively over the random initial orientations of the blob φ_i , over the statistics of $\dot{\epsilon}_i$ and ω_i , and over the duration τ of each period.

A.1.1 Derivation

We consider, first, a single arbitrary period i starting at $t = (i - 1)\tau$. For a small correlation strain scale ($\dot{\epsilon}\tau/\lambda \ll 1$) the blob does not deform much over the period duration τ and the value of \mathcal{A} , \mathcal{B} and \mathcal{F} can therefore be considered as constant, to the first order, over each period. Similarly, the orientation φ does not vary much from the random initial value φ_i . It can therefore be sought for as $\varphi(t') = \varphi_i + \delta\varphi(t')$, with $\delta\varphi(t') \ll 1$ and $t' = t - (i - 1)\tau$ the time since the beginning of the period. Linearizing the last equation in A.1 yields

$$\dot{\delta\varphi} = \omega_i - \mathcal{F} \dot{\epsilon}_i \sin(2\varphi_i + 2\delta\varphi) \simeq \omega_i - \mathcal{F} \dot{\epsilon}_i \sin 2\varphi_i,$$

which can be time integrated to obtain the reorientation of the blob in the flow

$$\delta\varphi \simeq (\omega_i - \mathcal{F} \dot{\epsilon}_i \sin 2\varphi_i) t'. \quad (\text{A.2})$$

To obtain the mean field evolution equation for $\langle a \rangle$, we start by averaging the instantaneous equation for a (the first one in A.1) over the random initial orientation φ_i , which gives, at first order,

$$\begin{aligned} \left\langle \frac{\dot{a}}{a} \right\rangle_{\varphi_i} &\simeq \mathcal{A} \dot{\epsilon}_i \langle \cos 2\varphi_i \rangle_{\varphi_i} - \mathcal{A} \dot{\epsilon}_i \langle \sin 2\varphi_i \times 2\delta\varphi \rangle_{\varphi_i}, \\ &\simeq -\mathcal{A} \dot{\epsilon}_i \langle \sin 2\varphi_i \times 2\delta\varphi \rangle_{\varphi_i}, \end{aligned}$$

after noticing that $\langle \cos 2\varphi_i \rangle_{\varphi_i} = 0$. Injecting the linearized expression A.2 for the small reorientation $\delta\varphi$ (and making use of $\langle \sin 2\varphi_i \rangle_{\varphi_i} = 0$) gives

$$\begin{aligned} \left\langle \frac{\dot{a}}{a} \right\rangle_{\varphi_i} &\simeq -2\mathcal{A} \dot{\varepsilon}_i \omega_i t' \langle \sin 2\varphi_i \rangle_{\varphi_i} + 2\mathcal{A}\mathcal{F} \dot{\varepsilon}_i^2 t' \langle \sin 2\varphi_i^2 \rangle_{\varphi_i}, \\ &\simeq \mathcal{A}\mathcal{F} \dot{\varepsilon}_i^2 t', \end{aligned}$$

where we see that the rotation rate ω_i does not contribute to the averaged kinematics (at first order and in the present case when ω_i is not much larger than $\dot{\varepsilon}_i$ on average).

The next step is to average both over the period duration ($0 < t' < \tau$) and over the statistics of $\dot{\varepsilon}_i$ prescribed by the distribution pdf($\dot{\varepsilon}$) to obtain the period-averaged mean field stretching rate of the blob

$$\begin{aligned} \frac{\langle \dot{a} \rangle}{\langle a \rangle} &\simeq \left\langle \frac{\dot{a}}{a} \right\rangle \equiv \left\langle \frac{\dot{a}}{a} \right\rangle_{\varphi_i, t', \dot{\varepsilon}_i} \simeq \mathcal{A}\mathcal{F} \langle \dot{\varepsilon}_i^2 \rangle_{\dot{\varepsilon}_i} \langle t' \rangle_{0 < t' < \tau}, \\ &\simeq \mathcal{A}\mathcal{F} \frac{\langle \dot{\varepsilon}^2 \rangle \tau}{2}, \end{aligned}$$

where the values of \mathcal{A} , \mathcal{B} and \mathcal{F} are those corresponding to the current mean field deformation $\frac{\langle a \rangle}{\langle b \rangle}, \frac{\langle b \rangle}{\langle c \rangle}$. An exactly similar expression is obtained for the mean field thinning rate

$$\frac{\langle \dot{b} \rangle}{\langle b \rangle} \simeq -\mathcal{B}\mathcal{F} \frac{\langle \dot{\varepsilon}^2 \rangle \tau}{2}.$$

Importantly, the evolutions of the three dimensions of the blob ($\langle a \rangle$, $\langle b \rangle$, $\langle c \rangle$) involve the same factor $\frac{\langle \dot{\varepsilon}^2 \rangle \tau}{2} \mathcal{A}\mathcal{F}$, which means that they can be recasted into the following form

$$\frac{1}{\langle a \rangle} \frac{\partial \langle a \rangle}{\partial T} = \mathcal{A} \left(\frac{\langle a \rangle}{\langle b \rangle}, \frac{\langle b \rangle}{\langle c \rangle}, \lambda \right), \quad \frac{1}{\langle b \rangle} \frac{\partial \langle b \rangle}{\partial T} = -\mathcal{B} \left(\frac{\langle a \rangle}{\langle b \rangle}, \frac{\langle b \rangle}{\langle c \rangle}, \lambda \right), \quad (\text{A.3})$$

which exactly matches that for a steady extensional flow (see §IV.3.3), albeit for the rate of the evolution set by the following relation between the real time t and the warped time T

$$\frac{\partial t}{\partial T} = \frac{2}{\langle \dot{\varepsilon}^2 \rangle \tau} \frac{1}{\mathcal{F} \left(\frac{\langle a \rangle}{\langle b \rangle}, \frac{\langle b \rangle}{\langle c \rangle}, \lambda \right)}. \quad (\text{A.4})$$

The mean field equations A.3 and A.4 apply to all periods except the first one, because at the beginning of the first period the blob is a sphere and, therefore, φ_i is not random but equal to 0. This implies that the initial condition to A.3 and A.4 is

$$\langle a \rangle \simeq e^{(\dot{\varepsilon})\tau/\Lambda}, \quad \langle b \rangle \simeq e^{-(\dot{\varepsilon})\tau/\Lambda}, \quad \text{at } t = \tau, \quad (\text{A.5})$$

where the rate $\langle \dot{\varepsilon} \rangle / \Lambda$ is the mean field average of the close-to-sphere rate $\dot{\varepsilon}_1 / \Lambda$ [87].

A.1.2 Isoviscous case & link with the Lyapounov exponent

As a reference case and also to make the link between the flow characteristics and the Lyapounov exponent, it is insightful to first apply the mean field formalism to the kinematics of an isoviscous blob ($\lambda = 1$). In this case one has

$$\mathcal{A} = \mathcal{B} = 1, \quad \mathcal{F} = \frac{a^2 - b^2}{a^2 + b^2},$$

(omitting from now on the averaging symbol $\langle \cdot \rangle$, for the sake of clarity) so that

$$a = e^T, \quad b = e^{-T}, \quad \frac{\partial t}{\partial T} = \frac{2}{\langle \dot{\varepsilon}^2 \rangle \tau} \frac{e^{2T} - e^{-2T}}{e^{2T} + e^{-2T}}. \quad (\text{A.6})$$

At long times ($T \gg 1$), Eq. A.6 becomes $\frac{\partial t}{\partial T} = 1$, which means that the isoviscous blob will eventually stretch like $e^{-\frac{\langle \dot{\varepsilon}^2 \rangle \tau}{2} t}$ when it is slender enough. This allows us to identify the Lyapunov exponent as

$$\kappa = \frac{\langle \dot{\varepsilon}^2 \rangle \tau}{2 \langle \dot{\varepsilon} \rangle}.$$

At short time, the blob is not slender, which implies that its stretching rate differs from that of a single fluid segment given by the Lyapunov exponent κ (the short time rate is larger because a close to spherical blob will align more rapidly with the main strain direction than a slender one). However, this transient only last for a is very short time $t \sim \frac{1}{\kappa \langle \dot{\varepsilon} \rangle}$. Indeed, integrating Eq. A.6 yields $t = \tau + \frac{1}{2\kappa \langle \dot{\varepsilon} \rangle} \ln \frac{e^{2T} + e^{-2T}}{e^{2\langle \dot{\varepsilon} \rangle \tau} + e^{-2\langle \dot{\varepsilon} \rangle \tau}}$, which follows $t \simeq \tau + \frac{1}{\kappa \langle \dot{\varepsilon} \rangle} (T^2 - \langle \dot{\varepsilon} \rangle^2 \tau^2)$ for $T \ll 1$. This gives the typical following thinning rate for the isoviscous case:

$$\begin{aligned} -\frac{\dot{b}}{b} &\simeq \frac{1}{2} \sqrt{\frac{\kappa \langle \dot{\varepsilon} \rangle}{t - \tau}}, & \text{for } \tau < t \lesssim \frac{1}{\kappa \langle \dot{\varepsilon} \rangle}, \\ -\frac{\dot{b}}{b} &= \kappa \langle \dot{\varepsilon} \rangle, & \text{for } t \gg \frac{1}{\kappa \langle \dot{\varepsilon} \rangle}. \end{aligned}$$

A.1.3 Case of a highly viscous blob ($\lambda \gg 1$)

For a blob more viscous than the bath, the evolution of the stretching rate is non monotonic. At very short times, the blob deviates from the spherical shape and realigns more slowly with the main strain direction, which decreases its average stretching rate (just like for the isoviscous case), but on longer times the blob is so slender that its own viscosity becomes unimportant and the long term isoviscous rate (Lyapunov exponent) is recovered.

For a viscosity ratio much above one ($\lambda \gg 1$) the maximal rate is obtained for a small deviation from the sphere, which allows to approximate the function \mathcal{A} , \mathcal{B} and \mathcal{F} by their first order development close to a sphere

$$\mathcal{A} = \mathcal{B} = \frac{1}{\Lambda}, \quad \mathcal{F} = \frac{1 + \Lambda(a - b)}{a - b}. \quad (\text{A.7})$$

At the smallest order in T , Eq. A.7 gives

$$a \simeq e^{T/\Lambda}, \quad b \simeq e^{-T/\Lambda}, \quad t \simeq t_0 + \frac{\Lambda}{4\kappa} \ln \frac{1 + 4T^2}{\Lambda},$$

with $t_0 \simeq (1 - \frac{2\langle \dot{\varepsilon} \rangle^2}{\langle \dot{\varepsilon}^2 \rangle}) \tau$ an integration constant set by the initial condition A.5. The thinning rate follows

$$-\frac{\dot{b}}{b} \simeq \frac{\langle \dot{\varepsilon} \rangle}{t_T} \simeq \frac{\kappa \langle \dot{\varepsilon} \rangle}{\Lambda^{3/2}} \frac{e^{\frac{4}{\Lambda} \kappa (t - t_0)}}{\sqrt{e^{\frac{4}{\Lambda} \kappa (t - t_0)} - 1}}, \quad (\text{A.8})$$

which recovers a similar short time trend as for the isoviscous $-\dot{b}/b \simeq \frac{1}{2\Lambda} \sqrt{\frac{\kappa\langle\dot{\epsilon}\rangle}{t-t_0}}$. The thinning rate given by Eq. A.8 is minimal for $e^{\frac{4}{\Lambda}\kappa(t-t_0)} = 2$, with a minimal value

$$-\dot{b}/b|_{\min} \simeq \frac{2\kappa}{\Lambda^{3/2}}.$$

The minimum is reached at a time $t \simeq \frac{\ln 2}{4} \frac{\Lambda}{\kappa\langle\dot{\epsilon}\rangle}$ of the order of the acceleration onset time t_{acc} , which actually sets the typical thinning rate over most of the slow stretching transient:

$$\kappa_{\text{eff}} \approx \frac{2\kappa}{\Lambda^{3/2}}. \quad (\text{A.9})$$

To determine the onset time of the fast stretching regime t_{acc} itself, which occurs when the blob has significantly deviated from a sphere, the close-to-sphere approximation A.7 is not precise enough. We therefore rely on a numerical integration of the mean field system (Eqs. A.3 and A.4). The mean field time evolution of the blob width b/b_0 is presented in figure A.2a for $\lambda = 30, 100$ and 300 and a Lyapounov exponent $\kappa = 0.17$ matching the experimental value in our chaotic flow. As for the steady extensional flow, we extract t_{acc} from the time shift of the long time stretching regime (see Fig. A.2a). The values of t_{acc} are reported in figure A.2b as a function of the viscosity ratio λ . They are found to follow closely

$$t_{\text{acc}} \simeq \left(1 + \frac{3 \ln \frac{\Lambda}{4}}{10}\right) \frac{\lambda - 1}{3\kappa\langle\dot{\epsilon}\rangle}, \quad (\text{A.10})$$

which has also been validated with larger values of λ and smaller values of κ (not shown), and is in practice close to the heuristic value $\frac{\lambda-1}{3\kappa\langle\dot{\epsilon}\rangle}$ derived in Chapter IV, for the range of viscosity investigated experimentally.

Last, figure A.2a also confirms that the width b_{acc} at the onset of the fast stretching regime does not vary much with λ . It also suggests that the actual value of b_{acc}/b_0 is somehow closer to 0.8 or 0.9, than to the value $e^{-1} \approx 0.4$ adopted for the heuristic model.

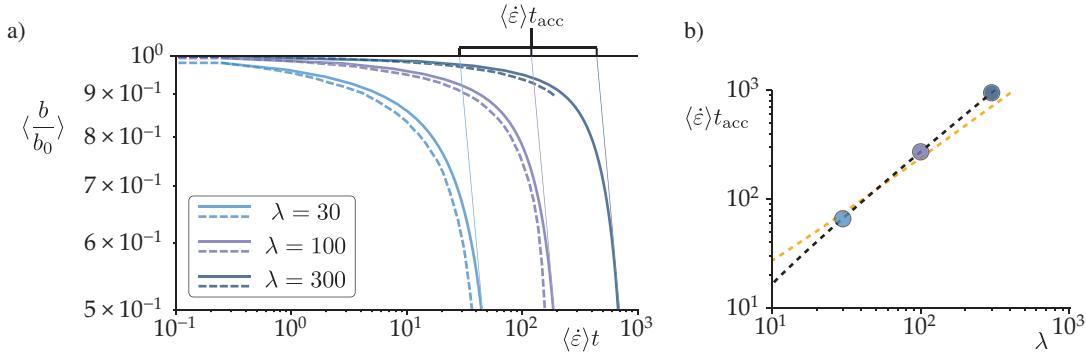


FIGURE A.2: *Deformation kinematics of the blob in a random sequence of linear flows – Mean field model.* (a) Normalized blob width versus accumulated strain. Solid thick lines: mean field approximation (time-integration of Eqs. A.3–A.5). Dashed lines: geometric average of the brute force simulation of Eq. A.1 (the period duration is set to $\tau = 2\langle\dot{\epsilon}\rangle\kappa/\langle\dot{\epsilon}^2\rangle \approx 3$ s with $\kappa = 0.17$). Solid thin line: long term stretching rate. (b) Onset time for the fast stretching regime. Symbols: values extracted from the integration of the mean field model. Solid line: Eq. A.10. Orange dashed line: equation obtained from the heuristic model in chapter IV (Eq. IV.10).

A.2 Brute force simulations

To validate the mean field approximation presented above, we also perform brute force simulations of the exact system A.1 for a large number of random flow sequences. For each period i , the values $\dot{\varepsilon}_i$, ω_i , and φ_i are randomly sorted from the model distribution of $\dot{\varepsilon}$, ω and φ obtained from the isoviscous flow characterization (see Fig. A.1 and §IV.2). The partial differential equation A.1 is time integrated from $t_i = (i - 1)\tau$ to $t = i\tau$. For the first period, the initial condition is $a_1(0) = b_1(0) = c_1(0) = 1$ and $\varphi_i = 0$, since the blob is initially a sphere. For all subsequent periods, it is set by the blob dimensions at the end of the previous period, $a_i(t_i) = a_{i-1}(t_i)$, $b_i(t_i) = b_{i-1}(t_i)$, $c_i(t_i) = c_{i-1}(t_i)$, with a random initial orientation, $\varphi(t_i) = \varphi_i$. The process is iterated over the successive periods until a sufficient stretching is obtained.

Figure A.3a presents the thinning history $b(t)/b_0$ for a sample of 100 random flow sequences and a viscosity ratio $\lambda = 30$. The thick blue line shows the evolution of the geometrical average of the width over 1000 realizations. Figure A.3b reports the average of b for different viscosity ratios λ ranging from 1 to 300.

The average thinning kinematics from the brute force simulations are also reported in figure A.2, where it is found to match the mean field approximation closely. This confirms that the results obtained from the mean field approximation, assuming a small correlation strain scale, are relevant for the typical Lyapounov number $\kappa \sim 0.2$ and viscosity ratios investigated experimentally.

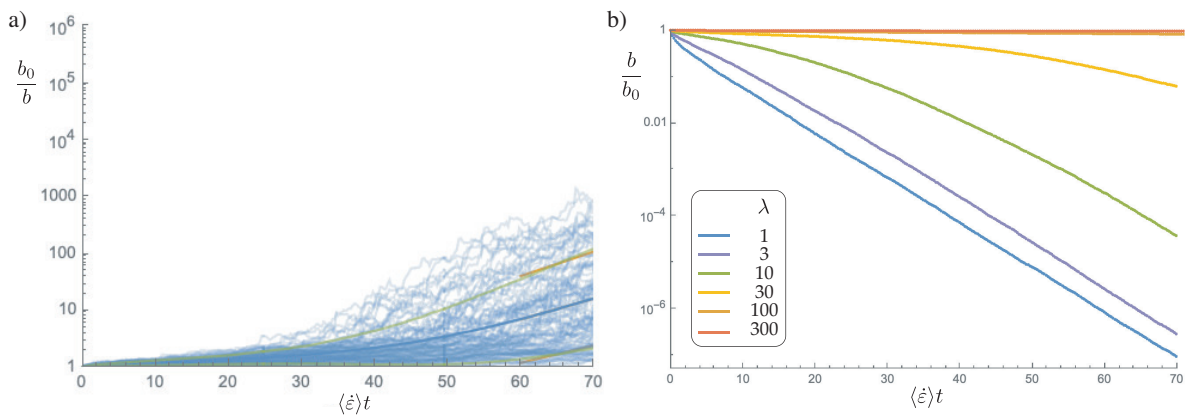


FIGURE A.3: Deformation kinematics of the blob in a random sequence of linear flows – Brute force numerical resolution. (a) Evolution of the blob width for a sample of 100 realizations of the random flow (thin blue lines) and geometric mean over 1000 realizations (thick blue lines). The viscosity ratio is $\lambda = 30$. The period duration is $\tau = 4$ s. (b) Average evolution of the blob width for different viscosity ratio (geometric mean over 1000 realizations).

Bibliography

- [1] E. Villiermaux, “Mixing versus stirring”, *Annu. Rev. Fluid Mech.* **51**, 245–273 (2019).
- [2] J. Ottino, “Lamellar mixing models for structured chemical reactions and their relationship to statistical models; macro- and micromixing and the problem of averages”, *Chemical Engineering Science* **35**, 1377–1381 (1980).
- [3] D. V. Khakhar, H. Rising, and J. M. Ottino, “Analysis of chaotic mixing in two model systems”, *J. Fluid Mech.* **172**, 419–451 (1986).
- [4] D. Khakhar, J. Franjione, and J. Ottino, “A case study of chaotic mixing in deterministic flows: the partitioned-pipe mixer”, *Chemical Engineering Science* **42**, 2909–2926 (1987).
- [5] P. D. Swanson and J. M. Ottino, “A comparative computational and experimental study of chaotic mixing of viscous fluids”, *J. Fluid Mech.* **213**, 227–249 (1990).
- [6] E. Villiermaux and J. Duplat, “Mixing is an aggregation process”, *Comptes Rendus Mécanique* **331**, 515–523 (2003).
- [7] F. Goirand, T. Le Borgne, and S. Lorthois, “Network-driven anomalous transport is a fundamental component of brain microvascular dysfunction”, *Nat. Commun.* **12**, 7295 (2021).
- [8] D. Spence, J. Ockendon, P. Wilmott, D. Turcotte, and L. Kellogg, “Convective mixing in the mantle: the role of viscosity differences”, *Geophys. J. Int.* **95**, 79–86 (1988).
- [9] G. Metcalfe, C. R. Bina, and J. Ottino, “Kinematic considerations for mantle mixing”, *Geophysical research letters* **22**, 743–746 (1995).
- [10] M. Manga, “Mixing of heterogeneities in the mantle: effect of viscosity differences”, *Geophysical Research Letters* **23**, 403–406 (1996).
- [11] N. M. Du Vignaux and L. Fleitout, “Stretching and mixing of viscous blobs in earth’s mantle”, *Journal of Geophysical Research: Solid Earth* **106**, 30893–30908 (2001).
- [12] D. J. Stevenson, “A planetary perspective on the deep earth”, *Nature* **451**, 261–265 (2008).
- [13] B. Kumar, J. Schumacher, and R. A. Shaw, “Cloud microphysical effects of turbulent mixing and entrainment”, *Theoretical and Computational Fluid Dynamics* **27**, 361–376 (2013).
- [14] J. Woodhead, “Mixing it up in the mantle”, *Nature* **517**, 275–276 (2015).
- [15] C.-c. P. Caulfield, “Open questions in turbulent stratified mixing: do we even know what we do not know?”, *Phys. Rev. Fluids* **5**, 110518 (2020).
- [16] C.-c. P. Caulfield, “Layering, instabilities, and mixing in turbulent stratified flows”, *Annu. Rev. Fluid Mech.* **53**, 113–145 (2021).
- [17] A. Celani, A. Lanotte, A. Mazzino, and M. Vergassola, “Fronts in passive scalar turbulence”, *Phys. Fluids* **13**, 1768–1783 (2001).
- [18] A. Celani, E. Villiermaux, and M. Vergassola, “Odor landscapes in turbulent environments”, *Phys. Rev. X* **4**, 041015 (2014).

- [19] T. Le Borgne, M. Dentz, and E. Villermaux, "Stretching, coalescence, and mixing in porous media", *Phys. Rev. Lett.* **110**, 204501 (2013).
- [20] I. Markale, M. Carrel, D. L. Kurz, V. L. Morales, M. Holzner, and J. Jiménez-Martínez, "Internal biofilm heterogeneities enhance solute mixing and chemical reactions in porous media", *Environmental Science & Technology* **57**, PMID: 37205794, 8065–8074 (2023).
- [21] Y. Kamidaira, Y. Uchiyama, H. Kawamura, T. Kobayashi, and A. Furuno, "Submesoscale mixing on initial dilution of radionuclides released from the Fukushima Daiichi nuclear power plant", *Journal of Geophysical Research: Oceans* **123**, 2808–2828 (2018).
- [22] A. De Wit and G. Homsy, "Viscous fingering in reaction-diffusion systems", *The Journal of chemical physics* **110**, 8663–8675 (1999).
- [23] C. Almarcha, Y. R'Honi, Y. De Decker, P. Trevelyan, K. Eckert, and A. De Wit, "Convective mixing induced by acid–base reactions", *J. Phys. Chem. B* **115**, 9739–9744 (2011).
- [24] A. De Wit, "Chemo-hydrodynamic patterns and instabilities", *Annu. Rev. Fluid Mech.* **52**, 531–555 (2020).
- [25] J. Henderson, "The raw materials of early glass production", *Oxford Journal of Archaeology* **4**, 267–291 (1985).
- [26] P.-T. Brun, C. Inamura, D. Lizardo, G. Franchin, M. Stern, P. Houk, and N. Oxman, "The molten glass sewing machine", *Philosophical Transactions of the Royal Society A: Mathematical, Physical and Engineering Sciences* **375**, 20160156 (2017).
- [27] D. Paul and J. Barlow, "Polymer blends", *Journal of Macromolecular Science—Reviews in Macromolecular Chemistry* **18**, 109–168 (1980).
- [28] C. Roland, "Rheology of a miscible polymer blend", *Journal of Polymer Science Part B: Polymer Physics* **26**, 839–856 (1988).
- [29] J. P. Valdés, L. Kahouadji, and O. K. Matar, "Current advances in liquid–liquid mixing in static mixers: a review", *Chemical Engineering Research and Design* **177**, 694–731 (2022).
- [30] T. K. Perkins and O. Johnston, "A review of diffusion and dispersion in porous media", *Society of Petroleum Engineers Journal* **3**, 70–84 (1963).
- [31] M. Dentz, J. J. Hidalgo, and D. Lester, "Mixing in porous media: concepts and approaches across scales", *Transport in Porous Media* **146**, 5–53 (2023).
- [32] T. Zwietering, "Suspending of solid particles in liquid by agitators", *Chemical Engineering Science* **8**, 244–253 (1958).
- [33] J. M. Ottino et al., "Mixing, chaotic advection, and turbulence", *Annu. Rev. Fluid Mech.* **22**, 207–254 (1990).
- [34] S. Mirfasihi, W. Basu, P. Martin, A. Kowalski, C. P. Fonte, and A. Keshmiri, "Investigation of mixing miscible liquids with high viscosity contrasts in turbulently stirred vessels using electrical resistance tomography", *Chemical Engineering Journal* **486**, 149712 (2024).
- [35] S. M. Kresta, A. W. Etchells III, D. S. Dickey, and V. A. Atiemo-Obeng, *Advances in industrial mixing: a companion to the handbook of industrial mixing* (John Wiley & Sons, 2015).
- [36] M. Zhang, Y. Hu, W. Wang, T. Shao, and Y. Cheng, "Intensification of viscous fluid mixing in eccentric stirred tank systems", *Chemical Engineering and Processing - Process Intensification* **66**, 36–43 (2013).

- [37] R. A. Pethrick, "Design and ageing of adhesives for structural adhesive bonding—a review", *Proceedings of the Institution of Mechanical Engineers, Part L: Journal of Materials: design and applications* **229**, 349–379 (2015).
- [38] W. E. Ranz, "Applications of a stretch model to mixing, diffusion, and reaction in laminar and turbulent flows", *AIChE Journal* **25**, 41–47 (1979).
- [39] J. Ottino, W. Ranz, and C. Macosko, "A framework for description of mechanical mixing of fluids", *AIChE Journal* **27**, 565–577 (1981).
- [40] E. Villermaux and C. Innocenti, "On the geometry of turbulent mixing", *J. Fluid Mech.* **393**, 123–147 (1999).
- [41] N. Hoffman and D. McKenzie, "The destruction of geochemical heterogeneities by differential fluid motions during mantle convection", *Geophys. J. Int.* **82**, 163–206 (1985).
- [42] E. Gouillart, N. Kuncio, O. Dauchot, B. Dubrulle, S. Roux, and J.-L. Thiffeault, "Walls inhibit chaotic mixing", *Phys. Rev. Lett.* **99**, 114501 (2007).
- [43] H. Aref, J. R. Blake, M. Budišić, S. S. Cardoso, J. H. Cartwright, H. J. Clercx, K. El Omari, U. Feudel, R. Golestanian, E. Gouillart, et al., "Frontiers of chaotic advection", *Reviews of Modern Physics* **89**, 025007 (2017).
- [44] J. Duplat, C. Innocenti, and E. Villermaux, "A nonsequential turbulent mixing process", *Phys. Fluids* **22** (2010).
- [45] T. Le Borgne, M. Dentz, and E. Villermaux, "The lamellar description of mixing in porous media", *J. Fluid Mech.* **770**, 458–498 (2015).
- [46] M. Kree and E. Villermaux, "Scalar mixtures in porous media", *Phys. Rev. Fluids* **2**, 104502 (2017).
- [47] M. Souzy, I. Zaier, H. Lhuissier, T. Le Borgne, and B. Metzger, "Mixing lamellae in a shear flow", *J. Fluid Mech.* **838**, R3 (2018).
- [48] R. Turuban, H. Lhuissier, and B. Metzger, "Mixing in a sheared particulate suspension", *J. Fluid Mech.* **916**, R4 (2021).
- [49] G. I. Taylor, "Dispersion of soluble matter in solvent flowing slowly through a tube", *Proceedings of the Royal Society of London. Series A. Mathematical and Physical Sciences* **219**, 186–203 (1953).
- [50] G. I. Taylor, "Conditions under which dispersion of a solute in a stream of solvent can be used to measure molecular diffusion", *Proceedings of the Royal Society of London. Series A. Mathematical and Physical Sciences* **225**, 473–477 (1954).
- [51] R. Aris, "On the dispersion of a solute in a fluid flowing through a tube", *Proceedings of the Royal Society of London. Series A. Mathematical and Physical Sciences* **235**, 67–77 (1956).
- [52] J. Marshall and F. Schott, "Open-ocean convection: observations, theory, and models", *Reviews of geophysics* **37**, 1–64 (1999).
- [53] B. Stevens, "Atmospheric moist convection", *Annu. Rev. Earth Planet. Sci.* **33**, 605–643 (2005).
- [54] D. Lohse and K.-Q. Xia, "Small-scale properties of turbulent rayleigh-bénard convection", *Annu. Rev. Fluid Mech.* **42**, 335–364 (2010).
- [55] B. Duplantier, "Le mouvement brownien, "divers et ondoyant"", *séminaire Poincaré* **1**, 155–212 (2005).
- [56] R. Brown, "Xxvii. a brief account of microscopical observations made in the months of june, july and august 1827, on the particles contained in the pollen of plants; and on the general existence of active molecules in organic and inorganic bodies", *The philosophical magazine* **4**, 161–173 (1828).

- [57] A. Einstein, "Über die von der molekularkinetischen theorie der wärme geforderte bewegung von in ruhenden flüssigkeiten suspendierten teilchen", *Ann. Phys.* **4** (1905).
- [58] W. Sutherland, "Lxxv. a dynamical theory of diffusion for non-electrolytes and the molecular mass of albumin", *The London, Edinburgh, and Dublin Philosophical Magazine and Journal of Science* **9**, 781–785 (1905).
- [59] M. Von Smoluchowski, "Zur kinetischen theorie der brownschen molekularbewegung und der suspensionen", *Ann. Phys.* **326**, 756–780 (1906).
- [60] P. Langevin et al., "Sur la théorie du mouvement brownien", *CR Acad. Sci. Paris* **146**, 530–533 (1908).
- [61] J. Perrin, *Les atomes* (1913).
- [62] J. Fourier, "Théorie analytique de la chaleur: paris", *Académie des Sciences* **3** (1822).
- [63] A. Fick, "V. on liquid diffusion", *The London, Edinburgh, and Dublin Philosophical Magazine and Journal of Science* **10**, 30–39 (1855).
- [64] M. Souzy, "Mélange dans les suspensions de particules cisillées à bas nombre de reynolds", PhD thesis (Aix Marseille Université, 2016).
- [65] M. S. Plesset and S. Zwick, "A nonsteady heat diffusion problem with spherical symmetry", *J. Appl. Phys.* **23**, 95–98 (1952).
- [66] E. S. Shaqfeh and D. L. Koch, "Polymer stretch in dilute fixed beds of fibres or spheres", *J. Fluid Mech.* **244**, 17–54 (1992).
- [67] D. R. Lester, M. Dentz, and T. Le Borgne, "Chaotic mixing in three-dimensional porous media", *J. Fluid Mech.* **803**, 144–174 (2016).
- [68] M. Souzy, H. Lhuissier, E. Villermaux, and B. Metzger, "Stretching and mixing in sheared particulate suspensions", *J. Fluid Mech.* **812**, 611–635 (2017).
- [69] F. Muzzio, P. Swanson, and J. Ottino, "The statistics of stretching and stirring in chaotic flows", *Phys. Fluids A: Fluid Dynamics* **3**, 822–834 (1991).
- [70] P. Meunier and E. Villermaux, "The diffusive strip method for scalar mixing in two dimensions", *J. Fluid Mech.* **662**, 134–172 (2010).
- [71] G. G. Stokes et al., "On the effect of the internal friction of fluids on the motion of pendulums", (1851).
- [72] C. Wilke and P. Chang, "Correlation of diffusion coefficients in dilute solutions", *AIChE journal* **1**, 264–270 (1955).
- [73] D. Pearson, G Ver Strate, E Von Meerwall, and F. Schilling, "Viscosity and self-diffusion coefficient of linear polyethylene", *Macromolecules* **20**, 1133–1141 (1987).
- [74] P.-G. de Gennes, "Entangled polymers", *Physics Today* **36**, 33–39 (1983).
- [75] P.-G. De Gennes, *Introduction to polymer dynamics* (CUP Archive, 1990).
- [76] E. B. Brown, E. S. Wu, W. Zipfel, and W. W. Webb, "Measurement of molecular diffusion in solution by multiphoton fluorescence photobleaching recovery", *Biophysical Journal* **77**, 2837–2849 (1999).
- [77] D. W. McCall, D. C. Douglass, and D. Falcone, "Nuclear magnetic relaxation in polytetrafluoroethylene", *J. Phys. Chem.* **71**, 998–1004 (1967).
- [78] J. E. Tanner and K.-J. Liu, "Nmr studies of polymer solutions. ix. time averaging of spectra to determine high molecular weight polymers", *Die Makromolekulare Chemie: Macromolecular Chemistry and Physics* **142**, 309–312 (1971).

- [79] H. Y. Carr and E. M. Purcell, "Effects of diffusion on free precession in nuclear magnetic resonance experiments", *Phys. Rev.* **94**, 630 (1954).
- [80] D. Paul, "Measurement of diffusion coefficients for concentrated binary polymer solutions", *Industrial & Engineering Chemistry Fundamentals* **6**, 217–222 (1967).
- [81] H. Al-Chalabi and E. McLaughlin, "Mutual and self-diffusion in binary mixtures", *Molecular Physics* **19**, 703–715 (1970).
- [82] A. C. Ribeiro, V. M. Lobo, D. G. Leaist, J. J. Natividade, L. P. Veríssimo, M. C. Barros, and A. M. Cabral, "Binary diffusion coefficients for aqueous solutions of lactic acid", *Journal of Solution Chemistry* **34**, 1009–1016 (2005).
- [83] E. Guilbert and E. Villermaux, "Chemical reactions rectify mixtures composition", *Phys. Rev. Fluids* **6**, L112501 (2021).
- [84] D. Anderson, J. Hall, and A. Babb, "Mutual diffusion in non-ideal binary liquid mixtures", *J. Phys. Chem.* **62**, 404–408 (1958).
- [85] M. Ye, R. Composto, and R. Stein, "A modified optical schlieren technique for measuring the mutual diffusion coefficient in polymer blends", *Macromolecules* **23**, 4830–4834 (1990).
- [86] G. B. Jeffery, "The motion of ellipsoidal particles immersed in a viscous fluid", *Proceedings of the Royal Society of London. Series A, Containing papers of a mathematical and physical character* **102**, 161–179 (1922).
- [87] G. I. Taylor, "The formation of emulsions in definable fields of flow", *Proceedings of the Royal Society of London. Series A, containing papers of a mathematical and physical character* **146**, 501–523 (1934).
- [88] D. Di Giusto, L. Bergougnoux, C. Marchioli, and É. Guazzelli, "Influence of small inertia on jeffery orbits", *J. Fluid Mech.* **979**, A42 (2024).
- [89] A. Einstein, "Berichtigung zu meiner arbeit: eine neue bestimmung der moleküldimensionen", *Ann. Phys.* **339**, 591–592 (1911).
- [90] R. Cox, I. Zia, and S. Mason, "Particle motions in sheared suspensions xxv. streamlines around cylinders and spheres", *Journal of Colloid and Interface Science* **27**, 7–18 (1968).
- [91] H. P. Grace, "Dispersion phenomena in high viscosity immiscible fluid systems and application of static mixers as dispersion devices in such systems", *Chemical Engineering Communications* **14**, 225–277 (1982).
- [92] S. Torza, R. Cox, and S. Mason, "Particle motions in sheared suspensions xxvii. transient and steady deformation and burst of liquid drops", *Journal of colloid and interface science* **38**, 395–411 (1972).
- [93] F.-D. Rumscheidt and S. Mason, "Particle motions in sheared suspensions xii. deformation and burst of fluid drops in shear and hyperbolic flow", *Journal of Colloid Science* **16**, 238–261 (1961).
- [94] B. Kalb, R. Cox, and R. S. J. Manley, "Hydrodynamically induced formation of cellulose fibers: ii. fiber formation by deformation of drops with zero interfacial tension", *Journal of Colloid and Interface Science* **82**, 286–297 (1981).
- [95] J. Rallison, "The deformation of small viscous drops and bubbles in shear flows", *Annu. Rev. Fluid Mech.* **16**, 45–66 (1984).
- [96] H. A. Stone, "Dynamics of drop deformation and breakup in viscous fluids", *Annu. Rev. Fluid Mech.* **26**, 65–102 (1994).

- [97] G. I. Taylor, "The viscosity of a fluid containing small drops of another fluid", *Proceedings of the Royal Society of London. Series A, Containing Papers of a Mathematical and Physical Character* **138**, 41–48 (1932).
- [98] C. E. Chaffey and H. Brenner, "A second-order theory for shear deformation of drops", *Journal of Colloid and Interface Science* **24**, 258–269 (1967).
- [99] R. Cox, "The deformation of a drop in a general time-dependent fluid flow", *J. Fluid Mech.* **37**, 601–623 (1969).
- [100] N. Frankel and A. Acrivos, "The constitutive equation for a dilute emulsion", *J. Fluid Mech.* **44**, 65–78 (1970).
- [101] J. Rallison, "Note on the time-dependent deformation of a viscous drop which is almost spherical", *J. Fluid Mech.* **98**, 625–633 (1980).
- [102] M. Tjahjadi and J. Ottino, "Stretching and breakup of droplets in chaotic flows", *J. Fluid Mech.* **232**, 191–219 (1991).
- [103] M. Manga and H. Stone, "Buoyancy-driven interactions between two deformable viscous drops", *J. Fluid Mech.* **256**, 647–683 (1993).
- [104] B. Bilby, J. Eshelby, and A. Kundu, "The change of shape of a viscous ellipsoidal region embedded in a slowly deforming matrix having a different viscosity", *Tectonophysics* **28**, 265–274 (1975).
- [105] J. D. Eshelby, "The determination of the elastic field of an ellipsoidal inclusion, and related problems", *Proceedings of the royal society of London. Series A. Mathematical and physical sciences* **241**, 376–396 (1957).
- [106] C. A. Florek and C. L. Tucker, "Stretching distributions in chaotic mixing of droplet dispersions with unequal viscosities", *Phys. Fluids* **17** (2005).
- [107] S. Comas-Cardona and C. L. Tucker III, "Measurements of droplet deformation in simple shear flow with zero interfacial tension", *Journal of Rheology* **45**, 259–273 (2001).
- [108] R. Callendar and D. G. Leaist, "Diffusion coefficients for binary, ternary, and polydisperse solutions from peak-width analysis of Taylor dispersion profiles", *Journal of solution chemistry* **35**, 353–379 (2006).
- [109] D. Siebel, P. Scharfer, and W. Schabel, "Prediction of diffusion in a ternary solvent–solvent–polymer blend by means of binary diffusion data: comparison of experimental data and simulative results", *Journal of Applied Polymer Science* **133**, <https://doi.org/10.1002/app.43899> (2016).
- [110] M. J. Hargather and G. S. Settles, "A comparison of three quantitative schlieren techniques", *Optics and Lasers in Engineering* **50**, *Advances in Flow Visualization*, 8–17 (2012).
- [111] G. S. Settles and M. J. Hargather, "A review of recent developments in schlieren and shadowgraph techniques", *Measurement Science and Technology* **28**, 042001 (2017).
- [112] B. R. Sutherland, S. B. Dalziel, G. O. Hughes, and P. Linden, "Visualization and measurement of internal waves by 'synthetic schlieren'. part 1. vertically oscillating cylinder", *J. Fluid Mech.* **390**, 93–126 (1999).
- [113] S. Wang, E. D. von Meerwall, S.-Q. Wang, A. Halasa, W.-L. Hsu, J. Zhou, and R. Quirk, "Diffusion and rheology of binary polymer mixtures", *Macromolecules* **37**, 1641–1651 (2004).
- [114] M. Adda-Bedia, S. Kumar, F. Lechenault, S. Moulinet, M. Schillaci, and D. Vella, "Inverse leidenfrost effect: levitating drops on liquid nitrogen", *Langmuir* **32**, PMID: 27054550, 4179–4188 (2016).

- [115] E. D. Wetzel and C. L. Tucker, "Droplet deformation in dispersions with unequal viscosities and zero interfacial tension", *J. Fluid Mech.* **426**, 199–228 (2001).
- [116] B. A. Bilby and M. Kolbuszewski, "The finite deformation of an inhomogeneity in two-dimensional slow viscous incompressible flow", *Proceedings of the Royal Society of London. A. Mathematical and Physical Sciences* **355**, 335–353 (1977).
- [117] T. Cubaud and T. G. Mason, "Swirling of viscous fluid threads in microchannels", *Phys. Rev. Lett.* **98**, 264501 (2007).
- [118] C.-S. Yih, "Stability of liquid flow down an inclined plane", in *Selected papers by chia-shun yih: (in 2 volumes)* (World Scientific, 1991), pp. 357–370.
- [119] C.-S. Yih, "Instability due to viscosity stratification", *J. Fluid Mech.* **27**, 337–352 (1967).
- [120] G. Taylor, "Kinematic reversibility", *Multi-Media Fluid Mechanics CD-ROM* (2000).
- [121] A. Acrivos, "Heat transfer at high pecelet number from a small sphere freely rotating in a simple shear field", *J. Fluid Mech.* **46**, 233–240 (1971).
- [122] G. Poe and A. Acrivos, "Closed streamline flows past small rotating particles: heat transfer at high pécelet numbers", *International Journal of Multiphase Flow* **2**, 365–377 (1976).
- [123] G. Batchelor, "Mass transfer from a particle suspended in fluid with a steady linear ambient velocity distribution", *J. Fluid Mech.* **95**, 369–400 (1979).
- [124] C. Bielinski, L. Xia, G. Helbecque, and B. Kaoui, "Mass transfer from a sheared spherical rigid capsule", *Phys. Fluids* **34** (2022).
- [125] Y. Wang, D. Vazquez Alvarez, H. Wan, R. Gonzalez Pizarro, and F. Shu, "Advection-enhanced heat and mass transport from neutrally suspended droplet in simple shear flow", *Phys. Fluids* **35** (2023).
- [126] J. M. Ottino, *The kinematics of mixing: stretching, chaos, and transport*, Vol. 3 (Cambridge university press, 1989).
- [127] P. Meunier and T. Leweke, "Analysis and treatment of errors due to high velocity gradients in particle image velocimetry", *Experiments in fluids* **35**, 408–421 (2003).
- [128] M. Souzy, H. Lhuissier, Y. Méheust, T. Le Borgne, and B. Metzger, "Velocity distributions, dispersion and stretching in three-dimensional porous media", *J. Fluid Mech.* **891**, A16 (2020).
- [129] G. Verhille, "Deformability of discs in turbulence", *J. Fluid Mech.* **933**, A3 (2022).
- [130] B. Metzger and J. E. Butler, "Clouds of particles in a periodic shear flow", *Phys. Fluids* **24** (2012).